Università degli Studi di Napoli Federico II

Ph.D Thesis on Fundamental and Applied Physics

cycle XXI

Development of a transportable atom interferometer operating as inertial and gravity sensor

Advisor:
Prof. **Guglielmo Maria Tino**

Candidate:
Dott. **Antonio Giorgini**

Referee:
Prof. **Lorenzo Marrucci**

Referee:
Dr. **Rosario De Rosa**

Dipartimento Di Scienze Fisiche Università di Napoli Federico II
Via Cinthia, I-80125, Napoli, Italy

Dipartimento Di Fisica Università di Firenze
and
European Laboratory for Non-linear Spectroscopy (LENS)
Polo Scientifico Università di Firenze
Via Sansone 1,
I-50019 Sesto Fiorentino (Firenze)
Italy

Abstract

Atom Interferometry methods open new prospectives for absolute acceleration measurements; the quantum features of matter and the employment of atomic test masses with manipulation technique of internal and external degrees of freedom lead to a new generation of quantum sensors. In this thesis I present the development of a prototype for a transportable sensor at system and subsystem level. An instrument with such characteristics can find applications in many fields. The work has been developed in the framework of two European projects respectively oriented to the realization of an atom interferometry based absolute gravimeter for geophysical and metrological applications and to the realization of a Space Atom Interferometer for tests in micro–gravity environment.
In order to focus on the possible scientific landscape I briefly illustrate in the introduction the existing devices and their characteristic performances, pointing out how the atom interferometry may represent a valid alternative leading to a new generation of quantum devices. The study, the development and the realization stages for our instrument are presented either for the laser system realization and for the the implementation of the whole apparatus. This work leads to the development of a very compact atomic physics interferometric system responding to the scientific requirements that represent our target.
From the laser system side it has been realized also a complete and compact apparatus organized in a modular framework with stand alone components characterized by high working performances. This laser subsystem also includes laser sources in an external cavity configuration specially oriented to transportable apparatuses; they are characterized by an intrinsical passive stability, robustness and very narrow emission linewidth.
The experience with neutral atom manipulation and with atom cooling and trapping technique has been integrated with a direct implementation, characterization and optimization of a Two Dimensional Magneto–Optical Trap as a cold atoms source for an operating Atom Interferometer. Such kind of implementation represents a fundamental topic for a transportable sensor realization.

keywords: *atom interferometry, inertial sensor, absolute gravity measurement, transportable devices*

Acknowledgment

This thesis work presents an experience which is born and grown at the Physics Department of Università degli studi di Firenze with the financial and scientific support of some European Institutions and research organizations. The Ph.D didactic and scientific learning trail has been accomplished under the supervision of the Università degli studi di Napoli Federico II. I wish to mention and acknowledge all the institutions and the people involved.

Università degli Studi di Napoli
Federico II

Università degli Studi di Firenze
Dipartimento di Fisica

European Space Agency
Space Atom Interferometer *project*

European Community
FINAQS, STREP *project*

Consiglio Nazionale Ricerche
Istituto di Cibernetica *Eduardo Caianiello*,
Pozzuoli, Napoli

Contents

Introduction, acceleration sensors and Atom Interferometry

From the early Stephen Chu's studies in Stanford (1992) it has been demonstrated as the atom interferometry represents a powerful method to develop absolute gravity measurement devices characterized by high accuracy performances [55, 61, 62, 63]. As we are going to see the enhancement is due to the employment of microscopic test masses and to the management of the quantum features of the matter.
In last years there was a growing interest in the possible application of such new generation of absolute devices that were going to be configured. From the meeting with Geophysical community by one side, and with the Space Physics community on the other, it has been clear how Atom Interferometry based accelerometers, if transportable from the lab to different research environments, can represent an useful resource and a prospective for the future. In this introductory section we want to present at the first the actual landscape on which transportable sensors can be employed, with a preliminary look to the ground based existing devices for the gravity measurement and to their principal characteristics. We want to provide then a brief introduction about the ongoing research application of gravity measurement in geophysics field, and in space born experiments. After having been presented Atom Interferometry basic principles it follows a treatment of the main two projects from which this work was born: The Absolute gravimeter apparatus and the Space Atom Interferometer for micro–gravity tests.

Existing devices for gravity measurement, relative and absolute gravimeters

In order to measure gravitational acceleration two types of devices can be employed grouped into the categories of *absolute* and *relative* gravimeters. To

the first category instruments addressing a direct gravity measurement from a time or length measurement belong, typically they can be derived from the free falling test mass physical model. On the other side to the relative devices category belong instruments from which the gravity measurement depends from indirect parameters such as spring constants, which cannot be readily determined. Even if developed in complex implementations these devices can be in principle described starting from the basic mass–spring model. The early instrument for absolute gravity measurement was designed by *H. Kater* [4]; it was based on the reversible pendulum principle where the period T, the length of the mathematical equivalent pendulum L and the gravity acceleration g are related from the simple relationship $T = 2\pi\sqrt{L/g}$. The resulting accuracy is of the order of $\Delta g/g \simeq 10^{-4}$. This kind of device was used for the first gravity measurement survey in 1939s in Europe and in North America.

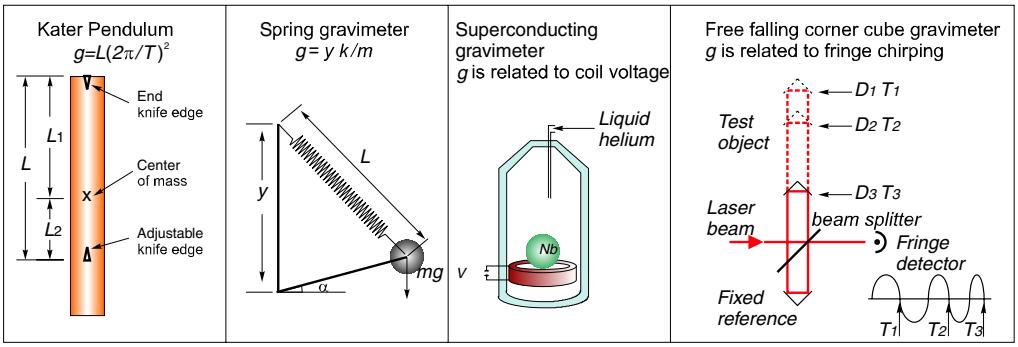

Figure 1: Examples of existing devices for gravity measurement. Relative working principles are illustrated, it's possible to distinguish between *relative* and *absolute* devices.

In order to introduce to the spring gravimeter we can start by considering a mass m bound on a massless spring with elastic constant k and total length L. A spring elongation δL corresponds to a gravity acceleration in agreement to the simple law $k\delta L = mg$, this means that to the mass–spring system also corresponds an oscillation period $T = 2\pi\sqrt{m/k}$. From there it follows that the sensitivity of a spring gravimeter is inversely proportional to the square of the oscillation. The new generation of spring gravimeters is based on zero length springs and it has been designed to have a very large oscillation period T. For devices mounted in the configuration shown in picture (1b) changes in gravity acceleration g can be measured from changes in y–length parameter. The main error source is due to the elongation measurement y that

leads to an error around $50 \times 10^{-8}\ m\ s^{-2}$. The second error source is due to spring hysteresis that leads to errors in gravity measurement of order of $1.5 \times 10^{-6}\ m\ s^{-2}$.
A superconductor gravimeter is a relative device working on the principle of a test mass levitation in a magnetic field. Gravity changes are compensated by the applied electrostatic force and the readout consists in a voltage measurement derived from the coils current: somehow it can be considered as an electro–magnetic mass–spring system (picture 1b). The instrument results in very high performances and sensitivity ($< 10^{-8}\ m\ s^{-2}$), but it is definitely not portable; on the other side interruptions due for example to liquid helium refilling, can reset the calibration factor that means the given relation between current readout and g measurement.
Besides the *Kater* pendulum, the free falling corner cube is at now the most advanced instrument for absolute gravity measurement also available as a commercial (but expensive) device (FG5 [130], shown in pict. (2)–right). In this setup a corner cube mirror represents the free falling test mass placed as the end mirror of one of the arms of a Michelson interferometer. The gravity estimation is derived from a length path interferometric measurement technic: during the mirror dropping a sensor reads the interference signal as a function of time. The detected signal is related to the number of half wavelength of interferometric light covered during the free fall. The typical dropping distance is around 20 cm, from fitting of the x and t values a measurement of g can be extrapolated (see picture (1c)). The main sources of errors stand in the wavelength λ uncertainty, electronic counting and timing errors, ground accelerations and non–gravitational forces. The last two sources dominate and result as the main limit in the instrument performances. Seismic noise affects the fixed mirror resulting in an error in gravity measurement $10^{-6}\ g$; such effect is limited by means of the employment of a super spring as active isolation system. The typical accuracy achieved is $4 \times 10^{-8}\ m\ s^{-2}$, but there are also some further implemented setup with better performances. One of the disadvantages for this instrument consists into the data continuous acquisition time limited to one week. On the other side the most accurate versions for this device are not transportable.
Nowadays gravimetric survey are conducted in open field by means of spring gravimeters, because of the easy transportability and of the quick use, whereas superconducting devices and corner cube gravimeters are used at fixed sites. In this research field also Global Position System (GPS) actually represents a fundamental tool for gravity reference network implementations in order to tracking the positions and for environment effects monitoring.

	Spring	Superconducting	Free Felling
Noise $(\Delta g/g)/\sqrt{Hz}$)	5×10^{-9}	1×10^{-12}	5×10^{-8}
Drift $\Delta g/g$	1.5×10^{-6} per month	1×10^{-9} per year	–
Accuracy $\Delta g/g$	–	–	4×10^{-9}
Measurement	relative	relative	absolute
Size (m^3)	0.04	~ 1.5	1.5
Weight (kg)	14	~ 320	127
Power (W)	24	400	350
Error Sources	Temperature and random drift, space and time variable calibration	magnetic and electrostatic effect	thermal drift magnetic and electrostatic effect

Figure 2: Transportable devices for gravity measurement, *spring relative gravimeter* (left), *absolute corner cube optical gravimeter* (*FG5*) (right), Micro–g LaCoste [130].

Some Geophysical Applications of Gravimetry, Volcano Monitoring.

In this thesis we are not going to deal with specific aspect connected to the micro–gravity changes in Earth environment; our point of view will be focused on the sensor development. For such purpose an evaluation of effects

and relative gravity variations could be interesting to provide.
The gravity value on planet Earth is a variable quantity in time and in space: it ranges between $9.78 \div 9.83$ m/s. Besides the well known height and latitude effects, gravity value changes depend upon many factors connected either with astronomical effects such as tides, moon and sun interactions, and with local sources density variation, but also with Earth shape or spin variation. In this research field the defined measure unity is called "Galileo" ($1\mathbf{Gal} \equiv 0.01$ m/s), usually micro–gravimetry land surveys are conducted in term of $\mu\ Gal = 10^{-8}$ m/s^2. The anomaly changes can be sorted for typical timescale variation: gravity changes due to Earth's spin or composition or shape changes appear over long timescale whereas variations due to tides or crustal variations happen on relative short timescale and also an high accuracy is needed to detect them.
Typical gravity changes due to moon or sun interaction range around $100 \div 200$ μGal, once the relative signal has been removed with help of well known models, the resulting detected signal represents the micro–gravity anomaly.
New technics have been approached in volcanology research field in order to investigate and monitoring the volcanoes activity. Temporal changes of the gravity field are related to sub surface mass/volume/density changes or elevation response to magmatic processes. According with the depth and rate evolution of the source, big changes can be detected in time and space. We brief report some results from volcanoes study and remand to specific literature for a detailed approach [14], [15], [16], [17]. In picture (3) it is reported the micro–gravity anomaly signal relative to the Etna eruption occurred during the night between 26 and 27 October 2002. A continuous micro–gravity sequence acquired with a LaCoste and Romberg spring gravimeters (pict. (2))[130] shows a marked gravity decrease of about 400 μGal in less then one hours and 4 hours before lava was first emitted from the eruptive fissures along NE–rift. The presented data displays the short–period reduced gravity signal, this means that Earth's tide effect (modeled) and the instrumental calibration time drift effect (first order curve) have been removed from such signal. Besides this aspects also ground tilt changes were measured (~ 30 μGal) together with height changes via GPS continuous monitoring $\Delta h \sim 20$ cm that means[1] $\Delta g \sim 50$ μGal.
On the other side we mention the paper from Battaglia, Robertz and Segall [14], as an example of geophysical application of long term gravity monitoring via a complex sensors network. In this study the *Long Valley* caldera has been monitored from July1982 to July 1998 for the uplift effects, changes of the depth of water table and local gravity variations. Uplifts associate

[1] $\Delta g/\Delta h = -2.33$ μGal/cm [18]

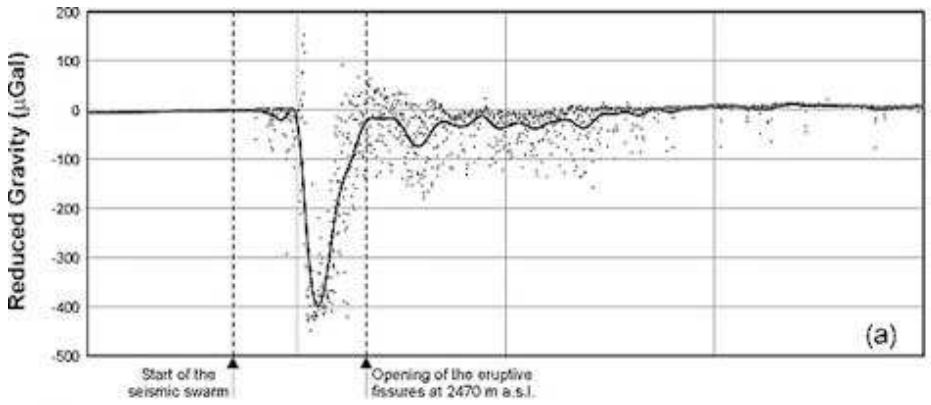

Figure 3: Etna Eruption began on October 2002, continuous micro–gravity sequence, a big anomaly announce the eruption [16].

with gravity increase remove the ambiguity between magmatic caldera intrusion and the possible thermal expansion and pressurization of the caldera hydrothermal system. Only micro–gravity measurement can discriminate between these processes. With a reference to the results in picture (4) the measurements show a residual gravity anomaly centered on a resurgent dome with a peak amplitude of 64 ± 16 μGal defined by a gravity changes in excess of 40 μGal at five stations. The positive residual gravity Δg_R signal suggests intrusion into the subcaldera crust, this residual change was used to constrain the density and the mass of deformation source.

Space Application of Gradiometry and Gravimetry, Spacecraft missions

From the 1990's The European Space Agency (ESA) has planned a new strategy for satellite Earth Observation (EO): "Living Planet Program". On the other side another program was inaugurated from NASA (National Aeronautics and Space Administration) with similar purposes: "Earth System Pathfinder Program". The main objectives for both sides are to further develop the knowledge of the complex Earth system. In this framework few space missions have been programmed for the Earth observation, from our point of view we focus as an example on the GOCE ESA mission (Gravity field and steady–state Ocean Circulation Explored) and on the GRACE NASA mission (Gravity Recovery And Climate Experiment). Both the missions, with similar methods, have the target to measure and to map the gravity field from satellite acquisitions. From this reference frame

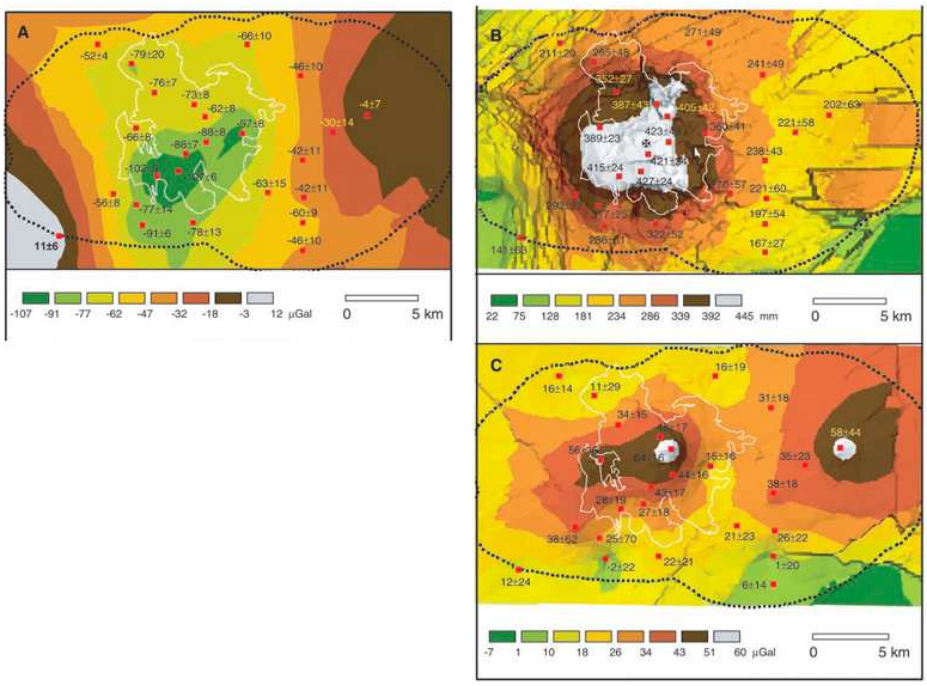

Figure 4: Gravity changes in Long Valley caldera measured between July 1982 to July 1998: (a) gravity changes (μGal), (b) uplifit, (c) residual gravity changes. White line marks the resurgent dome boundary [14].

it's possible a full acquisition of the geoid, defined from the Earth's gravity field as a surface of equal gravitational potential. A precise model for the Earth's geoid is fundamental in deriving accurate measurements of ocean circulation, sea level changes and terrestrial ice dynamics; of course all this parameters are affected by climatic changes. The GOCE is the last experiment in run in order of time with satellite launch in 2007. The fundamental objectives for this experiment can be summarized as: the determination of the Earth gravity field with an accuracy of 1 mGal via the measurement of the components of the gravity gradient tensor in combination with a satellite–to–satellite tracking and the determination of the geoid with an accuracy of 1 cm. These targets represent an useful support to many multi–disciplinary Earth research fields. The estimation of the quasi static marine geoid, in combination with satellite and in situ altimetry data, permits the quantitative determination of ocean circulation and transport of mass. On the other side the gravity data acquisition represent a big contribution for the understanding of the Earth geodynamics associated with the lithosphere and mantle composition. The measurement of gravity anomalies in combination

with topography technics also provides an useful instrument for the polar ices mass and thickness estimation.
The core of the described space missions is represented by a system of special designed space–born accelerometers based on an electrostatic working principle: Electrostatic Gravity Gradiometer (EGG). Each single device represents a relative gravimeter based on the measurement of the forces needed to maintain a proof mass at the center of a cage; a pair of these accelerometers are mounted on a carbon structure in order to realize a gradiometric configuration. The resulting performances are in the range of the atom interferometry based devices but, because they consist in relative instruments, they are affected from calibration drift.

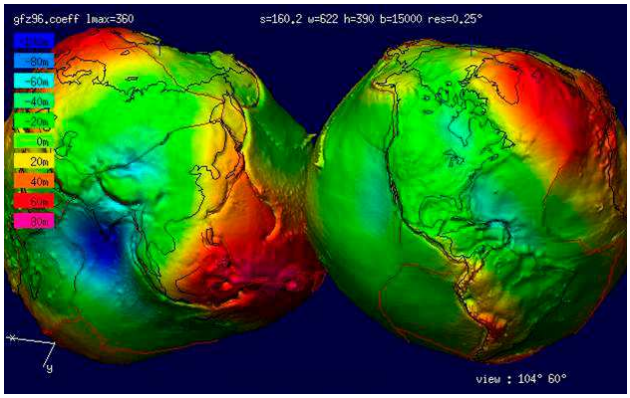

Figure 5: A model for the Earth geoid from GRACE mission data.

Matter Wave Interferometry

The first matter wave interferometer was realized in 1947 by Enrico Fermi [5]. In this experiment slow neutrons were *Bragg* diffracted by crystal planes with different chemical composition; the relative sign of the neutron scattering length from different nuclei was measured. Some years later the first matter–wave interferometry experiment on electrons was performed in a *Mach–Zehnder* configuration, with crystals of few hundreds of atomic layers as mirrors [6]. At that time it was already clear that neutral matter was most adequate than charged particle or photons for realizing high sensitivity devices for inertial acceleration shifts detection. The motivation is due first of all to the reason that neutral particles are more less sensitive to perturbing electric and magnetic effects than charged particles, and, on the other side, because typical speeds can be much lower than the speed of light, it is

possible to perform interferometric sequences with a longer interaction time within a fixed length scale. Neutrons were difficult to produce in laboratories because accelerators are needed; atoms, on the other side, do not easily penetrate media and are easily stick out form surfaces. Matter Wave Interference patterns from atoms, as more complex and massive system, were observed in 1990s and several groups around the word performed atom interferometers [51, 52, 53, 54].
Matter wavelength associated with a particle of mass M and momentum $\mathbf{p}$ is called *de Broglie wavelength* and it results from the following equation:

$$\lambda_{mw} = \frac{h}{p} = \frac{h}{Mv}$$

where h is the Plank constant and v is the particle velocity. For thermal atoms, with typical velocity $v \simeq 10^3\ m\ s^{-1}$, the matter wavelength results to be $\lambda_{mw} =\simeq (0.4/A) \times 10^{-9}$ m, where A is the mass number of the atom. For cold atoms, at temperatures on the range of 1 μK, this leads to a larger wavelength of the order of $\gtrsim 1$ μm. A complete analogy can be drawn between optical and matter wave interferometers, the wavepacket can be split and recombined leading to an interference signal at the same way. As a consequence of smaller atomic group velocity compared to the velocity of light we can note that in principle atom interferometers can be more sensitive to inertial forces than the optical sensors: an atom spends more time within the interferometric sequence allowing to a best recording of possible path length changes due to accelerations and resulting in a phase shift.
Different methods can be implemented in order to split, reflect and recombine the atomic matter waves: optical components role can be played either from material structures and from light fields. In the case of matter made optical components the experimental situation can be considered analogous to Young's double slits interferometer, the matter wave diffraction is performed by means of material structures that require high surface quality and ultra precise positioning. Starting from early days of atom interferometry atom–light interaction has been considered as the best candidate for the coherent beam–splitting technique including also the possibility to address atomic internal degrees of freedom. We can draw a picture in which *de Broglie* waves are diffracted or *Bragg* scattered by periodic potential made from standing waves working as perfect crystals. This configuration, on the other side, leads to easy experimental parameters control such as phase, intensity and lattice spacing. In such framework the interferometer setup can be generalized to few different implementations, we are going to deal with *Raman* diffraction configuration.
Each single atom participates independently to the interferometric sequence

and its contribution adds to the others from the sample providing to a detectable and statistically significant signal. The basic working principle for an atom interferometer working as an acceleration sensor can be easily depicted starting from a single atom model.

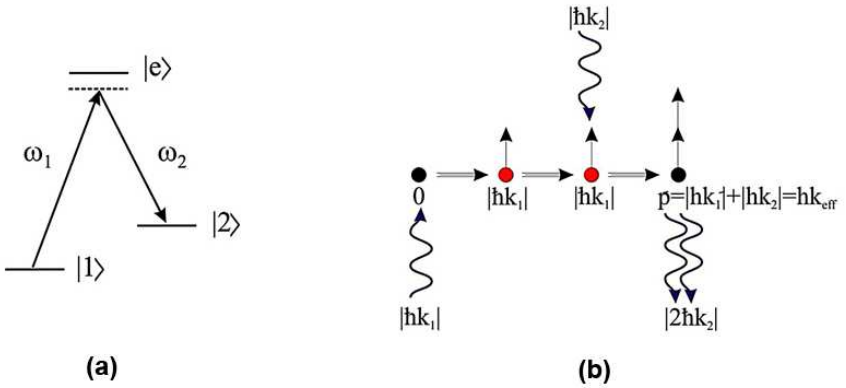

Figure 6: Multilevel atomic system in a two photons *Raman* transition: (a) simplified diagram for atomic energy levels and transitions, (b) momentum transfer diagram for a stimulated *Raman* transition in counter–propagating beams configuration.

Let's suppose for the moment to dispone of an at least three level atom and that its state can be described either from the internal and for the external degree by a *ket* in the form $|i, \mathbf{p}\rangle$ where i indicates the internal state and $\mathbf{p}$ the external momentum. Let's consider also an alkali atom as a three level system with $|1\rangle$ and $|2\rangle$ as hyperfine states of the ground level and $|e\rangle$ as a given state from the exited level (as shown in picture 6a). Suppose the atom being into the initial state $|1, \mathbf{p}\rangle$ and let's consider from the other side two counter–propagating laser beams with propagation vectors $\mathbf{k}_1$ and $\mathbf{k}_2 \simeq -\mathbf{k}_1$ and whose relative frequency difference being equal to the hyperfine splitting between atomic states $|1\rangle$ and $|2\rangle$. The interaction of the two laser fields with the atomic system can induce two–photons *Raman* transitions and as a function of interaction time *Rabi* oscillations on the internal state. The atomic state can be thus described as a function of the interrogation time as:

$$|\psi(t)\rangle = e^{-i\omega_1 t} cos\Big(\frac{\Omega_R \tau}{2}\Big)|1, \mathbf{p}\rangle + e^{-i\omega_2 t} e^{-i\frac{\pi}{2}} e^{i\phi_L} sin\Big(\frac{\Omega_R \tau}{2}\Big)|2, \mathbf{p} + \hbar\mathbf{k}_{eff}\rangle$$

Where Ω_R represents the effective two–photons *Rabi* frequency, $\mathbf{k}_{eff} = \mathbf{k}_2 - \mathbf{k}_1$ is the effective momentum transferred to the atom and ϕ_L is the

phase therm acquired from the interaction with the electromagnetic wave. From the phenomenological side the single two–photons transition can be separated into two steps, starting with a photon absorbtion from one laser beam followed by successive stimulated emission due to the interaction with the other laser (or the opposite sequence for the contrary transition). In this process a photon recoil is transferred to the atoms as shown in picture (6b), moreover the beams counter–propagating configuration leads to a big momentum transfer ($\mathbf{k}_{eff} = \mathbf{k}_2 - \mathbf{k}_1 \simeq 2|\mathbf{k}_2|\hat{k}_2$). This feature is important for the interferometer implementation side in order to achieve a large spatial separation between two wavepacket paths.
As resulting of the energy and momentum conservation, that holds for the photon–atom system, it follows that the atomic internal energy state and external momentum state are always coupled. From there we can define particular laser field pulses that are going to become the basic optical elements for our matter wave interferometer; they are defined, in agreement with the *Rabi* oscillation theory, from the values taken from the arguments in *sine* and *cosine* function in the previous population state function:

- A $\pi/2$ **pulse**, working as matter–wave splitter, is defined as the pulse so that $\Omega_R\tau = \pi/2$. An atom initially in one of the two states $|1\rangle$ or $|2\rangle$ is driven into an equal superposition of them.

- A π **pulse**, working as matter–wave mirror, is defined as the pulse so that $\Omega_R\tau = \pi$. It transfers the atom from one state to the other $|1\rangle \leftrightarrow |2\rangle$ (absorbtion – stimulated emission).

If we suppose now to prepare the atom in initial state $|1, \mathbf{p}\rangle$ at $t = 0$, in agreement with the optical interferometry analogy, it's possible to implement a matter–wave interferometer in a *Mach–Zehnder* configuration by means of a pulses sequence of kind $\pi/2 - \pi - \pi/2$. Such sequence at a first step splits and separates the atomic wavepacket into two different and independent evolutions paths, at the second pulse deflects each part and finally recombines them by the last $\pi/2$ pulse. The final result is shown in picture (7) where the action of each *Raman* pulse on internal and external atomic degrees of freedom is also reported. An atom in the two evolutions path can experiment common or separate effects due to external fields or accelerations. At the end of the interferometric sequence an interference signal can be recorded from the detection of atomic state at the output channel.

The atomic phase difference between the two different paths (pats I and II into the picture) accounts for two contributions $\Delta\phi_{tot} = \Delta\phi_{evol} + \Delta\phi_{laser}$: one contribution ($\Delta\phi_{evol}$) is due to the wavefunction free evolution and the other contribution is due to the phase imprint from the laser fields at each

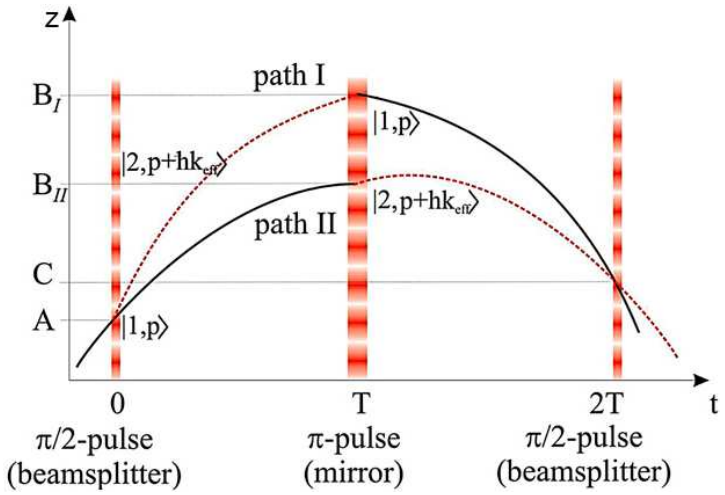

Figure 7: Space–time diagram for a matter wave *Mach–Zehnder* interferometer, parabolic path evolution is due to the presence of the gravity acceleration.

space–time interaction point ($\Delta\phi_{laser}$). The most direct approach to evaluate the evolution phase therm can be driven from the *Feynman* path integral formalism and it is valid for at most quadratic Lagrangians in position and momentum.
According to such hypothesis, the evolution of a quantum system in an external potential $V(\mathbf{z})$ from $(\mathbf{x}_A, t_i)$ to $(\mathbf{x}_B, t_f)$ can be determined from a quantum propagator in the form $\sum_\Gamma e^{iS_\Gamma/\hbar}$, where Γ represents all possible paths and S_Γ the action along each of them. For the action it follows:

$$S_\Gamma = \int_{t_i}^{t_f} \mathcal{L}[\mathbf{z}(t), \dot{\mathbf{x}}(t)]dt$$

In the classical limit it holds $S_\Gamma \gg \hbar$, and only paths close to the classical ones interfere constructively, this implies that the resulting phase shift for the interferometer is simply given by the differential action evaluated along the two possible paths, as follows:

$$\Delta\phi_{evol} = \frac{S_{II} - S_I}{\hbar} = \frac{1}{\hbar}\oint_{\Gamma_0} \mathcal{L}dt$$

On the other side the laser contribution accounts for laser fields phase evolutions in the form $\phi(\mathbf{x}, t) = \mathbf{k}_{eff} \cdot \mathbf{x} - \omega_{eff}t - \phi_{eff}$ where $(\mathbf{x}, t)$ identifies the single interaction space–time point and ϕ_{eff} is the relative phase offset between the two lasers. Accounting for each single contribution from a complete interferometric sequence (as shown in the picture 7), it follows

$$\Delta\phi_{laser} = \phi(\mathbf{x}^A, 0) - \phi(\mathbf{x}_I^B, T) - \phi(\mathbf{x}_{II}^B, T) + \phi(\mathbf{x}^C, 2T)$$

The presence of a frame acceleration or of a gravitational force results in a displacement of the atomic trajectory respect to the lasers wavefronts. If we consider an interferometer implemented as a single axis device for gravity acceleration measurements, with an atomic sample in free falling and supposing a constant and uniform g, it results that the free evolution phase contribution vanishes because the symmetry of the configuration $\Delta\phi_{evol} = 0$. The lasers contributions, on the other hand, for initial conditions $z(0) = 0$ and $v_z(0) = v_0$, results to be:

$$\begin{aligned}
\phi(\mathbf{x^A}, 0) &= 0 \\
\phi(\mathbf{x_I^B}, T) &= k_{eff}\Big[-\frac{1}{2}gT^2 + v_0T\Big] \\
\phi(\mathbf{x_{II}^B}, T) &= k_{eff}\Big[-\frac{1}{2}gT^2 + \Big(v_0 + \frac{\hbar k_{eff}}{m}\Big)T\Big] \\
\phi(\mathbf{x^c}, 2T) &= k_{eff}\Big[-2gT^2 + \Big(2v_0 + \frac{\hbar k_{eff}}{m}\Big)T\Big]
\end{aligned}$$

and thus:

$$\boxed{\Delta\Phi_{laser} = k_{eff}\ g\ T^2}$$

We have found the dependence of the atomic phase at the output of the interferometer from the acceleration experimented during the evolution. On the other side we have also found that, in analogy with the optical interferometers, the phase sensitivity to the accelerations scales as the square of the total interrogation time $\sim T^2$; the time duration T plays the role of the arm for our matter wave interferometer. At this level we only performed a first order calculation neglecting effects such as the finite duration of each single pulse or the presence of acceleration gradients; a more precise calculation can be found into the text.
The atomic phase at the end of the whole evolution is related to the populations from the following relations

$$\begin{aligned}
P_2 &= \frac{1 - \cos(\Delta\Phi_{tot})}{2} \\
P_1 &= \frac{1 + \cos(\Delta\Phi_{tot})}{2}
\end{aligned}$$

From there it is obvious as an acceleration measurement can be derived from the population detection and from fringes acquisition.

From this introduction it's clarified that the atom interferometer scheme in principle works for the wavepacket manipulation side also considering a two levels atomic system and single photons transitions. The choice to consider two photons transitions and to couple hyperfine levels of the ground state is derived from the demand to perform long interferometric time durations avoiding atomic decay during the sequence.
On the other side the choice of cold atomic samples is due to the requirement of a weakly interacting sample and in particular confined into a slow expanding cloud.

In order to provide a more phenomenological and intuitive approach to the physical situation we can introduce a very simple classical analogy. Let's consider a free falling particle under the action of an uniform gravity field, and let's also suppose to want to determine its acceleration just from space and time measurement as displayed in the picture (8).

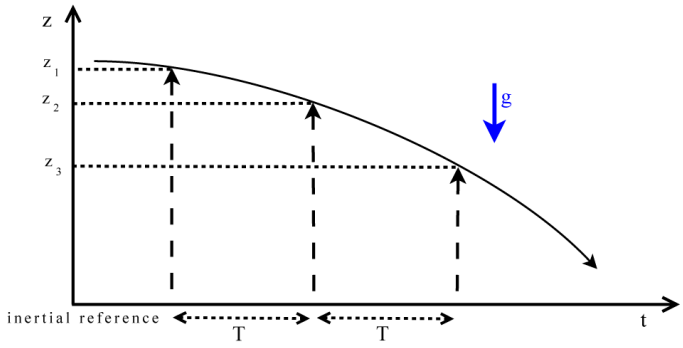

Figure 8: Average gravity acceleration measurement on a massive test particle in a kinematical picture.

We can detect its position from three equally spaced lasers pulses. The first two acquisitions are enough for average velocity determination in the first time interval T, from the third acquisition it's also possible to determine the velocity changes between the first and the second time interval, that means the average acceleration. Just from kinematic considerations it follows:

$$a = \frac{z_1 - 2z_2 + z_3}{T^2}$$

Thus we can consider laser fields as a ruler for our position measurements, and, if the laser phases at each interaction with the test mass are given from $\phi_i = k_{eff} z_i$, substituting in the previous equation the same equation for the atomic phase derived from the quantum calculation just holds.
Coming back to our quantum framework we can conclude that for the acceleration measurements, lasers wavefronts work as rulers at each interaction and the atomic test mass records the single phase contribution in its phase factor.
From this simple picture it is easy to figure the fundamental role played for the interferometer performances by the relative phase stability between the two *Raman* lasers. The residual phase noise represents one of the main source of technical noise and it is directly imprinted from laser fields to the atoms. In this framework part of this thesis has been dedicated to the implementation of an high performances *Phase Locked Raman* lasers system as a transportable apparatus subsystem.

Atom Interferometer as an acceleration sensor implementation

Some typical setup for acceleration detector devices based on atom interferometry are reported in picture (9). The atomic sample is cooled and trapped in a first chamber by means of Magneto–Optical trapping technics; the number of atoms ranges around $10^8 \div 10^{10}$ atoms, depending on the specific setup. In a fountain configuration (picture (9a)) after turning off the trapping magnetic field, the sample can be launched in vertical direction along the symmetry axis by means of a optical moving molasses technics. This molasses stage allows to achieve a temperature of the order of few μK. Atoms interact with *Raman* beams performing the interferometric sequence during their parabolic flight and, at the end, they drops in a detection region where a states population measurement is performed by means of spectroscopic technics (example of detected fringe in picture (10)). The diagram in picture (9b) illustrates the sample release configuration where no launch is performed; now the trapping chamber is on the top and the detection still on the bottom side. This last configuration results into an higher experimental repetition rate but it also implies a shorter interferometer time T.

In the picture (9c) the differential mode implementation is illustrated: it can be realized performing the interferometric sequence on two atomic clouds at the same time but at different heights. The phase difference $\Delta\Phi$ between the two resulting fringes will be proportional to the differential acceleration Δg. Considering the trap loading rate, in order to be able to launch or re-

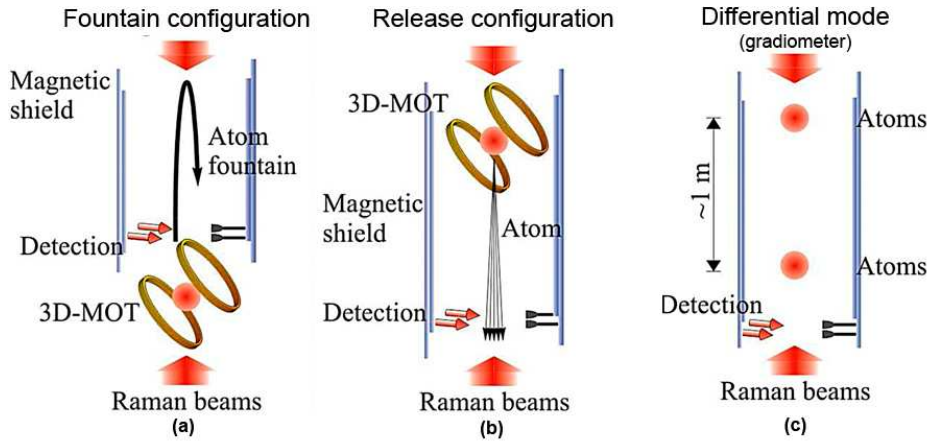

Figure 9: Implementations for acceleration sensors based on atom interferometry: (a) sample launching configuration for absolute acceleration detection, (b) sample release configuration for absolute acceleration detection, (c) differential mode configuration (gradiometer under Earth environment).

lease the two samples as a sequence with the right timing, it can be needed to implement a double chamber apparatus [65, 66] or to realize a sample juggling technics for the loading with a single chamber setup [67, 68].
It's important to note that for a typical gravimeter (9a, 9b), by increasing temporal separation between the *Raman* pulses seismic noise and acoustic noise completely wash out the fringes. This can be contrasted by means of few specific technics such as for example by the active insulation of the *Raman* mirror generating a feedback signal for the lasers phase [61, 63] or by recovering the noise effect by means of off–line technics [72]. However thanks to a differential mode operation it is possible to cut away all common mode noise and the $\Delta\Phi$ measurement can be recovered by plotting one fringe as a function of the other. The resulting ellipse is a special case for a Lissajous plot.
For all illustrate devices the atoms trapped into the sample can be loaded from the vapor produced from an heated getter and diffused into the chamber or can be loaded from a 2–dimensional *Magneto Optical Trap* (*2D–MOT*) as cold atom source. This further implementation is fundamental for transportable devices because it allows to increase the experimental repetition rate by one side, and, on the other side, it reduces the background gas pressure in the manipulation chamber. In the present thesis it is illustrated a direct experience with a *2D–MOT* implementation and characterization for a gradiometric instrument (MAGIA).

The laser field manipulation can be performed with few atomic species and in particular alkali; in our setup we choose ^{87}Rb atoms. Many reasons lead to this choice but we can consider as first the good performances in internal and external degree of freedom control and in cooling and trapping technics realization. Besides this, also the typical transitions wavelength simplifies from the technological point of view the laser sources realization.

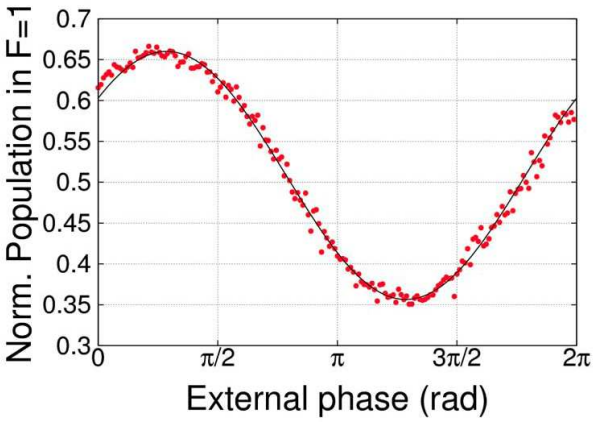

Figure 10: Interference fringes recorded in the gravity experiment in Firenze (MAGIA [68]), interrogation time between two pulses $T = 5$ ms.

Accurate Measurement of Gravitational Constant by Atom Interferometry: *MAGIA* experiment

In the framework of the gravitational signal detection, MAGIA[2] experiment has the target to perform an accurate measurement of the gravitational constant by means of Atom Interferometry technics [67, 68, 69, 73, 101]. The basic apparatus consists in a cold atom fountain in a gradiometric configuration; it is operating in Firenze and has represented the training pool for the transportable apparatus development presented in this thesis.
In the MAGIA experiment free falling rubidium atoms are used as microscopic probes for to detect the gravitational signal inducted by two macroscopic test masses. From the differential acceleration measurement and from the knowledge of the sources masses distribution it is possible to determine the value of the gravitational constant G.

[2]MAGIA stands for: Misura Accurata di G mediante Interferometria Atomica

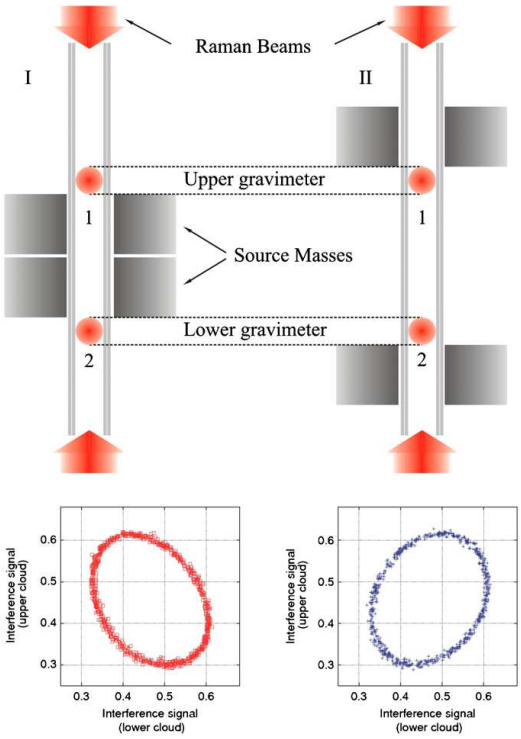

Figure 11: Experimental setup for the MAGIA experiment, the atomic fountain. On the top the two configurations are shown for the sources masses for the G measurement:(I) masses close each other, (II) masses far each other. On the bottom data recorded in a gradiometric configuration, fringes are plotted in form of Lissajous plots for source masses in the two different positions.

The masses are symmetrical arranged around the atomic fountain flight axis in a cylindrical geometry. They are positioned close to the atomic trajectory and generate a well known gravitational field. The signal can be detected as a variation of gradient of gravity acceleration. For the determination of G two gradient measurements are repeated, with the same condition for atomic flight side, but with two different positions for the sources masses. This way it's possible to compare the signal change between the two configurations, cut away all constant contribution and thus extrapolate the single contribution due to the source masses. The experimental setup is shown in picture (11) together with the resulting interferometric fringes plotted as Lissajous plots. The target accuracy for the G measurement is of $\Delta G/G = 10^{-4}$.

Transportable atom interferometer as absolute gravimeter and the FINAQS project

Part of this thesis has been developed in the framework of the Future Inertial Atomic Quantum Sensor (FINAQS) project (European Community STREP[3])[140] that comprises five European research groups with the aim of the study and of the realization a new generation of quantum sensors based on matter wave interferometry. The main goal for the project is to extend the range of application of these sensors to direct practical applications, such as on–site high precision local gravity measurement useful applications. In particular our objective has been focused on the development of an high performances transportable gravity gravimeter oriented to geophysical applications and to metrology. The target performances accuracy for such device is of $\Delta g/g = 10^{-9}$ that, as we have seen, totally fulfills the geophysical applications requirement. The system will operate in launching atomic fountain configuration on a cold rubidium sample. A big sensitivity enhancement is derived from a long interferometer time duration. The total launching height will be of ≈ 500 mm, thus on the terrestrial conditions it will be compatible with an interferometric sequence time of the order of $2T \lesssim 500\ ms$. On the other side it will be foreseen a total number of atoms trapped into the sample around $10^9 \div 10^{10}$ compatible with 10^6 atoms at the detection.
The gravimeter is in progress of realization at the Institute of Optic and Metrology of the University of Berlin with the contribution of the collaboration. The picture (12) illustrates a detail for the vacuum system core and a CAD view of the whole realization.
The vacuum chamber, reflecting the scientific requirements, consists of three regions: the first one is the main chamber for the atomic sample cooling and trapping, a second chamber is dedicated to the state preparation and to the final detections, a vertical tube stands for the atomic manipulation. As typical for atomic fountain of this kind, the atomic sample is prepared from a *2D–MOT* as a cold atoms source, capable of providing a total flux of $10^{12}\ atoms/s$. Considering that the presence of stray magnetic fields during the interferometric sequence results in a systematic effect from the coupling with the atoms, we must note that this specific configuration, oriented to terrestrial application, has been designed in order to be able to perform the interferometric manipulation only in the vertical tube; thus it has been possible to shield only this part of the apparatus. The vacuum system is suspended to an ultra–stiff frame that is supported by an high–performance vibration–isolation board; the structural frame can be rotated of 360 degree

[3]Specific Target REsearch Project

for Coriolis force compensation. The whole apparatus consists on a cuboid of 1900 mm height and 700 mm of diameter; the total weight is $< 300\ kg$. On the other side, also the laser system for atom cooling and manipulation implementation is oriented to the transportability and to the compactness; it consists in four separate modules housed in a mobile frame. The involved laser sources are specifically developed in a special External Cavity Diode Laser configuration in order to address the transportability requirement resulting in an intrinsical passive mechanical stability. The specific setup allows to separate the laser auto injection task from the wavelength selection tasks by means of a cavity implementation with a partial reflecting mirror as an output coupler and an interferential filter as wavelength selection element [98, 99]. Such implementation results in a very stable and narrow linewidth laser $< 200\ kHz$. Each laser system module utilizes custom made small and compact optical component specifically developed allowing to organize it in a breadboard of dimensions of $43\ mm \times 43\ mm$. The whole laser system consists in four modules.

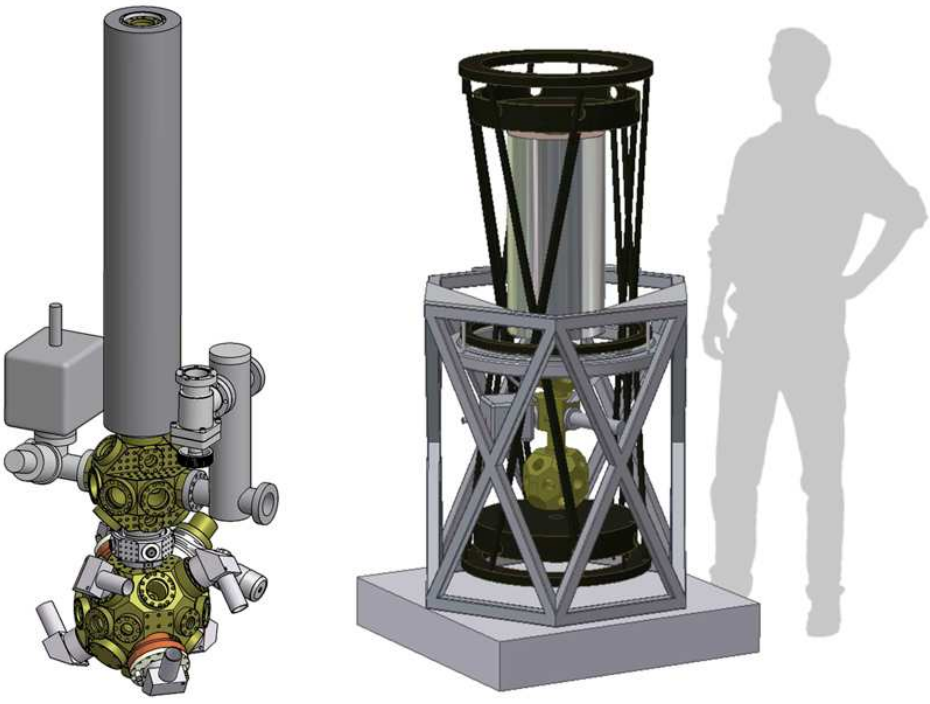

Figure 12: Apparatus for the FINAQS project (Berlin) atom interferometer working as an absolute gravimeter [109].

This experiment can be considered the early experience for our collaboration to the transportable atomic physics apparatus approach either for the system conception and for the subsystem level. The realized know–how has been thus exported to other framework as the *Space Atom Interferometer*. Our task in the collaboration framework has been the implementation of a working prototype for compact laser system module dedicated the atomic wavepacket manipulation via the two photons *Raman* transitions. These transitions are driven from two laser fields phase locked each other where the relative residual phase noise results in one of the main technical noise source for the interferometer. Thanks to a very narrow linewidth of the laser sources, by means of a digital frequency phase detector and a direct laser modulation, it has been possible to implement a very high performance Phase Locked Loop with a phase noise spectral density between 100 Hz and 60 kHz of less than 1 $\mu rad/Hz^{\frac{1}{2}}$ fully compatible for the gravimeter accuracy requirement on gravitational acceleration measurement.

Space Atom Interferometer

The experience described in this thesis converges to the realization of a transportable atom Interferometer as a single axis accelerometer oriented to space missions and to tests in micro–gravity environment. This challenge was born in the framework of a specific ESA project called the "Space Atom Interferometer" (SAI) [104], as for the FINAQS project, it joins a collaboration of some European University and research groups [134, 135, 136, 137, 138, 139]. The preceding FINAQS experience has been useful for the development of the new apparatus and to shortening the realization time. The development approach and the transportable apparatus concept is almost the same as for the FINAQS absolute gravimeter but with some critical differences due to the different task.
The relation that holds between the acceleration experimented from the atomic test mass and the matter wave dephasing in an interferometric sequence, $\Delta\Phi_{tot} = k_{eff}\ a\ T^2$, leads to the consideration that high sensitivities can be achieved in micro–gravity conditions for such kind of sensors: in small accelerations regime it's possible to expand the time sequence duration T.
The ultimate goal for the SAI project is to investigate experimental different aspects of placing an atom interferometer in space: development approach, equipment needs, resulting device sensitivities and what physics can be addressed with this kind of system. The first step is to demonstrate the possibility of construction of a space compatible atom interferometry sensor and test it at system and subsystem level in terrestrial environment. Moreover in order to investigate the realistically expected performances, limits and poten-

tial scientific applications in micro–gravity conditions the whole apparatus will be compatible with the tests in the Bremen Drop Tower and with the Zero G parabolic flights.
The physics system consists in a main chamber for the atomic sample cooling and trapping loaded from a *2D–MOT* as a cold atom source and in a vertical tube for the interferometric sequence. The apparatus will work under terrestrial conditions as a gravimeter/gradiometer in atomic fountain configuration (see scheme in picture (9a-b)) with an expected accuracy of $\Delta g/g = 10^{-7}$ on absolute measurement.
In micro–gravity operation mode we expect a small displacement of the sample from the main chamber, thus, unlike the FINAQS implementation, the same chamber works either for sample preparation and for detection. This specific experimental situation holds the necessity to shield all the physics chamber from stray magnetic field that can affect the interferometric results. On the other side also a specific choice of the materials for the apparatus has been needed. As shown in picture (13), the whole physics apparatus will be fitted in a cylindric capsule with diameter of 60mm and height of 60mm, either because of the compactness required from the space missions but in particular for being compatible with the Drop Tower tests; this requirement excludes all the commercial solutions for apparatus subsystem, vacuum, optical system and more.
From the laser system point of view the same approach of the FINAQS system has been followed with the development of custom made compact stand alone modules specific for each task.
The Space Atom Interferometer is now into the assembling stage into the dedicated lab in Firenze. The subsystems developed in other labs of the collaboration are also converging for the final realization.

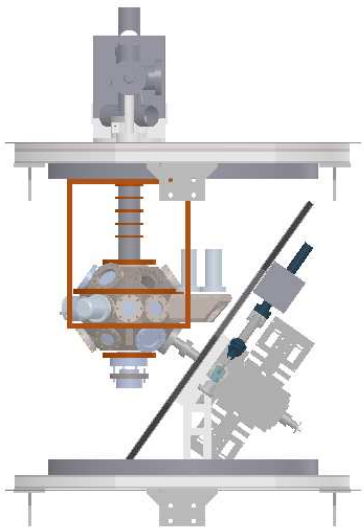

Figure 13: Basic concept for the SAI apparatus, a CAD view.

Micro–gravity tests and the Bremen Drop Tower

The Bremen Drop Tower is a groundbased short–term micro–gravity laboratory open to scientific community for tests [138]. It represents an economic alternative, with permanent access, to orbital and suborbital platform tests. The total tower height is 142 meters and 110 meters are utilized for the free fall system. The available free fall flight results in a 4.5 s duration, three drops can be performed per day. Micro–gravity conditions are reached during the flight with residual gravity of $\lesssim 10^{-5}g$. The scientific plant consists in a steel made 120 m height vacuum tube evacuated down to a pressure of $< 0.1hPa$. No mechanical connections hold the vacuum tube to the tower structure in order to guarantee hight quiescent conditions.
Each apparatus, to be tested, must be fitted in a special designed standard capsule with a rocket shape ($\backsimeq$ 2900 mm height , 81 mm diameter), see picture (14b-c). At the end of the drop sequence the capsule impacts in a deceleration system realized with polystyrene pellets; the resulting deceleration is of $\lesssim 50\ g$. In our case the whole scientific apparatus, including the lasers system, will be fitted inside the capsule and, on the other side, all constrains have been followed in order to guarantee the full compatibility.

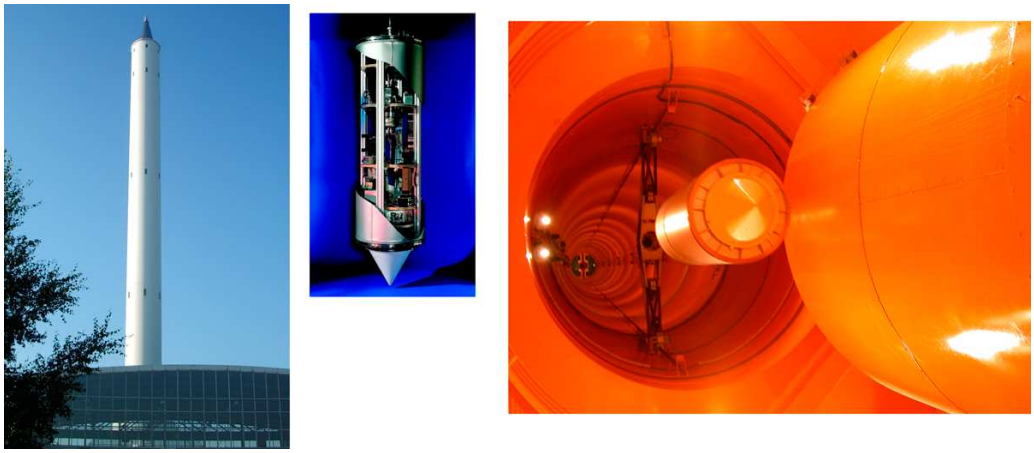

Figure 14: The Bremen Drop Tower laboratory: (left) the Tower, (center) standard capsule for micro–gravity experiments, (right) the inner drop plant. [138]

Figure 15: Spacecraft from *GOCE* space mission for the Earth's gravity gradient mission and geoid acquisition [131].

Chapter 1

Cold Atom Interferometer

From the introduction to this thesis basics elements to implement an atom interferometer have been provided, have also been addressed the enhancement and the results, in the acceleration measurement framework, derived from the utilization of neutral atoms as microscopic test masses and connected with the quantum features of the matter. Atomic manipulation technique allows to manage either internal and external degree of freedom.
For the realization of an atom interferometer the utilization of cold atoms is furthermore necessary in order to manage a weakly interacting and not extended sample. In this chapter we want to provide the basic theoretical tools to understand the atom interferometer principle and relative issues. Also brief topics about neutral atoms cooling and trapping technics are reported. In the last section we introduce atomic transitions to be addressed in order to realize an interferometer with cold ^{87}Rb atoms in agreement with our choice.

1.1 Electromagnetic wave interacting with two levels Atom

In Order to introduce the interaction of a radiating field with an atomic system, we can consider in a semiclassical model, an electromagnetic field $E(t)$ with angular frequency ω_L interacting with a simple two level atomic system with internal energy levels E_g (*ground*) and E_e (*exited*) (picture 1.1). Being the field linear polarized it can be expressed as:

$$\vec{E}(t) = \hat{z}E_0 cos(\omega_L t) \tag{1.1}$$

The hamiltonian of atomic system interacting with the field can be split into an unperturbed part plus a second part for the interaction $H = H_0 +$

$V(t)$, where $V_{ab} = -pE_0 cos(\omega_L t)$ and p is the atomic electric dipole moment expressed as $p = ez_{ge}$ and $z_{ge} = \langle u_g|z|u_e\rangle$. On the other side the general atomic wavefunction can be expressed as linear combination of eigenstates of unperturbed hamiltonian $\{u_e, u_g\}$.

$$\psi(t) = C_g(t)u_g(\vec{r})e^{-i\omega_g t} + C_e(t)u_e(\vec{r})e^{-i\omega_e t} \tag{1.2}$$

where $C_i(t)$ are time varying coefficients weights where $|C_g|^2 + |C_e|^2 = 1$, and the angular frequencies follow from energy eigenvalue $\omega_i = E_i/\hbar \quad (i = g, e)$. In order of find the system evolution, we substitute the expressions for the wavefunction ψ into the Schröedinger equation with the compete hamiltonian. The problem to find the atomic system time evolution becomes to solve this first order differential equations system for the coefficients:

$$\dot{C}_e = \frac{1}{2}ip\frac{E_0}{\hbar}\left\{ e^{i(\omega_{eg}-\omega_L t)} + e^{i(\omega_{eg}+\omega_L t)}\right\}C_g \tag{1.3}$$

$$\dot{C}_g = \frac{1}{2}ip\frac{E_0}{\hbar}\left\{e^{-i(\omega_{eg}-\omega_L t)} + e^{-i(\omega_{eg}+\omega_L t)}\right\}C_e \tag{1.4}$$

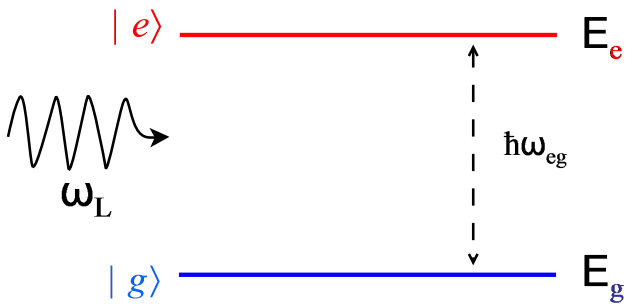

Figure 1.1: Two level atomic system, interaction with em radiation, basic representation for internal degree of freedom.

Depending on the physical situation we are dealing with few approaches can be followed in order to find the solution. Let's start with the *weak-field approximation* approach, supposing small coupling between atom and radiating field with a little value for the field E_0. In such framework the population of the upper state $|e\rangle$ remains small compared with the population of the lower state $|g\rangle$ during the interaction time t. In this approximation it is possible to develop the coefficients and proceeding by iterative sequence. Supposing that for $t = 0$ all atoms are into the ground state, that means $C_a(t = 0) = 1$ and $C_b(t = 0) = 0$, the equations (1.3) and (1.4) become:

$$\dot{C}_g \simeq 0 \tag{1.5}$$

$$\dot{C}_e = \frac{1}{2} ip \frac{E_0}{\hbar} \Big\{ e^{i(\omega_{ab}-\omega_L)t} + e^{i(\omega_{ab}+\omega_L)t} \Big\} \tag{1.6}$$

Thus at the first order the solution for the exited state evolution coefficient is given from:

$$C_e \simeq C_e^{(1)} = \frac{1}{2} ip \frac{E_0}{\hbar} \Big\{ \frac{e^{i(\omega_{eg}-\omega_L)t} - 1}{\omega_{eg} - \omega_L} + \frac{e^{i(\omega_{eg}+\omega_L)t} - 1}{\omega_{eg} + \omega_L} \Big\} \tag{1.7}$$

Into the optical frequency range and if $\omega_L \sim \omega_{eg}$ it's possible to apply the *Rotating Wave Approximation* (*RWA*) and thus we can neglect the frequency sum term. The surviving term gives:

$$\begin{aligned} C_e \simeq= C_e^{(1)} &= \frac{1}{2} ip \frac{E_0}{\hbar} \Big\{ \frac{e^{i(\omega_{eg}-\omega_L)t} - 1}{\omega_{eg} - \omega_L} \Big\} \\ &= \frac{1}{2} ip \frac{E_0}{\hbar} e^{i(\omega_{eg}-\omega_L)\frac{t}{2}} \, 2 \frac{sin\big(\frac{(\omega_{eg}-\omega_L)t}{2}\big)}{\omega_{eg} - \omega_L} \end{aligned} \tag{1.8}$$

The transition probability can be obtained from the module square of the coefficient $|C_e|^2$ as the probability to find the atom into the *exited* state.

$$|C_e|^2 \simeq |C_e^{(1)}|^2 = \frac{1}{4} \Big(p \frac{E_0}{\hbar} \Big)^2 \quad \frac{sin^2\Big(\frac{(\omega_{eg}-\omega_L)}{2} t \Big)}{(\frac{\omega_{eg}-\omega_L}{2})^2} \tag{1.9}$$

From this result we find that, in course of time, transitions are unlikely to occur unless the resonance condition is satisfied, that is unless the applied frequency field matches the transition frequency $\omega_{eg} \simeq \omega_L$.
In our sketch the spontaneous emission is totally neglect; we can account for it adding by hand two dissipative phenomenological terms $-\frac{1}{2}\gamma_e C_e$, $-\frac{1}{2}\gamma_g C_g$ [1] to evolution equations (1.3) and (1.4) (this means that the two level system is loosing atoms). The naked oscillating solution (1.9) now acquire a dumped behavior and in the simple case of $\gamma_e = \gamma_g = \gamma$ we find:

$$|C_e^{(1)}|^2 \propto \quad \frac{sin^2\Big(\frac{(\omega_{eg}-\omega_L)}{2} t \Big)}{(\frac{\omega_{eg}-\omega_L}{2})^2} \quad e^{-\gamma t} \tag{1.10}$$

[1] the second therm only in case that the lower state is not the ground state and the system can decay below

The simple model presented so far is useful to understand the basics oscillation mechanism derived from atoms and coherent light coupling. The $\sin^2(\omega' t)$ dependence of the transition probability, introduces to the oscillating behavior imprinted from the radiating field to the atomic internal degree of freedom. As we are going to see such hint will lead to *Rabi Oscillation* theory and to the *Optical Bloch equations* in another framework.
In order to approach to our experimental situation, for which the *small field* approximation is no longer valid and the *strong field*, the case with non–perturbative treatment is needed.

1.1.1 Single photons transition, a model for the interaction

Now we are going to handle the more general approach with an extended formalism useful to comprise both internal and external atomic degree of freedom, our target is to build the basic tools for the atom cooling and trapping technics and atom interferometry [55, 60].
Let's consider again a two level atomic system with energy $\hbar\omega_g$ and $\hbar\omega_e$ interacting with a traveling monochromatic electric field with frequency ω_L and wave vector $\vec{k}_L$

$$\vec{E}_L(\vec{r},t) = \vec{E}_0 cos[\vec{r}\cdot\vec{k}_L - \omega_L t + \phi_L] \tag{1.11}$$

If $\vec{p}$ is the atomic momentum and $\vec{d}$ the electric dipole, the Hamiltonian operator $\mathcal{H}$ including external and internal degree plus an interaction term, in the dipole approximation, can be written as:

$$\mathcal{H} = \frac{p^2}{2m} + \hbar\omega_g|g\rangle\langle g| + \hbar\omega_e|e\rangle\langle e| - \vec{d}\cdot\vec{E} \tag{1.12}$$

In order to describe the global atomic state–function it is necessary to choose a base–representation generated from a tensorial product of internal and external Hilbert space. In this framework let $\{|g\rangle, |e\rangle\}$ be the base for the internal space composed by eigenstate of the atomic quantized energy eigenvalue, whereas we can consider $\{|\vec{p}\rangle\}$ as continuous base for the external degrees of freedom relative to momentum eigenfunctions. The direct tensorial product leads to the following representation:

$$|\mathbf{g}, \vec{p}_g\rangle = |\mathbf{g}\rangle \otimes |\vec{p}_g\rangle \qquad |\mathbf{e}, \vec{p}_e\rangle = |\mathbf{e}\rangle \otimes |\vec{p}_e\rangle \tag{1.13}$$

The effect of interaction with the light on the atomic motion can be expressed by means of the completeness relation holding for the base of the

external *Hilbert* space[2]:

$$\mathcal{I} \cdot e^{\pm i\vec{k}_L\cdot\vec{r}} = \int dp^3\ e^{\pm i\vec{k}_L\cdot\vec{r}}\ |\vec{p}\rangle\langle\vec{p}| = \int dp^3 |\vec{p} \pm \hbar\vec{k}_L\rangle\langle\vec{p}| \tag{1.14}$$

By this method it's possible to introduce the coupling between internal and external degree in agreement with the statement that: as consequence of a photon absorbtion or stimulated emission the total atomic momentum acquire or loose a discrete amount $\pm\hbar k_L$ equal to photon momentum exchange. The equation (1.14) states that the transitions only occur within a closed momentum family of states (see [56]). From there must be also taken into account that the atomic wavefunction temporal evolution changes as a consequence of the interaction. In this picture could be convenient working on two new defined eigenstate relative to shifted eigenvalues; we can suppose the atomic system in the *ground* internal state and external momentum $\vec{p}$ before the interaction and will be driven to *exited* state with $\vec{p} \to \vec{p} + \hbar\vec{k}_L$ as a consequence of a photon absorbtion; on the other side the stimulated emission will lead to the inverse process. Thus the new definition for the eigenvalues and eigenstates will be:

$$\begin{aligned} |\mathbf{1}\rangle &\equiv |g, \vec{p}\rangle & \hbar\omega_1 &= E_1 \equiv \hbar\omega_g + \tfrac{|p|^2}{2m} \\ |\mathbf{2}\rangle &\equiv |e, \vec{p} + \hbar\vec{k}_L\rangle & \hbar\omega_2 &= E_2 \equiv \hbar\omega_e + \tfrac{|p+\hbar k_L|^2}{2m} \end{aligned}$$

if $\omega_{eg} = \omega_e - \omega_g$ is the frequency relative to the two bare states it's possible to define a new reference frequency ω_0 and a frequency detuning Δ.

$$\omega_0 \equiv \omega_2 - \omega_1 = \omega_{eg} + \frac{\vec{p}\cdot\vec{k}_L}{m} + \frac{\hbar k_L^2}{2m} \tag{1.15}$$

$$\Delta \equiv \omega_L - \omega_0 = \omega_L - \left(\omega_{eg} + \frac{\vec{p}\cdot\vec{k}_L}{m} + \frac{\hbar k_L^2}{2m}\right) \tag{1.16}$$

where the last two terms in (1.15) and (1.16) account respectively for frequency Doppler shift and momentum recoil.
In the new basis the atomic two levels wavefunction (1.2) and the *Hamiltonian* (1.12) operator becomes:

$$|\psi(t)\rangle = c_1(t)e^{-i\omega_1 t}|\mathbf{1}\rangle + c_2(t)e^{-i\omega_2 t}|\mathbf{2}\rangle \tag{1.17}$$

$$\mathcal{H} = \hbar\omega_1|\mathbf{1}\rangle\langle\mathbf{1}| + \hbar\omega_2|\mathbf{2}\rangle\langle\mathbf{2}| - \vec{d}\cdot\vec{E} \tag{1.18}$$

[2]completeness relation for a basis $\mathcal{I} = \int dp^3|\vec{p}\rangle\langle\vec{p}|$

looking for coefficients time evolution we can restart from the Schödinger equation

$$i\hbar\frac{d}{dt}|\psi(t)\rangle = \mathcal{H}|\psi(t)\rangle \tag{1.19}$$

this lead to a first order differential equations system as in (1.5), (1.6) and, in *rotating wave approximation* we find:

$$\dot{c}_1 = -i\frac{\Omega_R}{2}\, e^{i(\Delta\ t\ -\ \phi_L)}\ c_2 \tag{1.20}$$

$$\dot{c}_1 = -i\frac{\tilde{\Omega}_R}{2}\, e^{-i(\Delta\ t\ +\ \phi_L)}\ c_1 \tag{1.21}$$

Where Ω_R is the *Rabi frequency* defined as:

$$\Omega_R = \frac{\langle g|\vec{d}\cdot\vec{E}|e\rangle}{\hbar} \tag{1.22}$$

Such *Rabi* frequency contains the field–to–atom coupling strength and represents the oscillating angular frequency of the atomic system under coherent field interaction.
In order to find a solution for equations (1.20) (1.21) we can start with a test function in the form $c_2(t) = e^{i\mu t}$; its substitution into the equations leads to an eigenvalues equation in μ and to conditioned solutions in the form:

$$\begin{aligned} c_1(t) &= e^{i\frac{\Delta\ t}{2}}\Big\{c_1(0)\Big[\cos\Big(\tfrac{\Omega' t}{2}\Big) - i\tfrac{\Delta}{\Omega'}\sin\Big(\tfrac{\Omega' t}{2}\Big)\Big] - \\ &\qquad c_2(0)e^{i\phi_L}\Big[-i\tfrac{\Omega_R}{\Omega'}\sin\Big(\tfrac{\Omega' t}{2}\Big)\Big]\Big\} \end{aligned} \tag{1.23}$$

$$\begin{aligned} c_2(t) &= e^{-i\frac{\Delta\ t}{2}}\Big\{c_1(0)e^{i\phi_L}\Big[-i\tfrac{\Omega_R}{\Omega'}\sin\Big(\tfrac{\Omega' t}{2}\Big)\Big] + \\ &\qquad c_2(0)\Big[\cos\Big(\tfrac{\Omega' t}{2}\Big) + i\tfrac{\Delta}{\Omega'}\sin\Big(\tfrac{\Omega' t}{2}\Big)\Big]\Big\} \end{aligned} \tag{1.24}$$

where Ω' is the generalized *Rabi frequency* defined as follows:

$$\Omega' = \sqrt{\Delta^2 + \Omega_R^2} \tag{1.25}$$

Supposing the system into ground state ($|\mathbf{1}\rangle = |g, \vec{p}\rangle$) at time $t = 0$, this holds to equivalent initial conditions for evolution differential equations as $c_1(0) = 1$ and $c_2(0) = 0$. After an interaction time τ the probability to find atoms in state $|\mathbf{1}\rangle$ or $|\mathbf{2}\rangle$ is given from:

$$P_1(\tau) = |c_1(\tau)|^2 = \left(\frac{\Omega_R}{\Omega'}\right)^2 \cos^2\left(\frac{\Omega'\tau}{2}\right) = \left(\frac{\Omega_R}{\Omega'}\right)^2 \frac{1+\cos\Omega'\tau}{2} \quad (1.26)$$

$$P_2(\tau) = |c_2(\tau)|^2 = \left(\frac{\Omega_R}{\Omega'}\right)^2 \sin^2\left(\frac{\Omega'\tau}{2}\right) = \left(\frac{\Omega_R}{\Omega'}\right)^2 \frac{1-\cos\Omega'\tau}{2} \quad (1.27)$$

From these equations it's easy to understand that a two level atomic system under the interaction with an oscillating electric field of frequency ν_L oscillates between the ground and exited state; moreover the total population inversion of a sample prepared in the ground state is possible just only for resonant radiation $\Delta = 0$ whatever the interaction time. This picture is the foundation of the working principle of atomic clocks operating with the *Ramsey's method* and of many spectroscopical applications [31] (see *Bloch Optical Equations* and *Bloch Vector Picture* [76, 77]).
In the case of perfect resonant radiation, equations (1.23) (1.24) assume the more simple form

$$c_1(t) = c_1(0)\cos\left(\frac{\Omega_R t}{2}\right) - ic_2(0)e^{-i\phi_L}\sin\left(\frac{\Omega_R}{2}\right) \quad (1.28)$$

$$c_2(t) = -ic_1(0)e^{i\phi_L}\sin\left(\frac{\Omega_R t}{2}\right) + c_2(0)\cos\left(\frac{\Omega_R t}{2}\right) \quad (1.29)$$

From this coefficients, together with the previous assumption on the initial condition, the state function for the system (eq. 1.17) becomes:

$$|\psi(t)\rangle = e^{-i\omega_1 t}cos\Big(\frac{\Omega_R\tau}{2}\Big)|1\rangle + e^{-i\omega_2 t}e^{-i\frac{\pi}{2}}e^{i\phi_L}sin\Big(\frac{\Omega_R\tau}{2}\Big)|2\rangle \quad (1.30)$$

Now the total inversion as a consequence of the oscillations is easy to figure. The plot in (1.2) displays the internal state probability as a function of interaction time (*Rabi Oscillations plot*), the conditions $c_1(0) = 1$, $c_2(0) = 0$ and $\Delta = 0$ are also assumed. Considering the resulting expression in (1.30) it's possible to argue that a finite time duration *pulse* such that $\tau = \pi/\Omega_R$ will transfer all atoms into the state $|1\rangle$ with probability $P_R = 1$: this will be defined as π **pulse**; whereas a *pulse* such that $\tau = \pi/(2\Omega_R)$ will transfer atoms into a coherent superposition of states $|1\rangle$ and $|2\rangle$ with the same amplitude: this other will be defined as $\pi/\mathbf{2}$ **pulse**.

To came into a phenomenological view, considering both internal and external atomic degree of freedom, we can refer to the sketch in picture (1.3) where an atomic system traveling along the x direction is shown in interaction with an incoming beam; different situations are shown for π pulse and

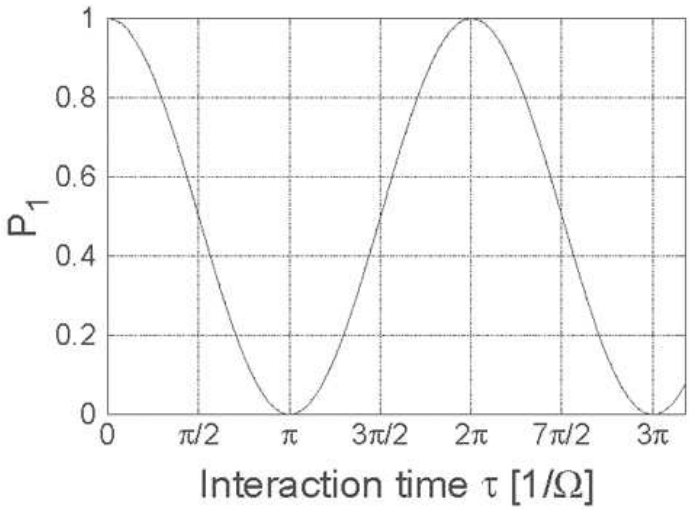

Figure 1.2: Probability to detect atom in First state after an interaction with e.m. field for a time τ (*Rabi oscillation plot*)

$\pi/2$ pulse. For the π pulse interaction it's possible to see an atom in initial state ground $|1\rangle$ absorbing a photon with energy $\hbar\omega_L$ and acquiring a momentum $\hbar\vec{k}_L$: a transition to exited $|2\rangle$ state occurs. On the other side the inverse process occurs as a stimulated emission for an atom in initial state $|2\rangle$ with the opposite internal state transition and the emission of a photon with energy $\hbar\omega_L$ and momentum $-\hbar\vec{k}_L$. For a $\pi/2$ pulse case interacting with the atomic system in initial state $|1\rangle$ we can see a part of atomic wavefunction still traveling in x direction with no extra phase, while another part in the state $|2\rangle$ with an additional phase term $(\phi_L - \pi/2)$ and an acquired momentum $\vec{p} + \hbar\vec{k}_L$ travelling in the direction of this last vector. Starting with an atomic system in initial state $|2\rangle$ and momentum $\vec{p} + \hbar\vec{k}_L$, after the interaction again the opposite process occurs but now part of the wavefunction is sent back into the $|1\rangle$ with a discrete momentum loss of the same amount. The situations described in this brief discussion and in particular the *wavepacket separation* in two parts independently evolving in two different paths are the foundation of the *matter wave interferometry*: they are going to become for us the basic theoretical tools to manage the Atom Interferometer theory. It's easy to see that π pulse and $\pi/2$ pulse, for recoil effect and state inversion by one side, and both for recoil effect and separation/recombination effects from the other side, can be considered as a matter–wave mirror and a matter–wave beamsplitter in an optical interferometer analogy, basic bricks for building an interferometer.

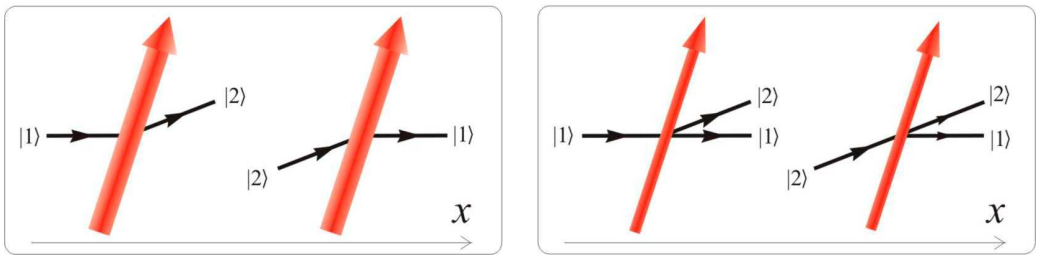

(a) π pulse (b) $\pi/2$ pulse

Figure 1.3: Action of a π pulse (a) and of a $\pi/2$ pulse (b) on a two level atom, matter–wave *mirror* and matter–wave *beamsplitter*

As we are going to see the acceleration sensitivity for an interferometer depends on the interferometer time duration T and the larger is it, higher will be the sensitivity, that's why to increase performances of the future device a coupling between states with lifetime superior to the interferometer time is mandatory. The previous description with a single photon coupling to a two level atomic system neglecting spontaneous decay it's far from the reality because the only infinite lifetime state is the ground state whereas for the others there is a well known probability of decay, for Rubidium the optical transitions of D_2 line exhibit a lifetime of 26 ns.
Looking to atomic spectra the appropriate transition choice for building an interferometer is to couple states the way to have the best approximation of a two level system but also to guarantee lifetimes compatible or higher of the experimental time. The choice of dipole forbidden transitions is inadequate because if the spontaneous emission is strongly suppressed the same holds for absorbtion probability. The best candidate states for the interferometers are atomic hyperfine splitting levels of the ground state, in particular for ^{87}Rb $D2$ transitions relative to the state $5^2S_{\frac{1}{2}}$ a hyperfine splitting into two sublevels occurs with 6.8 GHz of frequency distance (see app. A pages 205 and 205). These two levels can be coupled by microwave pulses in agreement with a common experimental setup adopted for atomic fountain clocks where momentum transfer is unwanted (velocity transfer $\sim 10^{-4}$ mm/s). For an Interferometer the momentum transfer is fundamental that's why the adopted scheme provides to couple the two hyperfine states by two photons *Raman* transitions generated by two counter–propagating laser beam with frequency difference matching the atomic hyperfine splitting. This configuration ensures to manage a good two level system with infinite lifetime but also a big momentum transfer from the two photons recoil (velocity transfer $2v_r \sim 12$ mm/s).

1.1.2 Two photons *Raman transitions*, multi level atomic system

As we have seen in the previous section, more theoretical tools and a specific treatment of the two photons transitions are needed in order to approach to the Atom Interferometer implementation and results . We are going to present a semiclassical model describing both internal and external degree of freedom as in the previous single photon case. Let's consider now a multilevel atomic system with ground state levels $|a\rangle$ and $|b\rangle$ and a set of exited state levels $|ij\rangle$. For ^{87}Rb we can consider $F = 1$ and $F = 2$ ground state $5\ ^2S_{1/2}$ hyperfine splitting and $F = 0, 1, 2, 3$ hyperfine levels from $5\ ^2P_{3/2}$ exited state.
Let's also consider two electric field oscillating at frequencies ω_{R1} and ω_{R2} with relative k-vectors $\vec{k}_{R1}$ and $\vec{k}_{R2}$, interacting with the atomic system, expressed as follows:

$$\vec{E}_{R1}(\vec{r}, t) = \vec{E}_{R1,0} cos[\vec{r} \cdot \vec{k}_{R1} - \omega_{R1} t + \phi_{R1}] \tag{1.31}$$

$$\vec{E}_{R2}(\vec{r}, t) = \vec{E}_{R2,0} cos[\vec{r} \cdot \vec{k}_{R2} - \omega_{R2} t + \phi_{R2}] \tag{1.32}$$

As in the previous case we introduce a picture describing the internal state and the external momentum state from the tensorial product of two *Hilbert* spaces. In order to treat the two photons transitions as two steps processes with an absorbtion followed by a stimulated emission passing from an intermediate state the introduction of virtual nonphysical[3] states $|ij\rangle$ is needed. In our case a complete set can be individuated in { $|1\rangle$, $|2\rangle$, $|i0\rangle$, $|i1\rangle$,$|i2\rangle$ } where $|1\rangle$ and $|2\rangle$ are the physical ground levels, $|i0\rangle$ is the main intermediate state that can be reached from $|1\rangle$ for absorbtion of a photon from the E_{R1} field or from the state $|2\rangle$ for absorbtion of a photon from E_{R2} field. The other two possible cases takes into account the possibility of an absorbtion of a photon from E_{R1} field by $|2\rangle$ ($|i1\rangle$ state) or of an absorbtion of a photon from E_{R1} by $|1\rangle$ ($|i2\rangle$ state). This situation can be clarified from the frequency diagram in picture (1.4) and from the following scheme describing the single states and the relative energies.

[3]the adjective "*nonphysical*" in the description of this model for two photons transitions refers to the impossibility to perform a measurement on any observable relative to intermediate steps of the process. From the other hand if physical possible intermediate states are absent the process not occurs

$$
\begin{array}{lcll}
|1\rangle & = & |a,\vec{p}\rangle & \hbar\omega_1 = \hbar\omega_a + \frac{|\vec{p}|^2}{2m} \\
|2\rangle & = & |b,\vec{p}-\hbar\vec{k}_{R1}-\hbar\vec{k}_{R2}\rangle & \hbar\omega_2 = \hbar\omega_b + \frac{|\vec{p}+\hbar\vec{k}_{R1}-\hbar\vec{k}_{R2}|^2}{2m} \\
|i0\rangle & = & |i,\vec{p}+\hbar\vec{k}_{R1}\rangle & \hbar\omega_{i0} = \hbar\omega_c + \frac{|\vec{p}+\hbar\vec{k}_{R1}|^2}{2m} \\
|i1\rangle & = & |i,\vec{p}+2\hbar\vec{k}_{R1}-\hbar\vec{k}_{R2}\rangle & \hbar\omega_{i1} = \hbar\omega_c + \frac{|\vec{p}+2\hbar\vec{k}_{R1}-\hbar\vec{k}_{R2}|^2}{2m} \\
|i2\rangle & = & |i,\vec{p}+\hbar\vec{k}_{R2}\rangle & \hbar\omega_{i2} = \hbar\omega_c + \frac{|\vec{p}+\hbar\vec{k}_{R2}|^2}{2m}
\end{array}
$$

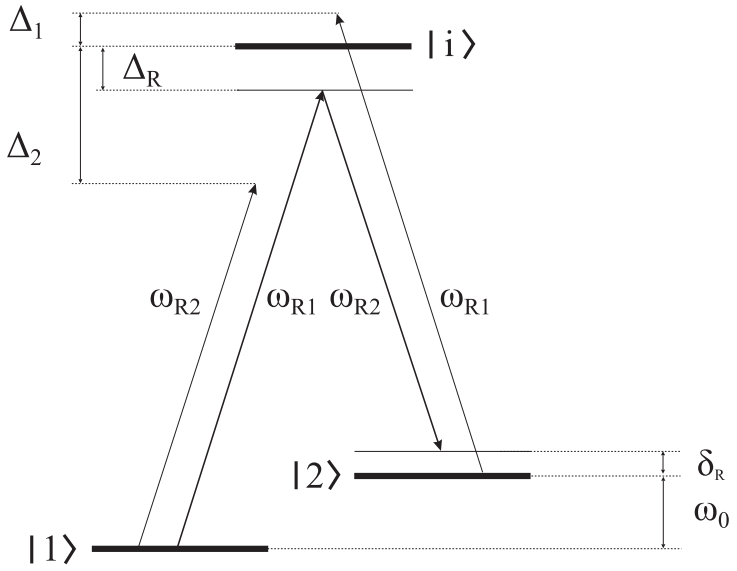

Figure 1.4: Two photons *Raman Transitions* frequency diagram.

From the diagram it's possible to individuate the frequency difference between the two fields given by $\omega_{R1}-\omega_{R2}$ whereas the difference between the two bare hyperfine levels is given by ω_0 thus the frequency disaccord between the first frequency difference and the second one will be named as δ_R.
On the other side the frequencies differences Δ_1 and Δ_2 indicate the detuning of a single laser field E_{R1} and E_{R2} respectively from the transitions $|2\rangle \rightarrow |i0\rangle$ and $|1\rangle \rightarrow |i0\rangle$. It's important to underline that, considering as a virtual state $|i0\rangle$ one from hyperfine $F = 0,1,2,3$ levels from 5 $^2P_{3/2}$, in order to avoid single photons transitions, both laser fields must be far detuned from transition driving atoms from the ground state to the exited ones. As indicated into the diagram the frequency Δ_R denotes the common detuning of both lasers from the exited state.
The Hamiltonian Operator for the defined close states system is given from:

$$\mathcal{H} = \sum_s \hbar\omega_s|s\rangle\langle s| + \vec{d}\cdot(\vec{E}_{R1}+\vec{E}_{R2}) \tag{1.33}$$

with ($s = 1, 2, i0, i1, i2$), whereas the generic atomic wavefunction including the time evolution dependence:

$$|\psi(t)\rangle = \sum_s c_s(t) e^{-i\omega_s t} |s\rangle \tag{1.34}$$

A new definition of *Rabi frequency* is needed to account the single field contribution and the single possible transition steps: here the letter $l = 1, 2$ stands for laser fields, $m = 1, 2$ for physical ground levels ($|1\rangle$, $|2\rangle$) and $n = i0, i1, i2$ for intermediate states.

$$\Omega_{lmn} = \frac{\langle n| - \vec{d} \cdot \vec{E}_{Rl,0} |m\rangle}{\hbar} \tag{1.35}$$

Substituting the wavefunction into the Srödinger equation, from the same method described in section (1.1.1) we reach to a differential equations system for coefficients evolution, and applying the *rotating wave approximation* it follows:

$$\begin{aligned}
i\dot{c}_1(t) &= c_{i0}(t)\frac{\tilde{\Omega}_{1,i0,1}}{2} e^{i(\Delta_R t - \phi_{R1})} + c_{i2}(t)\frac{\tilde{\Omega}_{1,i2,2}}{2} e^{i(\Delta_2 t - \phi_{R2})} \\
i\dot{c}_2(t) &= c_{i0}(t)\frac{\tilde{\Omega}_{2,i0,2}}{2} e^{i(\ (\Delta_R - \delta_R)t - \phi_{R2})} + c_{i1}(t)\frac{\tilde{\Omega}_{2,i1,1}}{2} e^{i(\Delta_1 t - \phi_{R1})} \\
i\dot{c}_{i0}(t) &= c_1(t)\frac{\Omega_{1,i0,1}}{2} e^{-i(\Delta_R t - \phi_{R1})} + c_2(t)\frac{\Omega_{2,i0,2}}{2} e^{-i(\ (\Delta_1 - \delta_R)t - \phi_{R2})} \\
i\dot{c}_{i1}(t) &= c_2(t)\frac{\Omega_{2,i1,2}}{2} e^{-i(\Delta_1 t - \phi_{R1})} \\
i\dot{c}_{i2}(t) &= c_1(t)\frac{\Omega_{1,i2,2}}{2} e^{-i(\Delta_2 t - \phi_{R2})}
\end{aligned} \tag{1.36}$$

From equation (1.34) the effect of time evolution terms of kind $e^{i\omega_1 t}$ and $e^{i\omega_2 t}$ is included; the same holds for laser detuning effect with exponentials in the form $e^{-i\Delta_j t}$. The integration of the equations cuts away terms relative to the intermediate levels for adiabatic elimination of slow varying contributes (see for reference K. Moler, D. S. Weiss, M. Kasevich, S. Chu, method [56]). It's possible to verify that the coefficients relative to $|i\rangle$ states oscillates with frequency given from Δ_R whereas the coefficients c_1 and c_2 oscillates with frequency slower as much Δ_R is big compared with the *Rabi* frequencies Ω_{lmn}. If we calculate the evolutions of coefficients c_{ij}, after considering c_1 and c_2 as constant, the resulting equations are:

$$\begin{aligned} c_{i0}(t) &= c_1\frac{\Omega_{1,i0,1}}{\Delta_R}e^{-i(\Delta_R t-\phi_{R1})} + c_2\frac{\Omega_{2,i0,2}}{2(\Delta_1-\delta_R)}e^{-i(\ (\Delta_1-\delta_R)t-\phi_{R2})} \\ c_{i1}(t) &= c_2(t)\frac{\Omega_{2,i1,2}}{2\Delta_1}e^{-i(\Delta_1 t-\phi_{R1})} \\ c_{i2}(t) &= c_1(t)\frac{\Omega_{1,i2,2}}{\Delta_2}e^{-i(\Delta_2 t-\phi_{R2})} \end{aligned} \tag{1.37}$$

thus substituting into the first two equations of (1.36) it follows:

$$\begin{aligned} i\dot{c}_1(t) &= c_1(t)\Big[\frac{|\Omega_{1,i0,1}|^2}{4\Delta_R}+\frac{|\Omega_{1,i2,2}|^2}{4\Delta_2}\Big] + \\ &\quad c_2(t)\Big[\frac{\tilde{\Omega}_{1,i0,1}\Omega_{2,i0,2}}{4(\Delta_R-\delta_R)}e^{-i(\phi_{R1}-\phi_{R2})+i\delta_R t}\Big] \end{aligned} \tag{1.38}$$

$$\begin{aligned} i\dot{c}_2(t) &= c_1(t)\Big[\frac{\tilde{\Omega}_{2,i0,2}\Omega_{1,i0,1}}{4\Delta_R}e^{i(\phi_{R1}-\phi_{R2})-i\delta_R t}\Big] + \\ &\quad c_2(t)\Big[\frac{|\Omega_{2,i0,2}|^2}{4(\Delta_R-\delta_R)}+\frac{|\Omega_{2,i1,1}|^2}{4\Delta_1}\Big] \end{aligned} \tag{1.39}$$

The definition of *AC Stark shifts* for the two states under interaction with the light fields simplify again the relative equations; we also define the *AC shift* sum and difference:

$$\Omega_1^{\mathrm{AC}} = \Big[\frac{|\Omega_{1,i0,1}|^2}{4\Delta_R}+\frac{|\Omega_{1,i2,2}|^2}{4\Delta_2}\Big] \qquad \Omega_2^{\mathrm{AC}} = \Big[\frac{|\Omega_{2,i0,2}|^2}{4(\Delta_R-\delta_R)}+\frac{|\Omega_{2,i1,1}|^2}{4\Delta_1}\Big] \tag{1.40}$$

$$\Omega^{\mathrm{AC}} = \Omega_1^{\mathrm{AC}} + \Omega_2^{\mathrm{AC}} \qquad \delta^{\mathrm{AC}} = \Omega_1^{\mathrm{AC}} - \Omega_2^{\mathrm{AC}} \tag{1.41}$$

after such definitions and holding the typical condition for the detuning $\delta_R \ll \Delta_R$, that means $\Delta_R - \delta_R \simeq \Delta_R$, it follows also $\Delta_R \gg \omega_D = \vec{p}\cdot\vec{k}_{eff}/m$ (*Doppler shift* term) and $\Delta_R \gg \omega_R = \hbar|\vec{k}_{eff}|^2/2M$ (*recoil shift* term); thus equations (1.38) and (1.39) take the form:

$$i\dot{c}_1(t) = c_1(t)\Omega_1^{\mathrm{AC}} + c_2(t)\frac{\tilde{\Omega}_{eff}}{2}e^{-i\phi_{eff}+i\delta_R t} \tag{1.42}$$

$$i\dot{c}_2(t) = c_1(t)\frac{\tilde{\Omega}_{eff}}{2}e^{i\phi_{eff}-i\delta_R t} + c_2(t)\Omega_2^{\mathrm{AC}} \tag{1.43}$$

Where the new introduced parameter ϕ_{eff}, Ω_{eff}, together with ω_{eff}, $\vec{k}_{eff}$, Ω'_{eff} are going to became the fundamental tools for the interferometry theory, defined as follows:

$$\begin{aligned}
\omega_{eff} &= \omega_{R1} - \omega_{R2} && (1.44)\\
\vec{k}_{eff} &= \vec{k}_{R1} - \vec{k}_{R2} = \frac{\vec{k}_{R1}}{|\vec{k}_{R1}|}(|\vec{k}_{R1}| + |\vec{k}_{R2}|) && (1.45)\\
\phi_{eff} &= \phi_{R1} - \phi_{R2} && (1.46)\\
\Omega_{eff} &= \frac{\Omega_{1,01,1}\Omega_{2,01,2}}{2\Delta_R} && (1.47)\\
\Omega'_{eff} &= \sqrt{\Omega_{eff}^2 + (\delta_R - \delta^{\mathrm{AC}})^2} && (1.48)
\end{aligned}$$

In the equation (1.47) we find the new definition *Rabi frequency* holding for the two photons transition: single contribution $\Omega_{i,0j,i}$ is calculated as for a single photon transition to the exited state. The last equality in equation (1.45) holds only for *Raman* counter–propagating beams, the same configuration as for our implementation. Such equality also shows as such configuration leads to the bigger momentum transfer from beams to atoms. In order to remove the exponential time dependence in the off diagonal terms of coefficients time evolution equations, let's define new coefficients in the following form:

$$c_1(t) = g_1(t)e^{i\frac{\delta_R}{2}t - i\frac{\Omega^{\mathrm{AC}}}{2}t} \qquad c_2(t) = g_2(t)e^{-i\frac{\delta_R}{2}t - i\frac{\Omega^{\mathrm{AC}}}{2}t} \qquad (1.49)$$

thus the system (1.42), (1.43) becomes:

$$\begin{aligned}
i\dot{g}_1(t) &= \frac{1}{2}\Big[g_1(t)(\delta_R - \delta^{\mathrm{AC}}) + g_2(t)\Omega_{eff}e^{-i\phi_{eff}}\Big] && (1.50)\\
i\dot{g}_2(t) &= \frac{1}{2}\Big[g_1(t)\Omega_{eff}e^{i\phi_{eff}} + g_2(t)(\delta_R - \delta^{\mathrm{AC}})\Big] && (1.51)
\end{aligned}$$

this last expression can be solved in an analytical way leading to:

$$c_1(t) = e^{\frac{i}{2}(\delta_R-\Omega^{\rm AC})t}\Big\{c_1(0)\Big[\cos\Big(\frac{\Omega'_{eff}t}{2}\Big) - i\frac{\delta_R-\delta^{\rm AC}}{\Omega'_{eff}}\sin\Big(\frac{\Omega'_{eff}t}{2}\Big)\Big] + c_2(0)e^{i\phi_{eff}}\Big[-i\frac{\Omega_{eff}}{\Omega'_{eff}}\sin\Big(\frac{\Omega'_{eff}t}{2}\Big)\Big]\Big\} \quad (1.52)$$

$$c_2(t) = e^{-\frac{i}{2}(\delta_R+\Omega^{\rm AC})t}\Big\{c_1(0)e^{i\phi_{eff}}\Big[-i\frac{\Omega_{eff}}{\Omega'_{eff}}\sin\Big(\frac{\Omega'_{eff}t}{2}\Big)\Big] + c_2(0)\Big[\cos\Big(\frac{\Omega'_{eff}t}{2}\Big) + i\frac{\delta_R-\delta^{\rm AC}}{\Omega'_{eff}}\sin\Big(\frac{\Omega'_{eff}t}{2}\Big)\Big]\Big\} \quad (1.53)$$

Here it is found that coefficients $c_1(t)$ and $c_2(t)$ oscillates with frequency Ω'_{eff}: thus the adiabatic elimination hypothesis is verified under the condition $\Delta_R \gg \Omega'_{eff} \simeq \Omega_{eff} = (\Omega_{1,01,1}\Omega_{2,01,2})/2\Delta_R$.
The equations have the same form of (1.23) and (1.24) holding for the single photon transitions; it's easy to define an analogy between the two cases thanks to the definition of the "*effective*" parameters (1.44 up to 1.48), the previous label "L" becomes "*eff*", a simple comparison comes out form the following table:

single photon transition	$\vec{k}_L$	ω_L	ϕ_L	Δ	Ω	Ω'
two photons transition	$\vec{k}_{eff}$	ω_{eff}	ϕ_{eff}	δ_R	Ω_{eff}	Ω'_{eff}

Under the condition $\Omega_{eff} \gg \delta_R$, $\delta^{\rm AC}$, that is equivalent for the formal point of view to the on–resonance condition for the single photon case leading to eqs. (1.28) and (1.29), the previous equations become:

$$c_1(t) = e^{\frac{i}{2}(\delta_R-\Omega^{\rm AC})t}\Big\{c_1(0)\cos\Big(\frac{\Omega_{eff}t}{2}\Big) - ic_2(0)e^{-i\phi_{eff}}\sin\Big(\frac{\Omega_{eff}}{2}\Big)\Big\} \quad (1.54)$$

$$c_2(t) = e^{-\frac{i}{2}(\delta_R+\Omega^{\rm AC})t}\Big\{-ic_1(0)e^{i\phi_{eff}}\sin\Big(\frac{\Omega_{eff}t}{2}\Big) + c_2(0)\cos\Big(\frac{\Omega_{eff}t}{2}\Big)\Big\} \quad (1.55)$$

Considering atoms in state $|1\rangle$ at $t = 0$ we find a well known oscillating form for the transition probabilities (1.56 , 1.57):

internal state	momentum state transition	phase transfer
$\|a\rangle \to \|a\rangle$	$\|\vec{p}\rangle \to \|\vec{p}\rangle$	$+\frac{\delta_R \tau}{2} - \frac{\Omega^{\mathrm{AC}} \tau}{2}$
$\|a\rangle \to \|b\rangle$	$\|\vec{p}\rangle \to \|\vec{p} + \hbar\vec{k}_{eff}\rangle$	$-\frac{\delta_R \tau}{2} - \frac{\Omega^{\mathrm{AC}} \tau}{2} + \phi_{eff} - \frac{\pi}{2}$
$\|b\rangle \to \|a\rangle$	$\|\vec{p} + \hbar\vec{k}_{eff}\rangle \to \|\vec{p}\rangle$	$+\frac{\delta_R \tau}{2} - \frac{\Omega^{\mathrm{AC}} \tau}{2} - \phi_{eff} - \frac{\pi}{2}$
$\|b\rangle \to \|b\rangle$	$\|\vec{p} + \hbar\vec{k}_{eff}\rangle \to \|\vec{p} + \hbar\vec{k}_{eff}\rangle$	$-\frac{\delta_R \tau}{2} - \frac{\Omega^{\mathrm{AC}} \tau}{2}$

Table 1.1: Phase and Momentum effects for a *Raman* transition, a picture for atomic internal and external states being τ the temporal pulse length

$$P_1(\tau) = |c_1(\tau)|^2 = \cos^2\left(\frac{\Omega_{eff}\tau}{2}\right) = \frac{1 + \cos\Omega_{eff}\tau}{2} \tag{1.56}$$

$$P_2(\tau) = |c_2(\tau)|^2 = \sin^2\left(\frac{\Omega_{eff}\tau}{2}\right) = \frac{1 - \cos\Omega_{eff}\tau}{2} \tag{1.57}$$

Thus it is possible to define again π **pulse** and $\pi/\mathbf{2}$ **pulse** like we did for single photons interaction in section (1.1) at page 41.
In order to evaluate the lasers contribution to the atomic wavefunction for two photons *Raman* transitions, considering a finite pulses temporal duration τ, it can be used as a reference the table (1.1), calculated from equations (1.54) (1.55) considering different initial states. This approach does not take into account the free evolution phase term during the pulse; to include such contribution the coefficients c_1 and c_2 in (1.54) (1.55) must be substituted by $C_k = c_k e^{-i\omega_k t}$, this leads to an additional pase term in the form $-i\omega_k t$ (see [71]). From the interferometer side the method presented so far is useful for a phenomenological picture letting to separate the free evolution phase contribution from the laser interaction one, by the other hand for a formal approach is important to work with coefficient of C_k kind.

1.2 Matter Wave Interferometer

The matter wave interferometer principle consists into a sequence of wavepacket manipulation the way to split the matter wave into two (or more) different paths and recombine it at the end of sequence; typically the sample is prepared in a well defined initial state at the beginning of the sequence and it ends in the same one (see pict. 1.6). The manipulation via interaction with a

radiation field, as in our case, of course is just a possible choice [5]. Quantum mechanical features of matter allows to be sensitive to possible symmetry differences between the two paths resulting in interference fringes at the output door. Such symmetry difference can be motivated by differences in space topology or into potentials experimented by the particle evolving by the two separated paths; for example such symmetry break could be of an electromagnetic nature (see Aharonov Bohm and Aharonov Casher effect [7, 8, 9]) or of a gravitational nature.
As we are going to see in this discussion, atom interferometers are sensitive also to uniform acceleration even if the the field coupled to the mass of the particle is the same for both the interferometric arms; moreover they are sensitive to all inertial effects too, such as rotations and reference frame accelerations.
For a *Mach Zehnder* scheme the interferometric sequence can be characterized by a sequence of laser-matter interactions in form of pulses of kind: $\pi/\mathbf{2}$ **pulse** - π **pulse** - $\pi/\mathbf{2}$ **pulse** (sec 1.1.1 pages 41, 41) whose time duration is $\tau - 2\tau - \tau$ and are separated each other by a free evolution time $T - \tau$. The whole sequence lasts $2T$ as displayed in pict (1.5). As already discussed in section (1.1.1) at page 43 interactions must typically couple long living states the way to let possible long interferometric duration time.

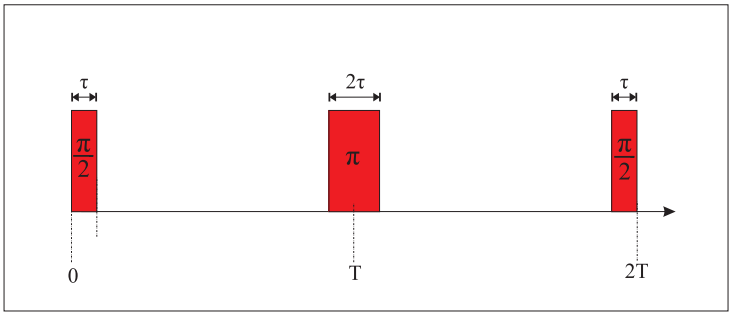

Figure 1.5: Time sequence for *Mach–Zehnder* type interferometer: it starts at $t = 0$ with a $\pi/2$ pulse, a π pulse follows at time $t = T - \tau$ after free evolution and a last $\pi/2$ pulse again follows after a time $t = T - \tau$.

Supposing to start with atoms in initial state $|1\rangle$ and momentum $\vec{p}$ at $t = 0$ with the help of results from sections (1.1.2) (1.1.2) it's also possible to take into the account the momentum recoils effect and state transitions. Taking as bricks the effects of $\pi/2$ pulses and π pulses on internal and external degree of freedom, as displayed in picture (1.3), it's possible also to build a complete scheme for the interferometric sequence as shown in picture

(1.6). Here the analogy between an optical and matter wave *Mach–Zender* interferometer must be underlined. For the first one the interference occurs between light fields and optical components are matter made, whereas for the second one the interference is detected between matter waves fields and the optical components role is played by light pulses. For both cases fringes detection declares a symmetry breaking between the two evolution paths.

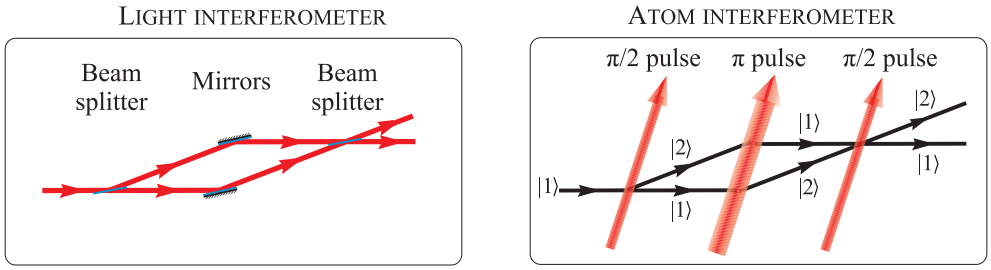

Figure 1.6: The Analogy between an Optical and a Matter Wave Interferometer, *Mach–Zender* type. The $\pi/2$ pulse operate on matter wave as a beamsplitter does on the light, the π pulse works as a mirror.

To calculate the atomic phase result at the end of the interferometric sequence two different approaches are possible: the first one follows a more phenomenological picture (see. [54, 59, 61, 63]) and allows to get a more simple understanding of the single phase contributions, whereas the second one, due to Ch.Bordè, is more formal but it simplifies for us the definition of a transfer function and of a sensitivity function for the interferometer[57, 58, 70, 71]. In the paper [57] a merging between two formalisms has been holden, of course the results are the same. In this thesis just a hint is reported for both approaches (sec. 1.2.1, 1.2.3).

1.2.1 Phenomenological model for the Matter Wave Interferometer

To account for the total atomic phase we are going to separate all the possible contributions following the atomic sample during his evolution along the interferometric sequence, at this level we neglect some spurious shift effects due for example extra stray electric or magnetic fields. It could be useful for the reader to follow the description from temporal and space diagrams in pictures (1.6) and (1.7). The points $\mathbf{x_I^B}$ and $\mathbf{x_I^B}$ into the diagram (1.7) corresponds to the space–time interaction point with the π **pulse**, the labels **I** and **II** identify the two different paths.
The total phase shift can be written as follows:

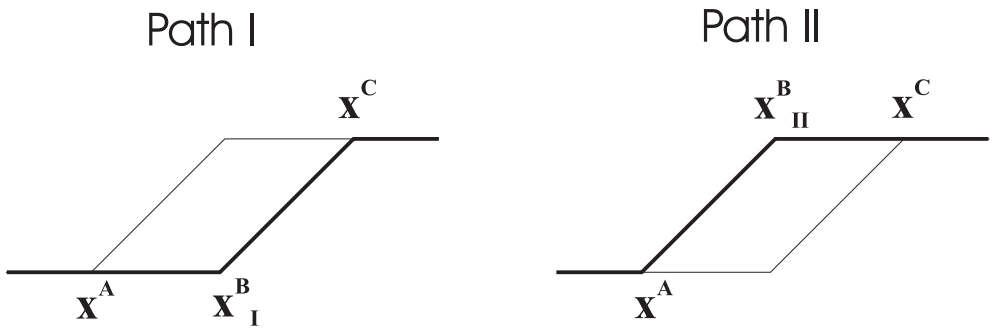

Figure 1.7: Matter Wave Interferometer in *Mach–Zender* configuration, individuation of the two different evolution paths and space–time X_J^I interaction points. The $\pi/2$ pulse operates on matter wave as a beamsplitter does on the light, the π pulse works as a mirror.

$$\Delta\phi_{tot} = \Delta\phi_{light} + \Delta\phi_{path} + \Delta\phi_{sep} \tag{1.58}$$

The last terms accounts for not perfect spatial superposition of the two wavepockets at the end of the sequence. In fact the superposition condition occurs only in presence of unform field, for our purpose it will be considered at the time of accounting acceleration gradients such as for the gravity.

$$\Delta\phi_{sep} = \frac{\vec{p}\cdot(\tilde{\mathbf{x}}_{\mathbf{I}}^{\mathbf{B}} - \tilde{\mathbf{x}}_{\mathbf{II}}^{\mathbf{B}})}{2\hbar} \tag{1.59}$$

Here $\mathbf{x}_{\mathbf{I}}^{\mathbf{C}}$ and $\mathbf{x}_{\mathbf{II}}^{\mathbf{C}}$ are the two different endpoints that identify the mismatching, the interference already occurs because of the extended spatial dimension of the wavepocket.

Light Phase shift

In order to evaluate the phase shift inducted on the atoms by the light field interaction during the whole interferometric sequence, is needed to take as reference results reported into the table (1.1) at page 50; here each single pulse contribution has been calculated. It's important to point out that phase shifts present into such table were coming out for interaction between atoms and light at time zero and position zero, and the spatial and temporal evolution for the field were not considered. For the interferometer the situation changes because the sequence of interactions follows in different points of the space time, while the electric fields progresses their own evolution. To account for this the laser field phase factors ϕ_{eff} in the table must be replaced by the following expression (see definitions (1.44), (1.45), (1.46))

$$\phi^t_{eff} \equiv \phi(\mathbf{x}, t) = \vec{k}_{eff} \cdot \vec{r} - \omega_{eff} t + \phi_{eff,0} \tag{1.60}$$

The accumulated phase in the two different paths is:

Phase in Path I state transitions ($|1\rangle \rightarrow |1\rangle \rightarrow |2\rangle \rightarrow |1\rangle$)

$$\begin{aligned} \phi_I &= (\tfrac{\delta_R \tau}{2} - \tfrac{\Omega^{\mathrm{AC}} \tau}{2}) + (\phi^{T-\tau}_{eff} - \delta_R \tau - \Omega^{\mathrm{AC}} \tau - \tfrac{\pi}{2}) + \\ &\quad (\tfrac{\delta_R \tau}{2} - \tfrac{\Omega^{\mathrm{AC}} \tau}{2} - \phi^{2T-\tau}_{eff} - \tfrac{\pi}{2}) \\ &= \phi^{T-\tau}_{eff} - \phi^{2T-\tau}_{eff} - \pi - 2\Omega^{\mathrm{AC}} \tau \end{aligned}$$

Phase in Path II state transitions ($|1\rangle \rightarrow |2\rangle \rightarrow |1\rangle \rightarrow |1\rangle$)

$$\begin{aligned} \phi_I &= (\phi^0_{eff} - \tfrac{\pi}{2} - \tfrac{\delta_R \tau}{2} - \tfrac{\Omega^{\mathrm{AC}} \tau}{2}) + (\delta_R \tau - \Omega^{\mathrm{AC}} \tau - \phi^{T-\tau}_{eff} - \tfrac{\pi}{2}) + \\ &\quad (\tfrac{\delta_R \tau}{2} - \tfrac{\Omega^{\mathrm{AC}} \tau}{2}) \\ &= \delta_R \tau + \phi^0_{eff} - \phi^{T-\tau}_{eff} - \pi - 2\Omega^{\mathrm{AC}} \tau \end{aligned}$$

Thus the total phase shift due to the interaction with the beams is given from

$$\begin{aligned} \Delta\phi_{las} = \phi_{II} - \phi_I &= [\phi^0_{eff} - 2\phi^{T-\tau}_{eff} + \phi^{2T-\tau}_{eff}] + \delta_R \tau \\ &\simeq \phi^0_{eff} - 2\phi^{T-tau}_{eff} + \phi^{2T-\tau}_{eff} \end{aligned} \tag{1.61}$$

we have seen that the AC Stark shift contributions cancels out and a definitive form can be summarized as.

$$\boxed{\Delta\phi_{las} = \phi(\mathbf{x^A}, 0) - \phi(\mathbf{x^B_I}, T) - \phi(\mathbf{x^B_{II}}, T) + \phi(\mathbf{x^c_{II}}, 2T)} \tag{1.62}$$

Evolution Phase shift

The *Feynman's path integral* approach [75] can be chosen to determine the dephasing on the wavefunction of a particle traveling toward the two different paths; here just few steps are reported in order to give a general idea for the results. For complete treatment see the paper from Pippa Storey and Claude Cohen-Tannoudji ([59]). The final wavefunction of a particle moving from a point $(\mathbf{x_A}, t_A)$ to $(\mathbf{x_C}, t_C)$ can be evaluated from the quantum operator

$$\psi(\mathbf{x_C}, t_C) = \int d\mathbf{x_A} K(\mathbf{x_A}, t_A, \mathbf{x_C}, t_C)\psi(\mathbf{x_A}, t_A) \tag{1.63}$$

if $\mathcal{L}$ is the lagrangian of the system, the action is defined from the integral:

$$S_\Gamma = \int_\Gamma \mathcal{L}[x(t), \dot{x}(t)]dt \tag{1.64}$$

The Feynman's expression for the quantum propagator is given from:

$$K(\mathbf{x_A}, t_A, \mathbf{x_C}, t_C) = \mathcal{N} \sum_\Gamma e^{iS_\Gamma/\hbar} \tag{1.65}$$

Where $\mathcal{N}$ is a normalization constant and the sum $\sum_\Gamma$ indicates the integral over all possible paths connecting $(\mathbf{x_A}, t_A)$ to $(\mathbf{x_C}, t_C)$. It can be shown that in the case of at most quadratic lagrangian in x and $\dot{x}$ the quantum propagator takes the simplest form of

$$K(\mathbf{x_A}, t_A, \mathbf{x_C}, t_C) = F(t_A, t_C)e^{i\frac{S_{cl}}{\hbar}} \tag{1.66}$$

Now S_{cl} is the classical action and the new unknown $F(t_A, t_C)$ function is just only dependent from the initial and final instants; following the procedure chosen by Pippa Storey and Claude Cohen-Tannoudji, it can be shown that a particle in a pure gravitational potential presents an evolution given from:

$$\psi(\mathbf{x_C}, t_C) = F(t_A, t_C)\sqrt{\frac{i\pi\hbar}{C(t_A, t_C)}}e^{iS_\Gamma/\hbar}\psi(\mathbf{x_A}, t_A) \tag{1.67}$$

with

$$C(t_A, t_C) = \frac{m}{2(t_C - t_A)} \quad \text{and} \quad F(t_A, t_C) = \sqrt{m21\pi\hbar(t_C - t_A)} \tag{1.68}$$

so that is possible to conclude that the phase evolution between point **A** and point **B** is given from

$$\Delta\phi_{A\to C} = \frac{1}{\hbar}S_{cl}(A, C) \tag{1.69}$$

In the interferometer framework, where two different paths must be considered, and using the definition (1.64), the phase shift difference becomes:

$$\boxed{\Delta\phi_{path} = \frac{S_{clI} - S_{clII}}{\hbar} = \frac{1}{\hbar}\oint_{\Gamma_0} \mathcal{L}dt} \tag{1.70}$$

1.2.2 Inertial Shifts Effects and interferometric measurement

In this sections the inertial shifts measurable by an atom interferometer are evaluated. Here we are going to account only for accelerations and acceleration gradients included into the principal target of this thesis. By means of Atom Interferometry also direct measurement of rotation effects can be addressed, for this purpose specific configurations are needed, we remanded to literature for details [113, 114, 115].

Uniform Accelerations and Gravity

The discussion will start with a gravity uniform field as a familiar example and then it will be easily generalized to a generic uniform acceleration. Suppose to consider a vertical configuration for the interferometer with *Raman* counter–propagating beams parallels to the acceleration to be measured (for fields space evolution $\vec{r}_i \Rightarrow z_i$). It's easy to understand that the separation contribution $\Delta\phi_{sep}$ and the evolution one $\Delta\phi_{path}$ vanishes because of the totally symmetric physical configuration so that the inertial phase shift can just coming out from the laser field contribute. Both for a launching sequence and for a falling sequence the vertical atomic velocity changes according with the well known linear law:

$$v_z(t) = v_z(0) - gt \tag{1.71}$$

therefore it's fundamental to guarantee the interferometric sequence performances keeping the *Raman* beams in resonance with the atoms in their frame or to keep constant the detuning δ_R if not null. From the experimental side the technics employed to compensate for the doppler shift is to ramp linearly the *Raman* beam frequency difference in agreement with the free falling linear law. Besides such technical considerations, from basics kinematic consideration, supposing to start with $z(t=0) = 0$, $v_z(t=0) = v_0$ and $\phi_{eff,0} = 0$, single laser fields contributions present in eq. (1.62) becomes:

$$\begin{aligned}
\phi(\mathbf{x^A}, 0) &= 0 \\
\phi(\mathbf{x_I^B}, T) &= k_{eff}\Big[-\frac{1}{2}gT^2 + v_0T\Big] \\
\phi(\mathbf{x_{II}^B}, T) &= k_{eff}\Big[-\frac{1}{2}gT^2 + \Big(v_0 + \frac{\hbar k_{eff}}{m}\Big)T\Big] \\
\phi(\mathbf{x^c}, 2T) &= k_{eff}\Big[-2gT^2 + \Big(2v_0 + \frac{\hbar k_{eff}}{m}\Big)T\Big]
\end{aligned}$$

The fields time depending phase part $i\omega_{eff}t$ from eq. (1.60) can be evaluated at same way but the total results substituted in (1.62) vanishes.
If it is true that, from a kinematic point of view, in order to measure an average acceleration performed by a particle in a certain space evolution interval, just from some space and time measurement, at least three detection points are needed. Equations above point out as such measurements can be acquired form a well known time space sequence of pulses, moreover the relative beam wavefronts works as space–time reference for free falling atoms. This could be an hint for the reader to figure as the relative phase noise between the two *Raman* beams configures as one of the principal trouble for the interferometer.
Leaving aside such phenomenological considerations and coming back to the interferometer formalism framework, from the equations above and from equation (1.62) the total phase shift can be calculated as:

$$\boxed{\Delta\Phi_{light} = -k_{eff}\ g\ T^2} \tag{1.72}$$

This is a well known formula for a constant acceleration shift as can be found in literature; it's important to underline as the time duration T of the matter wave interferometer works as the arm for an optical interferometer. Increasing the time duration it also increases the sensitivity to accelerations according with a square power law $\sim T^2$. This will be the crucial point for space born and microgravity born interferometers where big interrogation time will be allowed.
Formula (1.72) does not account for finite time duration of each *Raman* pulse: from a more detailed calculation it comes out:

$$\Delta\Phi_{light} = -k_{eff}g\Big(T + \frac{4\tau}{\pi}\Big)\Big(T + 2\tau\Big) \tag{1.73}$$

From the discussion so far emerges an experimental technical hint for the first order uniform acceleration measurement. Considering the *Raman* beams frequency ramp needed to address the linear velocity changes (1.71), an acceleration measurement can be easily derived from a determination of the best frequency ramp slope that exactly compensates for the Doppler shift: a direct measurement of phase shift is not needed. This is the typical approach for atom interferometry based terrestrial gravimeters [71, 73], of course it can be also exported to space atom interferometry applications.

Acceleration gradients

Here we are going to estimate the phase contribute to a single interferometer due to non uniform accelerations: in presence of a gravity field different

accelerations affect the motion of the wavepacket evolving into the upper and lower path. Another matter regards the gradiometric devices or interferometers working in the differential mode. For such kind of the devices two different atomic clouds are launched in sequence at different height, in other words they measure the acceleration difference between two different interferometers.
For a single interferometer the two paths separate each other by a distance given from $\delta z = v_{rec}T$, where $v_{rec} \simeq 6$ mm/s is the recoil velocity due to *Raman* pulses, for a typical sequence $T = 150$ ms the total separation distance is $\delta z \simeq 0.9\ mm\ T$, for the Earth environment conditions this quantity is enough to detect gradient effects. To calculate such effect and the others to higher orders in terrestrial gravitational framework a complete treatment is reported in [63]. The gravity distance dependence can be express by considering an initial value g_0 at the origin of the interferometer reference frame ($z = 0$) and then a constant linear variation can be added with a gradient $\gamma \sim 3 \times 10^{-6}\ /s^2$; thus the motion equation for a free falling body becomes $\ddot{z}(t) = -g_0 + \gamma z(t) + z_0$. In this conditions an additional atomic phase contribution from the path evolution term must be considered, so an additional term has to be added into the atomic Lagrangian

$$\mathcal{L} = \frac{1}{2}m\dot{z}^2 - mg_0 z + \frac{1}{2}m\gamma z^2 \tag{1.74}$$

The phase shift can be evaluated with different methods, the final results takes the form

$$\Delta\Phi_{grad} = k_{eff}\gamma\ T^2\Big(\frac{7}{12}gT^2 - v_0 T - z_0\Big) \tag{1.75}$$

Accounting for typical interferometer parameter in the Earth gravitational field ($g_0 \simeq 9.8\ \mathrm{ms}^{-2}$) it results that the gradient contribution on a single interferometer is $\sim 10^{-8}$ smaller than the therm from the uniform field contribution. By the other hand the equation (1.75) shows a dependence of the phase shift from the gradient to the forth power of T, ($\Delta\Phi_{grad} \sim k_{eff}\gamma\ T^4$), whereas the sensitivity to the uniform component of the field scales just only with the square power, this means that in microgravity conditions where largest interferometer times are easiest to be performed the gradient contribution takes more importance.

For multisample interferometric devices dedicated to gradients measurement the common mode uniform field contribution cancels out together with all common mode vibration noise effect coming from the environment and affecting for instance the *Raman* beam. Supposing to perform two different

simultaneous gradiometric sequences at different altitude with distance Δh, the resulting phase shift is given by:

$$\Delta\Phi_g^{up} - \Delta\Phi_g^{dw} = -k_{eff}(g_{up} - g_{dw})T^2 = -k_{eff}\gamma\Delta h T^2 \tag{1.76}$$

Where g_{up} and g_{up} are the two different accelerations into at the relative altitude of the two interferometers. For the terrestrial conditions considered before and for typical operative conditions for an interferometer $\Delta h \simeq 1.12$ rad/m therefore for a distance of 30 cm the differential acceleration is around $10^{-7}g$.

1.2.3 The *ABCD* calculations for a Matter Wave Interferometer

Here are reported the basic idea and results for the Matter Wave Interferometer phase output calculation as formulated by Ch. Borde' in the paper [57]. The model follows a matrix form for evolution equations in terms of $ABCD$ matrices in a similar way as in optics approach. A single interaction with the laser field can be written as:

$$\begin{pmatrix} C_1(t_0+\tau) \\ C_2(t_0+\tau) \end{pmatrix} = M(t_0, \phi, \Omega_{eff}, \tau) \begin{pmatrix} C_1(t_0) \\ C_2(t_0) \end{pmatrix} \tag{1.77}$$

where $C_k = c_k e^{-i\omega_k t}$ (see pag 50), thus from equations (1.54) (1.55) for an interaction of time τ it has:

$$M(t_0, \phi, \Omega_{eff}, \tau) = \tag{1.78}$$

$$\begin{pmatrix} \cos\left(\frac{\Omega_{eff}\tau}{2}\right)e^{-i\omega_1\tau} & \sin\left(\frac{\Omega_{eff}\tau}{2}\right)e^{-i\phi_{eff}-i\omega_1\tau} \\ \sin\left(\frac{\Omega_{eff}\tau}{2}\right)e^{i\phi_{eff}-i\omega_2\tau} & \cos\left(\frac{\Omega_{eff}\tau}{2}\right)e^{-i\omega_2\tau} \end{pmatrix}$$

The free evolution matrix can be easily evaluated from the previous one by assuming $\Omega_{eff} \to 0$

$$M(T) = \begin{pmatrix} e^{-i\omega_1 T} & 0 \\ 0 & e^{-i\omega_2 T} \end{pmatrix} \tag{1.79}$$

The interferometric sequence is thus described by a transfer matrix obtained as the product of five matrix for interactions and free evolutions. To simplify the calculation here we move the time origin to the center of the π pulse, so that the interferometric sequence starts from instant $-T-\tau$.

$$\begin{aligned} M_{int} &= M(T+\tau,\phi_3,\Omega_{eff},\tau)\times M(T)\times M(-\tau,\phi_2,\Omega_{eff},2\tau)\times \\ &\quad M(T)\times M(-T-2\tau,\phi_1,\Omega_{eff},\tau) \end{aligned} \tag{1.80}$$

where for the field phase must be considered the expression

$$\phi_i = \vec{k}_{eff}\cdot\vec{r}_i - \omega_{eff}t_i + \phi_{eff,0} \tag{1.81}$$

assuming that the interferometric sequence starts at time $-T-\tau$ with the sample in the state $|1\rangle$ so that $C_1(-T-\tau)=1$ and $C_2(-T-\tau)=0$, the probabilities to find atoms in state $|2\rangle$ and $|1\rangle$ at the output channel are given by

$$P_2 = |C_2(T+2\tau|)|^2 = \frac{1-\cos(\Delta\Phi)}{2} \tag{1.82}$$

$$P_1 = |C_1(T+2\tau|)|^2 = \frac{1+\cos(\Delta\Phi)}{2} \tag{1.83}$$

with the phase given from

$$\Delta\Phi = \phi_1 - 2\phi_2 + \phi_3 \tag{1.84}$$

That is the same result presented in eqs. (1.61), (1.62). The importance of previous equations stands for the theoretical an experimental point of view into the identification of two output channels for the interferometer: *the total dephasing can be measured from a measurement of populations into the two levels at the end of the sequence, phase shift and levels populations are related by oscillating functions.* Supposing to split the phase output into a "physical" one plus a controlled phase offset between the two *Raman* laser fields in the form $\Delta\Phi_{tot} = \Delta\Phi_{ph} + \Delta\Phi_0$ varying the latter it's possible to scan the whole interferometric fringe picture over a series of repeated sequences. The discussion presented so far is useful to supply an introduction to the method; it's easy to verify that the performed calculation does not account for high order effects, for instance the free evolution contribute has been considered just only involving the matrix (1.79), this is not enough to account for acceleration gradients acting also on this part of sequence. A more complex development of this method including also high order effect is remanded to the papers.

1.2.4 Sensitivity Function

To evaluate the interferometer response to the possible phase noise sources, and in particular to the *Raman* pulses phase noise, the definition of a sensitivity function and of a transfer function is useful; this approach was imported from the atomic clocks framework to atom interferometry [84]. The target can be considered the calculation of the response of the interferometer to an infinitesimal variation of the lasers phase $\delta\phi$ as function of the time, such a response is named *sensitivity function*. From this method also sensitivity to dephasing due to accelerations or to others inertial shifts can be evaluated. If to a laser phase variation $\delta\phi$ corresponds a variation of the probability of finding atoms in a certain final state δP (see eqs. 1.82, 1.83) the sensitivity function can be defined as follows:

$$g_s(t) = 2 \lim_{\delta\phi \to 0} \frac{\delta P(\delta\phi, t)}{\delta\phi} \tag{1.85}$$

It's convenient without loss of generality to evaluate the function into the fringes region where the interferometer is more sensitive thus at $P_i = 1/2$ with $\Delta\Phi = \frac{\pi}{2}$. Here the probability depends almost linearly from the phase and a function development is possible:

$$\begin{aligned} P_1 &= \frac{1 + \cos(\Delta\Phi)}{2} = \frac{1 + \cos(\frac{\pi}{2} + \delta\Phi)}{2} \\ &\simeq \frac{1}{2}(1 + \delta\Phi) \end{aligned} \tag{1.86}$$

and more in general

$$P_{1,2}(\delta\phi, t) = \frac{1}{2}(1 \pm \delta\Phi) \tag{1.87}$$

therefore the sensitivity function becomes

$$g_s(t) = 2 \lim_{\delta\phi \to 0} \frac{\delta\Phi(\delta\phi, t)}{\delta\phi} \tag{1.88}$$

Calculating the function in the time intervals between two pulses is not hard; suppose to start with $P_2 = \frac{1}{2}(1 - \cos(\Delta\Phi))$ with $\Delta\Phi$ given from eq. (1.84), thus if a phase jump occurs between the first and second pulse we can set $\phi_1 = 0$, $\phi_2 = \delta\phi$ and $\phi_3 = \pi/2 + \delta\phi$ ([4]), applying the definition (1.85) this leads to

[4] the value $\pi/2$ is chosen to be at maximum sensitivity region of the fringe

$$P_2 = \frac{1}{2}(1 - \sin(\delta\phi)) \tag{1.89}$$

$$g_s(t) = -2 \lim_{\delta\phi \to 0} \frac{1}{2} \sin(\delta\phi) = -1 \tag{1.90}$$

The same can be done for a phase jump between the second and the third pulse. By the other hand to derive the value of the function for a jump occurring during a pulse we must separate the interaction into two steps: before and after the phase jump. To calculate a jump into the $i-th$ pulse at time $\tilde{t}$ the pulse relative matrix (see 1.78) can be split into two successive matrices, the first one with phase ϕ_i and the second one with $\phi_i + \delta\phi$ i.e. for a phase jump into the second pulse it gives

$$M_{\tilde{t},\delta\phi} = M(\tilde{t}, \phi + \delta\phi, \Omega_{eff}, \tau) \times M(-\tau, \phi + \delta\phi, \Omega_{eff}, \tilde{t}) \tag{1.91}$$

At the end the sensitivity function takes the following form, the plot is shown in picture (1.8). For an atom interferometry based gyroscope it was experimentally measured, the results are published in [70]. A complete theoretical calculation can be also find in [67]).

$$g_s(t) = \begin{cases} 0 & t < -T - 2\tau \\ \sin(\Omega_{eff}(t+T)) & -T - 2\tau < t < -T - \tau \\ -1 & -t - \tau < t < -\tau \\ \sin(\Omega_{eff} t) & -\tau < t < \tau \\ 1 & \tau < t < T + \tau \\ \sin(\Omega_{eff}(t+T)) & T + \tau < t < T + 2\tau \\ 0 & t > T + 2\tau \end{cases} \tag{1.92}$$

The calculations performed in sec. (1.73) to evaluate the phase response to inertial shifts can be performed also in this formalism, here just few steps are reported. Supposing $\delta\Phi$ to be the interferometer phase response whereas $\phi(t)$ lasers phase:

$$\delta\Phi = \int_{-\infty}^{+\infty} g_s(t) d\phi(t) = \int_{-\infty}^{+\infty} g_s(t) \frac{d\phi(t)}{dt} dt \tag{1.93}$$

then supposing to be in presence of an uniform gravitational field and to be in the same initial position and velocity conditions of the previous calculation the instantaneous phase for *Raman* beams is given from:

$$\phi(t) = \frac{k_{eff}\ gt^2}{2} + v_0 t + \phi_0 \tag{1.94}$$

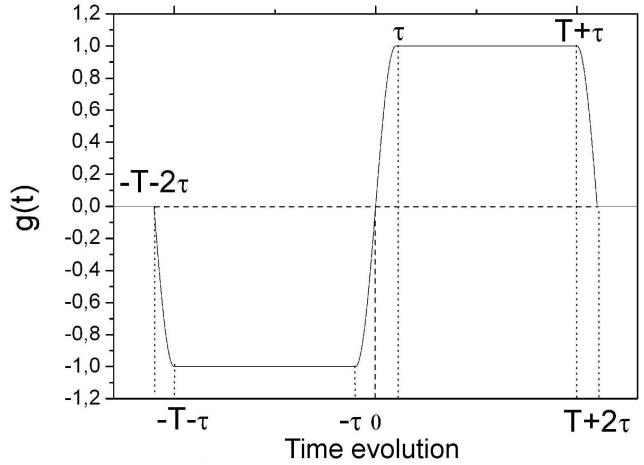

Figure 1.8: Interferometer sensitivity function.

Substituting this expression into the eq. (1.93) and considering the v_0 contribution vanishing because of the symmetry of sensitivity function $g_s(t)$ exactly the same result as in (1.73) is reached.

1.2.5 The transfer function and the Phase Noise

Raman beams phase noise will be transmitted to the interferometric measurement process, we have already seen as fields wavefronts represents a reference for the atoms motion into the determination of the accelerations (see page 57). For now a stable amplitude for the beams is assumed and also frequency relative fluctuation between the two beams are assumed as small thanks to *Phase Lock* feedback. By the other hand absolute frequency shift will be the same for both; they will not affect the *Raman* transition probability till such variations will be small comparing with the detuning from the resonance.
In this section our purpose is to define the tools to understand the weight for the phase noise transfer from beams to atoms. To have an idea of necessary quality for phase stability needed for an interferometer operating as gravimeter under the Earth field conditions, we can consider some typical parameters as: $T = 150$ ms, and $g = 9.8$ ms^{-2}. The resulting interferometric phase shift is $\delta\Phi = k_{eff} g T^2 \approx 3.9 \times 10^6$ rad. To achieve a measurement accuracy in 1 Hz of $\Delta g/g = 10^{-9}$ a maximum phase noise of 1 *mrad* is needed.

To approach at a Fourier components analysis of the phase noise we can suppose the phase noise component of frequency ω oscillate with the law

$\phi(t) = A_0 \cos(\omega t + \psi)$, and the derivative $\frac{d}{dt}\phi(t) = -A_0\omega \sin(\omega t + \psi)$ (see also sec. (3.2)), thus the interferometric phase effect, as we did in (1.93), is given from

$$\delta\Phi = \int_{-\infty}^{+\infty} -g_s(t) A_0 \omega \sin(\omega t + \psi) dt \tag{1.95}$$

To move to the frequency domain we calculate the fourier transform of the sensitivity function g_s

$$G(\omega) = \int_{-\infty}^{+\infty} e^{-i\omega t} g_s(t) dt \tag{1.96}$$

Expressing the exponential term as $\cos(\omega t) - i\sin(\omega t)$ only the *sine* part survive because the odd symmetry of the function g_s

$$G(\omega) = \int_{-\infty}^{\infty} -i \sin(\omega t) g_s(t) dt \tag{1.97}$$

The same can be done for the eq. (1.95) with the help of trigonometric formula $\sin(\omega t + \psi) = \sin(\omega t)\cos(\psi) + \cos(\omega t)\sin(\psi)$, the integral relative to the second term vanishes

$$\delta\Phi = A_0\omega \int_{-\infty}^{+\infty} -g_s(t) \sin(\omega t)\cos(\psi) dt \tag{1.98}$$

Thus from (1.97) it has[5]

$$\delta\Phi = -iA_0\omega G(\omega)\cos(\psi) = -A_0\omega |G(\omega)| \cos(\psi) \tag{1.99}$$

Starting from this equation and considering a series of successive measurement with aleatory phase ϕ the root mean square of the deviation for the interferometric phase is given from $\sigma_\Phi A_0 \omega |G(\omega)|/\sqrt{2}$. If we treat with a phase noise spectral density $S_\phi(\omega)$ the standard deviation on Φ is given from [87]:

$$\sigma_\Phi^2 = \int_0^\infty |\omega G(\omega)|^2 S_\Phi(\omega) \frac{d\omega}{2\pi} \tag{1.100}$$

this equation can be considered as a definition of *transfer function* for the interferometer $H(\omega) = |\omega G(\omega)|$; from eqs (1.92) and (1.97) $|G(\Omega)|$ can be derived

[5] for last step see eq. (1.97)

$$G(\omega) = \frac{4i\Omega_{eff}}{\omega^2 - \Omega_{eff}^2} \sin\left(\frac{\omega(T+2\tau)}{2}\right)\left[\cos\left(\frac{\omega(T+2\tau)}{2}\right) + \frac{\Omega_{eff}}{\omega}\sin\left(\frac{\omega T}{2}\right)\right] \tag{1.101}$$

so that the *transfer function* is given from

$$\boxed{H(\omega) = \frac{4\omega\Omega_{eff}}{\omega^2 - \Omega_{eff}^2} \sin\left(\frac{\omega(T+2\tau)}{2}\right)\left[\cos\left(\frac{\omega(T+2\tau)}{2}\right) + \frac{\Omega_{eff}}{\omega}\sin\left(\frac{\omega T}{2}\right)\right]} \tag{1.102}$$

It exhibits an oscillating behavior, the plot is displayed in pictures (1.9) and (1.10), the basics characteristic can be summarized as follows

- Because of the term $\sin\left(\frac{\omega(T+2\tau)}{2}\right)$ the function vanishes at frequency multiple of $\frac{1}{T+2\tau}$
- For low frequency so that $\omega \ll \Omega_{eff}$ the transfer function can be approximated by $|H(\omega)| = 4\sin^2(\omega T/2)$
- For high frequencies, compared with the *Rabi* frequency, the phase fluctuation are averaged over the pulse duration therefore the function exhibit a first order low pass filter and tends to $2\Omega_{eff}/\omega$ for $\omega \to \infty$. Such effect is due to the first factor $\frac{4\omega\Omega_{eff}}{\omega^2-\Omega_{eff}^2}$, the -3 dB frequency is Ω_{eff}/π
- The last term $\cos\left(\frac{\omega(T+2\tau)}{2}\right) + \frac{\Omega_{eff}}{\omega}\sin\left(\frac{\omega T}{2}\right)$ introduces a second series of zeros for the function, strongly dependent on the position of the *Rabi* frequency. This last behavior can be just simulated or directly measured (see [70, 71])

Phase Noise to Interferometric noise

Into the atom interferometer context as into the atomic clock context the standard deviation upon a single measurement is not appropriate description for long average times, for some kind of noise such as Random Walk and Flicker frequency noise this variance does not converge. For this reason a two sample variance without dead time, *Allan variance*, must be introduced [48, 49].

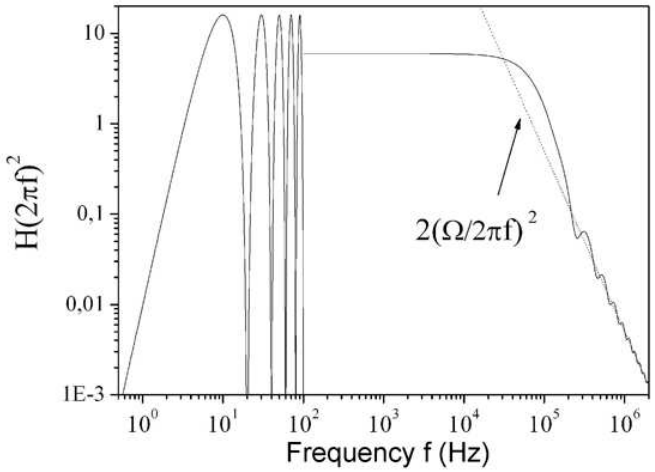

Figure 1.9: Transfer function for an effective *Rabi frequency* of 2π *times* 50 kHz, and $T = 50$ ms, for frequency above 100 kHz the average value is plotted [70, 71].

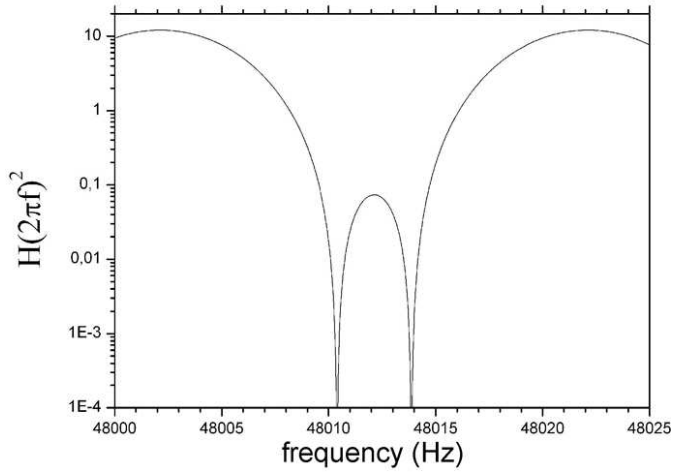

Figure 1.10: Transfer function detailed plot around the *Rabi frequency*. Only the first zero is due to the oscillating term $\sin\left(\frac{\omega(T+2\tau)}{2}\right)$, the second one is due to the last term [70, 71].

Suppose that the interferometer operates over a sequence of $m = 10000$ measurement with a repetition rate T_{rep}, we can collect consecutive measure-

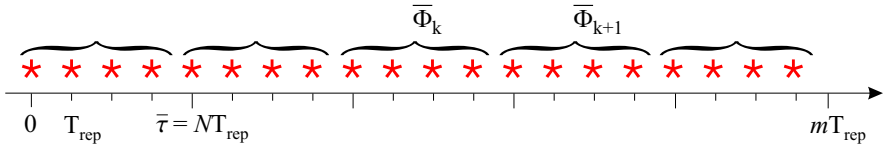

Figure 1.11: Interferometric sequence, with repetition rate T_{rep}, measurement are grouped in $N - folds$ arrays.

ments in groups of $N = \tilde{\tau}/T_{rep}$ where $\tilde{\tau}$ is a multiple of T_{rep} and identify the grouping time[6] (see picture (1.11)). We can calculate the Allan variance as the variance of the difference between the average phase noise of two consecutive measurement cycle (each containing N single measurement), so that it can be defined as

$$\sigma_\Phi^2 = \frac{1}{2} \lim_{m/N \to \infty} \left\{ \frac{1}{m/N} \sum_{k=1}^{m/N} (\delta\overline{\Phi}_{k+1} - \delta\overline{\Phi}_k)^2 \right\} \tag{1.103}$$

Where $\delta\overline{\Phi}_k$ is the interferometric average phase noise on N measurement performed at time $t_k = k\tilde{\tau}$, which is given from

$$\delta\overline{\Phi}_k = \frac{1}{N} \sum_{l=0}^{N} \int_{t_k + lT_{rep}}^{t_k + (l+1)T_{rep}} g(t - t_k + (l + 1/2)T_{rep}) \frac{d\phi}{dt} dt \tag{1.104}$$

we can define the sensitivity function $g_{N,k}(t)$ as the sum of the the sensitivity functions over the cycle

$$g_{N,k}(t) = \frac{1}{N} \sum_{l=0}^{N} g(t - k\tilde{\tau} - lT_{rep}) \tag{1.105}$$

thus eq. (1.104) becomes:

$$\delta\overline{\Phi}_k = \frac{1}{N} \int_{t_k}^{t_k + \tilde{\tau}} g_{N,k}(t) \, \frac{d\phi}{dt} dt \tag{1.106}$$

and differences of averages over two consecutive sets are given from

[6] do not confuse with *Raman* pulses time duration τ, for this section we replace $\tau \to \tau_R$ avoiding ambiguity.

$$\delta\overline{\Phi}_{k+1} - \delta\overline{\Phi}_k = \frac{1}{N}\int_{t_k}^{t_k+\tilde{\tau}} (g_{N,k+1}(t) - g_{N,k}(t))\frac{d\phi}{dt}dt \tag{1.107}$$

The difference between two consecutive $g_{N,k}(t)$ functions will be defined as $\tilde{g}_k(t) = (g_{N,k+1}(t) - g_{N,k}(t))$ Now if we are handling an aleatory phase noise $\phi(t)$ characterized from a phase noise spectral density $S_\phi(\omega)$, for long averaging times $\tilde{\tau}$, under the reasonable hypothesis that the phase noise between two different measurement cycles i.e. $\delta\overline{\Phi}_k - \delta\overline{\Phi}_{k-1}$ and $\delta\overline{\Phi}_{k+1} - \delta\overline{\Phi}_k$ is not correlate, we can assume $\widetilde{g}_{N,k}(t)$ to be the same for all grouping differences, in the form:

$$\begin{aligned} \widetilde{g}_k(t) &\equiv (g_{N,k+1}(t) - g_{N,k}(t)) \\ &\Rrightarrow \widetilde{g}_0(t) = \sum_{l=0}^{N-1}\Big[g(t-\tilde{\tau}-lT_{rep}) - g(t-lT_{ref})\Big] \end{aligned} \tag{1.108}$$

where the sum is extended over a single cycle of N measurements. We can now calculate the Fourier transform of $\widetilde{g}_0(t)$ as follows $(2\pi\nu = \omega)$ [7]

$$\begin{aligned} |\tilde{G}(\nu)|^2 &= |\sum_{l=0}^{N-1}\Big(G(\nu)e^{2i\pi\nu(\tilde{\tau}+lT_{rep})} - G(\nu)e^{2i\pi\nu lT_{rep}}\Big) \\ &= 4\frac{\sin^4(\pi\nu\tilde{\tau})}{\sin^2(\pi\nu T_{rep})}|G(\nu)|^2 \end{aligned} \tag{1.109}$$

Getting in mind the relation $|\omega G(\omega)| = H(\omega)$ for a single measurement case, it is possible to move quickly to the transfer function of the latter case with the new definition $\tilde{H}(\nu) = 2\pi\nu|\tilde{G}(\nu)|$

$$\tilde{H}(\nu) = 4\frac{\sin^4(\pi\nu\tilde{\tau})}{\sin^2(\pi\nu T_{rep})}|H(\nu)|^2 \tag{1.110}$$

Now is possible to substitute the expressions of the differences of averages (1.107) into the expression of the Allan Variance (1.103) and, with the help of the Fourier transform tools and the transfer function, the final expression is given from:

$$\sigma_\Phi^2(\tilde{\tau}) = \frac{1}{N}\int_0^\infty |\omega\tilde{G}(\omega)|^2 S_\phi(\omega)d\omega \tag{1.111}$$

[7] $N = \tilde{\tau}/T_{rep}$, time shift property of Fourier transform are used so that a shift of t_0 correspond to a multiplication with $e^{i\omega t_0}$,
moreover formula $\sum_{l=0}^{N-1} e^{\alpha l} = \frac{-1+e^{\alpha N}}{-1+e^{\alpha}}$ was involved.

in the limit of long averaging times $\tilde{\tau} \to \infty$, $\tilde{H}(\nu)$ can be rewritten as

$$\tilde{H}(\nu)_{\tau\to\infty} \Rrightarrow \frac{2\tau}{T_{rep}^2} \sum_{n=-\infty}^{+\infty} \delta(2\pi\ (\nu - n/T_{rep})\ )|H(\nu)|^2 \tag{1.112}$$

thus under this hypothesis the Allan variance (1.111) simplifies to

$$\boxed{\sigma_\Phi^2(\tilde{\tau}) = \frac{1}{\tilde{\tau}} \sum_{n=1}^{\infty} \left|H\Big(\frac{2\pi n}{T_{rep}}\Big)\right|^2 S_\phi\Big(\frac{2\pi n}{T_{rep}}\Big)} \tag{1.113}$$

As first we can note that under the condition of long averaging time it appears an aliasing effect called *Dick Effect*, a well known effect into the atomic clocks community [85]: noise at frequency multiple of $1/T_{rep}$ will be down converted to low frequencies.
As second , in the particular case of white phase noise $S_\phi(\nu) = S_\phi^0$ eq. (1.113) becomes:

$$\boxed{\sigma_\Phi^2(\tilde{\tau}) = \big(\frac{\pi}{2}\big)^2 \frac{S_\phi^0}{\tilde{\tau}} \frac{T_{rep}}{\tau}} \tag{1.114}$$

From the last equation we can note that the phase noise on the interferometer, as a propagation of the *Raman* beams phase noise, depends from the inverse of the pulses duration $1/\tau_R$, so it increases as much shorter are the pulses. A minimum typical value for an atomic interferometric gyroscope was found at $\tau_{R,min} = 5\ \mu$s (see.[70]). Moreover from this formula is possible to evaluate a white noise level compatible with an interferometric phase noise inferior to 1 mrad rms, that corresponds for a gravimeter to a sensitivity on the acceleration measurement of $\Delta g/g \sim 10^{-9}$ in one Hz. Therefore a reasonable value for a white noise plateaux is given from :

$$\boxed{S_\phi^0 = -117 \text{ dB rad}^2 \text{ Hz}^{-1}}$$

At low frequencies white noise is dominated by a $1/\nu$ term (see also eq. (3.25) at page 131), a noise level at 1 Hz can be fixed to -76 dB rad^2 Hz^{-1}. On another side, considering the FINAQS gravimeter standard operative parameters ($\tau = 100\ \mu$s and $T = 150$ ms) and the achieved residual phase noise level (sec. 4.3), integrating over all frequency spectrum, the device sensitivity will be limited by the *Raman* phase noise to $\Delta g/g \sim 10^{-10}$ in one second [110]. As the reader can find later, part of this thesis work has been dedicated to achieve such residual phase noise on *Raman* beams.

1.2.6 Sensitivity to Quantum Projection Noise

The target item for the atom interferometer consists in a states coherent superposition of the two hyperfine levels $F = 1$ and $F = 2$ with (almost) the same probability; the readout is performed from a measurement of number of atoms in each level. According with the quantum mechanics[8], after the measurement the wavefunction of the single atom will be projected in one of the two levels with probability P and $(1 - P)$, that can be calculated in our case, neglecting contrast lost, from eqs. (1.82), (1.83). For a sample of N atoms this situation configures a statistic following a binomial law, thus the probability to find n atoms from the total sample in a given level is:

$$P(n) = \frac{N!}{n!(N-n)!} P^n (1-P)^{N-n} \tag{1.115}$$

thus into the limit of a big number of atoms this probability tends to the distribution

$$P(n) = A exp\Big\{ \frac{(n/N - P)^2 N}{2P(1-P)} \Big\} \tag{1.116}$$

with A as normalization constant.
Intrinsic statistic fluctuations, characterized by the standard deviation $\sigma_P = \sqrt{\frac{P(1-P)}{N}}$, are called *Quantum Projection Noise* [11, 12]; such fluctuations also affect the interferometer transition probability, their contribution on interferometric phase can be evaluated as:

$$\sigma_\Phi = \sigma_P \times \Big| \frac{d\Phi}{dP} \Big| = \sqrt{\frac{P(1-P)}{N}} \frac{2}{\sin \Phi} \tag{1.117}$$

Substituting the expression for the probability P

$$\sigma_\Phi = \frac{1}{2} \sqrt{\frac{(1 - \cos^2 \Phi)}{N}} = \sqrt{\frac{1}{N}} \tag{1.118}$$

This means that the *quantum projection noise* scales with $1/\sqrt{N}$ and for an ideal case to achieve a noise level of 1 *mrad* are needed 10^6 atoms at the detection. This represent up to now the ultimate physical limit to atom interferometry below all the technical noise contribution. For the future some possible detection scheme are under study with the employment of quantum sqeezing and entanglement technics that probably will lead below this frontier (see [120]).

[8] Copenaghen School's interpretation of quantum mechanics, see [10]

1.3 Cooling and trapping of neutral atoms

In section (1.1.1) it was discussed in details the interaction of an atomic two level system with monochromatic electromagnetic radiation field. The way to quickly converge to the atomic interferometry theory a specific formalism was adopted that directly couples the atomic internal and external degree of freedom; the recoil momentum transfer was directly taken into account. In order to analyze the mechanical effects of the interaction with the e.m. field, the recoils effect must be pointed out, let's start again from the simple two level atomic system model with energies E_g and E_e for the exited and ground state(pict. 1.2). The net resulting force experienced by the atoms under the interaction with the radiating field is a consequence of energy and momentum conservation. Unlike previous treatment for the single photon transitions and also for the two photons *Raman* transition, where a single light-matter interaction was considered with a well defined interaction time, for the cooling processes we are going to consider a situation where the atomic sample is subject to an indefinite interaction time long enough to allow a big number of cyclic absorbtion-emission processes and, for the sample's population evolution, we are going to consider a steady state condition.

1.3.1 Optical *Molasses*

In order to introduce the laser cooling mechanism we can start from few considerations about a single atom interacting with e.m. filed. If a photon absorbtion process is followed by a stimulated emission process no net momentum is transferred to the atom; because the emitted photon will follow the same direction of the absorbed one, the momentum transfer form the absorbtion will be canceled from the momentum lost from the emission. By the other hand if a spontaneous emission follows the absorbtion process it's possible to account for a net momentum transfer: photons in each spontaneous process are emitted in random directions with no average contribution to the total momentum budget. In this picture for each absorbtion and emission processes if the momentum recoil is $\hbar k_L$ and m the atomic mass we can define the *recoil velocity* as

$$v_r(x) = \frac{\hbar k_L}{m} \tag{1.119}$$

If $\Gamma = 1/2\pi\tau$ is the natural linewidth of the considered transition where τ is the typical exited state lifetime, it's possible to evaluate the rate of

absorbtion-emission cycling processes, under stationary condition[9], by multiplying the spontaneous emission rate $1/\tau$ times the exited level occupancy $\mathcal{N}_e$ [76, 33, 77, 128],

$$\mathcal{N}_e = \frac{\Omega_R^2}{4\Delta^2 + \Gamma^2 + 2\Omega_R^2} \tag{1.120}$$

where $\Delta = \omega_L - \omega_A$ is the detuning and Ω_R the *Rabi* frequency as defined at page 40. The net radiative force can be evaluated by multiplying the cycling rate times the transferred momentum each cycle

$$F_{sc} = \hbar k_L \Gamma \mathcal{N}_e \tag{1.121}$$

Considering from the laboratory frame the atomic motion and the relative *Doppler* effect it's possible to replace the detuning Δ with $\Delta' = \Delta - \vec{k} \cdot \vec{v}$ in the equation for the population occupancy (1.120), thus the scattering force can be written as

$$F_{sc} = F_{sc}(\vec{v}) = \hbar k_L \Gamma \frac{\Omega_R^2}{4[\Delta - \vec{k} \cdot \vec{v}]^2 + \Gamma^2 + 2\Omega_R^2} \tag{1.122}$$

or in terms of experimental easy handling parameters, as the beam intensity I and saturation intensity I_s

$$\Omega_R = \Gamma \sqrt{\frac{I}{I_s}} \quad \text{with} \quad I_s = \frac{4\pi^2 \hbar c \Gamma}{6\lambda_0^3} \tag{1.123}$$

(For ^{87}Rb, $I_s = 1.6\ \mathrm{mW/cm^2}$, see app. (A) or [141]), the equation (1.122) becomes

$$F_{sc}(\vec{v}) = \hbar k_L \frac{\Gamma}{2} \frac{I/I_s}{1 + (I/I_s) - \frac{4}{(2\pi\Gamma)^2}[\Delta - \vec{k} \cdot \vec{v}]^2} \tag{1.124}$$

As function of Δ the radiating scattering force F_{sc} has a lorentian profile and for $I \ll I_s$ is proportional to the beam intensity, whereas the maximum value is $\hbar k_L \Gamma/2$ that corresponds to a maximum acceleration

[9] In order to describe the atomic system interacting with the radiating field it can be useful to consider a description in term of *density matrix*:
$\rho = |\psi\rangle\langle\psi| \quad ; \quad \rho_{ab} = \langle a|\rho|b\rangle = \langle a|\psi\rangle\langle\psi|b\rangle = c_a c_b^* \quad$ (for a two level atomic system)

the evolution of the system is described from the equation $\dot{\rho} = -\frac{i}{\hbar}[H, \rho]$
the stationary condition mentioned in the text refers to the equilibrium $\dot{\rho} = 0$
eq. (1.120) holds from there
for a complete and detailed treatment see [77]

$$\vec{a}_{max} = \frac{\hbar \vec{k}_L}{m} \frac{\Gamma}{2} \tag{1.125}$$

For Rubidium atom with $\lambda = 780$ nm and $\Gamma^{-1} = 27$ ns the maximum acceleration is $a_{max} \simeq 10^5$ m/s^2.
In the limit of $\vec{k} \cdot \vec{v} \ll \Delta$ and $\frac{\vec{k}\cdot\vec{v}}{\Gamma} \ll 1$ we can expand the denominator of (1.124) in the last term leading to an equation in the form:

$$F_{sc}(\vec{v}) = F_{sc}(0) - \beta v + \dots \tag{1.126}$$

with

$$F_{sc}(0) = \hbar k_L \Gamma \, \frac{I/I_s}{1 + \left(\frac{2\Delta}{\Gamma}\right)^2} v \tag{1.127}$$

and

$$F_{sc}(v) = 4\hbar k_L^2 \frac{\Delta}{\Gamma} \frac{I/I_s}{\left[1 + I/I_s + \left(\frac{2\Delta}{\Gamma}\right)^2\right]^2} \tag{1.128}$$

Because of the presence of such a velocity dependent force $F(v) = -\beta v$ this cooling mechanism is called ***optical molasses***.
Now let suppose that an atom is moving with velocity $\vec{v}$ and interacting with two counter–propagating beams with the same frequency ω and with the same detuning ($\Delta < 0$) from the atomic transition, being one beam parallel to its velocity and the other with the opposite direction. In the atomic motion frame the first beam appears with a frequency increased from the *Doppler* shift, thus the detuning is almost compensated up to the resonance, whereas the other beam frequency results decreased and the net detuning from the resonance is further on increased. The atom will tend to absorb a photon from the first beam; such configuration is illustrated in picture (1.12)

In the described situation the resulting force on the atom is the sum of the two molasses forces contributions

$$\begin{aligned} F_{sc}^{tot} &= F_{sc}(\Delta + \vec{k}_L \cdot \vec{v}) - F_{sc}(\Delta - \vec{k}_L \cdot \vec{v}) \\ &= -8\hbar k_L^2 \frac{\Delta}{\Gamma} \frac{I/I_s}{\left[1 + I/I_s + \left(\frac{2\Delta}{\Gamma}\right)^2\right]^2} \quad v = -2\beta v \end{aligned} \tag{1.129}$$

In picture (1.13) the resulting force of eq. (1.129) is illustrated together with the two single contributions

The model discussed so far can be extended to a three–dimensional configuration with cooling beams in the three directions, this drives to a cooling

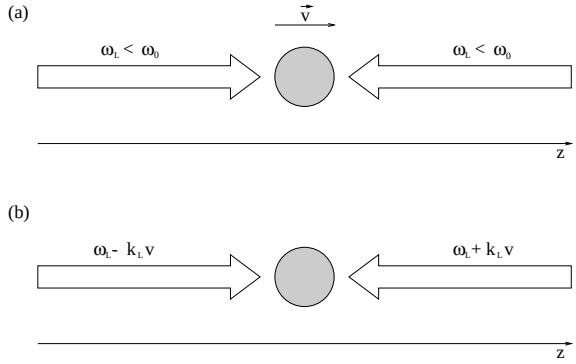

Figure 1.12: Atom moving with velocity $\vec{v}$ in the path of two counter–propagating beams with frequency ω_L and *red-detuned* from the atomic transition $\Delta < 0$. In (a) lab frame view, in (b) atomic moving frame view.

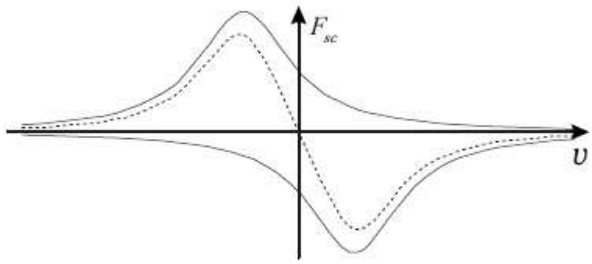

Figure 1.13: Mono-dimensional model for the optical molasses with two counter-propagating beams, the continuous curve stands for the two single contributions from the two beams whereas the dashed one stands for the resulting force.

in all atomic motion directions.
In order to evaluate the resulting temperature for the atomic sample into the optical molasses it must be considered that the absorbtion and emission processes lead to two competitive effects: cooling by one hand (viscose force) and heating from the other hand, due to the randomness of the momentum transfer between light and atoms. In other words the heating is due to the fluctuation around the average value. We can define as sample temperature the equilibrium temperature between these two processes. We remand to literature for a detailed treatment and just introduce the resulting formula

as:

$$k_B T = \frac{\hbar\Gamma}{4}\Big(\frac{\Gamma}{2\Delta} + \frac{2\Delta}{\Gamma}\Big) \tag{1.130}$$

The minimum value is reached for $\Delta = -\Gamma/2$ thus to the doppler limit is given from

$$k_B T_{min} = \hbar\frac{\Gamma}{2} \tag{1.131}$$

that for rubidium is $T_{min} = 140\mu K$ and corresponds to a velocity of $v_{min} = 14cm/s$.

1.3.2 Subdoppler Cooling and *Sisyphus* effect

The *Doppler* cooling theory holds a limit for the lower temperature achievable (eq 1.131). In the year 1988 for an experiment on a sodium optical molasses temperature below this limit were measured [22] (*recoil limit* $T_R = \hbar^2 k_L^2/mk_B$) and soon other experiments on alkali atoms confirmed the result [26, 27]. The existence of a new subdoppler cooling mechanism was theorized from the groups of Dalibard and Cohen Tannoudji (Paris) [23] and S. Chu (Stanford) [24] based on optical pumping effects in presence of optical polarization gradients. For the process a fundamental role is played by the atomic *AC Stark shift* that for a two level system interacting with a near resonance radiation is:

$$\Delta > 0 \qquad \begin{aligned} \omega_g' &= \omega_g + \tfrac{1}{2}(\Delta - \Omega') \\ \omega_e' &= \omega_e - \tfrac{1}{2}(\Delta - \Omega') \end{aligned} \tag{1.132}$$

$$\Delta > 0 \qquad \begin{aligned} \omega_g' &= \omega_g + \tfrac{1}{2}(\Delta + \Omega') \\ \omega_e' &= \omega_e - \tfrac{1}{2}(\Delta + \Omega') \end{aligned} \tag{1.133}$$

and (see def. (1.25) at page 40)

$$\Omega_R \ll \Delta \qquad \begin{aligned} \omega_g' &= \omega_g - \tfrac{\Omega_R^2}{4\Delta} \\ \omega_e' &= \omega_e + \tfrac{\Omega_R^2}{4\Delta} \end{aligned} \tag{1.134}$$

Let's introduce as first the case of atomic sample interacting with two counter-propagating beams with the same frequency, red–detuned from the transition, and with two orthogonal linear polarizations

$$\begin{aligned} \vec{E}_1 &= E_0 \hat{x} e^{-ikz+\omega t} \\ \vec{E}_2 &= E_0 \hat{y} e^{-ikz+\omega t} \end{aligned}$$

if for circular polarization holds

$$\begin{aligned}\sigma_+ &= \frac{1}{\sqrt{2}}(\hat{x} + i\hat{y}) \\ \sigma_+ &= \frac{1}{\sqrt{2}}(\hat{x} - i\hat{y})\end{aligned}$$

the resulting field is given by the following equation, a graphical representation is shown in picture (1.14)

$$\begin{aligned}\vec{E}_{Tot} &= \vec{E}_1 + \vec{E}_2 \qquad (1.135)\\ &= E_0 e^{-i\omega t}\Big[\sigma_+(1-i)\sin\big(kz+\pi/4\big) + \sigma_-(1+i)\cos\big(kz+\pi/4\big)\Big]\end{aligned}$$

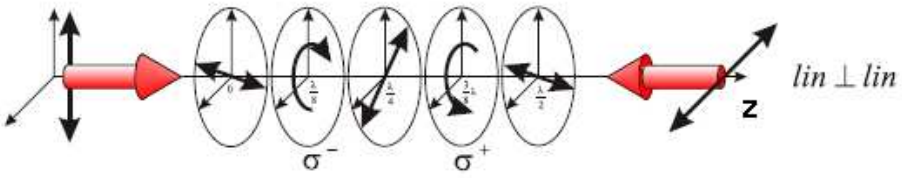

Figure 1.14: Resulting polarization gradient for two linear polarized counter propagating fields.

The resulting field polarization changes on the z axis and it results circular σ_- polarized at a distance $\lambda/8$, σ_+ at $\lambda 3/8$ and linear polarized at $\lambda/4$ and $\lambda/2$. Suppose to have atoms with fundamental state $F = 1/2$ and exited $F' = 3/2$, let's analyze the case of an atom at position $\lambda/8$ with σ_- field polarization and pumped into the state $m_F = -1/2$. From the *Clebsh–Gordan* coefficients calculation it's possible to see that the transition with $\Delta m_F = -1$ and ($F = -1/2 \rightarrow F' = -3/2$ transition) is three times more intense than the other one from $m_F = 1/2$. From the energetic point of view this means that the *AC Stark shift* decreases the energy value for $m_F = -1/2$ state and increases the value for $m_F = -1/2$. In a σ_+ position the situation is exactly specular. So if our atom moves to $\lambda 3/8$ position where finds a σ_+ polarization, its energy increase at expense of kinetic energy but now will be pumped in a $m_F = 1/2$ state in agreement with the previous description and so on. Any cycle the atom looses a kinetic energy equal to the hyperfine level separation. This mechanism is called "*Sisyphus Effect*" because as in the *Sisyphus* myth [1, 2, 3] the atom climbs a potential mountain and once is at the top it dissipates the accumulated potential energy with a transition

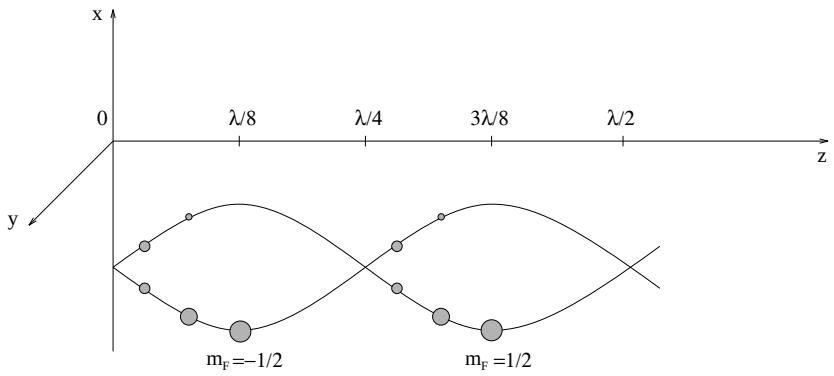

Figure 1.15: Basis for the *Sisyphus effect*: *Zeeman levels light shift* for the fundamental state. The circles's dimensions stand for the atomic populations.

to another state at lower energy. The energetic level shift is illustrated in picture

In the previous discussion just a fundamental hint for the *sub-doppler* cooling has been drown, details are remanded to literature (see [23, 24, 28]). For our purpose it's important to suggest that a similar mechanism works also for atoms with fundamental level $F = 1$ and exited $F' = 2$ but for this case two counter-propagating beams circular polarized are needed and the mechanism is more complex: a new picture for the polarization gradient comes out (see picture (1.16)).

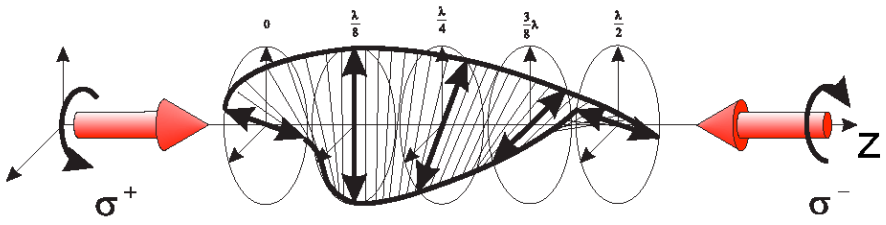

Figure 1.16: Resulting polarization generated from two counter-propagating circular polarized cooling beams.

At this level it is possible to say that the minimum temperature achievable depends on the dissipated energy for each pumping cycle, by the other side

such temperature is still bounded to the discrete nature of photon absorbtion and emission process

$$T_{min} \sim \frac{\hbar\Omega_R^2}{k_B|\Delta|} \tag{1.136}$$

1.3.3 Magneto Optical Trap (*MOT*)

Besides the discussion about the doppler and subdoppler cooling in the molasses the model presented so far shows a fundamental limit for the trapping point of view; the *optical Earnshaw theorem* [21] holds that it's impossible to trap an atomic sample just with the apport of a dispersive scattering force proportional to the intensity of the field and not dependent on the position. Moreover we can start from the consideration that if the field oscillates at a given frequency (detuned from the atomic transition), an atom moving in the forward direction and decreasing speed because the cooling process, at a certain time will be not addressed by the radiation because the frequency detuning will not compensate for the doppler shift anymore. The cooling mechanism seems to be limited just for a certain atomic velocity class of the sample. Before the introduction of a position dependent therm, in order to address the largest number atomic velocity classes into the molasses many experimental configuration have been developed based on the cooling lasers frequency variation compensating for the doppler shift reduction. The basic idea for the magneto–optical trapping is to implement an optical molasses configuration with counter-propagating beams σ^+/σ^- polarized in presence of a magnetic field gradient with the related field vanishing at the center of the trap and increasing outside. If the atom is provided of intrinsic magnetic moment, thus sensitive to magnetic fields, the internal magnetic levels are shifted by *Zeeman* effect as much the atom moves outside the trap, this effect will match the laser fields detuning with the energy shift as a compensation.

The situation is illustrated with a simple mono dimensional model in picture (1.17), again the atom is considered as a two level system $F_g = 0$ and $F_e' = 1$, with angular momentum sublevels $m_{F'} = -1, 0, 1$, the atomic sublevels degeneracy is totally removed by a magnetic field linear variation $\vec{B} = b\vec{x}$. Because the selection rules the beam coming form left side σ^+ polarized can drive just the transition $m_F = 0 \rightarrow m_{F'} = 1$ and at the same way the beam form right side σ^- polarized can drive just the transition $m_F = 0 \rightarrow m_{F'} = -1$. If the laser is *red–detuned* $\Delta = \omega_L - \omega_A < 0$ and supposing the atom is localized in a $x > 0$ position, the latter will interact much more with the σ^- polarized beam than with the σ^+ one because in the first case *Zeeman* shift on the atomic levels will compensate for the laser

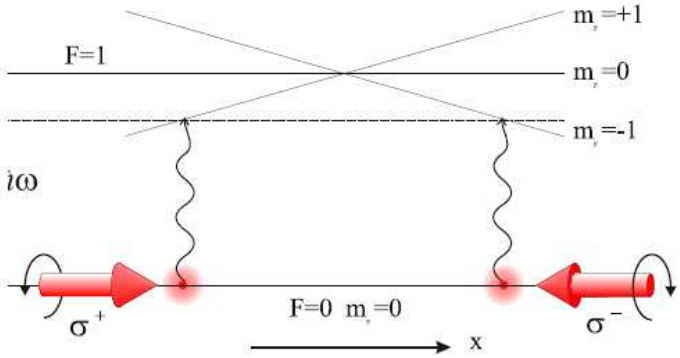

Figure 1.17: Mono-dimensional model for a Magneto Optical Trap. The dashed line indicate the beams detuning from the transition, the *Zeeman* shift of atomic levels compensate for the detuning.

detuning (see picture). The same picture can be reversed for the other side ($x < 0$), the final result is an interaction with beams in one or in the other side of the trap such a way that the force is always directed toward the center as a restoring force. The calculation of the net effect can be performed just like it was done for the optical molasses. The *Zeeman* shift due to the Field gradient can be written as follows

$$\Delta E_B(x) = \mu_B m_F g_F B(x) \sim \mu_B m_F g_F \frac{dB(x)}{dx} dx \tag{1.137}$$

where μ_B is the *Bohr magneton* and g_F the *Landè factor*. As for equation (1.124), accounting both for *Doppler* shift and *Zeeman* shift, the force due to a single beam is given from

$$F_{\sigma^\pm}(z, \vec{v}) = \pm \hbar k_L \frac{\Gamma}{2} \frac{I/I_s}{1 + (I/I_s) - \frac{4}{(2\pi\Gamma)^2}[\Delta \mp (\vec{k} \cdot \vec{v} + \mu z)]^2} \tag{1.138}$$

with

$$\mu = \frac{1}{\hbar} \mu_B m_F g_F \frac{dB(x)}{dx} \tag{1.139}$$

Again we can develop the equation in the limit $(\vec{k} \cdot \vec{v} + \mu z)/\Gamma \ll 1$ and can add the contributions form the two beams

$$\begin{aligned} F_{MOT} &= F_{\sigma^+}\big(\Delta - kv - \frac{\mu_B}{\hbar}B(x)\big) - F_{\sigma^-}\big(\Delta + kv + \frac{\mu_B}{\hbar}B(x)\big) \\ &= 4\hbar k_L \frac{2\Delta}{\Gamma} \frac{I/I_s}{\Big[1 + (2\Delta/\Gamma)^2\Big]^2}\big(k_L v + \mu x\big) \\ &= -\beta \mathbf{v} - \mathbf{K}\mathbf{x} \end{aligned} \tag{1.140}$$

where the constants are given from

$$\beta = -4\hbar k_L^2 \frac{2\Delta}{\Gamma} \frac{I/I_s}{\Big[1 + (2\Delta/\Gamma)^2\Big]^2} \tag{1.141}$$

$$K = -4\hbar\mu \frac{2\Delta}{\Gamma} \frac{I/I_s}{\Big[1 + (2\Delta/\Gamma)^2\Big]^2} \tag{1.142}$$

The atomic motion in the trap follows the dumped oscillator model

$$\ddot{x} + \gamma\dot{x} + \omega_{trap}^2 x = 0 \tag{1.143}$$

with $\gamma = \beta/m$ and $\omega_{trap}^2 = K/m$. As for the molasses the cooling configuration can be extended to a two dimensional or a three dimensional setup. In order to trap and cool atoms in three dimension a couple of coils in *anti-Helmholtz* configuration generate a quadrupole adequate magnetic field (see picture(1.18)) [10], the three direction cooling beams must cross the center of the trap at the zero point of the magnetic field [25].

The number of atoms trapped into a magneto optical trap can be evaluated from a rate equation model as the resulting budget between atoms trapped and atoms lost

$$\frac{dN}{dt} = R + A\ N \tag{1.144}$$

where R is the loading rate and the A is the loss rate that accounts for losses due to collisions with background gas (γ term) and with trapped atoms (κ term)

$$A = \gamma + \kappa n \tag{1.145}$$

Under stationary conditions

[10] Is easy to show that the with such coils configuration the field gradient on the symmetry axis is twice than the other direction.

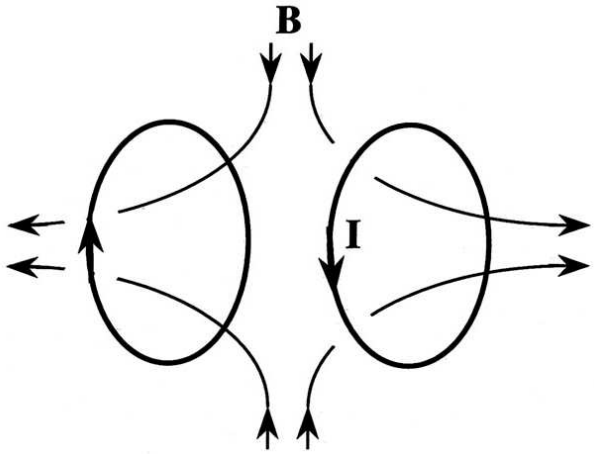

Figure 1.18: Quadrupole magnetic field generated from two anti-Helmholtz coils.

$$N_{st} = \frac{R}{\gamma + \kappa n_{st}} \tag{1.146}$$

If $\kappa n_{st} \ll \gamma$ (κ depends on the temperature, typically for a *Rb MOT* $\simeq 5 \times 10^{-11}$ cm^3/s), equation (1.144) holds as solution for the loading process

$$N(t) = N_0 e^{-t/\tau} + R\tau(1 - e^{t/\tau}) \tag{1.147}$$

N_0 is the initial number of atoms in the trap and $\tau = 1/\gamma$ is called the *trap mean lifetime*. As we are going to see a *Magneto Optical Trap* can be loaded by few methods, thus the loading rate depends on the adopted method. If we load the *MOT* just from the background gas R depends just only from the vapor temperature. It's possible define as *capture velocity* v_c the maximum atomic velocity to be trapped on a distance equal to the cooling cell. A specific detailed example regarding the *2–Dimensional Magneto Optical Trap* configuration will be illustrated in sec (5.1). In the general case if we define r as the photons emission rate, d the beams diameter and v_R the *recoil velocity* (see 1.119), the final form for the *capture velocity* can be simply evaluated from the consideration that for an atom with initial velocity v_c must absorb a discrete number of photons $v_c = l\ v_r$ (with $l \in \mathbb{N}$) to be stopped.

$$\begin{aligned} v_c &= l\ v_R \\ &\simeq r\frac{2d}{v_c}\ v_R \\ v_c^2 &= r2dv_R \end{aligned} \tag{1.148}$$

From gasses kinetic theory it's possible to evaluate the loading rate from background gas (where n_b is the density and T the temperature) [25]

$$R = 0.5 n_b V^{2/3} v_c^4 \Big(\frac{m}{2k_B T}\Big)^{3/2} \tag{1.149}$$

neglecting the presence of other atomic species in the background gas the loss rate can be evaluated as

$$\gamma = \sigma n_b \Big(\frac{3k_B T}{m}\Big)^{1/2} \tag{1.150}$$

where σ is the cross section for collisions between trapped atoms and background gas. At the end the number of atoms in stationary condition N_{st} for a MOT loaded from background gas at temperature T

$$N_{st} = R\tau = \frac{1}{\sqrt{6}}\frac{V^{2/3}}{\sigma} v_c^4 \Big(\frac{m}{2k_B T}\Big)^2 \tag{1.151}$$

this number depends from the forth power of the beams diameter cause $N_{st} \sim V^{2/3} v_c^4 \sim d^2 \times d^2$. The typical number of atoms for a Rubidium trap is $N_{st} \sim 10^9 \div 10^{10}$ but it depends on many experimental parameters..

1.4 Rubidium Atom Energy Levels, transitions and lasers' frequency

Now we have designed all the theoretical tools needed to understand the fundamental cold atom interferometer working principles. In our applications we are going to manipulate rubidium ^{87}Rb atoms and, in order to operate on internal and external degree of freedom, specific atomic transitions must be addressed by laser fields. In particular $D2$ level transitions will be considered as shown in picture (1.19), the wavelength distance between the ground $5^2S_{\frac{1}{2}}$ and the $5^2P_{\frac{3}{2}}$ exited state is $780nm$, also hyperfine sublevels splitting with relative frequency distances are shown (details about Rb transitions in appendix A). For the atomic cooling and trapping mechanism the best choice is to consider the transition $|5^2S_{\frac{1}{2}}, F = 2\rangle \rightarrow |5^2P_{\frac{3}{2}}, F' = 3\rangle$. As we have

seen the cooling mechanism is strongly dependent on the laser detuning, and in some conditions a large red detuning leads to good cooling performances; the choice of a transition far in frequency from the others is adequate in order to avoid superpositions due to the strong detuning operation. Moreover exited state sublevels *Zeeman* shift is fundamental for *Magneto Optical Trapping* thus is mandatory to address an exited level with $m_F \neq 0$ (see sec. (1.3.3)), this exclude $F = 1 \rightarrow F' = 0$ transition even if it satisfies the previous detuning requirements. From the other side the the laser field linewidth must be enough smaller than the transition natural linewidth thus $\Delta\nu_L \lesssim 1MHz < \Gamma \approx 6MHz$ is adequate. Besides the $F = 2 \rightarrow F' = 3$

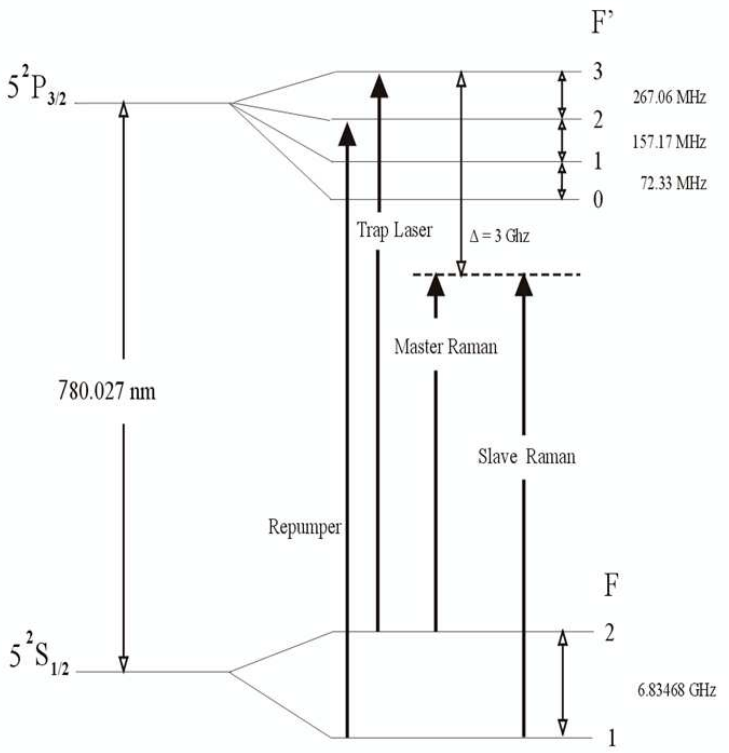

Figure 1.19: Diagram for $D2$ level rubidium (^{87}Rb) transitions considered for atomic manipulation in a typical atom interferometry experiment

desired transition there is a small probability to drive atoms in $F' = 2$ with a not-resonant $F = 2 \rightarrow F' = 2$ transition which might leads atoms to decay to the $F = 1$ ground state sublevel from where they can not be exited from the cooling field anymore. In order to avoid losses from the sample an supple-

mentary *repumping* field, stabilized on $F = 1 \rightarrow F' = 2$, must be added and overlapped to the the cooling. This last field cyclic drives atoms in $F' = 2$ until they decay in $F = 2$ and are included in the cooling cycle. Because the relative low probability for the atomic loss process (1/1000) a low power requirement corresponds for the *repumping* laser ($2 \div 10$ mW), also the laser linewidth is less critical $\lesssim 10$ MHz. At this level we want also to introduce that such *repumping* field can be also involved for detection experimental setup as will be detailed illustrated in section (2.7)
For the *Raman* transition side the frequency requirement have been already illustrated in details in section (1.1.2) about two photons transitions while full laser's phase stability requirement have been treated in (1.2.5), in the present section we just recall that for Rubidium interferometric manipulation two laser fields with relative frequency difference equal to ground state hyperfine splitting (6.834 GHz) and sufficiently detuned from the single photons transition to $5^2P_{\frac{3}{2}}$ levels are needed.
For the detection at the end of the interferometric sequence an additional laser beam is needed which can be tuned from $+10MHz \div -40MHz$ from $F = 2 \rightarrow F' = 3$ transition, usually can be adopted a shifted beam from cooling laser source (details about a detection scheme in section (2.7)).
An additional blow away laser field locked to $F = 1 \rightarrow F' = 0$ can be used in order to remove $F = 1$ atoms if needed.
For the interferometer a technical realization a common method to address all the "physics" lasers to the designed transitions frequencies is to utilize a further stable laser field as a *reference* locked on a certain atomic transition individuated by doppler free saturation spectroscopy. All the other lasers will be opportunely frequency shifted and locked to it. To stabilize the the *master* laser to the transition is needed to convert the frequency reference to a voltage signal with zero crossing at the lock point ad feed back to the source. A signal like this is obtained from the absorbtion of the atomic transition and the dispersive behavior from modulation and demodulation of light with *Frequency Modulation* spectroscopy technics (FM) (see literature for details [29, 30]).
The possible choices for the *reference* transition can change according with the different experimental requirements and electronics setups. Besides the "natural" atomic transitions, for saturation spectroscopy with counter-propagating pump and probe beam also *cross–over* extra transitions (CO) must be considered (see pictures A.1 and A.2 at page 205). For a spectroscopic setup of this kind atoms that have a certain velocity component along the propagation beam axis experience a *Doppler* shift of the light for both, because probe and pump are counter–propagating they will be shifted by the same amount with different sign in the atomic reference system. For a given atomic ve-

locity class, if the laser frequency is centered between two atomic transitions frequencies, atoms may absorb photons from each because Doppler width overlap (see[29]).
Coming back to our experimental project, different setups and reference transitions, but always with the same principle, are adopted for the experiments described or mentioned in this thesis. For the *MAGIA* experiment and thus for the *2D–MOT* described in (5.2) *reference* laser is 184.2 MHz red detuned and locked to the $F = 2 \rightarrow F' = 3$, $D2$ Rubidium transition whereas the *reference* laser for the *Space Atom Interferometer* is stabilized to *CO23* transition between $F = 2 \rightarrow F' = 2$ and $F = 2 \rightarrow F' = 3$ and 263.33 MHz blue detuned up to there (sec. 4.1.1).
After this introduction to laser field frequency requirement we remand to the following specific sections for the technical implementations.

Chapter 2

Space Atom Interferometer

As it was already presented into the introduction Atom Interferometry configures a new frontier for accelerations and rotations precise measurements. A wide range of research fields based on this kind of measurements may benefit from such a new generation of inertial sensors. A new path has been already drown by the introduction of atomic clocks for spaceborne experiments oriented to general relativity tests.
The main part of research work described in this thesis has been focused into the study, the development and the realization of a **Space Atom Interferometer** (**SAI**) *Project* [104]. The previous experience for the FINAQS [140] absolute gravimeter (pag.27), in which we have been also involved together with part of the collaboration, has been a fundamental hint for this further project in terms of know–how development.
In this chapter the general features of the whole system are illustrated together with specific characteristics of the scientific apparatus.

2.1 Basic Idea and motivations

The basic proposal of the SAI project, in agreement with the ESA commissioning, is to demonstrate the possibility of construction of a space–compatible Atom Interferometry sensor. Additionally the realistically expected performances limits and potential scientific applications in a micro–gravity environment sensor operation will be investigated, focusing the attention on all quantum, relativistic and metrological scientific aspects. Efforts provided from the European collaboration have been joint together in the framework of this enterprise; a strong knowledge and know-how sharing between the research groups and the institutions already experienced into Atom Interferometry field has been planned and realized.

At a first level a earth-based transportable device is under realization in Firenze, it is already oriented for space mission basic layout constrain. A preliminary step is the realization of a sensor full compatible with the micro–gravity tests at the *Bremen Drop Tower* (pag. 31) but also with the *Zero G Parabolic flight*. With purpose of demonstration of the technology readiness a prototype is going to be assembled as a *single-axis accelerometer* based on ultracold ^{87}Rb atoms. The design target is to keep the prototype as compact as possible without degradation of sensitivity as compared with existing laboratory instruments: a trade–off between performance and technology readiness for space applications will be unavoidable. Besides the future implementations for micro–gravity environment operation, the goal for sensitivity in acceleration will be of $3 \cdot 10^{-7}$ m/s for 1 second of integration time as from specification. Because the device will be tested in terrestrial environment as a gradiometer, thus in a differential mode, no special care will be taken for seismic isolation. The preliminary performance demonstration will be provided on the basis of acceleration measurement extrapolated for low vibration noise and will be confirmed from gradiometric operation or transporting the device in an ultra–quiet environment with low acceleration noise.
It's important to underline that the space experiment operation sets strict limitations on the volume of the apparatus to the space craft science cell as well on its weight, moreover for this kind of operation a selection of materials, mechanical design and implementation strategy must to be taken into account as strong bounding parameters. From technological and conceptual point of view the differences between a device operating in Earth environment and one operating in micro–gravity are fundamental; the result of our study is to draw a baseline design for such a kind of transportable device.

2.1.1 Micro–gravity tests motivations

As we have saw in chapter 1 the sensitivity of an atom interferometer scales as the square of the interrogation time $\sim T^2$, thus we can say that the first limit for such kind of device in Earth based experiments is the atom sample expansion time and the free fall time. Atom cooling allows to manipulate atomic samples with temperature of order of μK, thus minimizes the expansion time constrains. By the other side, the free fall time seems to be still a problem, cause to operate with long interrogation time, very long apparatus should be needed leading to big technological troubles for the realization. In micro–gravity environment, because of the low acceleration affecting the sample, a small displacement from the trapping position can be considered; this results into the possibility to perform interferometric sequences without launch and with a very large time duration. This features collocate inertial

atomic sensor in a new landscape from the sensitivity range point of view, so while ground atomic gravity sensors, thanks to the efforts of last years, becomes a good performing alternative for conventional devices, the same happens in space application context with a new prospect of applied and fundamental physics that is going to be open. As applicative sensor an atom interferometer can work as high sensitivity inertial sensor for spacecrafts: acceleration measurements can be considered as a reference to address gravitational fields. A complete device for navigation can be considered from the integrations of different interferometric configurations in order to provide also the gyroscope tasks [113, 114].
There are four way to reach a micro–gravity environment; the first one is obviously to send the sensor into the deep space far from big masses, the second one can be realized by the *parabolic Zero G flight*, the third one is orbiting around the planet at big distances from the ground and the forth one is free falling by from drop towers.

Equivalence Principle tests

The *Equivalence Principle* postulates the *equivalence between Inertial and Gravitational Mass* or states in a different formulation that *bodies with different mass and/or composition fall with the same acceleration in a uniform gravitational field*. This means that all forms of energy contribute in the same way to the weight and to inertial mass. This contention can not be proven but just only tested with higher and higher precision. From the *Pisa's Tower* Galileo's tests the principle was recover and generalized to by Einstein and made as foundation of *General Relativity*. A violation at some level would required also a modification of the theory or constitute the discovery of a new force. The idea that *General Relativity* is not an ultimate theory for gravitation is not totally unfunded and the starting point is that it is a classical quantum field theory based on space time curvature challenging at macroscopic distances; no match point at moment has been found with the other three fundamental interaction operating between elementar particle at short distances and moreover no realistic theory of quantum gravity exists. The outstanding problem seems to be the construction of a consistent quantum theory of gravity for a complete description of all particle interactions. For this construction *superstring* theories are the only candidates and they require the existence of spinless partners of the *graviton* such as *dilatons* and *axion-like* particles. The existence of *dilatons* in particular will imply a tiny violation of *Equivalence Principle* in the range of space missions. The violation of the principle may produce a modification on the gravitation law with, for example a component dependent inverse square law and charges q_1 and

q_2 [119].

$$V = V_{grav} + V_{unknown} = -G\frac{m_1 m_2}{r} - \frac{q_1 q_2}{r}$$

Other general expression have been formulated for possible modifications of the interaction, the composition dependent term can be parametrized as a Yukawa type potential.

$$V_{NF} = \pm\frac{g_{NF}}{4\pi} q_1 q_2 \frac{e^{-r/\lambda}}{r}$$

Here λ is the *Compton* scattering wavelength, g_{NF} a new coupling constant for the *novelle force*, q_i the charge attributed to test particle and signs minus and plus refer to interaction mediated by scalar or vector bosons.
Starting from the point that to perform *Equivalence principle tests* two different species of test masses are needed it's important to underline that such tests are are out of target respect the project we discuss in this PhD thesis. The argumentation above is useful to contextualize the efforts in realization of the new generation of high sensitivity sensor, by the other hand the step to a sensor operating in micro–gravity with two different atomic isotopes is not very long.

2.2 The General Scheme

The baseline for the Space Atom Interferometer transportable sensor is organized either for the laser system and for the vacuum apparatus into several modular subsystems developed singularly by the groups involved into the project and assembled for tests in the Florence dedicated lab. A schematic sketch summarizing all components and tasks for the apparatus is illustrated in picture (2.1). Laser system is organized in separate compact standing alone breadboards for atom cooling and atomic manipulation (see section (4.1)), breadboards are linked each other and to the atomic vacuum system by means of optical fibers as interface.
The interferometer will operate as a single axis vertical device in launching scheme for a rubidium cold atomic sample. The sample will be cooled and trapped by a three dimensional *Magneto Optical Trap* loaded by a *2D–MOT* as cold atoms source. Because of the required acceleration measurement performances in micro–gravity environment, unlike other gravity gravimeter setups (see *FINAQS*, picture (12)), for this system will be used the same chamber for sample preparation ad interferometric detection. Under low acceleration conditions the atomic parabolic trajectory will produce a small

vertical displacement from the starting point. This feature introduces a lot of specific issues for the sensor design: first of all, if the interferometric sequence will be performed not only into a dedicated section (vertical tube), a magnetic shield for whole physics chamber is needed in order to avoid systematic effects due to magnetic fields and, moreover, all the component inside such shield must be not magnetic or magnetizable (this holds from screws to photodiodes).
The expected performances are evaluated starting from the expected interferometric atomic phase shift and form the signal to noise ratio. The equation (1.72) for the phase shift due to a general acceleration a simply becomes $\Delta\Phi = k_{eff} a T^2$, where the effective wavenumber associated to Rubidium *Raman* transitions in our setup is $k_{eff} = 1.6 \times 10^7$ m^{-1}. The ultimate phase resolution depends on the signal to noise ratio at the detection, that is limited as we have seen in sec (1.2.5) from the quantum projection noise, thus if the phase resolution per shot is $\delta\Phi \approx 1/\sqrt{N}$ the acceleration resolution per shot will be given from:

$$\delta a \approx \frac{1}{\sqrt{N} k_{eff} T^2} \tag{2.1}$$

With a detecting of 10^4 atoms with an interaction time of $2T = 100$ ms the quantum projection noise holds a noise limit on 10 mrad/shot corresponding to an acceleration sensitivity of 2.5×10^{-7} m/s^2 at 1 s: that is in the range of the project required sensitivity. By the other hand with the help of a cold atoms source featuring 10^9 atoms/s flux it will be possible to launch at least 10^7 atoms with 100 ms of loading time. Moreover with the employment of a microwave field for a preliminary internal state selection it is expected to detect at least 10^5 atoms at the end of the interferometric sequence. The experimental cycle will take 500 ms and thus will be compatible with a repetition rate of 2 Hz.

2.3 Mechanical layout and vacuum system

In order to be compatible with *Drop Tower* tests the apparats has been designed to be fitted in the pre-designed capsule. The relative layout is very similar to ones involved in other experiments (see [111, 121]), such capsule and the external frame have been now standardized by the Bremen engineering team [138]. The mechanical structure is illustrated in picture (2.2a): the capsule is 278 cm length and have an external diameter of 72 cm, custom made control electronics and special designed power supply will be arranged in the bottom part, the middle stage will be occupied by the *science cell* (b) whereas the laser system will fills the upper part. The mechanical structure,

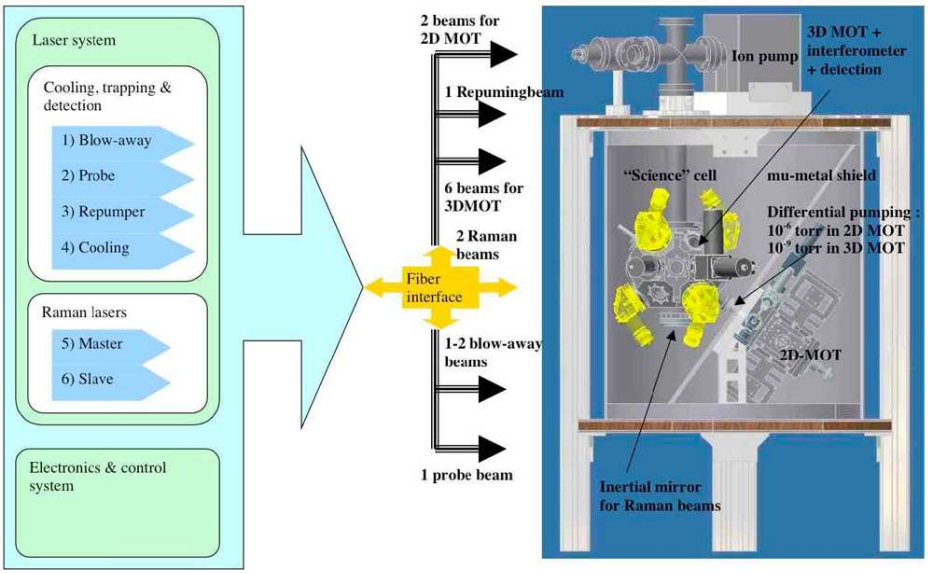

Figure 2.1: Illustrative sketch for *Space Atom Interferometer* apparatus.

holding the vacuum system and laser modules, will be contained in a cylindrical volume with diameter of 60 cm with height of ≈ 150 cm. The *science cell* (2.2b,c) includes the vacuum system for atom manipulation that consists in a main chamber with an interferometric tube and a *2D–MOT* as cold atom source. The cell is delimited by the external magnetic shield layers: the internal dimensions are 601 mm height times 530 mm diameter and the external dimensions are 663 mm height times 708 mm diameter. The vacuum system will be equipped with an ion pump for 20 l/s (*VacIon20*, from VARIAN) mounted on top and outside the magnetic shield capsule. Such pump will provide for an ultra vacuum environment only for the interferometer tube and for the main chamber, on the other side a separate vacuum pump system will operate for the *2D–MOT*.

The expected performances for such differential pumping scheme will guarantee a pressure of $\approx 10^{-10} \div 10^{-9}$ mbar into the main chamber side with a background pressure of $\approx 10^{-6}$ mbar on *2D–MOT* side at operative conditions (see 2.5). Some results about differential pumping obtained with a scheme of this kind are presented in section (5.4).
The main vacuum pump will be interfaced to a four way crossed tube fitting, providing also on the opposite side an additional access for a turbo pump (needed for pre-vacuum conditions). In vertical direction the cross fitting is linked to the interferometer tube on bottom and on the upper side provides an optical access for *Raman* beams injection (see picture (2.2b,c)).

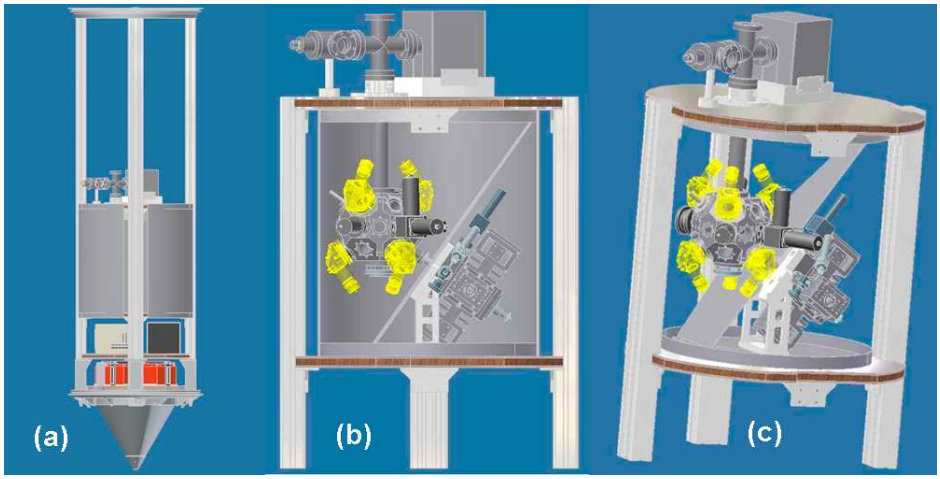

Figure 2.2: 3D view of mechanical structure and core system of the *SAI* sensor. (a) *Drop Tower Capsule* mechanical frame, (b),(c) *science cell*.

The *2D–MOT* will be linked to the main chamber from the bottom side with a 102 mm length tube, with internal diameter of 20 mm; such connector is designed as a bellow in order to compensate possible oscillations and to additionally protect the ultra hight vacuum connections from longitudinal impact forces. The inclination of the cold atomic source is 45 degree respect to the vertical interferometric axis. An optical view–port As access point on the main chamber lower hemisphere has been chosen as access point as shown in picture picture (2.2b).
Cooling beam collimators are represented in the picture from yellow devices, the specific setup will be presented in details in section (2.4).
From static end mechanical point of view the "*science vacuum system*" composed by the *3D-MOT* cell plus the vertical vacuum tube will be clamped to the upper platform and suspended into the capsule. Such kind of holding system has been derived from the *AKTAT* experiment and adapted to *SAI* apparatus, a mechanical detail is shown in appendix in picture (B.3).
The *2D-MOT* is rigidly connected to the lower capsule platform through an aluminium support attached to the massive square connector. The technical solution described so far have been adapted and approved from *Zarm Drop Tower*'s engineering team [138] in order to consider them adequate to big impact stresses due to a dropping experiment ($\lesssim 50$).

2.3.1 Physics chamber

The whole physics chamber, composed from the *3D–MOT* main chamber/ detection plus the interferometric tube, has been designed to be compatible with a free flight under terrestrial conditions of $T_{flight} \approx$ 500 ms that is compatible with a repetition rate for the experiment of 2 Hz and a maximum interferometer duration of $2T_{interf} = 200$ ms. Considering a reasonable launching initial velocity of 2.4 m/s the total height reached from the sample will be 300 mm. The vacuum system is totally titanium made and realizes a whole height of 448.7 mm, the useful launching height from the *MOT* position up to the end of tube is of 341.65 mm. The interferometric tube is 260 mm length with internal diameter of 36 mm and external 43 mm. The projected layout for the designed apparatus is illustrated in picture (2.3).

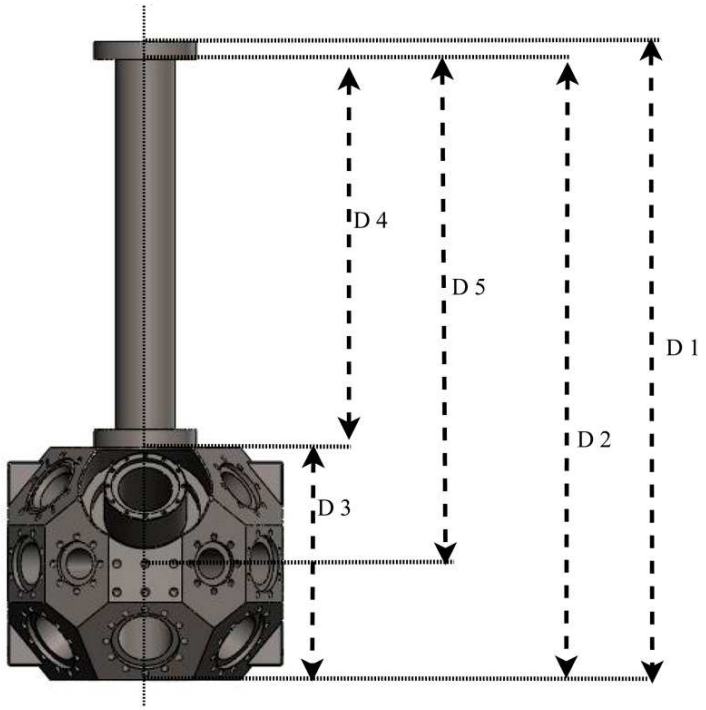

Figure 2.3: *SAI* Physics Chamber Layout, total height $D1 = 448,7$ mm, main chamber total height $D3 = 163,3$ mm, tube length $D4 = 260,0$ mm, launching height $D5 = 341,65$ mm.

Main Chamber

The main chamber for the tridimensional cooling and trapping of the atomic sample and for the interferometric detection is derived from the one adopted for the *FINAQS* gravity sensor [140], designed by Alexander Senger [108] [135]. The chamber is composed by a titanium made single body, the quasi-spherical shape is realized by a football ball like system of 26 angled plane faces for optical accesses, external dimensions are 163.3 mm height and 193 mm × 192.94 mm width on the equatorial plane (the equatorial dimensions are not symmetric because two sides faced are specific shaped for additional mechanical supports), the layout is shown in picture (2.3). Details and different views are illustrated in picture (B.4) at page 210. The total shape can be considered as divided in an equatorial plane, an upper hemisphere, and a lower hemisphere that are totally symmetric and inversion equivalent either for dimensions, angles and windows dimensions. Two facet of the total 26 are not occupied from a window, thus the system accounts for 24 total optical accesses. The two accesses located on the vertical direction are are dedicated to the *Raman* beams. Because of the *3D–MOT* cooling beams configuration (see sec. 2.4) all the facets of the two hemispheres (thus also the windows) are angled the way that an incoming incident beam will be angled at 45° respect to the *Raman* direction and to the equatorial plane. Chamber access windows are four kinds designed with different internal/external diameters, as follows: $D1$ = 21.5/31.6 mm, $D2$ = 30/40.1 mm, $D3$ = 30/48.26 mm, $D4$ = 30/48.1 mm. An idea of their disposition on the chamber can be provided by the table 2.1. The ones dedicated to a simple optical access have a flat housing 4 mm deep dedicated to glass windows fitting. Housing internal diameter is 10 mm inferior of the external one, this means that for each access a radial length of 5 mm on the internal surface is dedicated to windows sealing. The accesses dedicated to interface between different components such as *2D–MOT* or interferometric tube (with diameter $D3$), are designed in a different way: an internal knife edge is included in order to accept insulation copper rings.

The optical windows, $BK7$ glass made, are custom designed for the apparatus and will be attached to the chamber by the indium sealing technics. The main drawback is a low backing temperature allowed for indium but by means of special indium alloy it is possible to heat up to 180°. Windows are antireflection coated $R < 0.25\%$ on both sides but according with our experience, in order to leave them easily removable, at the sealing side the surface in contact with indium will be free from coating treatment. Considering that interferometer optics components will be holden to the flanges and considering also the special application the system is addressed, the mechan-

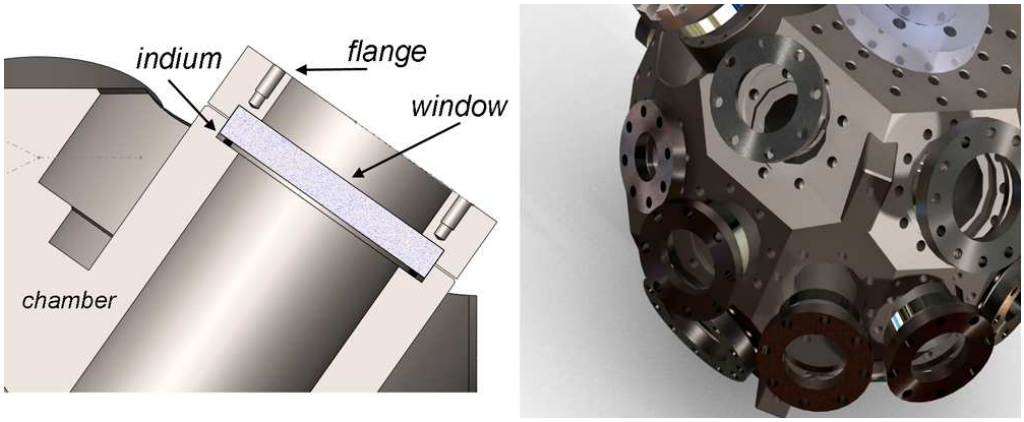

Figure 2.4: *SAI* main chamber's windows details, on left side illustrated the applied sealing technics.

diameter (int/ext)	21.5/31.5 mm	30/40.1 mm	30/48.26 mm	38/48.1 mm
upper hemisphere	0	1	$1+1*$	4
equatorial plane	4	6	0	0
lower hemisphere	0	1	$1+1**$	4

Table 2.1: *SAI* Main Chamber optical accesses table, values in the cells identify the number of accesses for the specific dimension, " * " identify vertical windows for *Raman* beams access.

ical layout for windows–flange–chamber system has been designed the way that each flange is in touch with the chamber body and pressed on it (see details in 2.4 left side). The windows thickness (6 mm) and relative flange rear housing deepness (3 mm) have been designed in order to guarantee this condition. We consider to employ a ≈ 2 mm thick indium wire to be compressed by the flange pressure to ≈ 1 mm; moreover the flanges rear housing allows the employment of few aluminium sheets or ultra thin teflon rings in order to avoid the direct glass–metal contact. In case the pressure of the window on the indium wire will be not enough once the flange is in touch with the chamber wall and vacuum leakage occurs, it will be possible to add additional aluminium sheets between the flange and the glass window.
In order to connect optical systems such as laser beam collimators or mirrors to the apparatus, a special design has been developed for flanges. The system has been designed to screw part of the optical components directly to the main chamber trough four free screwing holes of the flange. For some com-

ponents, such as cooling beams collimators, dedicated custom made flanges have been designed that provide specific housing for vacuum screws and additional threaded holes for collimators connection. Some details about this specific task are shown in technical draw B.6 at page 212, a generic designed flange for our system is shown in technical B.5 at page 211.

2.4 Atom Cooling and trapping system

The *3D–MOT* system for cooling and trapping the atomic sample will be realized by six counter-propagating beams polarized σ^+/σ^- and direct along three orthogonal axis. The configuration adopted is the so-called $1-1-1$, where three beams comes from upper hemisphere and three from the lower; the *Raman* beams direction, parallel to the acceleration measurement axis, is free from cooling beams. We must also observe that such described cooling beam configuration is not the only possible for a single axis accelerometer: in different experiments also other configurations for cold sample preparation are adopted. For example, another choice provides for four crossing counter-propagating beams in the equatorial plane and other two in the vertical direction following the same *Raman* beam path and the same acceleration direction: this specific setup can be convenient for sample dropping configurations with separate detection chamber but can be unadequate for launching schemes [71].
The magnetic field gradient needed for the trap is generated in our implementation by two *anti-Helmholtz* coils with the axis along one *MOT* beams direction; the laser system is designed the way to cross the beams at zero point of magnetic field (see picture (2.5)). Because in our setup each cooling beam is provided from a dedicated collimator (2.4.2), without any retro-reflection system, the single beam frequency can in principle be controlled independently.

Besides the Magneto Optical Cooling and Trapping task, after switching off the magnetic field, the laser beams are also used for further molasses cooling up to few μK of temperature (see 1.3.1) and for launching of the atomic sample in the vertical direction as preliminary step for the interferometric sequence. As usual for such kind of atomic fountain setup the launching is realized by optical molasses frequency unbalance between the beams from downside an the others from the upside. A lower frequency of the upper lasers respect to the lower lasers results in a upward moving optical molasses which cool the atomic sample to a non zero upward velocity: for this purpose a separate frequency control for the two beam sets is mandatory. From optical molasses approach it is possible to estimate that a relative frequency

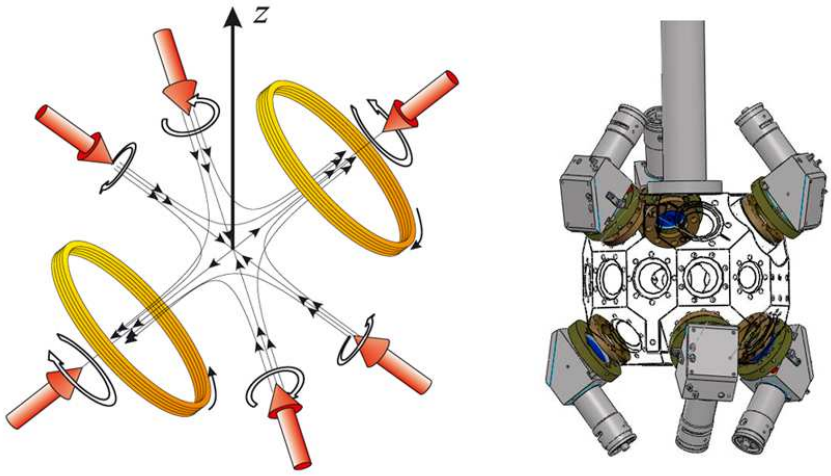

Figure 2.5: Cooling and trapping system setup for *Space Atom Interferometer*, six counter–propagating beams in configuration $1-1-1$, magnetic coils concentric with one cooling direction, "z" axis as launching direction. On the right side the mechanical realization with mounted special designed independent collimators.

detuning below 1 MHz can be sufficient to achieve a initial launching velocity of 1 m/s leading to a 200 ms fountain in terrestrial gravity conditions.
For the described purposes the *3D–MOT* laser beams will be red tunable between 0 and 40 MHz from the $F = 2 \rightarrow F' = 3$ transition (see 1.4 and app. A) with a linewidth of 1 MHz and a power per beam on the atoms of 20 mW that means 120 mW of total optical power (specific details for laser system realization in sec. 4.1.2). A *repumping* beam is overlapped to cooling beams and locked to the transition $F = 1 \rightarrow F' = 2$ with a linewidth of $\lesssim 10$ MHz and a total power of 2 mW (section 4.1.3).

2.4.1 *3D–MOT* magnetic field system and realization

A magneto Optical Trap for rubidium atoms requires a magnetic field gradient of few Gauss/cm at the center of the trap; two coils in *anti–Helmholtz* configuration generate a quadrupole magnetic field along the symmetry axis given from:

$$B(x) = \frac{\mu_0 N I R^2}{2}\left[\left(\frac{1}{(R^2+(x-d)^2)^{\frac{3}{2}}}\right) - \left(\frac{1}{(R^2+(x+d)^2)^{\frac{3}{2}}}\right)\right] \qquad (2.2)$$

thus the gradient in the center is given from

$$\frac{\partial B(x)}{\partial x}\Big|_{x=0} = \mu_0 N I R^2 \frac{-3d}{(R^2+d^2)^{\frac{5}{2}}} \tag{2.3}$$

where N is the number of windings, R the coils radius, I the current flowing i and d the relative distance between the coils. In our setup coils are incorporated into the body of the *MOT* chamber, this allows to get them as much as close as to the center is possible the way to decrease the current needed for a certain gradient (see picture (2.6)). With our design parameters ($N = 80$, $d \approx 160$ mm and $R = 60$ mm) the typical value for the gradient relative to a current of $I = 10$ A is $\frac{\partial B(x)}{\partial x}\Big|_{x=0} \approx 10$ G/cm. With such value for the current, giving for wires section 4×1 mm^2 and for resistance 0.1 Ω each turn, the dissipated power ranges around 10 W. Considering from the other hand that the maximum allowed temperature for wires insulation is 150°, may be needed to control and to minimize heating effects with a cooling system. This problems have been already treated by A. Senger for the *FINAQS* apparatus by means of simulation and of direct measurements [106, 108, 140].

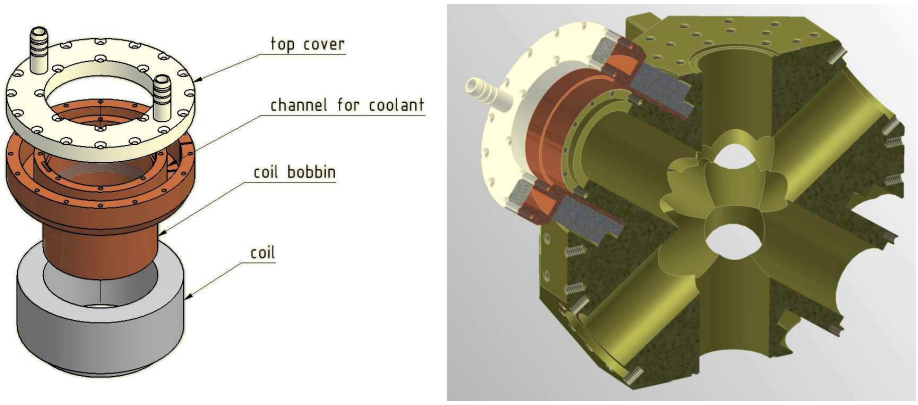

Figure 2.6: *SAI* design for magnetic field gradient coils, housing and cooling system [108].

Each coil is mounted on special designed cylindrical shaped copper shell allowing, from one hand, a good mechanical fitting with also quick replacement operation and, from the other hand, a good heat dissipation due to the copper thermal property. The poor thermal conduction behavior of titanium allows to consider the vacuum chamber out of the game. Performed simulations shows the highest temperature reached at the inner edge of the coils

copper shell (vacuum side) whereas temperature at the external side is almost the same as the environment (22 °C), also without any cooling system. The external part of the shell is shaped as a radiator for a good dissipation but it also provides for a groove to accept an additional water cooling system adapted from commercial devices employed in personal computers CPU cooling (see left side of picture 2.6). Such a system provides a water circulation roughly of 10 l/s and also an additional radiator with a mounted fan of 100 mm diameter. From the *FINAQS* experience, by a temperature monitoring in different operation modes for the setup described so far, have been individuated some typical heating limits. Operating with a coils current of 10 A (that means $\approx$ 10 G/cm of field gradient) and without the additional cooling system the temperature on the hottest part of the coils shell rises up to 30 °C after 35 min with an asymptotic value at 40 °, whereas starting with a current 19 A, that roughly duplicate the field gradient and quadruple the dissipated power, the temperature grows up to 80 °C in few minutes. In this last current condition the cooling system is needed: it ensures a measured temperature limit at thermal equilibrium of 50 °C in air environment at 22 °C.
We can thus summarized the operative magnetic field conditions for our device in three settings: (a) coils current 20 A driving a big field gradient of 20 G/cm (water cooling needed), (b) coils current of 10 A driving a field gradient of $\approx$ 10 G/cm (environmental air cooling sufficient), (c) coils current of 5 A driving a field gradient of $\approx$ 5 G/cm (low heat dissipation). The operative condition (a), because of the big field gradient, will lead to the higher performances for the atomic trapping but, on the other hand, the water cooling system limits it to terrestrial applications. The condition (b) is fully adequate to dropping tower operations whereas the (c) condition will be considered for space applications where a low heating dispersion is a mandatory requirement; such configuration is still compatible with $\approx 10^9$ atoms in the *MOT* sample. We can also consider that in micro–gravity conditions the interferometric duty cycle, the ratio between sample loading time and the interferometric sequence time duration, will be $\ll 1$ leading to a reduction of the described heating effects.

2.4.2 Cooling Beam Collimators

The optical system for *3D–MOT* collimating beams consists in six assemblies designed by A. Senger from University of Berlin for the *FINAQS* sensor apparatus [108, 135]. The original design has been adapted also to the *SAI* apparatus that utilizes the same vacuum chamber but a different windows sealing and flanges. The complete beam system mount is illustrated on the

right side of picture (2.5). A schematic draw for the single collimator is shown in picture (2.7): in order to ease the description understanding the numbers on the vertical cut view on left side tag the the single component. Cooling beams are driven to the vacuum chamber by fibers and hold on the collimator by an adaptor (1), because of the small numerical aperture of the beam fiber output the beam diameter is first enlarged from a plano concave lens with focal $f = -30$ mm (point 4) and then reflected from a 45 degree golden plated mirror (point 5) (Edmund Optics), such a mirror is needed to give enough length for the beam waist expansion with a good compactness for the module. At the end the beam is collimated by an acromatic doublet with focal length of 100 mm and a diameter of 35 mm (custom made from Belfort Wetzlar). A wave plate $\lambda/4$ is placed in position 3 in order to provide the right polarization to the beam for the cooling process. A system of springs and pushing screws has been developed for tilting the collimator body, one side is supported from a single ruby ball with 8 mm diameter. The collimator base is screwed on special designed vacuum flanges.

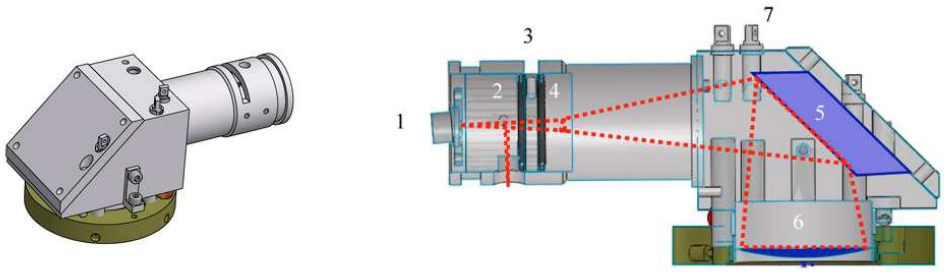

Figure 2.7: Custom made cooling beam collimators for *SAI* experiment, a cut view on the right side.

2.5 *SAI* cold atom source

The atomic source (*2D–MOT*) for the *Space Atom Interferometer* has been developed by the Cold Atoms and Sensors Group of Hannover University [136] and adapted for the project. The setup has been derived and reprogrammed from the original implementations developed for the *Cold Atom*

Sagnac Interferometer (*CASI*)[47] and the *ATLAS* experiment[1]. The apparatus design results in a compact implementation in the longitudinal dimension in order to be compatible with the *Drop Tower* capsule constrains (picture (2.2)); the whole dimensions are 320 mm depth, 540 mm length and 290 mm width. The core consists in a glass cell pressed and indium sealed on a non magnetic aluminium frame. From the physical point of view the cooling cell is delimited from the lateral optical accesses that configures internal dimensions of $100 \times 20 \times 30$ mm^3, the glass walls are 5 mm and not antireflection coated.
The Magneto Optical cooling and trapping setup is typical for such kind of devices; four independent crossed cooling beams provide for laser cooling in the radial direction, each of them, driven from fibers, are linked to a specific collimator frame and collimated from quadrangular custom made lenses. The four collimators are screwed and integrated into the main frame. An additional *pushing beam* is plugged on the backside. Four magnetic coils integrated into the main body provide for a magnetic field of 12.5 G/cm (a detailed treatment about theoretical working principle for the *2D–MOT* together with some experimental issues are reported in sections (5.1), (5.3), (5.4)). In picture (B.7) (at page 213) a 3D-view of collimators assembling to the main body is shown providing a representation of the resulting layout. In picture (2.8) technical details are illustrated, numbers in our description correspond to items into the draw. Vacuum conditions are provided for a first setup by two ion pumps with pumping speed of 2 l/s (*Varian VacIon2*) (8) but the system is designed to accept also other two titanium sublimation pumps; an additional connector is available for a turbo–molecular pump providing pre–vacuum conditions. A graphite made differential pumping stage conical shaped with 3 mm of inner diameter and 37.5 mm length works as diaphragm for differential vacuum (7). Rubidium pressure will be obtained in a traditional way from an heated dispenser(6), but the system is also equipped for a *LIAD*[2] implementation (16), in our design is just foreseen as an option. The expected performances for our setup are been derived from the experience of the operative performances on the *Cold Atoms Sagnac Interferometer*: output atomic flux will be $\simeq 10^{10}$ atoms/s with a consequent *3D–MOT* loading rate from the atomic source of at least $\approx 10^9$ atoms/s, required working conditions are summarized in the following table [47, 104].

[1]experiment aiming for an all optical produced *Bose-Einstein condensate*; all-optical ATom LASer (ATLAS)
[2]LIAD: Light Inducted Atomic Desorbtion

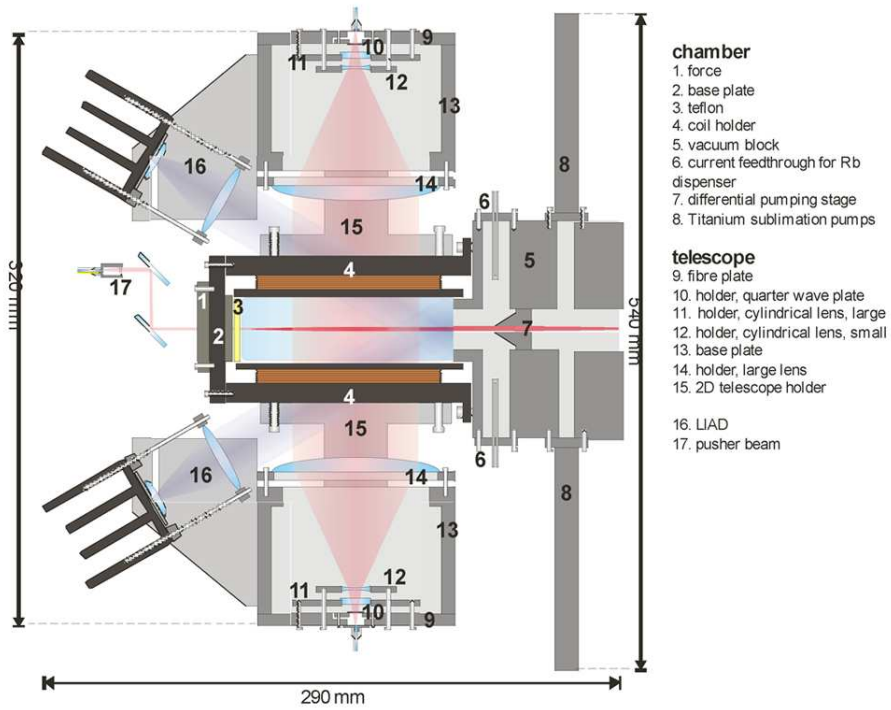

Figure 2.8: Construction sketch for the *SAI 2D–MOT* (design study).

	atomic flux $\Rightarrow 10^{10}$ atoms/s	*loading rate* $\Rightarrow 10^{9}$ atoms/s
	2D-MOT	***3D-MOT***
average power per beam	$35 \div 50$ mW	10 mW
pushing beam power	0.9 mW	$\sim$
magnetic field gradient	12.5 G/cm	$\approx$ 12 G/cm
cooling beams diameter	$\sim$	30 mm
Rb dispenser temperature	82 °C	$\sim$

2.6 Configuration for *Raman* beams

Starting from our theoretical treatment of atom interferometry basics it's easy to figure that the *Raman* beams configuration setup is the most critical for the interferometer's apparatus implementation. According the scheme presented so far two counter–propagating beams traveling in vertical direction are needed for our kind of single axis acceleration sensor.

2.6.1 Optical and Magnetic requirements

Besides two photons *Raman* transitions theory (sec. 1.1.2) and interferometric theory extension (1.2) it's important also to consider magnetic induced accelerations from stray magnetic fields. Supposing a bias magnetic field direct along the z *axis* an atom with magnetic moment μ accounts an extra energy $U = \vec{\mu} \cdot \vec{B}$ and thus is subject to an acceleration given from:

$$\vec{a} = \frac{1}{m}\vec{\nabla}(\vec{\mu} \cdot \vec{B}) = \frac{1}{m} m_F \mu_B g_F \frac{dB_z}{dz}\frac{\vec{z}}{|\vec{z}|} \tag{2.4}$$

such acceleration vanishes if the magnetic field is uniform, but if a spatial variation is introduced, the acceleration is still present and depends on the atomic mass and on the m_F quantum number. At this level for $m_F = 0$ the (2.4) acceleration contribution also vanishes whereas, on the other side, the first non vanishing energy therm is given from:

$$U_{II}(m_F = 0) = \frac{\mu_B g_J |\vec{B}|^2}{4\Delta E_{hf}} \equiv \frac{1}{2} h a_{z,II} |\vec{B}|^2 \tag{2.5}$$

that means a resulting acceleration on $m_F = 0$ equal to:

$$\vec{a}(m_F = 0) = \frac{1}{2m}\vec{\nabla}(h\ a_{z,II}\ |\vec{B}|^2) = \frac{h}{m} a_{z,II} |\vec{B}| \frac{dB_z}{dz}\frac{\vec{z}}{|\vec{z}|} \tag{2.6}$$

considering a field bias of $B_z = 300$ mG and a gradient $B'_z = 5 \times 10^{-5}$ G/mm is possible to compare the different accelerations experimented by the two different atomic quantum numbers $m_F = 1$ and $m_F = 0$ as follows

$$\begin{array}{lll} m_F = 1 & a_z & \sim\ 2 \times 10^{-5} g \\ m_F = 0 & a_{z,II} & \sim\ 4 \times 10^{-9} g \end{array}$$

We can than conclude that in order to to minimize such magnetically inducted effects it can be adequate to perform the interferometric sequence on atoms in $m_F = 0$. After a preliminary sample preparation in the state $|F = 1, m_F = 0\rangle$ it is important to continue the sequence with $\Delta m_F = 0$ *Raman* transitions (π-light transitions suppressed). This can be ensured by performing the interferometric sequence in a configuration with a vertical magnetic field bias parallel to $\vec{k}_{eff}$, *Raman* effective wave vector, and by using circular polarized laser fields. The magnetic field induces a first order *Zeeman* shift on energy levels and moreover the parallelism with the circular polarized light suppresses net transitions with a π-light absorbtion–emission transition as intermediate step. A full calculation must be performed by evaluating the probability contributions of the all possible intermediate transitions from $|F = 1, m_F = 0\rangle$ to $|F = 2, m_F = 0\rangle$ including all intermediate

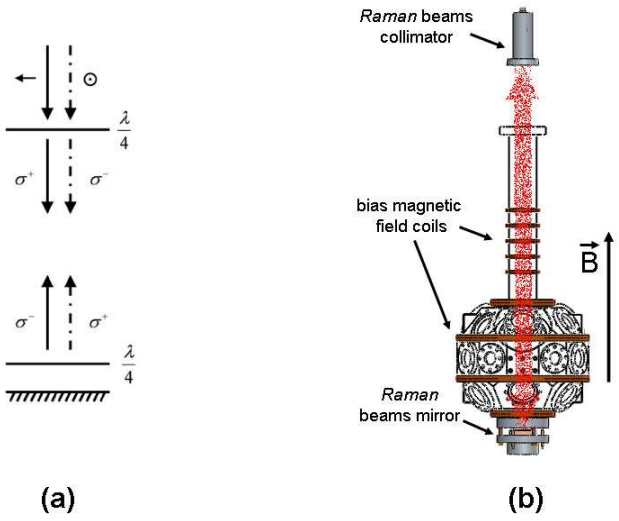

Figure 2.9: Scheme for *Raman* beams propagation configuration, (a) light–fields polarization setup, (b) optical assembling on the interferometer's apparatus, beams collimator and retro-reflection mirror, bias magnetic field and relative coils setup.

states $|F' = 1, 2, m_{F'} = 0, \pm 1\rangle$ accessible by absorbtion and emission of σ^+, σ^-, π light. One finds that $\pi - \pi$ transitions and $\sigma - \pi$ transitions are suppressed by selection rules together with those with wrong net energy shift $\Delta E_Z \neq 0$, moreover those transitions with intermediate $\sigma^\pm$ absorbtion and $\sigma^\mp$ stimulated emission are also suppressed because net probability adds to zero. We remand to literature for a complete calculation of transitions probability (see [32, 33, 67, 73]).
Coming back to the experimental point of view and to the apparatus realization in order to obtain the described configuration with laser *Raman* fields circular polarized for the forward and backward propagating beams the employment of two $\lambda/4$ waveplates at the beginning of the path and before the retro-reflection mirror can be a choice. A possible approach can be to drive beams from the fiber with orthogonal linear polarization and then to dispone the first $\lambda/4$ waveplate after the collimator the step before projecting lasers into the interferometric tube: this way fields acquire a $\sigma^\pm$ polarization respectively. At the end of the first one-way path they can pass through the second waveplate on the down side out of the vacuum system before the retro-reflection mirror, after the second passage their polarization sign will

result inverted for the back-way path as shown in picture (2.9a). By means of such scheme an atom initially in $|F = 1, m_F = 0\rangle$ can absorb a photon from σ^+ light field downward propagating and can emit a photon with the same polarization for stimulated emission by interaction with the other *Raman* beam σ^+ polarized and upward propagating. This will lead to a $\Delta m_F = 0$ resulting net transition, such scheme is totally symmetric changing σ^+ with σ^- at the first step.
The *Raman* optics and magnetic design concept is shown as mounted on the main apparatus in picture (2.9b), an optical collimator equipped with fiber interface will drive the two beams up to vacuum "physics" system whereas a special designed mirror holder will be housed on the back side flange.
For the same physical target also other experimental implementations are possible. Considering that the linear polarized light can be written as $\vec{E}_{\uparrow} = 1\sqrt{2}\vec{E}_{\sigma^+} + i\vec{E}_{\sigma^-}$ and $\vec{E}_{\rightarrow} = 1\sqrt{2}\vec{E}_{\sigma^+} - i\vec{E}_{\sigma^-}$ it's possible to realize the same transition scheme with orthogonal linear polarized fields after the collimator and with a single $\lambda/4$ waveplate before the mirror. This further configuration it's equivalent from the physical point of view but it implies an useful power loss, details in [73].
For the magnetic field coils a mechanical setup has been designed in order to provide a bias field of ≈ 50 mG during the interferometric sequence. Because our particular requirements for micro–gravity operations, the magnetic bias field must be extended not only to the vertical tube for fountain path but also to the main chamber. For this purpose a setup with five coils 50 mm diameter along the *Raman* tube and other four winding the main chamber has been designed; around the chamber two coils with a diameter of 100 mm are positioned on top and two on the rear side, whereas other two coils, with diameter 221 mm, provide for the central section. The resulting field must account also for shielding system contribution and the relative internal compensation coils system, the final result has been calculated by the ZARM Group [138].
The beams collimator and the polarization preparation stage will be realized following an approach similar to the one adopted for probe beams collimators (sec. 2.7.1). Considering that such optical component will be mounted on the cross vacuum fitting outside the magnetic shield (pict. 2.2(b),(c)), this will relax most of the geometrical and layout constrains that holds for other optical components. A prototype for the retro-reflection mirror has been developed within many technical details.

2.6.2 *Raman* mirror

As we have seen the baseline for the project provides to address for tests in terrestrial environment a gradiometric configuration, allowing to neglect all environmental seismic vibrations effects that will propagate from *Raman* optics to field wavefronts. Such vibrations in a gravimetric implementation configure an additional phase noise source because they can not be distinguished from acceleration[3]. In a gradiometric setup simultaneous measurement on two different atomic sample clouds will remove all common mode vibrations effects.
On the other side, for an absolute gravity/acceleration measurement in seismic noisy environment many approaches have been followed. The most common one is to seismic isolate the retro–reflection mirror by a springs system and providing also an accelerometric readout. Such readout can be fed back to the lasers in order to correct for vibrations acting on the phase [61, 63]. Some recent experiences in this field have demonstrated that an employment of the mirror vibration readout for off–line data correction results in many cases as an higher performing method [71, 72].
Coming to our purpose all described approaches to the seismic noise question are not needed but of course is still fundamental to control the *Raman* beams verticality respect to the acceleration direction. For Earth based performances the verticality can be optimized calibrating the retro–reflection mirror position monitoring the acceleration signal maximization but it is also fundamental providing for a reference system for the periodic apparatus restoring. For such purpose the *SAI Raman* mirror will be equipped with an high-precision two axis tiltmeter mounted on the back facet and screwed on it, such device will provide for a tilt readout in two direction as a reference. A commercial *755-Series High Gain Miniature Tilt Sensor* model *-1129* from Applied Geomechanics has been chosen, cylindrical shaped has 20.5 mm height and 50.3 mm diameter as layout dimensions. The main nominal performances parameters can be summarized as follows

total range	± 0.9 *degree*
resolution	0.1 μrad
repeatability	1 μrad
linearity	1% half span, 7% full span
natural frequency	0.8 Hz
time constant	0.5 s

[3]Einstein's equivalence principle

A 3D-view for the *Raman* mirror prototype assembled with the tiltmeter is shown in picture (2.10). In order to ensure a long term mechanical stability and high movement precision the screwing system, as for collimators and some other optical components for this project, accounts for three pushing screws plus other three pulling screws concentric with pushing springs (custom brass made non magnetic micrometric screws form RADIAN DYES LASER company, thread $M4.15 \times 0.15$, 150 μm/turn). A specific technical draw with an explosion view is illustrated in picture (B.8) at page 214, screws details in picture (B.9).
The whole mirror system is designed to be fitted on the rear vacuum flange and the base presents a specific housing for the vacuum screws.

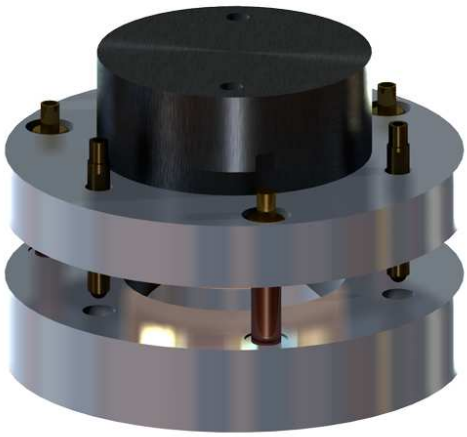

Figure 2.10: Prototype for *Raman* retro-reflection mirror, tiltmeter provided.

2.7 Detection

The sample population in two hyperfine atomic levels $F = 1$ and $F = 2$ of the ground state at the end of interferometric sequence has been already addressed in our discussion as the output channel for the matterwave dephasing measurement (see section (1.2.3), eqs. (1.82),(1.83) at page 60). Such phase contains all information about the impressed acceleration on atoms and about a wide range of other effects. The final detection scheme has been developed to acquire a number of atoms measurement either from atoms in $F = 1$ and from those in $F = 2$ even if the acquisition on just one state should in principle be enough.
For the Earth environment operation mode we can consider the following method based on the atomic fountain trajectory addressing. The falling atomic sample entering into the detection area (that for this setup coincides with the MOT chamber) encounters a first probe beam resonant with atoms in $F = 2$ and a first florescence signal is detected. After $F = 2$ atoms have been removed from the sample by means of a blow away technics the cloud encounters another beam probing the remaining atoms in $F = 1$ with a subsequent fluorescence detection as well (see picture (2.11)). For our setup the two different florescence signals will be recorded by two different photodiode as shown in the picture, moreover the whole detection performance will be enhanced with another lens photodiode system on the opposite window. At the first step the F=2 probe is realized by means of a beam slightly red detuned from $F = 2 \rightarrow F' = 3$ transition (≈ 800 kHz) (cooling transition, see pict. 1.19). In order to avoid losses trough dark states a cycling sequence is realized on the transition $|F = 2, m_F = 2\rangle \rightarrow |F' = 3, m_{F'} = 3\rangle$ by means of circular polarized light and of an additional magnetic field biasing. If for the considered transition the saturation intensity is $I_S = 1.67$ mW/cm^2 the estimated intensity for the beam will be of the order of ≈ 0.6 mW/cm^2

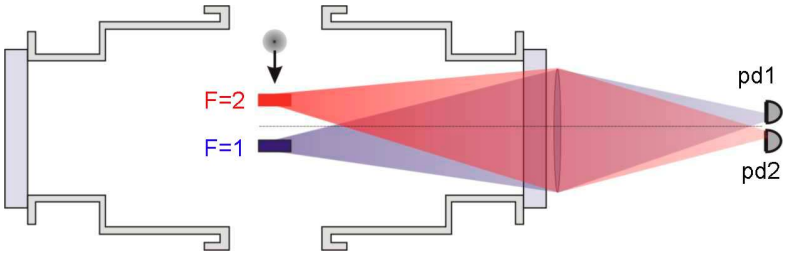

Figure 2.11: Probe beams implementation scheme, and fluorescence detection for $F = 1$ and $F = 2$ atomic states, (Earth environment).

For the $F = 1$ state detection, in the second position, a *repumping* beam with small intensity $\approx 200\ \mu W/cm^2$ is overlapped to the previous one, this way atoms in $F = 1$ are pumped to $F = 2$ via the transition $F = 1 \rightarrow F' = 2$ followed by a spontaneous emission $F' = 2 \rightarrow F = 2$, once atoms decay into $F = 2$ they can be considered as being in a dark states for *repumping* field. After the *repumping* process the detection sequence can go on on $F = 2$ states as in the previous case. Both the measurement stages are performed in a spectroscopic configuration with beams retro–reflection on a specific mirror. The blow away on the first stage, after the $F = 2$ detection, is realized creating a shadowed section on the lower laser beam part by means of retro–reflection shadowing. The whole probing implementation can be clarified from the scheme illustrated in picture (2.12).
The described method and realization can be modified for micro–gravity conditions environment: in this case will be needed to perform the atomic probing for the two states in time sequence at the same position.

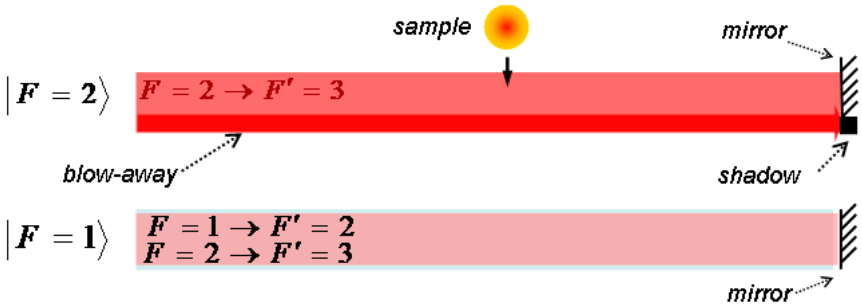

Figure 2.12: Probe beams implementation for $F = 2$ and $F = 1$ states detection (Earth environment). First stage beam addresses $F = 2 \rightarrow F' = 3$ transition for $F = 2$ detection, a blow–away setup follows. At the second stage a *repumping* beam ($F = 1 \rightarrow F' = 2$ transition) is overlapped to the previous laser field.

2.7.1 Optical realization

An integrated optics system dedicated to probe beams will be mounted on a 21.5 mm diameter window of the equatorial plane of the main chamber (*2D–MOT* side) and the retro–reflection mirror will be mounted on the opposite one (see sec. (2.3.1) and table 2.1). The two detection optics systems with photodiodes will be placed on the same plane on windows of 30 mm diameter

in a configuration at 90 degree respect to the probing direction (see picture (2.13)). The beam shaping for the probes is realized by two slits of 4 mm × 10 mm with 4 mm of distance each other

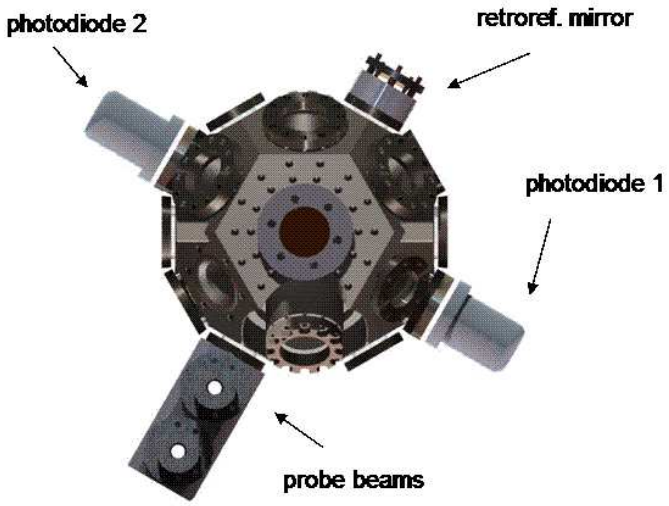

Figure 2.13: Picture of the complete detection optical system mounted on the *Space Atom Interferometer* apparatus. Photodiodes system at 90 degree respect to the probe beams direction.

The principle for detection scheme described so far is derived from the application of spectroscopic technics and it is quite common for atom interferometers: the challenge in our case is to develop a scheme compatible with the transportable sensor and accounting for all layout constrains. First of all beams and all optical components must be integrated into the capsule and into the magnetic shield mantle. For this purpose was necessary to develop custom made dedicated optics either for probe beams and for detection, a detailed description follows below.
In order to overlap and to shape the detection beams there was not any commercial device compatible with the interferometer dimensions constrains: the design of a new system has been needed. In Picture (2.14) is shown the found solution for this task (single components involved are identified by numerical labels). The basic principle is to overlap the two beams with a waveplate and polarizing beam splitter system. The whole apparatus is designed and shaped to be fitted directly on the vacuum system flanges relative to windows of diameter 21 mm; the entire flange together with vacuum screws will

be hidden in a dedicate shell. The system will be holden by means of a configuration of four screws in a cross vertical–horizontal disposition: two of them will be screwed and housed trough two dedicated fitting on the upper and rear body sides, whereas the other two will pass trough the device main body and will be screwed to the vacuum chamber passing trough two flange free vacuum screwing holes.

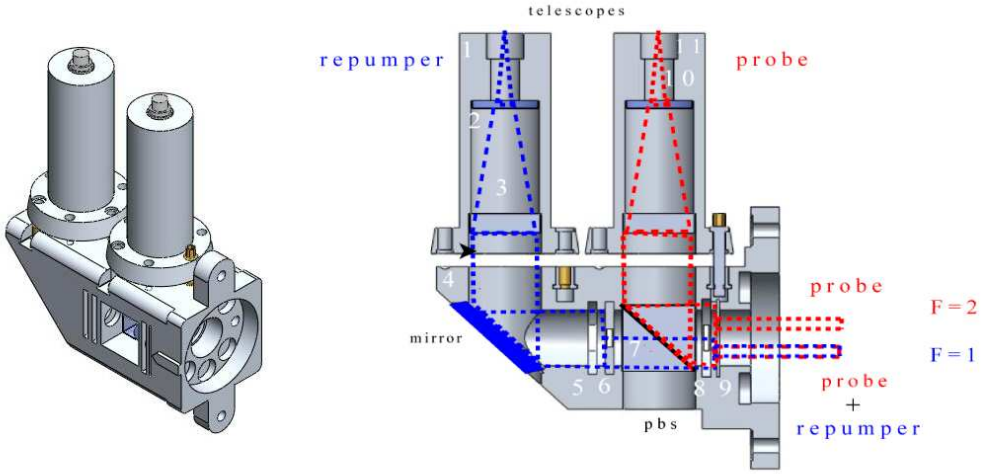

Figure 2.14: Optical System for detection beams designed for *SAI* apparatus, on the right side a vertical cut view is shown. Involved components are fiber adaptor, reflecting mirror, waveplates, Polarizing beam splitter and slits.

The system is designed in a modular setup in order to allow to account for as much as possible degrees of freedom, all components are removable an replaceable. Two telescopes have the task of collimate and enlarge the beams diameter up to one inch. Each beam comes from optical fibers and the telescope design is compatible with SCHÄFTER–KIRCHHOFF fiber adaptor model $10AF - 4 - FC$.
The *repumping* beam comes from the first telescope and is reflected from a golden plated elliptical mirror (EDMUND OPTICS)(4). Such beam is polarized by a waveplate (position 5) thus the upper part is cut away from a first removable slit (position 6), then it passes trough a polarizing beam splitter in order to be overlapped with the other probe beam. The the latter beam follows a similar path: after a polarization rotation stage is deviated at 90° from the beamsplitter and overlapped with the *repumper* in the bottom at $F = 1$ position height.

The Polarizing beamsplitter is a commercial 30 mm × 30 mm × 30 mm× from CVI to be glued inside on the edges. The final beam cuts shaping is realized for both beams in position (9) by two slits that are inserted as coins into the main body and holden inside, this feature allows a very easy replacement: the user can change the beam shape just replacing the last slit. A similar modular technics holds for waveplates.
Both telescopes are tiltable with a complex system of three $M4$ micrometric pushing screws and three $M4$ micrometric pulling ones with concentric pushing springs, this push–pull technics ensure a good stability and a fine tuning. Micrometric screws realized by Radian Dye are all brass made and customized for the specific task.
The optical principle for telescopes is very simple: some details are illustrated in picture (2.15). Again we find a modular design this system is based on free rings and threaded ones holding lenses.

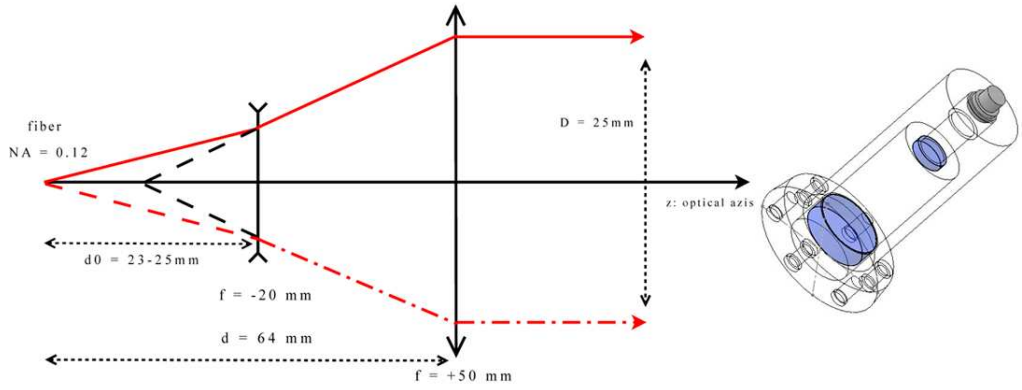

Figure 2.15: Spectroscopy demodulated signal from spectroscopy

The fiber adaptor is fitted on the upper part, it is holden by a ring that is screwed on the cylindric body and pushes on an additional rubber ring (the same system used for MOT collimators (see (2.4.2)). A typical fiber numerical aperture is $NA = 0.12$ thus to enlarge the beam in a short distance a two lenses system was needed. The first one is a plano concave lens with $f = -20$ mm and a diameter of 12.5 mm (CVI $LPK - 12.5 - 10.4 - C$), the second one is a plano convex lens with $f = 50$ mm and diameter 25.4 mm (Thorlabs $LA1131 - B$)[78, 79]. A fine collimation can be performed by adding and removing some additional thickness rings between lenses and ring adaptors.
The retro-reflection mirror needed for the spectroscopic implementation (see

picture 2.13) is not reported in details there: it follows similar setup and principle holding for the *Raman* retro–reflection mirror but is simplified from the absence of the tiltemeter integration (section 2.6.2).

For the fluorescence detection the typical method provides to collect the emitted light on a photodiode with the help of a single lens with a diameter as much as large is possible the way to consider the wider collection solid angle. For this point of view some trade off has been taken accounting for the sensor overall dimensions and for the view windows diameter. The photodiode module is designed to be fitted on the flanges relative to 30 mm windows of vacuum system with the same method that holds for other components, in particular no additional screw housings are considered but only four free screws hole from the flange will be used in order to hold the component to the main chamber.

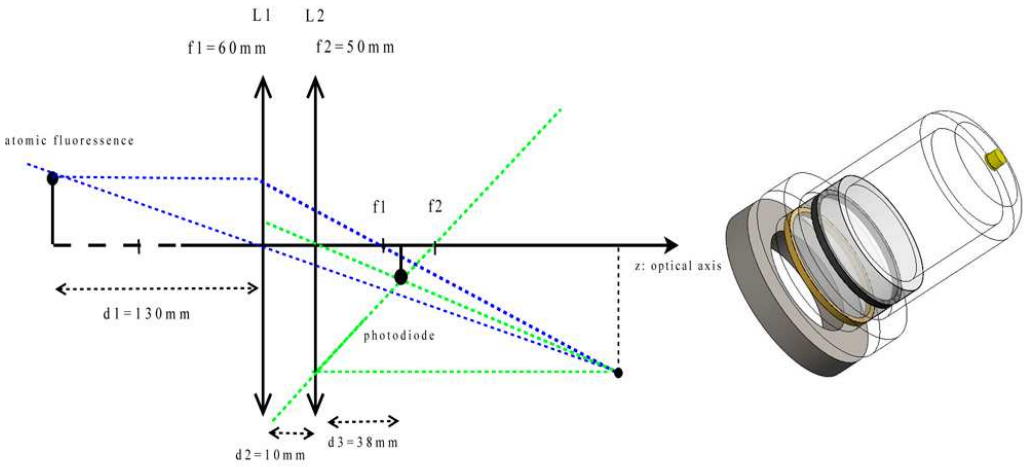

Figure 2.16: Optical scheme for fluorescence light collection on photodiode in detection (not in scale).

The distance between the atomic cloud sample to be detected and the external side of the chamber has been estimated to be roughly 130 mm. From the other hand because of the very small distance from the vacuum system to the external magnetic shielding mantle a preferable configuration with a single fluorescence collection lens was not possible to be implemented. Moreover a vertical optical path lengthening configuration realized by means of a 45° mirror (as we did for beam collimators) is not advisable fluorescence detection. A double lenses design was inevitable to shortening the imaging length and improving the module compactness. The designed optical system

is shown in picture (2.16), the firs lens is a plano convex with focal length $f = 60$ mm and diameter $D = 38.1$ mm (CVI $PLCX - 38.1 - 30.9 - C - 780$) whereas the second one is a biconvex lens with focal length $f = 50$ mm and diameter $D = 38$ mm. The cloud fluorescence image will be formed at a distance of 38 mm from the second lens where the photodiode is placed, a spacing ring system similar to the one for the telescopes will allow in operative conditions to fine tuning the focusing on it. As discussed before the system is designed to collect the fluorescence signals from $F = 1$ and $F = 2$ atoms on both sides of apparatus by means of two photodiodes on each side (see pictures (2.11) and (2.13)). Remembering that the detection beams are shaped from two quadrangular slits of 4 mm $\times$ 10 mm with a distance edge to edge of 4 mm, the designed detection system for fluorescence will project the two imagines to be detected with roughly 1 mm of diameter and a distance of roughly 2.5 mm each other, of course this is a very critical situation because of the risk of possible cross talks between the two photodiodes. In order to allow a fine relative photodiodes positioning a bodies sliding system has been designed for them. On the other side the choice to implement a single photodiode configuration for each side with active area multi–fold commercial devices is still open. This last choice allows to acquire two different signals from two very close active areas (relative distance < 1 mm), to avoid cross talks effects a dark separation segment can be added (≈ 2 mm diameter) to mark the separation. The designed photodiodes for the first case is a ceramic body HAMAMATZU $S1087$ and for the second one ceramic body for fold active $S2387$.

Chapter 3

Laser sources

The project we are talking about in this thesis is also strongly characterized by the introduction of a new generation of laser sources oriented to transportable atomic physics devices. We are dealing with External Cavity Diode Lasers with an interference filter as wavelength selection element. In this chapter we illustrate the specific characteristics and also introduce a comparison with the *Littrow* configuration as the most common setup in atomic physics applications. Some characterizations measurements relative to our specific setup follow.

3.1 The External Cavity Diode Laser

We can start to consider a laser source in *external optical cavity* configuration as composed by two elements for light *auto-injection* and *wavelength selection*. The usual technic in our research field utilizes some kind of commercial laser diode chip inserted directly into the *external cavity*. The active medium spatial extension already represents an intrinsic optical cavity; a cavity just made from the chip components has a length of few hundred microns and is characterized by a low finesse.
The External Cavity setup guarantees an additional laser optical feedback and moreover configures an additional wavelength selection element. From another point of view the extra auto injection of the laser field back to the active medium provides all proper benefits on linewidth characteristics derived from a longer cavity setups (see Schawlow–Townes formula (3.18) and Linewidth theory in sect.(3.2)).
The most common setup for external cavity involved in atomic physics conventional experiments is the *Littrow* configuration in which the collimated beam is sent on a diffraction grating (*Grating External Cavity Laser*, GECL)

aligned the way to send back the first diffraction order "1" to the chip, whereas the " 0" order, from the opposite side, is sent to the output. The grating is introduced for its wavelength selection propriety and it works also as *auto–injection* element.
Several methods are possible to reach an external cavity configuration; we consider one proposed a few years ago, realized by using a partially reflecting mirror as outcoupler and an *Interference Filter*, mounted on the beam path inside the cavity, for *wavelength selection* (*Filter External Cavity Laser*, FECL). A *cat's eye* optical configuration, realized for the feedback–outcoupling stage, is the main ingredient working to guarantee an intrinsic passive stability to such laser sources. The complete setup of the external cavity is simply sketched into picture (3.1): it can be be summarized by a sequence of few steps. The beam coming from diode laser source is collimated by a first lens and travels into the cavity passing through the filter, after this path reaches another lens that focus it on a semi-reflecting mirror as outcoupler and feedback element. The fraction of the beam coming out from there is collimated again by a third lens to the output. The beam focalization on the outcoupler and the following collimation of the output proper realizes the so called *cat's eye* configuration.

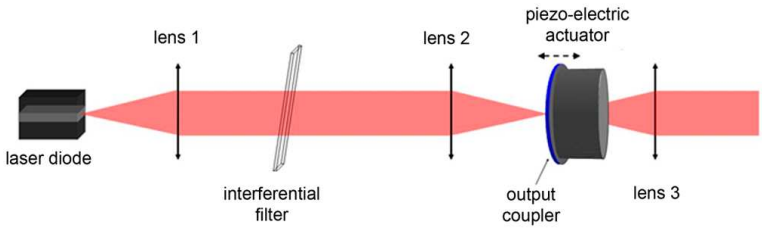

Figure 3.1: Scheme for External Cavity Diode Laser in *Cat's Eye* configuration [99].

3.1.1 *Grating External Cavity Laser* Vs *Filter External Cavity Laser*

The most important concept in which we are going to fucus on, as fundamental for our setup, is the separation between optical feedback element and *wavelength selection*: such feature represents configures the possibility to focus the beam on the mirror output mirror without loosing in wavelength selection performance.
We report here as starting point some characterization results from Lemonde

et al. [99] and from P. Zorabedian and W.R. Trurna Jr. [98]; from such papers we can widen and stress a comparison between the grating (GECL) and the *filter cavity* configurations (FECL). Moreover such comparison could be a good way to emphasize the importance of laser setup selection in agreement with the features of an apparatus such as a transportable sensor and to easily motivate the *filter cavity* choice. The differences between the two reported papers implementations consist essentially into the filter characteristic: for the last paper setup [98] the filter consist in a commercial single cavity with passband of 2 nm and a peak transmission of 70% whereas for the first paper setup the [98] filter is custom made with special coating layers working with a peak transmission of 90% and a passband of 0.3 nm: the principle is the same. The new generation of narrow band filters is the same involved in our transportable system project.

For a ***Littrow*** mounted grating the *wavelength selection* follows from the *Bragg*'s diffraction equation that holds the wavelength λ in a relation between the incidence angle θ and grating line spacing d.

$$\lambda = 2d\ sin\ \theta \tag{3.1}$$

For a *Filter External Cavity Laser*, because the filter works on beam internal multi–reflection on dielectric coating layers, we can threat it as an Ethalon with refraction index n_{eff} (typical $n_{eff} = 2$); the wavelength selection equation can be derived from the Fabry Perot model. If the beam incidence angle on the filter is θ and λ_{max} the normal incidence wavelength, we have:

$$\lambda = \lambda_{max}\sqrt{1 + \frac{sin^2\ \theta}{n_{eff}^2}} \tag{3.2}$$

If we choose for proper parameters some typical values it' s possible to compare the two wavelength sensitivity from the two cases above (see the tabular)

wavelength sensitivities	
GECL	FECL
$\left(\frac{d\lambda}{d\theta}\right)_{grt} \approx -1.4nm/mrad$	$\left(\frac{d\lambda}{d\theta}\right)_{flt} \approx -23pm/mrad$

That results into a ratio between the two sensitivity around 60. Let's underline that, from another point of view for one *mrad* of tuning angle a grating laser changes its wavelength of 1.4 nm whereas a filter laser changes

of 23 pm. So at this level we have found a first result as an intrinsic enhancement in passive stability versus components tilt misalignment; as we are going also to show such a gain is not at tunability expense.
To treat the characteristic optical feedback sensitivity we start with the calculation of the feedback function as the square of the scalar product of outgoing electrical fields times the incoming one (eq. 3.3). This calculation stands from the consideration that multiorder gaussian beams as solutions of Maxwell equation in paraxial approximation are a complete basis for a generic beam into the cavity. Because such basis is composed of orthogonal vectors, in our calculation for a generic beam, only the first order as progressive and regressive propagating wave can survive. In principle the calculation must be performed between fields at $z = 0$, that means at outgoing surface of laser chip. On the other hand, in our situation, as first we can separate a generic component misalignment into two independent movements such as a tilt or a position shift and, as second, we can consider any component tilt or translation misalignment to being manifested at the cavity last element. So any possible degree of freedom is represented on the outcoupler or on the grating: in this picture the feedback calculation can be performed on the output cavity element. If E_{do} is the outcoming electric field and E_{dr} is the reflected one, whereas $1/R$ is the normalization factor with R a the reflectivity of the outcoupler, we can define the feedback parameter as follows:

$$F = \frac{1}{R}\left| \int\int \; E^*_{do} E_{dr} \; dxdy \right|^2 \tag{3.3}$$

Let's suppose the output element to be rotated by an angle α, the feedback function assumes the form:

$$F = e^{-\left(\frac{\pi w_0}{\lambda}\;\alpha\right)^2} = e^{-\left(\frac{\alpha}{\theta_d}\right)^2} \tag{3.4}$$

where w_0 is the beam waist and θ_d is the gaussian beam divergence angle. We find that angular misalignment can be considered negligible from the optical feedback point of view if the misalignment angle projects the reflected beam inside the gaussian divergence cone (see picture 3.2a at page 122) that means if $\alpha \ll \theta_d$. The angular misalignment sensitivity in the limit where $\alpha \to 0$ becomes:

$$\frac{\partial^2 F}{\partial \alpha^2} = -\frac{2\pi^2 w_0}{\lambda^2} \tag{3.5}$$

This sensitivity is determined only by the beam waist and it is proportional to it: thus the little value of the waist suppresses such sensitivity.

Suppose the reflecting element to be shifted into the direction of the optical axis of a quantity δ at point $z = z_{out}$. If the curvature radius for a gaussian beam is given $r(z) = z[1+(\frac{z_R}{z})^2])$ whereas the waist is $w(z) = w_0\sqrt{1+(\frac{z_R}{z})^2})$ ($z_R = \pi w_0^2/\lambda$), holding the origin at $z = z_{out}$, the reflected beam must account a double path of 2δ (see picture 3.2b) and we find for its parameters $r(\delta) = z[1 + (\frac{z_R}{2\delta})^2])$ and $w(\delta) = w_0\sqrt{1+(\frac{z_R}{2\delta})^2})$. Substituting this results into equation (3.4) for the feedback we find:

$$\begin{aligned} F &= \left(1+\frac{\delta^2}{z_R}\right)^{-1} \\ &= \left(1+\frac{\lambda^2}{\pi^2 w_0^2}\delta^2\right)^{-1} \end{aligned} \tag{3.6}$$

and for the sensitivity in the limit where $\delta \to 0$:

$$\frac{\partial^2 F}{\partial \delta^2} = -\frac{2\lambda^2}{\pi^2 w_0^4} \tag{3.7}$$

From this equation we find that the sensitivity to translational misalignment depends from the beam waist as $\sim 1/w_0^4$: thus for a focused beam the system is strongly sensitive to this degree of freedom.
We must underline that equations found for the optical feedback (3.4), (3.6), and the relative sensitivity relations (3.5) (3.7) do not depend from which external cavity configuration has been chosen, they holds both for *Littrow* and for the *Filter* configuration.
So far we have focused only on the optical feedback point of view; now we can give a brief look to the wavelength selection. For the *Filter* configuration case the wavelength selection depends only on the filter constructive features and there is no direct dependence on the setup that determines the performances quality on this side: for the new generation filter we have a 0.3 nm transmission bandwidth. In the framework of the analogy between the *filter* and *grating* configurations it's necessary to remind that for a grating the *resolving power* is given by:

$$R = \frac{\lambda}{\Delta\lambda} = mN \tag{3.8}$$

Where m is the diffraction order and N represents the number of grating lines shone by the beam light. In other words the wavelength selection for the grating depends on the beam waist and on the grating angle. For the *Littrow* configuration the waist value must be chosen as a compromise between misalignment sensitivity and wavelength selection. In this sense we can say

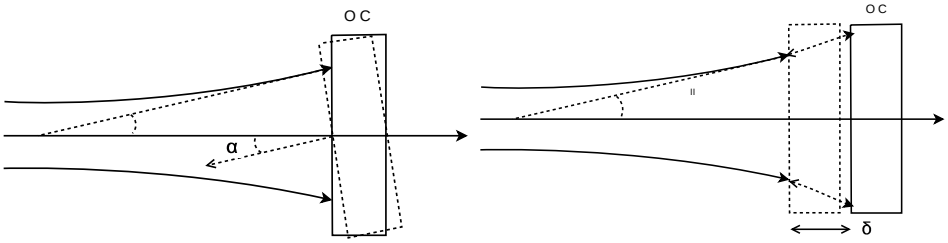

(a) angular tilt (b) longitudinal shift

Figure 3.2: ECL: possible misalignment for the output coupler mirror.

that for a *Filter External Cavity Laser* totaly removes such kind of trade off: thus it's possible to focus the beam on the outcoupling mirror, implementing a *cat's eye* configuration, without loosing wavelength selection performance and optimizing the feedback stability versus mechanical misalignments.
In order to provide a quantitative comparison between the two configurations stability we can evaluate for both what angle or shift misalignment corresponds to a 10% of feedback reduction. If we choose for laser parameters: 1 mm of waist for *Littrow* configuration and 1 μm for *EFCL*.

Feedback reduction 10%	
grating ECL ($w_0 = 1$ mm)	filter ECL ($w_0 = 1$ μm)
$\alpha = 100$ μrad	$\alpha = 9$ mrad
or	
$\delta = 1$ m	$\delta = 0,1$ mm

The sensitivity to angular misalignment is strongly suppressed for the *filter* configuration whereas this setup is very critical to translational misalignment; for our laser system characteristic 0.1 mm is well into the range of the mechanical tolerance.
As a last comparison between two configurations we report a tunability comparative measurement from P. Zorabedian and W.R. Trurna paper [98]. A tuning curve is plotted for current threshold variation as wavelength changing (fig. 3.3). In their setup the filter was at 70% transmission so the relative threshold curve is shifted. From the plot a comparable tunability results.

3.1.2 Laser Source Setup and Characterization

The *External Cavity Diode Lasers* involved in our Project are realized in a modular setup that allow to separate the different fundamental tasks in five principal subcomponents [107]: Laser diode mount, collimator, interference

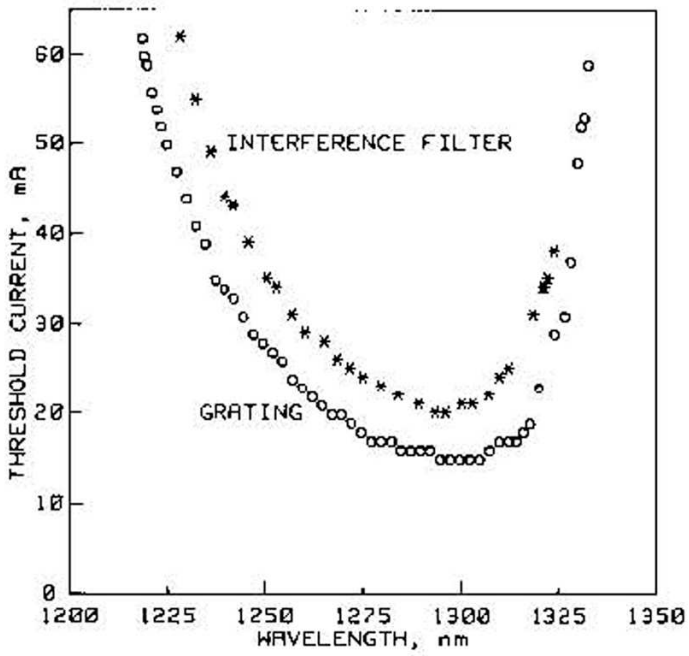

Figure 3.3: External Cavity tuning curves (form [98]).

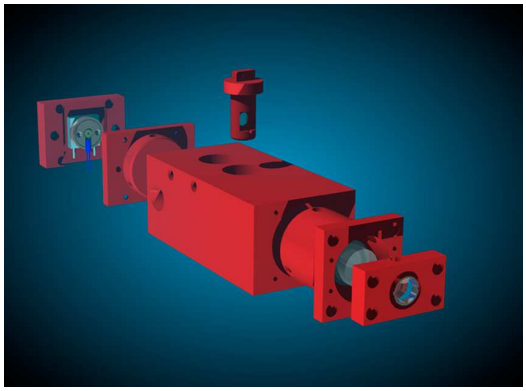

Figure 3.4: External Cavity Diode Laser CAD explosion scheme [107]

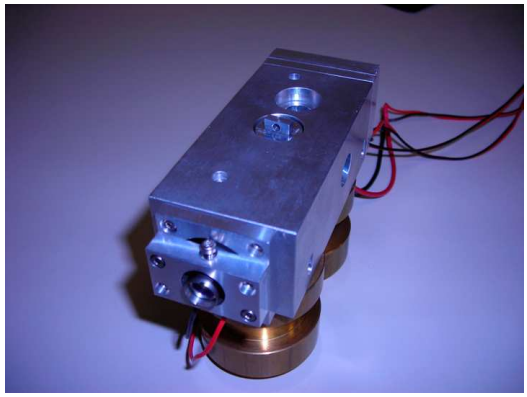

Figure 3.5: Picture For the *ECDL* for the transportable apparatus

filter, beam outcoupler plus *Cat's Eye* optical setup (see fig. 3.4). As laser source we employ a laser diode in a socket of 5.6 mm (Sharp GH0781JA2C) with a typical output wavelength of 784 nm and a maximum output power of 120 mW for a typical operating current of 160 mA. The laser–chip is holden into two copper plates housing shaped for this specific purpose (see draw in

picture (B.1) at page 208), a 10 $k\Omega$ thermistor is glued by SYLVER ARTIC thermal glue on the housing front facet. The rear facet, on the other side, is thermal–glued to a Thermoelectric Cooling Element (TEC) (THORLABS TEC1.4–6). The laser–diode temperature stabilization feedback implementation is realized by the reading out the thermistor resistance value and by acting on the thermoelectric element current by means of custom made electronics. The module for collimation houses a $f = 3.1$ mm mounted aspheric collimating lens ($C330TM - B$) from THORLABS; an external thread allows to adjust the collimation acting on the lens position in the z axial beam direction. The $x - y$ beam optimization can be performed by the relative positioning of the laser holder to the lens holder. The output stage is realized by means of a 30% partially reflecting cylindric mirror, for 0° of incidence beam, as outcoupler (custom made from LASER COMPONENTS); such component is mounted on on a tubular ring-shaped piezoelectric element for cavity length servo control (PIEZOMECHANIK Ringaktuator HPSt). The *Cat's Eye* optical setup is realized by means a of first aspheric lens $f = 18.4$ mm focusing on the mirror and of a second one $f = 11$ mm collimating the beam output, before and after the mirror (see picture (3.1)) (lenses THORLABS C280TM–B, C220TM–B).
These described removable modules plus the interference filter holder are mounted on the main body that guarantee the whole alignment. System mechanical setup original development is due to M.Shmidt [107] whereas for the basic Filter External Cavity basic implementation we refer to [99].
A further thermal stabilization feedback can be implemented for the whole external cavity: the main body houses another thermistor and is mounted on the two further TEC elements working as a single one (PELTRON PKE 72 A 0021). The complete cavity setup results in a total length of $L = 80$ mm that drives to a rough evaluation for the free spectral range of

$$\Delta\nu \;=\; \frac{c}{2L} \;\approx\; 1.9\; GHz \tag{3.9}$$

The principal parameters for the operative lasing conditions control can be summarized as follows: laser diode current, chip temperature and cavity length control as piezo actuator voltage. The external cavity thermal control in this implementation don't result into a dominant contribution to the wavelength tuning but in particular conditions it can play a determinant role in terms of long time stability improvement. In our experience, relative to this specific realization, the effect of the external cavity temperature control results just in a little but not vanishing support to the external cavity length changes control. On the other hand, its great contribution is to configure the main cavity body as a stable temperature sink for the laser diode mount

(see picture 3.4).
As will be clarified into the incoming sections for feedback loops implementation *piezo* actuator will be utilized for low frequency bandwidth stabilization (< 10 kHz); whereas for faster controls two current channels can be considered as a direct and as an indirect current modulation (HF and IF).
The role of the filter as we have seen before is the wavelength selection, such tuning can be performed preliminary simply rotating the filter holder the way to change the incidence angle of the beam. Unlike the others external cavities lasers configurations (see (3.1.1)) no active control is applied on it.
Filter operation principle can be summarized by the sketch in picture (3.6), the blue line represents the wide range laser chip gain curve, possible lasers modes are represented by dashed curve whereas the red one represents the filter transmission curve. If the full width at half of maximum of the filter curve is 0.3 nm, that is twice the mode spacing of a typical laser diode: just a single mode can be transmitted at once. For a set angle of the filter, changing the laser current will move the modes through the filter transmission curve so that modes are going to be transmitted as a sequence. What we see at the output as final result of this model is a mode jump.

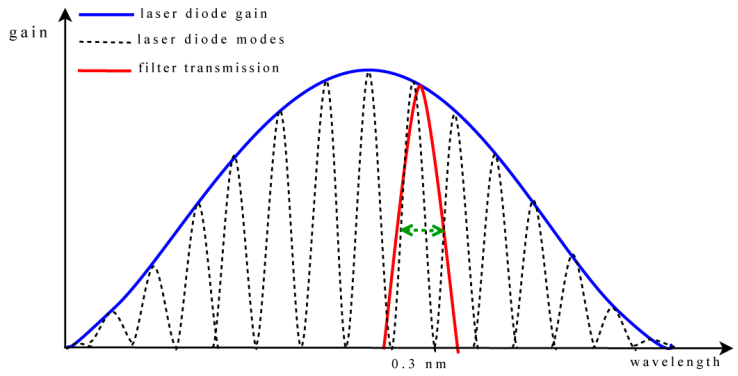

Figure 3.6: Sketch for laser mode selection from the filter.

The main operative conditions for this new laser devices have been characterized from us before the integration into complete optical systems.
The diode typical measured threshold current is ≈ 34 mW whereas it drops as consequence of coupling to the external cavity at ≈ 31 mA, such values can have small changes from a laser diode to another but, however, according with our experience, they can be used as reference values for future assembling in order to check the right coupling. The total power output is roughly of 20 mW at 75 mA of operating current (output coupler 30% R).
From the acquisition of the beat note with an ultra–stable laser locked to

an atomic transition, was possible to define the frequency to piezo voltage response and the frequency to laser current response. In picture (3.7a) the response to piezo actuator is shown: modes jumps of 1.5 GHz are found and the same value is found for the mode–hop free range. From a linear fit evaluation the frequency–voltage response is 277 ± 1 MHz V^{-1} before the first mode jump (applied voltage $0 \div 6$ V) and 306 ± 1 MHz V^{-1} after it (applied voltage $6 \div 12$ V); the difference between the slopes declares some deviation from the linearity of the piezo in different voltages ranges. The mode jump found for current variation is of 1.6 GHz whereas the mode–hop free range is 150 MHz (3.7b). In this case the current–frequency response results in small changes in different current operative ranges (i.e. : 180 ± 10 MHz mA^{-1} for $60.3 \div 61$ mA, 210 ± 10 MHz mA^{-1} for $61.0 \div 61.9$ mA and 180 ± 10 MHz mA^{-1} for $62.0 \div 62.7$ mA); thus for our purpose we can assume a typical value of ≈ 200 MHz mA^{-1}. For the implementation of servo loops involving such sources but also for the selection of operative condition with the best performances it's important to consider the possibility of small changes in frequency response for different modes.
A *Fabry-Perot* cavity with a *FSR* of 435 MHz was an useful tool for further frequency response characterizations. From the count of the number of the *FP* modes between two lasers mode jumps the precedent evaluation for the piezo–frequency range and current range were roughly confirmed. The possible extended mode–hop free range was measured by application of two synchronized combined voltage and current ramp on the two different control channels (measured ≈ 9 GHz).
The frequency response was moreover characterized by the acquisition of the laser's transfer function. For the piezo channel a mechanical resonance was found around 9 kHz, thus this will be the upper limit for the related servo loop bandwidth. On the other side the frequency–current transfer function has been acquired by locking the piezo laser channel with a low servo bandwidth (100 Hz) to the slope of a *Fabry–Perot* peak and by directly modulating the current in a frequency range from 10 kHz up to 1500 kHz. With this method a narrow resonance was found at 30 kHz and a roll–off from 80 kHz.

Some information about the thermal drift effects on the frequency output were obtained by the observation of the beat note between a free–running laser and a stable reference laser (picture 3.8); in particular this section was focused on the contribution of the cavity thermalization. We have found a typical frequency drift of 7.5 MHz/min for a laser working without cavity thermalization, whereas for a thermalized cavity fluctuation were reduced of one order of magnitude (plot (b)). An equivalent result was found from the observation of a non thermalized cavity laser into an ultra–stable environment

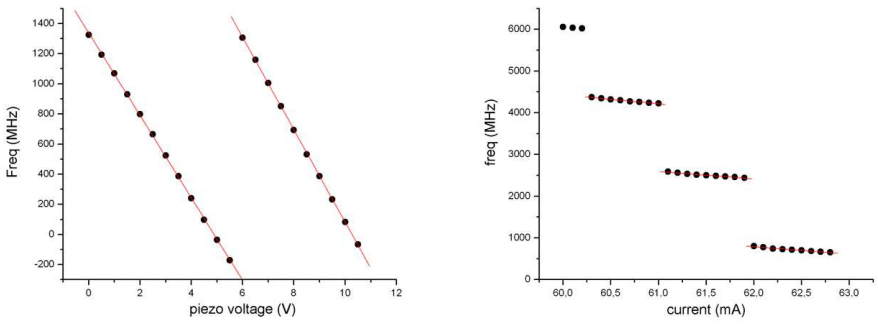

(a) piezo response (b) current response

Figure 3.7: External Cavity Laser Sources, (a) frequency-piezo voltage characteristic, (b) frequency-current characteristic.

($\Delta T = 0.1$ °C).

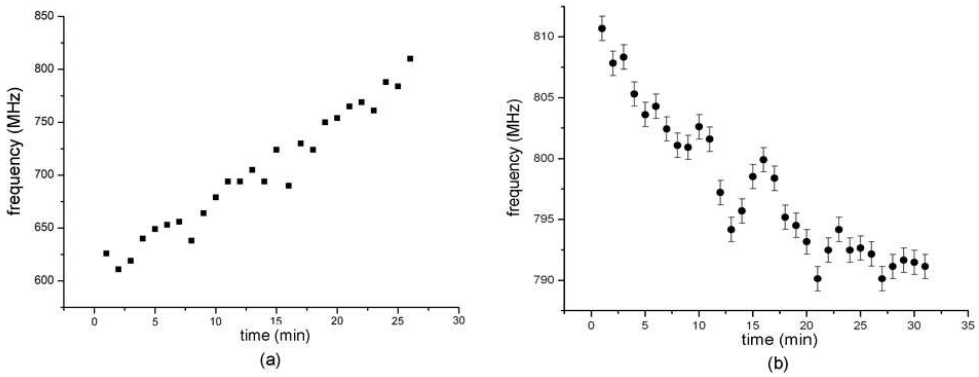

Figure 3.8: *ECL* frequency thermal drift monitoring as function of the time, a comparison between two operative conditions: with(b) and without (a) temperature control on the extended cavity.

3.2 About The Phase noise, Frequency noise and the theory of Linewidth of Semiconductor Lasers

The temporal and spatial coherence of lasers fields plays a fundamental role in a lot of experimental methods as in our case. The lasers oscillators spectrum is broadened by several random phenomena, in particular the emission line shape and width are related to phase and frequency noise. In this section we are going to introduce the spontaneous emission as random mechanism leading to the linewidth broadening (see Schawlow-Townes theory [82], [80]). Also we are going to focus on the semiconductor lasers particular case in agreement with Henry's theory as presented into the paper [83].

3.2.1 Spontaneous Emission and Phase Noise

A simple model can be useful to illustrate how the randomness of spontaneous emissions leads to a linewidth broadening effect. We can start with the representation of the electric output field (eq. 3.10) and, with the help of the picture (3.9), in a vectorial framework it is easy to sketch the effect of any single spontaneous emission event.

$$E(t) = E_0 e^{i\omega_0 t} e^{i\theta(t)} \tag{3.10}$$

Here ω_0 is the carrier frequency and $\theta(t)$ the instantaneous phase. The E_0 is the field amplitude we suppose to be slowly varying compared to ω_0.

Any spontaneous emission must to be considered as a totally random event and so it exhibits no correlation with the sequence of photons emitted as an effect of stimulated emission. For simplicity the chosen normalization for the electric field is: $|E|^2 = q = I$, so $\sqrt{q} = |E|$, where q is the number of photons. From geometrical considerations on the picture (3.9) the phase effect for a single spontaneous emission is given by:

$$\Delta\theta \simeq \frac{1}{\sqrt{q}} \sin\phi \tag{3.11}$$

Here we neglect the amplitude contribution of the spontaneous emission in comparison with the stimulated one, so that on many events average it is possible to write $\Delta I^{1/2} \sim 1$. Averaging over the time[1] we find: $\langle \Delta\theta \rangle = 0$ and

[1] here ergodic and stationary hypothesis can be applied so that the time average is equivalent to spatial averaging on the configurations space

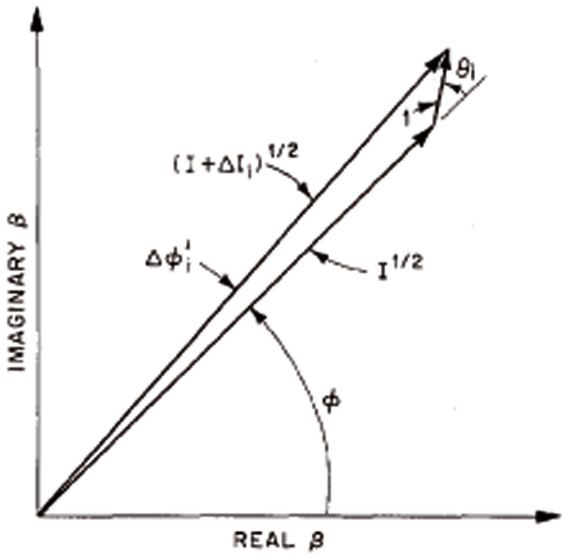

Figure 3.9: Instantaneous Phase and Intensity change caused by a single spontaneous emission event [83].

$\langle \Delta\theta^2 \rangle = \frac{1}{q}\langle sin^2\phi \rangle = \frac{1}{2q}$, multiplying for the rate of spontaneous emission, we find as time evolution:

$$\langle \Delta\theta^2 \rangle = \sigma^2_{\Delta\theta} = \frac{1}{2q}\frac{n_{sp}}{\tau_c}|t| \tag{3.12}$$

where n_{sp} are the number of atoms that decay for spontaneous emission in time unit and τ_c is the time decay for the laser cavity.
Calculating the autocorrelation function for the electric field we have:

$$\begin{aligned} g_E(\tau) &\equiv \langle E^*(t)E(t+\tau)\rangle \\ &= |E|^2 e^{-i\omega\tau}\langle e^{i[\theta(t+\tau)-\theta(t)]}\rangle \\ &= |E|^2 e^{-i\omega\tau}\langle e^{i\Delta\theta(\tau)}\rangle \qquad (3.13) \\ &= |E|^2 e^{-i\omega\tau} e^{-\frac{1}{2}<\Delta\theta^2>} \qquad (3.14) \end{aligned}$$

Where it's possible to pass from the equation (3.13) to equation (3.14) because we can suppose that $\Delta\theta$ is a gussian variable normally distributed with zero average [2]. Now it's possible to apply the Wiener-Khintchine theorem

[2] if $x \in \mathsf{N}(0,\sigma^2) \quad \Rrightarrow \quad \langle e^{ix}\rangle = e^{-\frac{\sigma^2}{2}}$

that holds for the connection from power spectral density and autocorrelation function via *Fourier* transform link.

$$S_E(\omega) = \int_{-\infty}^{+\infty} g_E(\tau) \quad e^{i\omega\tau}\, d\tau \tag{3.15}$$

Substituting the (3.14) result into the (3.15) a Lorentian power Spectra is found as

$$S_E(\omega) = |E|^2 \frac{2}{T} \frac{1}{(\omega - \overline{\omega})^2 + (1/T)^2} \tag{3.16}$$

where

$$\Gamma = FWHM = \frac{2}{2\pi} 1/T = \frac{1}{4\pi} \frac{n_{sp}}{q} \frac{1}{\tau_c} \tag{3.17}$$

If we substitute the relations between laser output power and photons number $P_{out} = \hbar\omega \frac{q}{\tau_c}$ and the relation between cavity time decay and cavity frequency width $\Delta\nu_c = \frac{1}{2\pi\tau_c}$ the Shalow–Townes result is found, connecting the laser linewidth to spontaneous emission phenomenon. It's important to underline the quadratic dependence on the cavity frequency linewidth[3].

$$\Delta\nu_L = \left(\frac{N_2}{N_2 - N_1}\right) \frac{2\pi h\nu_L\ \Delta\nu_c^2}{P_{out}} \tag{3.18}$$

In the case of semiconductor laser in agreement with the Henry's theory [83] an additional line broadening must be accounted due to a coupling mechanism between intensity and phase changes in spontaneous emission. The enhanced linewidth is attributed to variation of the real part of the refractive index with the carrier density. The laser response to this carrier density variation is to restore its steady state; this results in a variation of the imaginary part of the refractive index $\Delta n''$. A variation of real part of refractive index $\Delta n'$ is also accompanied to these changes rising to additional phase fluctuation. If the "*alpha*" parameter is defined as $\alpha = \Delta n'/\Delta n''$ the linewidth for semiconductor lasers is given by:

$$\boxed{\Delta\nu_{DL} = \left(\frac{N_2}{N_2 - N_1}\right) \frac{2\pi h\nu_L\ \Delta\nu_c^2}{P_{out}} (1 + \alpha^2)} \tag{3.19}$$

Where α is a parameter ranging from 4 to 6.5.

[3]Here the so called *inversion factor* has been defined as $\frac{N_2}{N_2 - N_1}$, in this form it refers to a generic three level oscillator, for a semiconductor laser typically ranges into the values interval $1.5 \div 2.5$

3.2.2 Frequency Noise and Laser Linewidth

The treatment we are going to report below is useful to display the connection between phase noise and frequency noise and also their connection to the laser (oscillator) linewidth. Restarting from the expression of the electromagnetic field (3.10)

$$E(t) = E_0 e^{i\Phi(t)} = E_0 e^{i\omega_0 t} e^{i\theta(t)} \tag{3.20}$$

The field frequency is defined as instantaneous variation of the phase so that it holds:

$$\nu(t) \equiv \frac{1}{2\pi}\frac{d\Phi}{dt} = \nu_0 + \frac{1}{2\pi}\frac{d\theta}{dt} \tag{3.21}$$

In our picture, the last term represents the frequency noise $\delta\nu(t) = \dot{\theta}(t)/2\pi$. Phase noise power spectral density (PSD) can be defined starting from phase autocorrelation function (3.22)

$$g_\theta(\tau) \equiv \langle \theta(t+\tau)\theta(t) \rangle \tag{3.22}$$

$$S_\theta(\omega) = \lim_{T\to\infty} \frac{1}{2T} \int_{-T}^{+T} g_\theta(\tau) e^{i\omega\tau} d\tau \tag{3.23}$$

Because of the derivative relation between phase and frequency and of the *Fourier* integral connection between Power Spectral Density and autocorrelation function it is easy to derive the relation between frequency PSD and phase PSD

$$S_\nu(\nu) = \nu^2 S_\theta(\nu) \tag{3.24}$$

Where of course $\nu = \omega/2\pi$. Random processes that result in phase and frequency fluctuations can be expressed in a power-law for the power spectral density as sum of terms [49], [86]. Each term varies as an integer power of the frequency over a certain range and is totally specified in a log-log plot by a slope and an amplitude; this model results in the following formula:

$$S_\nu(\nu) = \sum_{\alpha=-2}^{+2} h_\alpha \nu^\alpha \tag{3.25}$$

The values $\alpha = 2$ and $\alpha = 1$ corresponds respectively to *white phase noise* and *flicker phase noise*, the values $\alpha = 0, -1, -2$ are related to *white,flicker* and *random walk frequency noise.*
Let's consider again the spectral distribution of electric field (PSD) $S_E(\omega)$,

directly related to the linewidth $\Delta\nu$, and also the equations (3.14),(3.22). If we explicit the phase distribution quadratic deviation it has:

$$\begin{aligned} \langle \Delta\theta^2 \rangle &= \langle [\theta(t+\tau) - \theta(t)]^2 \rangle \\ &= 2\langle \theta^2(t) \rangle - 2\langle \theta(t+\tau) - \theta(t) \rangle \\ &= 2[g_\theta(0) - g_\theta(\tau)] \end{aligned} \tag{3.26}$$

so that eq. (3.14) becomes:

$$g_E(\tau) = |E|^2 e^{-i\omega t} e^{-[g_\theta(0) - g_\theta(\tau)]} \tag{3.27}$$

If the phase autocorrelation is related to the relative *PSD* via inverse *Fourier* transform:

$$g_\theta(\tau) = \frac{1}{2\pi} \int_2^2 S_\theta(\omega)\ e^{-i\omega\tau}\ d\omega \tag{3.28}$$

$$g_\theta(0) = \frac{1}{2\pi} \int_2^2 S_\theta(\omega)\ \ d\omega \tag{3.29}$$

if we substitute the last two expressions found in (3.27), with the help of eq. (3.24) and of trigonometric conversion formulas it follows:

$$\begin{aligned} g_E(\tau) &= |E|^2 e^{-i\omega\tau} e^{\frac{1}{2\pi}\int_{-\infty}^{+\infty} S_\theta(\omega)(e^{-i\omega\tau}-1)\ d\omega} \\ &= |E|^2 e^{-i\omega\tau} exp\Big[-4\pi \int_{-\infty}^{+\infty} S_\nu(\omega) \frac{sin^2(\omega\tau/2)}{\omega^2}\ d\omega \Big] \end{aligned} \tag{3.30}$$

In general this integral exhibit no analytical solution except for some particular cases such as the *white frequency noise* or the result can be evaluated by means of some approximations as in the *flicker noise* case. These two sources are dominant for laser diodes.
For the *white frequency noise* that is strictly connected to the quantum mechanical nature of spontaneous emission we can assume:

$$S\nu(\nu) = S_w \quad \forall\ \nu \tag{3.31}$$

moreover considering that any physical noise modulation mechanism exhibit a finite bandwidth and that such bandwidth is related to finite correlation time $\bar{t} \sim 1/B$ of the specific noise process, the integral in eq. (3.30) becomes:

$$\int_{-\infty}^{+\infty} S_\nu(\omega) \frac{sin^2(\omega\tau/2)}{\omega^2}\ d\omega = S_w \int_0^B \frac{sin^2(\omega\tau/2)}{\omega^2}\ d\omega \tag{3.32}$$

for our purpose it can be interesting to evaluate the integral in presence of frequency cut–off and approximating the frequency power spectral density as a rectangular function:

$$S_\nu(\nu) = \begin{cases} S_w & \forall\ \nu \leq B \\ 0 & \forall\ \nu > B \end{cases} \tag{3.33}$$

- In the case of large bendwidth respect to noise *coherence time* $B \gg 1/\bar{t}$

$$\begin{aligned} S_w \int_0^B \frac{sin^2(\omega\tau/2)}{\omega^2}\, d\omega &= S_w \frac{t}{2} \int_0^{Bt/2} \frac{sin^2(\xi)}{\xi^2}\, d\xi \\ &\simeq S_w \frac{t}{2} \int_0^{+\infty} \frac{sin^2(\xi)}{\xi^2}\, d\xi \\ &= S_w \frac{t}{2} \frac{\pi}{2} \end{aligned} \tag{3.34}$$

$$\tag{3.35}$$

where $\xi = \frac{\omega t}{2}$. The last step follows by the application of a well known integral [4], this gives rise to a correlation function as:

$$g_E(t) = |E_0| e^{i\omega t} e^{-\pi^2 |t| S_w} \tag{3.36}$$

from the application of the Wiener–Khintchine theorem, we find a Lorentian shaped power spectral density as in eq. (3.16)

$$S_E(\omega) = |E_0| 2\pi^2 S_w \frac{1}{(\omega - \omega_0)^2 + (\pi^2 S_w)} \tag{3.37}$$

from there the important relation between the laser linewidth and the white frequency noise power spectral density follows:

$$\Delta\nu = \pi S_w \tag{3.38}$$

- In the case of short bandwidth respect to noise *coherence time* $B \leq 1/\bar{t}$ we can develop the function $sin^2(\xi)$ around the value $\xi = 0$ so that the eq. (3.32) becomes:

[4] $\int_0^{+\infty} \frac{sin^2(x)}{x^2}\, dx = \frac{\pi}{2}$

$$
\begin{aligned}
S_w \int_0^B \frac{sin^2(\omega\tau/2)}{\omega^2}\, d\omega &= S_w \frac{t}{2} \int_0^{Bt/2} \frac{sin^2(\xi)}{\xi^2}\, d\xi \\
&\simeq S_w \frac{t}{2} \int_0^{Bt/2} d\xi \\
&= S_w B \frac{t^2}{2} \qquad (3.39)
\end{aligned}
$$

(3.40)

now instead of the equation (3.36) for the autocorrelation function we find

$$g_E(t) = |E_0| e^{i\omega t} e^{-\frac{t^2}{2\sigma_t^2}} \qquad (3.41)$$

With a gaussian shape, where $1/2\sigma_t^2 = \pi S_w B$. If we apply as in previous case the Wiener–Khintchine we find gaussian shaped Power Spectral Density with $\sigma_\omega^2 = 2\pi S_w B$. The relation with the laser linewidth for low frequency noise is:

$$\Delta\nu = \sqrt{8 S_w B \ln 2} \qquad (3.42)$$

Now the laser linewidth is proportional to $\sqrt{S_w B}$ instead of to the *PSD* as for frequency *white noise*.

Flicker frequency noise is also present in laser diodes as in all electronic devices, sometime is considered belonging to the technical noise class. As usual approach in literature is expressed as:

$$S_\nu(\nu) = \frac{S_F^2}{\nu} \qquad (3.43)$$

In presence of this noise from the eq. (3.30) will rise to an infinite value for the variation of phase change, but the finite measurement time results in a low frequency cut–off ν_l. In this case the results for the linewidth contribution will drive to a time measurement dependent relation with the noise [88].

$$\Delta\nu = 2 S_F \sqrt{2 \ln 2 \ln(5\pi\nu_l \tilde{t}/2)} \qquad (3.44)$$

Laser sources linewidth experimental determination

As we have seen so far, because of many contribution results in the laser linewidth and part of them are bandwidth dependents, there is not an univocal way to determine laser linewidth as a definitive parameter; it is common to define a "*fast linewidth*" refering to the spectral frequency range where the white frequency noise dominates, thus it follows: $\Delta\nu_{fast} = \pi S_w$.
In order to provide a complete characterization of laser sources involved in our transportable device project we have proceeded to a fast laser linewidth measurement. It was performed by the acquisition of the spectral distribution of the beat note between two identical *External Cavity Filter Lasers* by means of *RF* spectrum analyzer; the two laser sources were phase locked each other by means of a low bandwidth feedback loop on the piezo channel ($BW \approx 100$ Hz). The result is shown in picture (3.10); the linewidth plot in in this specific situation can be considered as the convolution of the two shape contributions provided from the single lasers. At this level we can simplify assuming as upper limit a lorentian shape for the single laser fast linewidth leading to: $\Delta\nu_{fast} = \frac{1}{\sqrt{2}} \times FWHM \approx 200$ kHz.

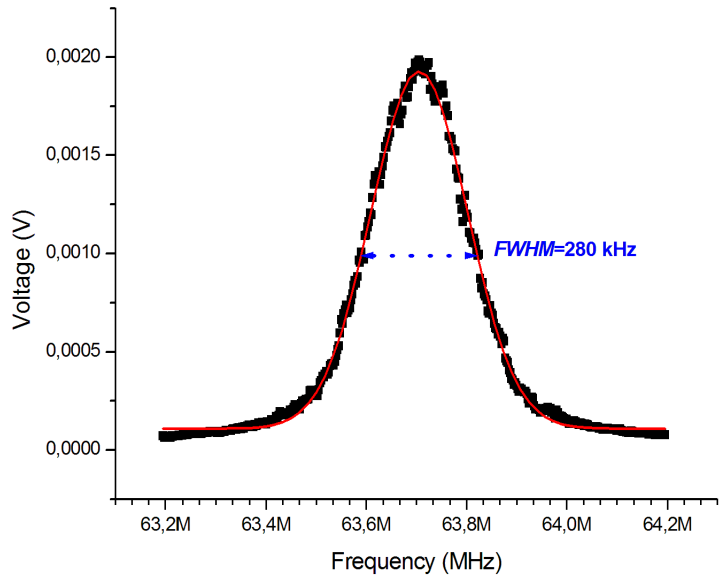

Figure 3.10: Free Running *External Cavity Laser* Linewidth

3.3 Optical Amplifier

We have seen that the average power output for each laser sources involved in our laser system setup ranges around 20 mW at operative current: this value is not enough for our propose such as atom cooling and interferometric manipulation. For this reason additional optical amplifier are needed, resulting in a *Master–Oscillator–Power–Amplifier* (*MOPA*) configuration. The amplifying element is a Tapered Amplifier EAGLEYARD (EYP–TPA–0780–01000–3006–CMT03–000) which gives an output power of 1 Watt at an operational current of approximately 1.8 A (maximum 2.5 A) once is injected by at least 20 mW from a master beam.

The seeding beam needs to be focused on the amplifier input facet in order to address the active medium; for this purpose we employ an aspherical lens ($f = 3.1$ mm). The amplifier output beam is intrinsically divergent and astigmatic, thus it is needed an optical system composed by an aspherical lens to collimate the beam on the vertical axis (THORLABS C390TM–B) as well as an additional cylindrical lens to collimate the beam on the horizontal axis (THORLABS LJ1810L2– B); the optical setup is illustrated in detail in picture (3.11). For easy temperature stabilization, both aspherical lenses are mounted together with a thermistor (THORLABS $TH10K$) and the amplifier itself on a large copper body that is connected to the laser module wall via a TEC element (PELTRON PKE 72A0021), see figure (3.12). The cylindrical lens is mounted separately. As shown in the picture, the optomechanical setup for such amplification sources is very compact and robust; it

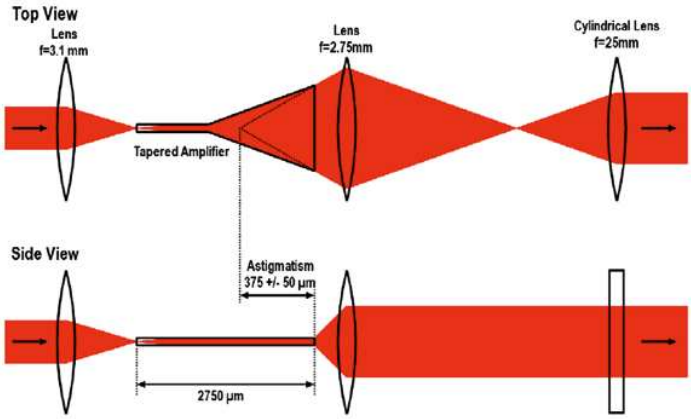

Figure 3.11: Optical setup for special designed *Tapered Amplifier* oriented to transportable laser systems.

was introduced in the *FINAQS* collaboration framework but it was derived from pre–existing transportable devices experiences. The implementation presented so far is strictly relative to the Raman board setup that is common to *FINAQS* project as to the *SAI* project. On the other side the same design is adopted for *TA*s involved in the others *SAI* laser modules but a different active medium is employed (see section 4.1.2 for specific details).

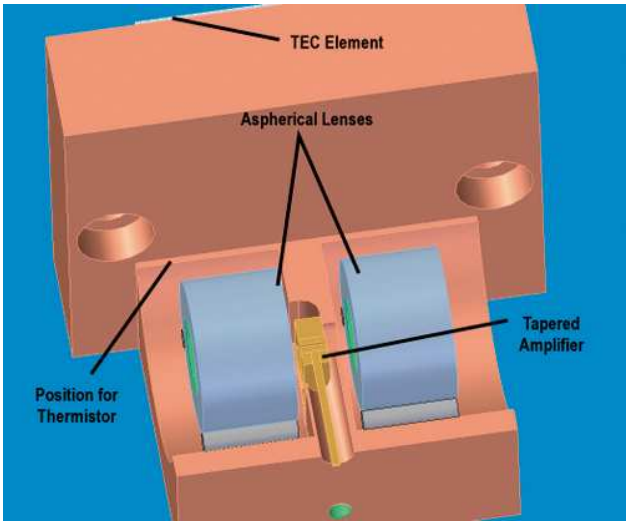

Figure 3.12: CAD view for mechanical setup of the *Tapered Amplifiers* [107].

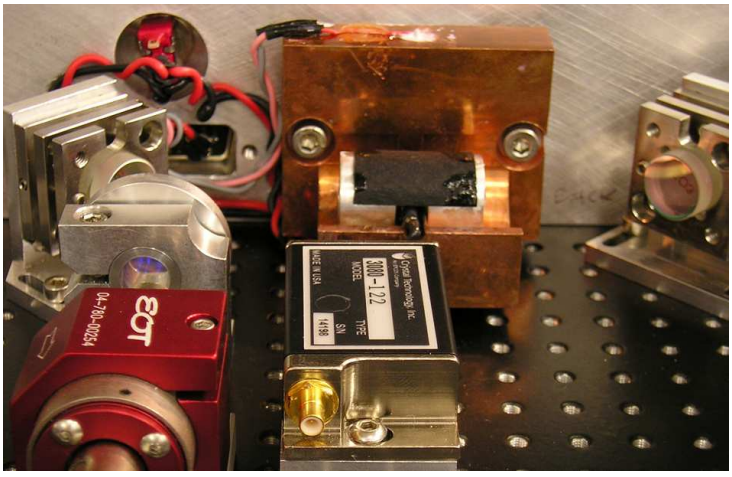

Figure 3.13: Picture of the *Tapered Amplifier* assembled on the *Raman* module.

Chapter 4

Complete Laser System for the transportable interferometer

4.1 Laser system structure

The laser system for the *Space Atom Interferometer* follows the approach already defined for previous transportable devices development, in particular we start from the *FINAQS* gravimeter experience [140],[110]. The basic concept is to separate the different tasks in different modular units linked each other by optical fibers. These criteria allow to achieve a good level of compactness because the final result consists in a few stand alone breadboards that can be easily fitted and piled in a small frame. For the gravimetric application in open field the optical system realized for *FINAQS* has been fitted at all in an electronics mobile frame to be easily loaded in a small van and transported in the designed experimental area. For the Space applications side of course the system compactness is mandatory in order to fulfill spacecraft volume and layout constrains, the same holds for the *Drop Tower* experiment.
Because commercial components did not fulfill the compactness requirements for such application a new standard has been defined for optical and optomechanical components mounted on the breadboards (some example are shown in picture B.10 at page 216). These components standard holds the beam height for each module to 20 mm from the board floor. The fiber optical coupling, that links boards each other and them to the physics apparatus, has been realized with adjustable and lockable fiber ports from SCHÄFTER–KIRCHHOFF model $60SMS-1-4-a4$ with optional 4.5 mm.

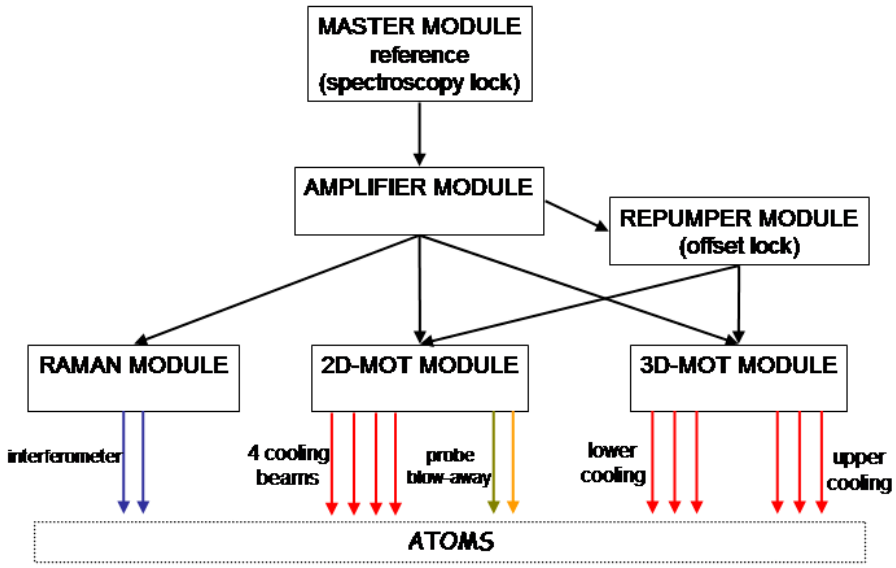

Figure 4.1: Block Scheme for *Space Atom Interferometer* Laser System

In section (1.4) rubidium transition to be addressed for atom cooling and for the interferometric sequence have been presented together with the relative frequencies, see picture (1.19) at page 83. The basic diagram for the *SAI* laser system implementation is illustrated in picture (4.1) that shows the links between modules and to the atoms, basic functions can be summarized as follows:

- ***Master Module*** occupies the vertex role for the laser apparatus with a laser source locked to a reference transition via a saturation spectroscopy, the output beam will provide the reference frequency to the others boards.

- ***Amplifier Module*** represents the amplification stage for the reference laser; power output from *master module* is not enough to to be shared between all the boards.

- ***Repumper Module*** provides for the generation and for the offset lock stabilization of the *repumping* beam. Such laser field is involved in cooling process and detection (sec (1.4), (2.7)).

- ***3D–MOT Module*** generates $3+3$ beams for atomic sample cooling, these beams are grouped by three with two independent frequency control for each group, this setup is functional to atomic fountain launch.

- ***2D–MOT Module*** provides for 4 cooling beams for the cold atomic source, each frequency can be not separately controlled. This board also provides for a variable frequency pushing beam involved in the *2D–MOT* and for the detection beam in some optional configurations.

- ***Raman Module*** consents the atomic manipulation for the interferometric sequence: it follows the same configuration used for atomic gravimeter from *FINAQS* projet. Such module provides for two lasers beams phase locked with a frequency difference equal to the hyperfine splitting of two levels of rubidium ground state.

The total optical power needed for atomic cooling can be estimated from the *2D–MOT* and *3D–MOT* requirement. We find for the first one 4×50 mW $= 200$ mW power, $+1$ mW for *pushing beam*, whereas for the *3D–MOT* are needed 6×20 mW $= 120$ mW of power. This is equivalent to $321mW$ of total cooling power on the atoms, but for boards performances dimensioning also the fiber coupling efficiency must be considered (70%) together with the other efficiencies relative to $AOMs$[1] (65%) and optics (90%). In our setup we consider the *amplifier module* as the main amplification stage; the total power provided from it is enough to be shared between the *3D–MOT* cooling and the reference signals for *Raman* module and for *repumper* module. On the other hand an additional amplification stage is needed for *2D–MOT*: with 20 mW of injection power provided from the *amplification module*, ≈ 530 mW of total power will be generated for atomic cooling.
Thus considering that in order to implement a frequency lock 5 mW of optical power are needed for each reference signal, it is possible to estimate the total power budget for the amplification stage as follows:

Raman Reference	5 mW
Repumper Reference	5 mW
2D–MOT	20 mW
3D–MOT	300 mW
total	330 mW

[1] AOM: Acusto–Optic Modulator

On the other side the *Raman* board just requires power for the *Raman master* frequency lock, the optical power for the interferometric sequence is provided from dedicated laser sources and amplification stages (sec 4.2).

From the mechanical point of view each module is aluminium made and closed by walls on lateral sides and by covers on the top. The layout dimensions for the optical modules are given from:

Module	Width (mm)	Dept (mm)	Height (mm)
Master Module	236	250+	63
Amplifier Module	240+	190+	66
Repumper Module	186	260+	63
2D–MOT Module	350+	260+	63
3D–MOT Module	350+	260+	73
Raman Module	430+	430	113

Where symbol + in the table means that extra space is needed for fiber and electronics connection. *Raman* module follows a different standard for the board that consists in a vibration isolated THORLABS board.
The described laser system, except for *Raman* module, has been developed for *SAI* collaboration from Cold Atom group of University of Hamburg, see [122, 123], [105].

4.1.1 *Master* module

The whole laser system for the *Space Atom Interferometer* will be referred to a laser frequency 130 MHz blue detuned above the $F = 2 \rightarrow F' = 3$ cooling transition (see (1.4)). Such result is achieved shifting the reference light by 263.33 MHz in a AOM double pass and stabilizing it on the $CO23$ Cross-Over Transition that is 130MHz below the cooling transition (see rubidium transition schematics in picture (A.1) at page 205). Basic setup diagram for master module is illustrated in picture (4.2), the implementation realize a *frequency modulation (FM)* saturation spectroscopy. A sample from the output beam is sent as first to a double pass in AOM and then to the saturation spectroscopy branch. The AOM is a Crystal Technology model 3110–120, 110 MHz, with an applied frequency of 131.67 MHz, the -1^{st} deflection order is sent back by a mirror reflection. The resulting beam is split into a *pump beam* and a *probe beam*: the *pump beam* goes straight to a rubidium cell whereas the *probe beam* passes through an *Electro Optical Modulator* (EOM) , 2 mm $\times$ 2 mm $\times$ 20 mm $LiNO_3$ crystal with electrodes on the top and bottom, that creates sidebands at $\simeq$ 10 MHz from the carrier frequency. Probe and Pump beams are superposed for the path inside the rubidium cell and the probe is deflected to a fast photodiode which picks up the *FM-spectroscopy* signal. Such signal is sent to a *lock box* and fed back to the laser source via two different channels driving *piezo* voltage control and current modulation.

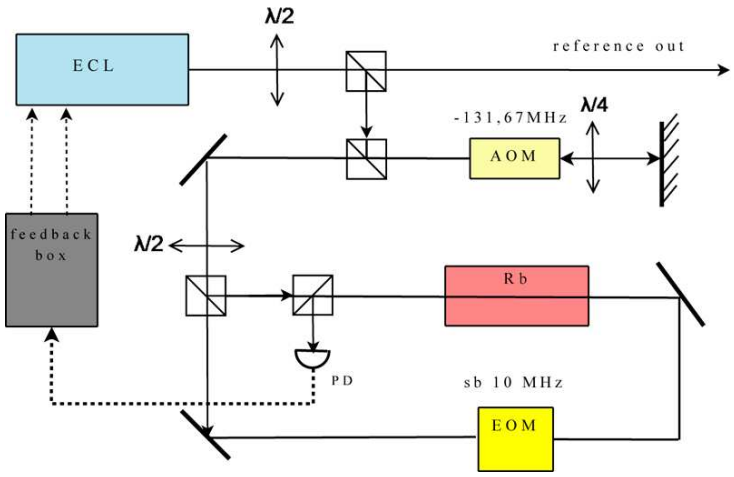

Figure 4.2: Frequency Modulation Spectroscopic setup for *SAI reference* laser.

The basic schematics for the spectroscopy lock box is illustrated in picture (4.3). After a simple proportional stage a conventional *PID*[2] stage follows. In between these stages a bias voltage is added in order to adjust the locking point. The signal resulting from *PID* is sent directly to the laser source current channel from one side and to an additional integrative stage and thus to the *piezo* channel from the other side. If the lock function is disabled the board works in a scan mode: an oscillating signal with tunable amplitude and frequency is sent from an internal oscillator to the *piezo* channel in order to generate a frequency scan on both probe and pump beams and to address atomic transitions.

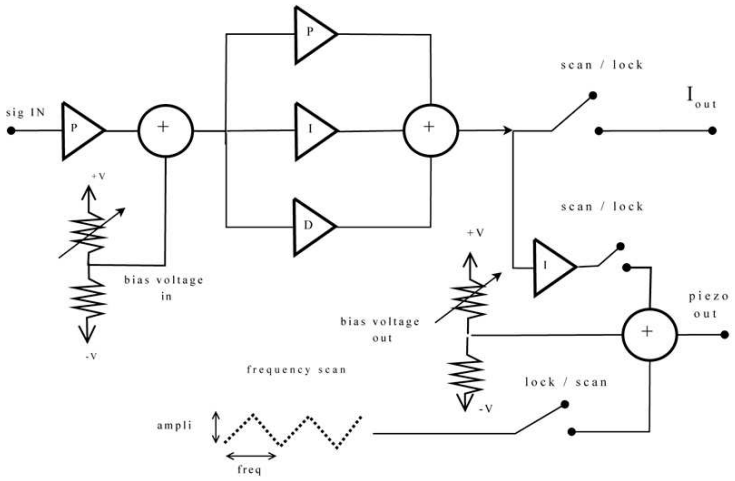

Figure 4.3: Basic schematics for *Reference* laser *lock-box*.

A spectroscopy signal acquired form the *master module* is shown in picture 4.4. From the signal–to–noise ratio between the lock condition and scan condition the frequency stability has been roughly estimated to be $\Delta\nu \approx 3.5$ MHz, that is not satisfactory. Further measurement with specific methods are going to be performed and if it will be needed, also further implementations will be approached to the electronics side in order to enhance these performances.

In picture 4.5 a CAD view for the *master module* is shown. $D1$ and $D2$ are 35 dB two optical isolators from OFR, components marked with S are mirrors and PD is the photodiode, the single output is in C.

[2] *PID: Proportional Integrator Differential*

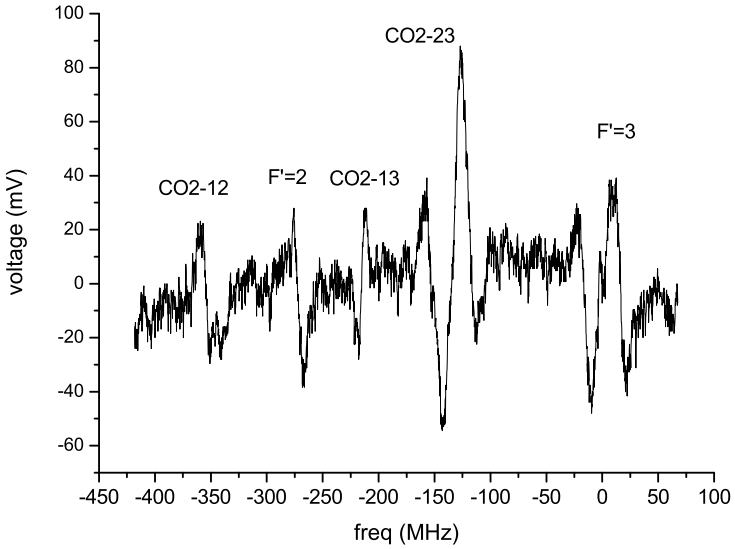

Figure 4.4: Spectroscopy demodulated signal from spectroscopy, locking point at the middle of $CO23$ transition.

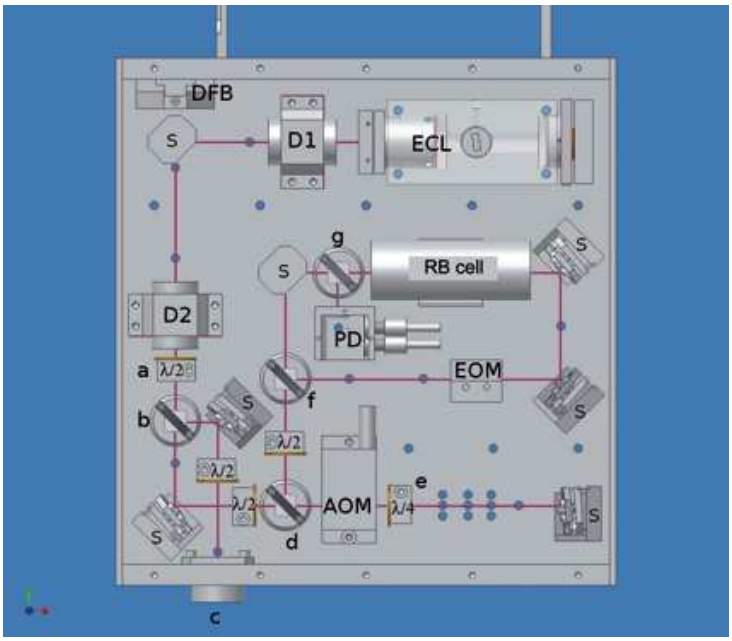

Figure 4.5: *Master Module* CAD view.

4.1.2 Amplification Module

The basic schematics for the Amplification module is shown in the picture (4.6), the task for this board is to amplify the input power from gate E and to share the resulting light power between the four output gates $A1, A2, A3, A4$. The optical power distribution among these gates has been realized by means of a simple Polarizing–Beam–Splitters and half–wave plates system. The involved amplifier follows the same setup than the ones utilized for the *Raman* board (sec. (3.3), (4.2)) In this case a 2 W maximum output power anode–ground laser chip is mounted with 3 A of maximum current. A cylindrical lens ($L3$) with $f = 25$ mm follows the amplification stage in order to correct horizontal output divergence (see picture (3.11) at page 136). An optical isolator prevents the amplifier from retro–reflections from optical components on the path.

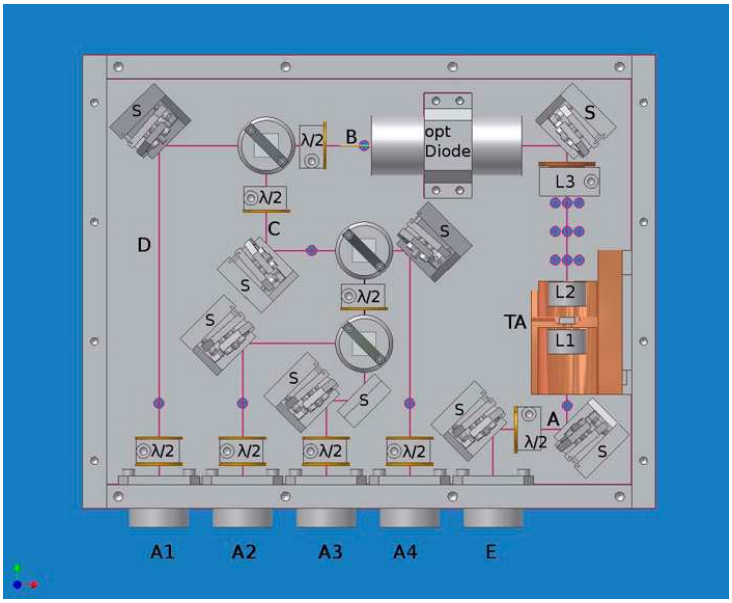

Figure 4.6: *Amplification Module* CAD view.

In pictures (4.6) we report some characterization measurements for the amplification stage performances. The plot in (4.6a) shows the power behavior as a function of seeding input power for two different current values: the *TA* power output begins to saturate above $\simeq 4$ mW and around 6 mW just slight changes are prospected for injection power variation. For our purposes this means that the *master module* fiber coupling efficiency for the seeding beam will not change significantly the *amplification module* power output.

In (4.7b) the amplification output is shown as a function of the current for a given seeding power of $P_{in} = 8.3$ mW: the two plots display the measured power before the optical isolator (point B) and after the output fiber. Total power reaches a value of 1.828 W after the isolator at the maximum current of 3 A and it drops to 730 mW after the fiber (efficiency 40% due to not optimal output beam profile from *TA*): according with our power budget estimation for *SAI* system the total power after the fiber is enough for a configuration with an active *2D–MOT module* and a passive *3D–MOT module* (see table at page 142), also considering efficiency losses.

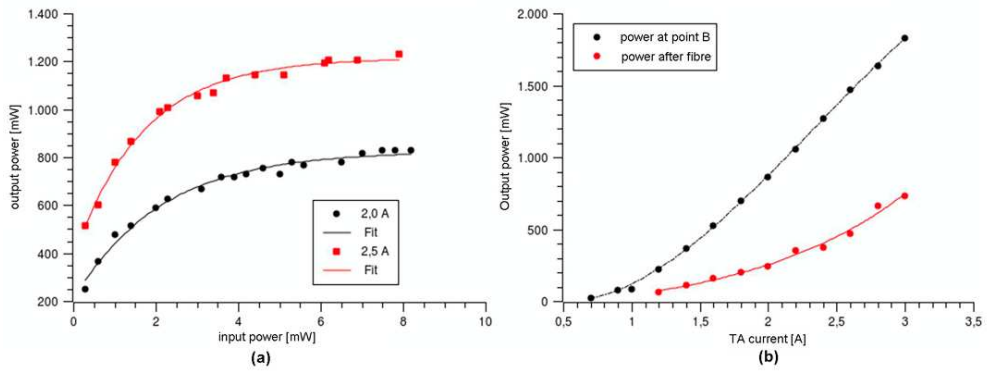

Figure 4.7: *Amplification Module* output power characterization, (a) output changes as a function of the seeding injection power (current $I = 2.0$ A, 2.5 A), (b) power changes as function of the current and for a seeding power of $P_{in} = 8.3$ mW, before and after the fiber. [105], [123, 124]

4.1.3 *Repumper* module

The *repumper* module implementation for *SAI* project is illustrated in the CAD view in picture (4.8): a single *External Cavity Diode Laser* with filter setup is utilized (sec. (3.1)) followed by two -38 dB optical isolator stages from Optics For Research ($D1$, $D2$). A first *PBS* splits the beam from the *ECDL* and a mirrors system drives it to a photodiode for the detection of the beatnote with the reference beam coming from the master module and injected from gate E. The relative polarization adjustment for maximum interference signal is performed by the *PBS2* together with a half–wavelength plate just before the photodiode. The other beam emerging from *PBS1* is deviated through an *AOM* modulator in order to implement a fast intensity switching. This *AOM*, Crystal Technology *AOM* mod. $3080 - 120$, is

used as a single pass at a fixed operation frequency of 80 MHz. In other to provide output beam fields for *2D–MOT* and *3D–MOT modules* the resulting beam from the *AOM* is delivered in two output gates ($A1$, $A2$) by means of the waveplate–*PBS3* combination. The offset lock for the *repumping* field has

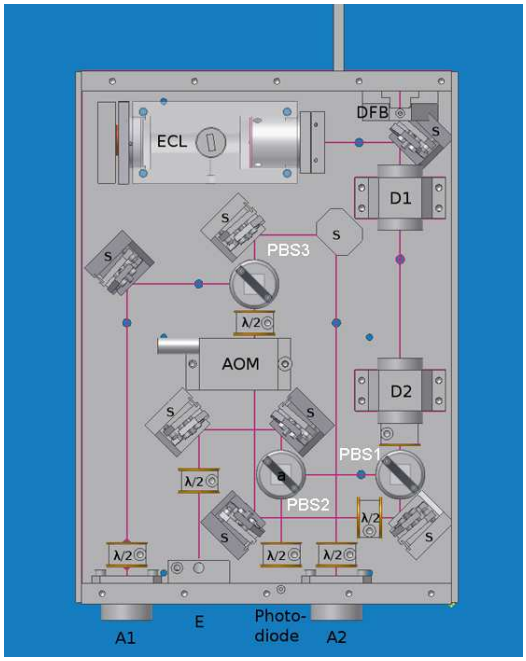

Figure 4.8: *Repumper* module CAD view.

been realized via a conventional *Phase Locked Loop* as shown in picture (4.9) [124]. The beat note between reference and *repumper* laser is detected from a Hamamatsu $G4176$ photodiode suitable for the 6282 MHz frequency difference between the two fields. We recall that the *reference* laser is 263.33 MHz blue detuned from $CO23$ between $F = 2 \rightarrow F' = 2$ and $F = 2 \rightarrow F' = 3$ transitions and the *repumper* is locked to the $F = 1 \rightarrow F' = 2$, see section (1.4) for details (the relative frequency difference can be evaluated from rubidium transition scheme in picture (A.1) and (A.2) at pages 205, 206). The AC photocurrent from the photodiode is coupled from a *bias–tee* and, after an amplification stage, the signal is frequency divided by a factor 8 by means of a first external *prescaler*; a further *prescaler* stage is integrated into the *Phase Frequency Detector* (Hittite HMC440QS17G) which divides again for a factor 8. The *PFD* compares the phase between the frequency divided beat note signal and a frequency reference signal provided by the control

module, a loop filter and a *PI–controller*[3] operate to configure the loop response. From the *PI–controller* a low frequency signal is sent directly to *ECL piezo* actuator and an high frequency signal to the laser current driver controller.
The laser field for the *repumping* transition results from a local oscillator frequency of 100.60 MHz whereas for the *blow–away* light field a 98.15 MHz frequency signal is needed (see [105]).

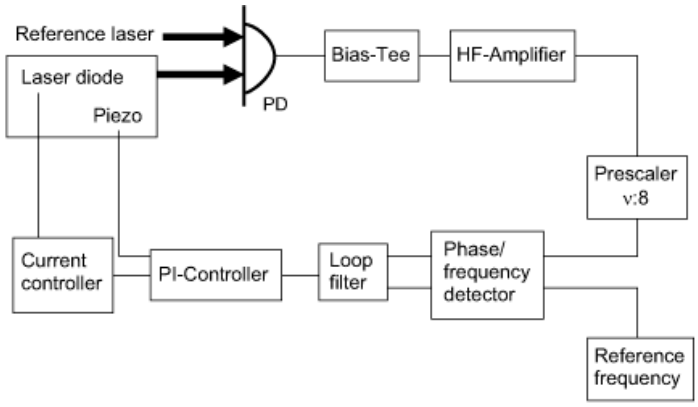

Figure 4.9: Diagram for the *Phase Lock Loop* implemented for the *Repumper* module offset lock [105].

4.1.4 *2D–MOT* module

2D–MOT module implementation is presented in the CAD–view in picture (4.10). Such module is not much different form the amplification module but for the specific task also two frequency shift stages are needed [105]. *Reference* light from master module enters from the gate E whereas the *repumping* light enters from *Rp* gate and it is directly overlapped to the cooling light by a *PBS*–half–wavelength system. The reference beam is amplified from a single *TA* stage and then separated into two branches in point a, a first beam is sent in double pass through $AOM1$ for cooling light frequency shift whereas the other one is sent in double pass through $AOM2$ for *2D–MOT pushing* beam and for *detection* beam frequency generation (both AOM model $3080-125$ from Crystal Technology). The resulting cooling beam is split into four individual power controllable beams and output coupled in gates $K1--K4$. In this board a cat's eye with a lenses configuration is realized for AOM

[3]Proportional–Integrator

double passes in order to ensure a good selection of the first diffraction order.

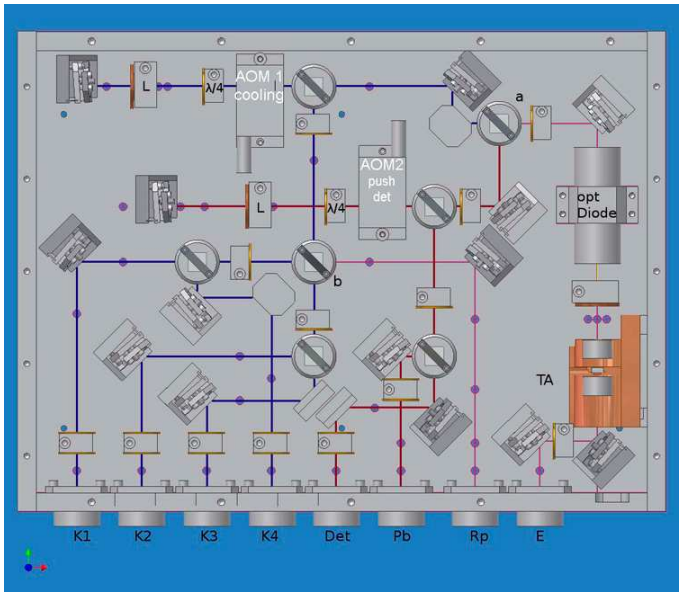

Figure 4.10: CAD implementation for the *2D–MOT module*.

4.1.5 *3D–MOT* module

The general implementation for the *3D–MOT* is almost the same as for *2D–MOT*. In picture (4.11) a full equipped version including an amplification stage is shown, for the actual version such stage is not needed (see sec. 4.1.2). The reference beam generated from the amplifier module enters through the gate E and goes straight to be shared between two frequency shifting double pass *AOM* stages in order to generate the cooling frequency. The frequency shift has been separated into two independent branch and two different *AOMs* (*AOM up* and *AOM dw*) for the three upper *MOT* beams and for three lower ones (see section 2.4 and picture (2.5)). In *MOT* regime the frequency of the two beams groups must be the same, but in order to perform the sample launch, in a molasses regime operation, a frequency difference is needed between lower and upper groups. The *repumping* beam enters from the gate *Rp* and is overlapped to the six cooling beams. In this implementation *AOMs* work also for intensity control for the cooling beams but, in order to achieve a complete shutoff of the beams during the interferometric sequence, two mechanical shutters operate respectively on the cooling

beam paths, just after the *AOMs*, and another one operates on the *repumper* optical path, just after the input port.

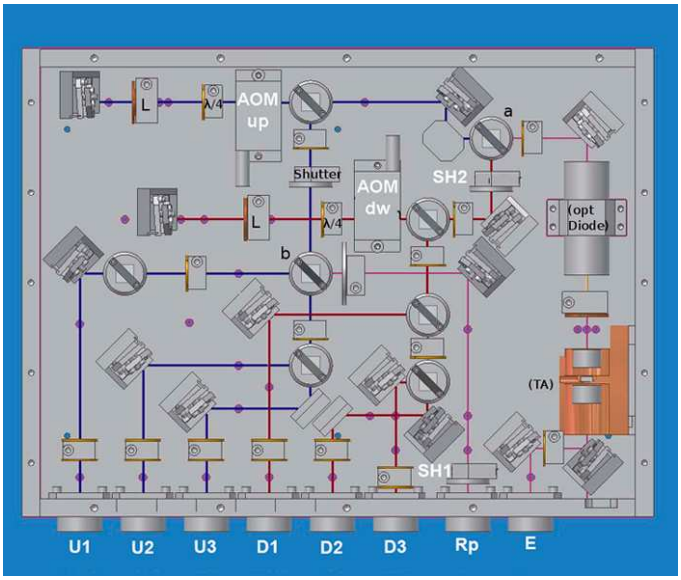

Figure 4.11: Implementation for the *3D-MOT module*.

4.2 The Raman Laser System

The described *Raman* board was developed for the Berlin *FINAQS* gravimeter apparatus, the same implementation follows the *SAI* system. We are going to see into incoming sections as some further modification can be yielded, a CAD view for the original setup is shown in picture (4.12). The laser sources needed for the two frequencies *Raman* fields are realized by two *External Cavity Diode Lasers* with interference filters, see (3.1). We define such lasers as *Master Raman* and *Slave Raman* because the first one is frequency locked to the main experiment *reference* laser, providing for the frequency reference to the interferometer (see 1.4 and 4.1.1), on the other side the *slave* laser is phase locked to the *master* in agreement with the interferometer requirements.
In order to avoid laser chip damage but also optical feedback effects each source is isolated by a 60 dB optical isolator (ISOWAVE $I-80U-4$, 4 mm aperture). Part of beam power from *master* (≈ 5 mW) is split by two polarized beam splitters and sent to beating on two photodiodes for slave phase lock from one side and reference frequency lock on the other side. The same

follows for the *slave* laser in order to lock to the *master*. After the beams sampling for the locks both beams follow the same kind of path for their own side. Each of them is amplified from a dedicated 1 W *Tapered Amplifier* (presented in (3.3)); its output is again isolated from optical feedback by a 30 dB high power optical isolator (EOT $WT-04-I780-HP-000$). Beams emerging from isolators are filtered by rubidium cells in order to cut away any residual light resonating with single photons rubidium $D2$ transition ((1.1.2) and (1.4)). *AOMs* stages oscillating to a fixed frequency of 80 MHz have been implemented for intensity control and fast beam switching, additional mechanical shutters (SUNEX) have also been added before the fiber injection: each beam is injected in two different fibers. An implementation with the two different beam paths for the *Raman* beams, as presented so far and as shown into the picture, adds an unwanted level of additional phase noise into the acoustic frequency range. From the experimental experience we can conclude that *AOMs* can be also used for a further *PLL* channel implementation (see 4.3.2 pages 164–169). For the *SAI* interferometer the board setup can be easily changed to a single fiber injection setup or moreover also to a single TA setup.

4.3 Raman Phase Lock System

Into the introductory sections about the Atom Interferometer we have seen the fundamental role played by the *Raman* laser for the two photons transitions. Moreover in the section (1.2.5) was shown in details how and how much the presence of a relative phase noise between such fields ($\phi_{eff}(t) = \phi_{R2} - \phi_{R2}$) directly affects the interferometric performances via the transfer function, also an ideal limit level was evaluated for a desired measurement accuracy in gravimetric framework. By the other hand in section (3.2) and relative subsection a detailed approach to the basic theory of spontaneous emission in laser diode as a source of phase noise and the effects of phase and frequency noise on the emission linewidth have been reported. A Laser linewidth measurement gives an estimation of how much chaotic is laser behavior.
For our purpose the two *Raman* beams must oscillate to frequencies far detuned from the transitions to hyperfine levels of rubidium exited state $5^2P_{3/2}$ and the relative frequency difference must address the ground state $5^2S_{1/2}$ hyperfine splitting (6.835 GHz) (see sec. (1.4)). To achieve the desired setup the beat note between *master* and *slave*, that oscillates at the frequency difference between such fields, will be phase locked to an ultra–stable local oscillator as radio–frequency reference (details about this implementation in sec. (4.3.2)). In this picture, for an ideal feedback loop, the residual phase

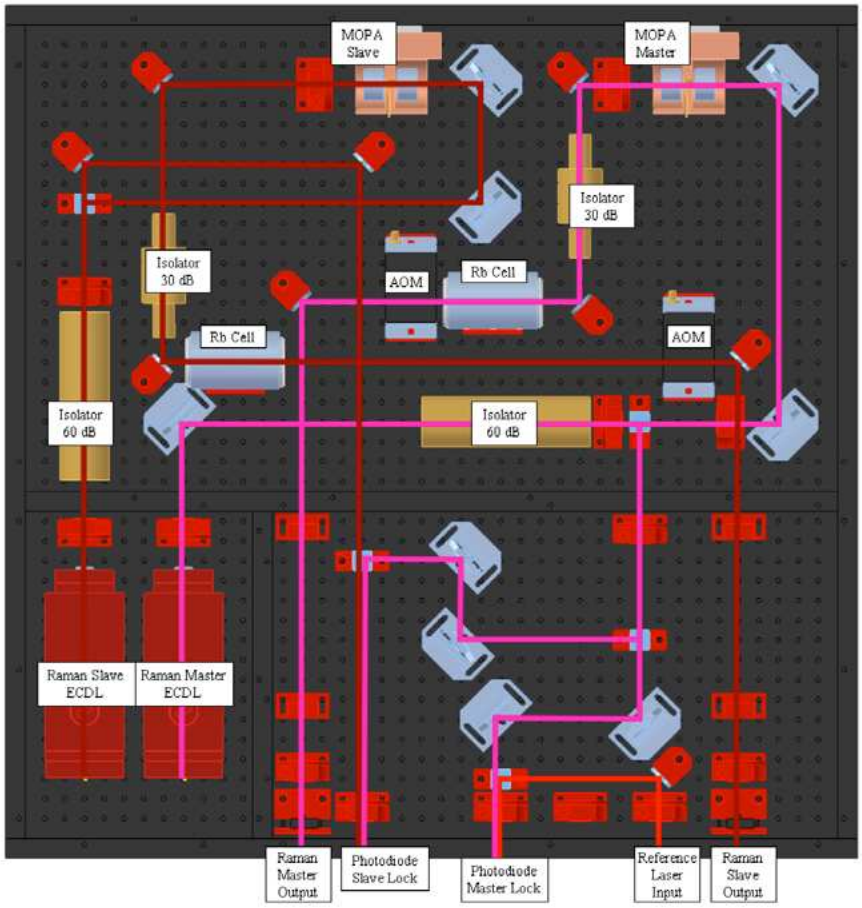

Figure 4.12: *Raman* board CAD view and beam–path.

noise relative to the fields phase difference should be equal to the intrinsic noise from the local oscillator. In other words the phase noise affecting the interferometer performance should be dominated from the oscillator contribution.
At this level we don't illustrate details, implementation and performances about the local oscillator frequency chain assembled to generate the *RF* signal reference at 6.8 GHz: this is out of the target of this thesis. The relative implementation is under the responsibility of Berlin group [135] for *FINAQS* gravimeter and of SYRTE[4] for *SAI* interferometer. Thus we can go on

[4]SYRTE department –Sytèmes de Référence Temps Espace, Paris Observatory, also associated with the CNRS - National Research Center and University Pierre et Marie Curie (Paris 6).

to illustrate steps relative to the development for the *Raman phase locked loop* compatible with the project requirements. If the *PLL* implementation performances will be into the limit of interferometer requirements, the ultimate interferometric performances will be limited at most from the frequency chain.

4.3.1 Phase Lock Loop generalities

A *Phase-Locked Loop* (*PLL*) is a feedback system that combine a voltage–controlled oscillator (*VCO*), or a current–controlled oscillator (*CCO*), and a *Phase Detector*: the way the oscillator maintains a constant phase angle relative to a reference signal [89]. Such kind of implementation can be involved to generate stable output frequency signals from a fixed low–frequency signal. In our applications we focus on lasers that behave, from this point of view, as a Current Controlled Oscillator to be locked in phase or in frequency to a reference. In picture (4.13) a simple generic block model for a *Phase-Locked-Loop* is shown: in this case a *VCO* (in our case it is laser as a *CCO*) oscillates at a frequency ω_{VCO}, a portion of the signal coming from it is fed back and reports the phase θ_{VCO} into the *Phase Detector* that compares the latter with the phase θ_{RF} relative to the *local oscillator* with frequency ω_{RF} and generates a signal "e" at a first level proportional to the phase difference $e(\omega) = K_d(\theta_{VCO} - \theta_{RF})$. The *loop filter* is the component that allows closed loop transfer function shaping and calibrating in order to achieve the best trade off between high performance, readiness and stability for the feedback loop. The loop filter assigned transfer function is $F(\omega)$ whereas $L(\omega)$ is assigned to the *VCO*, in many real cases, as for laser diode response, it can be unnecessary to estimate these two transfer function separately.

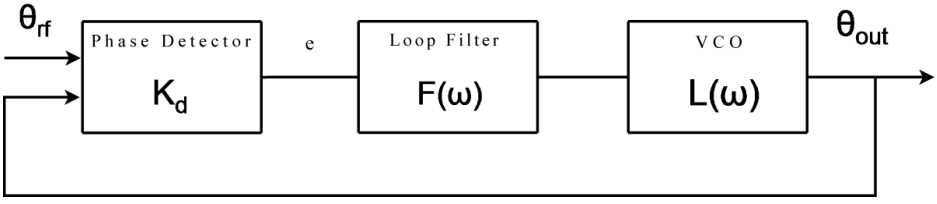

Figure 4.13: Basic Model for a *Phase-Locked-Loop*.

The open loop transfer function is given from the product of the functions of the three single contribution depicted into the scheme $G_{op}(\omega) = K_d F(\omega) L(\omega)$, where in general $F(\omega)$ and $L(\omega)$ are complex. In this picture the closed loop gain can be written as follows:

$$H_{cl}(\omega) = \frac{G_{op}(\omega)}{1 + G_{op}(\omega)} \tag{4.1}$$

At a first level we can point out that if the real part of $G_{op}(\omega)$ acquires a negative sign and $|G_{op}(\omega)| \sim 1$ a positive feedback occurs that may cause instabilities in the control loop. If there is a frequency $\bar{\omega}$ for which $G_{op}(\omega) = -1$ the loop is said to be *unstable*; this situation can correspond to an increasing of oscillations at frequency $\bar{\omega}$ or to a departure from the locking point.
For this framework the closed loop stability criteria can be broadened by the analysis of the transfer functions as Laplace transform with the help of *Nyquist* theory [92, 94]. In our case we want to define some approximative criteria useful to deducting information about the loop stability from easily measurable quantities. By the way a full analytical approach for us may be inadequate because of the impossibility to dispone of a model for all components involved; this is due to the presence of components as laser diodes, whose theoretical electrical behavior can be just only roughly modeled, and also due to the deviation of the other components from their ideal model at high frequencies.
We can start pointing out that an unstable loop operation is expected if positive feedback with unitary gain is present at some frequencies. Thus an intuitive method may consist into the requirement that the gain $|G_{op}(\omega)|$ reaches the value $0dB$ before the open loop phase reaches $\phi = -\pi$. For a practical application this criteria must be widened because we can aspect time change in loop constant (thermal for instance) leading the system to dumped oscillations around the equilibrium steady point: some *phase* and *amplitude margins* must be considered (se picture 4.14). In particular we can define *phase margin* as "*How far from* 180° *the phase shift is when the loop gain falls below the unity gain* (or 0 dB)". As general safety criterion we can say that if such phase shift is less than 45° the loop will tend to oscillate.

To the effective phase lag the contribution of many components can be added, in particular we know from the models and from the experience that a laser diode response produces a phase delay above a thermal cut–off ($\sim$ 100 kHz), (80 kHz measured for us). The challenge than becomes to design a feedback loop calibrating loop filter parameters the way to increase as much as possible the gain at low frequencies keeping the unity gain frequency low enough to get the system stable and, moreover, to widen the loop bandwidth as much as possible. At a first level we note that this scenario leads to the necessity to implement a servo loop feedback with a negative gain vs frequency slope.

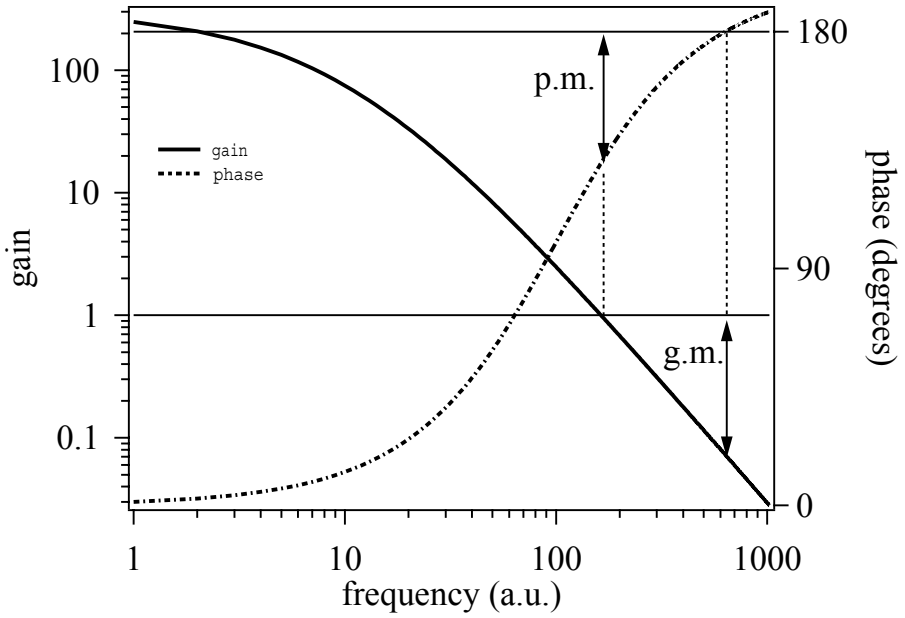

Figure 4.14: Example for a Gain Phase plot, gain and phase margins are shown.

An Intuitive Approach for *Phase Lock Loop* implementation

To explain the semi–empirical method adopted to implement the *Phase Locked Loop* for *Raman* lasers we present an intuitive example of transfer function shaping for a generic loop ([92, 93, 96]). At first we introduce some basic compensation networks that usually are adopted for loop design. In picture (4.16) the relative diagrams are illustrated together with the qualitative Bode plot; the calculation of the single transfer function and of the single roll off frequencies ω_i is trivial (see [92, 95]). Moreover each single behavior can be assumed as an useful model for a generic compound network analysis by the decomposition in elementary components.
The simple network (4.16a) is a pure *integrative* network and introduces to the loop a maximum phase delay of $-\pi/2$ reached asymptotically to high frequencies; if used as a single stage, this may became the definitive contribution for the stability, with a good enhancement of low frequencies gain but unsatisfactory for the high frequencies: the typical roll–off gain-frequency slope is -6 dB/octave. Network in picture (4.16b) is named *phase lag*, characterized from the same frequency-gain slope of the latter, it stops the roll–off to a value depending from the parallel of the two resistors, the typical phase

delay ranges around $-\pi/4$. An important difference with a pure integrative network is the phase lag effect stopping at upper frequency ω_2. In picture (4.16c) a *phase lead* is illustrated: with a positive roll–off gain–frequency slope introduces into the loop a positive phase shift around $+\pi/4$ depending from the parameters. As we are going to see such last network may play a fundamental role for loop bandwidth enlargement because an additional *phase lead* inserted just before the frequency range close to the $\phi = -\pi$ point can contribute with an additional phase margin. On the other side it works as high pass filter for high frequency noise. For each illustrated scheme an equivalent network can be implemented with active feedback components involving operational amplifiers, in our case because low noise and high frequency performances requirement this choice is unfeasible thus we are going to focus on passive filters.
All described networks can be cascade realizing a higher order loops: for instance for two *phase lag*, to the overlapping frequency range will correspond a -12 dB/oct gain-frequency slope, the same for the phases that adds each other, this could mean $\sim -\pi/2$ in such frequency range, the net result for the network will account of both contributions.
Coming back to a loop stability point of view, assuming as a general criterion a phase margin of $\pi/4$ convenient, it's possible to extrapolate as a *golden rule* to design the servo loop the way to cross the zero gain level with a gain–frequency slope of -6 dB/oct; in fact with a pure integrative behavior around this point we ensure a phase shift at most of $-\pi/2$ for the closed loop. By the other hand a frequency-gain slope of -12 dB/oct in such frequency range will be undesirable.

To illustrate an example for loop design with bandwidth enhancement, we can refer to the plots in picture (4.15). Here the open loop gain $|G(\omega)_{op}|$ is given from the plot (a): it is constant up to a frequency ω_1 and then exhibit a first order roll-off of -6 dB/oct from ω_1 to ω_2 (due for instance to the laser cut off), thus a second order roll off from ω_2 up to ω_3 (-12 dB/oct) and at last another higher order roll–off from ω_3.
As first step let's point out that if we increase the gain just only in a proportional way the entire curve will be shifted upward until it will cross the 0 dB level and thus some were not far above ω_2 (in the range of -12 dB/oct) the loop will change to positive feedback mode or will overcome the phase margin limit. If we stop the proportional grow just few steps before such unbalance, a bandwidth limited to $\lesssim \omega_2$ will result and a gain non boosted for low frequencies.
In the picture, the curves (b), (c), (d) plots the individual behavior of single loop filter network components, curves (b) and (c) represent two cascade *phase lag* whereas (d) a *phase lead*. The whole net result is shown in (e):

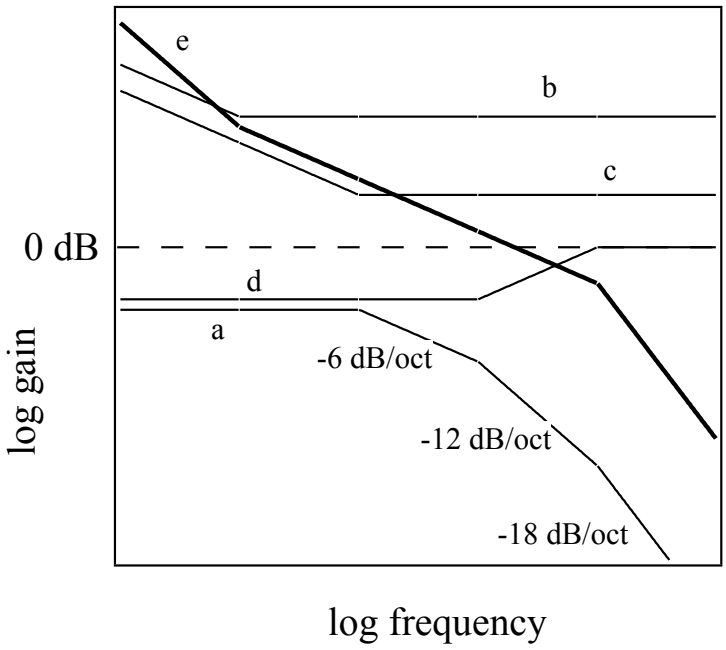

Figure 4.15: Bode gain-frequency plot for a generic loop, (a)open loop gain, (b) first *phase lag* contribution, (c) second *phase lag* contribution, (d) *phase lead* contribution, (e) resulting close loop net gain.

the *phase lags* overlaps for a first range with a big low frequencies gain enhancement with -12 dB/oct as gain–slope, then a single phase lag contribute continue (-6 dB/oct slope) up to the frequency ω_1. Just before the second roll–off frequency ω_2 the effect of a *phase lead* compensate the phase of the open loop function enlarging the -6 dB/oct gain range. The net effect is at low frequency and very far from the unity gain point a function with a slope of -12 dB/oct, then continues with -6 dB/oct and crosses the zero point with the same slope. At high frequency and at gains smaller than one it's free to fall down with higher slopes.
After a previous dimensioning of a rough loop filter network, based on a basic knowledge frequency response of the system, the designer can adjust the loop parameters with the help of a *RF* spectrum analyzer. The trace displayed by this instrument will show a central carrier frequency peak and two sidebands. Such broad further peaks represents a noise enhancement, their position in terms of frequency roughly corresponds to the feedback switching point from active to positive feedback. To a gain enhancement will correspond a side-

bands amplitude grow as the loop oscillates.

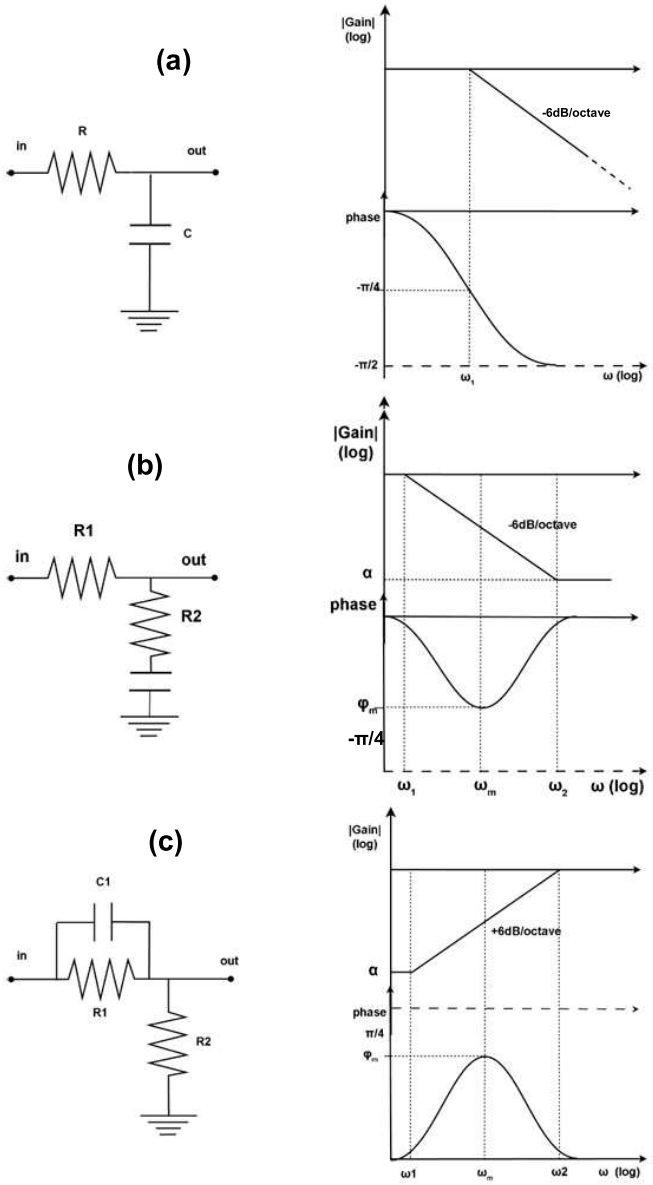

Figure 4.16: Phase compensation networks for loop filter implementation, (a) pure *integrative*, (b)*phase lag*, (c) *phase lead*.

Phase Frequency Detector

The role of the Phase Frequency Detector is to generate the error signal to phase lock the Voltage Controlled Oscillator (VCO). In the described work we refer with this notation to a complete integrated custom device that includes also input and output stage for the error signal and part of the loop filtering stage, the basic diagram is shown in picture (4.17). The complete device has been developed by M. Prevedelli [90, 91] with the employment of commercial *ECL* fast electronics [95]. It is composed by two receivers that digitize the analog signal, a proper digital phase-frequency detector for the signals phase comparison and a differential amplifier stage that operate difference of the two detector output U and D. The differential amplifier gain can be modified by the user for servo loop design purpose. After the amplifier an additional network splits and filters the output into a high frequencies channel and a low frequencies channel. The Detector involved is a three state low noise device, $MC100EP140$ from ON Semiconductor, with a maximum operating frequency of 2.1 GHz and an output swing of 400 mV, the state diagram is illustrated in picture (4.18) and the connected operational state–transitions table in (4.1). The amplifier stage is realized by an $AD8129$ fast differential amplifier (stable for $G \geq 10$). The linear output response range is obtained for phase difference $\Delta\phi_{lin} \pm 2\pi$.

The whole board assembling has been realized with SMD[5] components

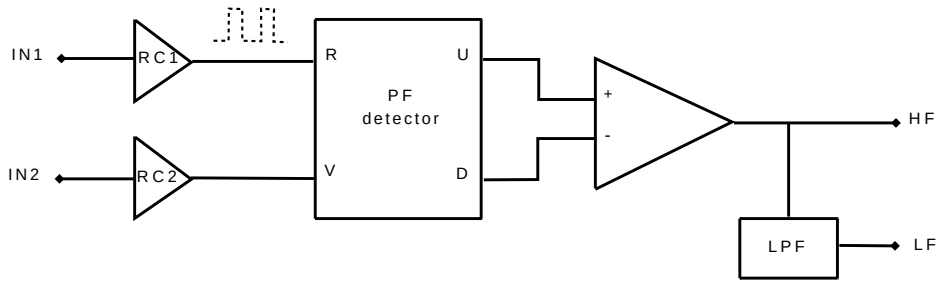

Figure 4.17: Basic diagram for Phase Frequency Detector device.

with a low resistance and inductance at the connection leading to a better performances in high frequency regime.

The operative condition of the device were tested and the intrinsic noise spectrum has been acquired before the implementation of the *Raman PLL* system. For the phase noise spectral density acquisition the same signal at 80 MHz fixed frequency was sent to the two inputs; the measurement

[5]Surface Mount Device

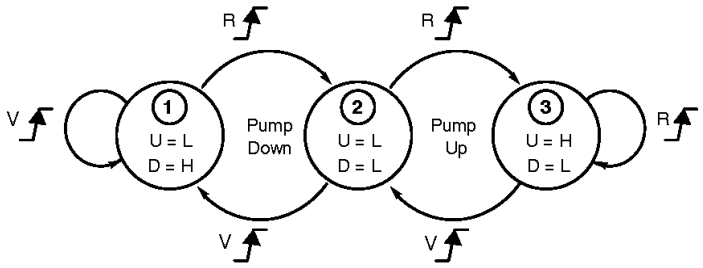

Figure 4.18: Input–Output State diagram for *Phase Frequency Detector* $MC100EP140$.

state	input		output	
Pump Down transition $2 \rightarrow 1 \rightarrow 2$	R	V	U	D
2 $2 \rightarrow 1$ $1 \rightarrow 2$	L L H	L H L	L L L	L H L
Pump Up transition $2 \rightarrow 3 \rightarrow 2$				
2 $2 \rightarrow 3$ $3 \rightarrow 2$	L H H	L L H	L H L	L L L

Table 4.1: Truth table, Operational State for $MC100EP140$

was repeated for different value of the input signal amplitude. The typical phase white noise level was found at -138 dB rad^2/Hz (picture 4.19) thus 10 dB rad^2/Hz smaller than the servo loop requirements (see section 1.2.5 page 69). On the other side a little noise enhancement was found decreasing the input signal amplitude but also for small value (220 mV pk $-$ pk) the noise level is fully acceptable. From a detailed circuit noise analysis performed comparing each single contribution was found the main noise contribute coming from the phase detector.

4.3.2 Servo Loop Implementation and Results

Specific details and results relative to the *Raman beams (PLL)* implementation are reported, the setup is the typical adopted for the *FINAQS* system and will be almost the same for the *Space Atom Interferometer*. Beat note

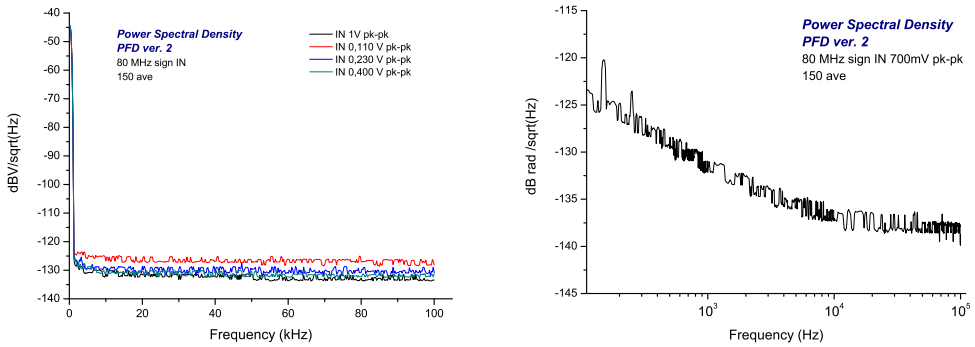

(a) (b)

Figure 4.19: *PFD* intrinsic phase noise spectral density ($dBV\ Hz^{-1/2}$), (a) Spectral density for different input amplitudes, (b) phase noise spectral density ($dBrad\ Hz^{-1/2}$) for input signal 700 mV pk–pk.

between *master* and *slave* laser has been detected by HAMAMATSU fast photodiode $G4176$, with responsivity 0.3 A/W. Beams from lasers overlaps with a power of 2 mW from each. The photodiode is connected to a *Pulsar Microwave* bias tee $BT - 29 - 463/1D$, and the biasing has been derived from there with the application of a 9 V battery. The output drives a *MiniCircuits* *RF* mixer $ZMX - 10G$ connected to the input of a $ZFL - 500LN$ amplifier (also from *MiniCircuits*) with a gain of 24 dB, a bandwidth of 500 MHz and a low noise figure (smaller than 3 dB). Such detection/amplifier group ends with a directional coupler that sends 90% of the signal to the *PFD* and the other 10% is sent to *RF* spectrum analyzer for monitoring.
The frequency chain (developed for *SAI* from SYRTE [134]) provides for the 6934 MHz reference signal to lock lasers at the frequency difference relative to the ground state hyperfine splitting of ^{87}Rb atom (see sec. (1.4) and (A)). For our first prototype of *Raman* laser system, now operative for tests on *MAGIA* experiment, such reference signal has been also supplied by an ANRITSU synthesizer (MG3692A, 20 GHz). The typical implementation diagram is shown in picture (4.20). In order to obtain a frequency down-conversion the frequency chain provides an ultra–stable signal at 6934 MHz that is analog mixed with the beat note signal between *master* and *slave* *Raman* beams to be locked at 6834 MHz, the resulting signal at the frequency difference is sent to the first *PFD* input. On the other side frequency chain also provides for an additional 100 MHz signal, obtained as down–conversion from the previous one, that is sent to the other *PFD* input channel. This technic allows the utilization of electronics for feedback loop designed for

hundred Mz range instead of thousand.

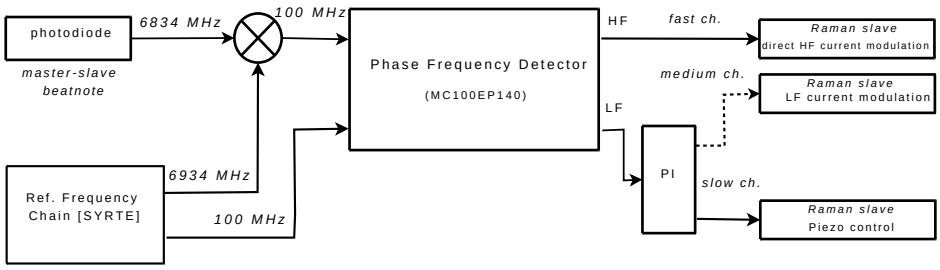

Figure 4.20: *Raman* locking system implementation diagram.

For our first *PLL* tests before the full setup implementation the frequency chain and the downconversion branch in the diagram was omitted, the lasers were locked at 80 MHz of frequency distance with a signal provided from a commercial quartz.
As shown into the diagram the output control has been divided into a fast channel (*HF*) and a slow channel (*LF*). The *HF PFD* output is sent to a special designed board for laser direct current modulation such board represents a fundamental element for loop filtering operations. The *LF* output is sent to a *Proportional–Integrator* servo controller and then to the piezo actuator. An additional low frequency current channel can be implemented in order to enhance the long term stability employing laser extended tunability range features (see sec (3.1.2)), up to now this further implementation was not needed.

Low Frequency piezo control channel

The piezo control channel bandwidth must be limited far below the naturally intrinsic mechanical resonance (9 kHz measured); in our implementation such channel is employed just for very low frequency controls thus in order to compensate for long term drifts. The LF channel operative performances can be described as follows: if the laser frequency tries to change, current correction responds and supply as first, piezo response follows just after to restore a new steady state position. Piezo loop was implemented by means of *PI* board developed by *LENS* electronic workshop [133] and customized by us for this application. It consists essentially in a proportional amplifier stage with variable gain cascaded with a semi–integrator, that means a transfer function with a *zero* limiting the -6 dB/oct roll–off (the behavior similar to diagram in picture (4.16b)). The semi-integrator holds the overall *LF* piezo bandwidth at ≈ 160 Hz.

High Frequency direct current modulation channel

The specific board converting the *HF* voltage signal output to a laser diode applied current represents the most important loop filtering element, the modulated signal is added to the *DC* operative current level provided from the laser driver. Such board also allows to set and calibrate the definitive loop filtering contribution to the overall gain–phase to frequency closed loop transfer function; the final result also accounts for piezo contribution. Many different setups were experimented looking for the best performance, the final one is shown into the schematics in picture (4.21). It's important to underline that the board must be installed as close as possible to the laser diode the way to shortening the connection cables and avoiding additional phase lag due to the cable length delay and to parasistic capacitances. For this purpose, in order to guarantee a perfect housing, the rear facet of the *ECLs* has been modified also for future applications.
The voltage–to–current conversion is operated by an N-Channel *FET* $2N5457$ working as a current source. On the safety side a diode $1N5711$ prevents for laser voltage polarization inversion due for unsought voltage swings from the electronics. A similar task is assigned to the two LEDs before the *FET*, their combined effect holds gate the voltage in the range $-0.6\ \text{V}, +0,6\ \text{V}$. The loop filtering is realized by a conventional *lead–lag* network, the lag contribution begins at ≈ 5 kHz and stops ar ≈ 650 kHz whereas the lead begins from ≈ 200 kHz, the complete result is shown into the simulation in picture (4.21).

The *PLL* results

The *PLL* performances have been monitored an characterized by means of a *RF* spectrum analyzer Agilent ESA–E series E4407B ($9\ \text{kHz} \div 26.5\ \text{GHz}$) and a *Fast Fourier Transform* analyzer HP 3561A ($1.25 \times 10^{-4}\ \text{Hz} \div 100\ \text{kHz}$). The residual phase noise has been measured from the acquisition of the beat note between *master* and *slave Raman* lasers. From the signal *RF* spectral analysis the loop bandwidth can be estimated by the servo bumps relative position to the carrier ≈ 4.5 MHz (picture (4.23)). At low frequencies the phase noise is dominated by the quartz oscillator intrinsic noise and the acquisition is limited from the *RF* spectrum analyzer bandwidth, thus for an estimation of the servo loop intrinsic noise a differential measurement was needed. Such acquisition was performed demodulating the signal by mixing the beat note with the reference oscillator signal in a MiniCircuits analog mixer *RPD1*; an adequate phase delay between the two signals is needed and also a further calibrated LF amplification stage. The output spectrum was analyzed with

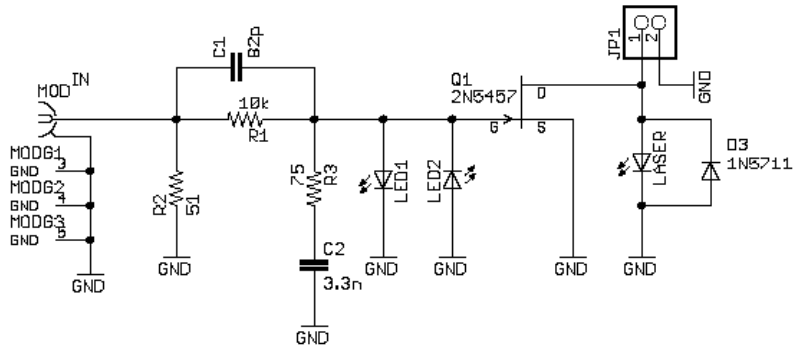

Figure 4.21: Fast modulation circuit implementation schematics.

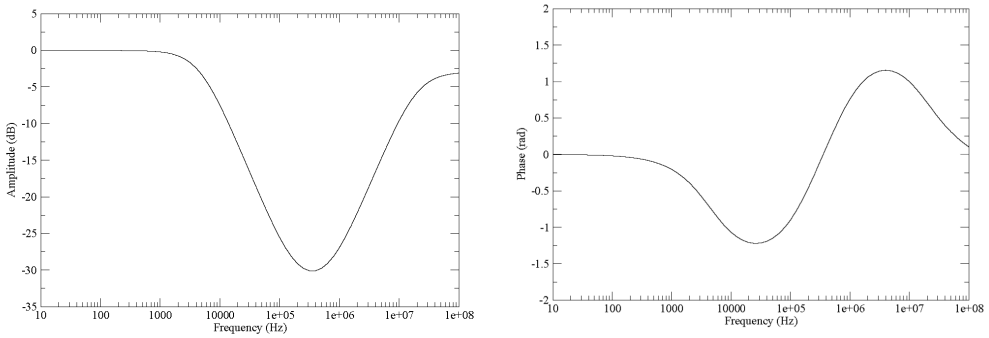

Figure 4.22: Fast modulation circuit simulation: (a) amplitude response, (b) phase response.

a *Fast Fourier Transformer* up to 100 kHz bandwidth. Full Phase Noise Spectral density plot matching both *LF* and *RF* acquisitions is reported in picture (4.24) considering the relation between *Single Side/Double Side Band phase noise* $L(\nu) = 1/2 S_\phi(\nu)$, thus $L[dBc/Hz] = 10 \log_{10} \frac{S_\phi(\nu)/2}{1 rad^2}$).

The spikes presents into the first part of the plot starting from 50 Hz, and superior harmonics have been found to be due to the AC current supply. The white phase noise level, around 100 kHz, is -120 dB rad^2 Hz^{-1}, thus totally fulfills the interferometer requirements for *FINAQS* gravimeter (see page 69). At this point of analysis and from the electronics side the inter-

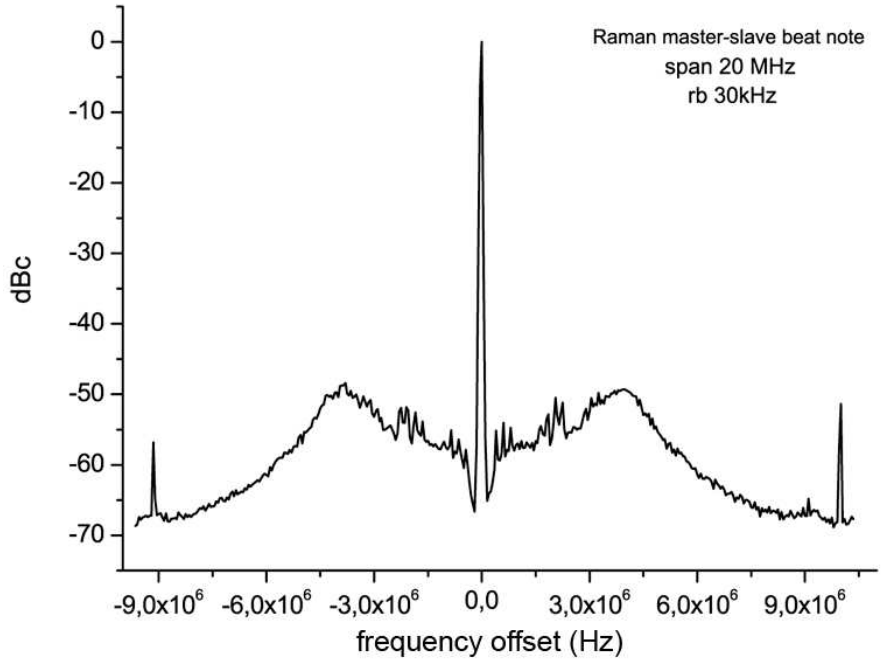

Figure 4.23: Beat Note between phase locked *master* and *slave Raman* lasers.

ferometer seems to be limited just from the frequency chain phase noise level.

From the other hand a phase noise acquisition after the fiber driving *Raman* light to atoms reveals a spoiling effect at low frequencies connected to acoustic vibrations. This measurement is presented in picture (4.25), it was performed in a single fiber implementation. We recall that in *FINAQS* original setup *Raman master* and *slave* beams from laser sources are amplified by two different *TA*s and follow two different optical paths with many different optical components (mirrors and waveplates) whereas the beam sampling for the *PLL* is performed before as first step (details about *FINAQS* and *SAI* optical implementation in sec. 4.2 and picture 4.12). Also a double separate fiber linking should be implemented. From the described experience, relative to a single fiber injection setup for the two beams, it has been possible to individuate into the long beam path separation after the feedback sampling a phase noise source. Thus we can conclude that extending the beam path separation to the linking fibers will be unadequate: each different optical component on single separate path contributes with its amount of phase noise.

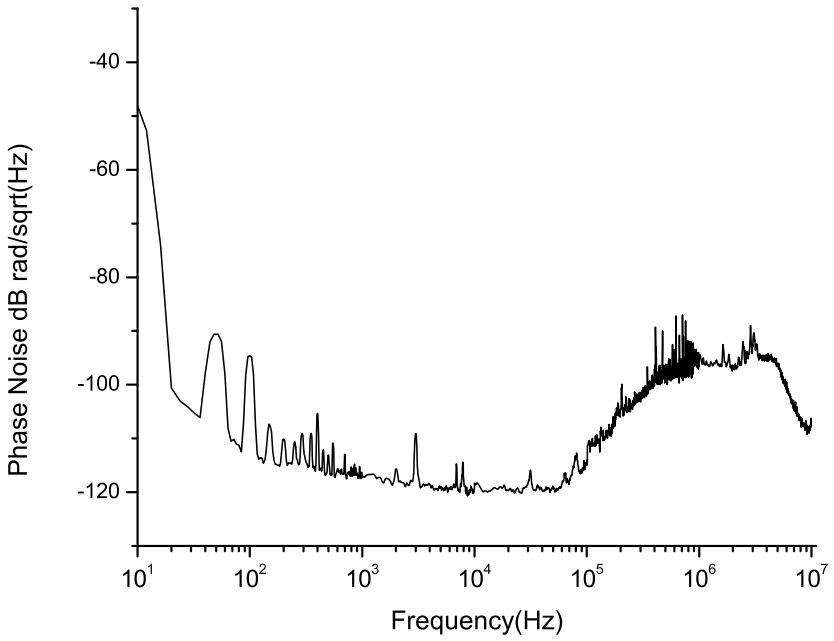

Figure 4.24: Phase Noise Spectral Density for *Raman* phase lock servo loop.

In order to compensate for the measured noise enhancement an additional feedback network has been implemented detecting the *Raman master–slave* beat note, amplified by *TA*s, just a step before the fiber injection and using one of the two *AOM*s on the optical path as feedback actuator. The basic scheme for the implementation is illustrated in picture (4.26) the *AOM1* on the *master* laser still oscillate at 80 MHz fixed frequency, whereas the *AOM2* for the *slave* is now driven from a *VCO*, an additional *PFD* is also needed. The comparison between the bare implementation an the new one is shown as preliminary characterization in picture (4.27) as phase noise spectral density measured before the fiber injection.

4.3.3 *Raman Master* to *Reference* lock

Raman Master laser is locked to the *reference* laser detecting the relative beat note with the implementation of a *Phase Locked Loop* by means of an ADF–4108 Analog Devices commercial integrated *Phase Frequency Detector*. The beat signal is locked to a stable 100 MHz signal provided by

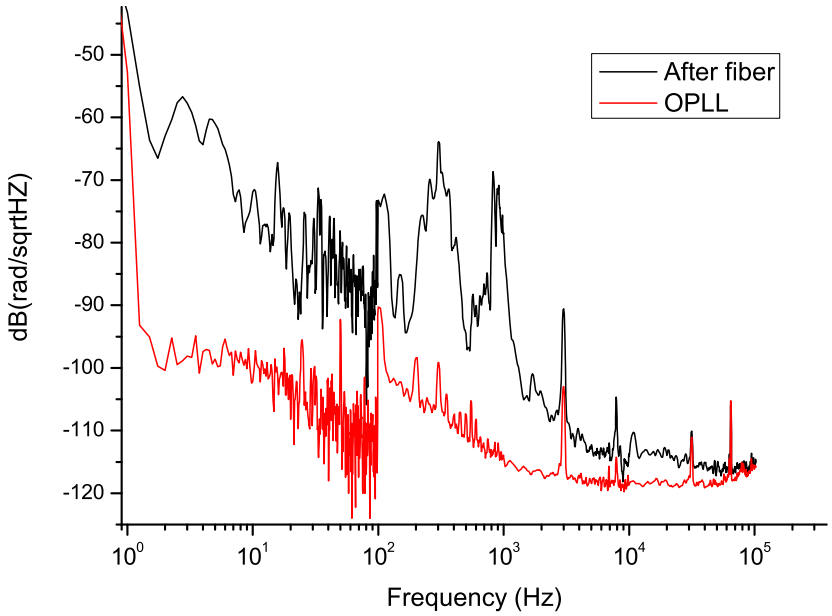

Figure 4.25: Comparison between *PLL* residual phase noise before and after fiber.

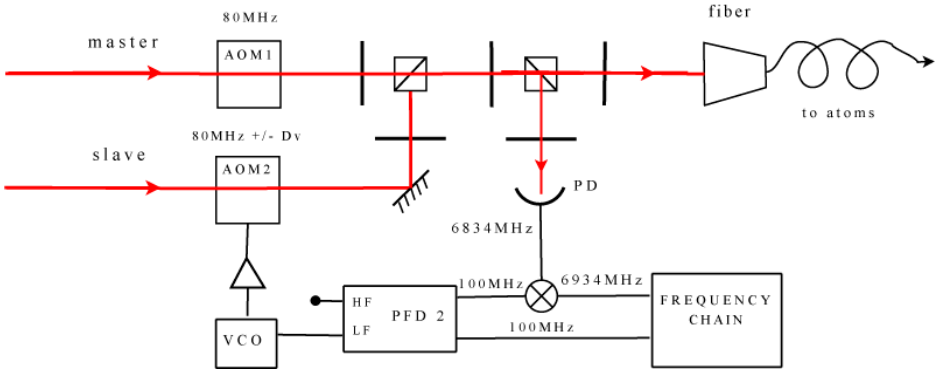

Figure 4.26: Compensation network for acoustic noise suppression via *AOM* feedback channel.

the frequency chain [134]. The frequency difference between *Raman master* and *reference* must be of 3400 MHz thus the downconversion to 100 MHz reference signal is performed by the divider integrated into the *PFD* as shown

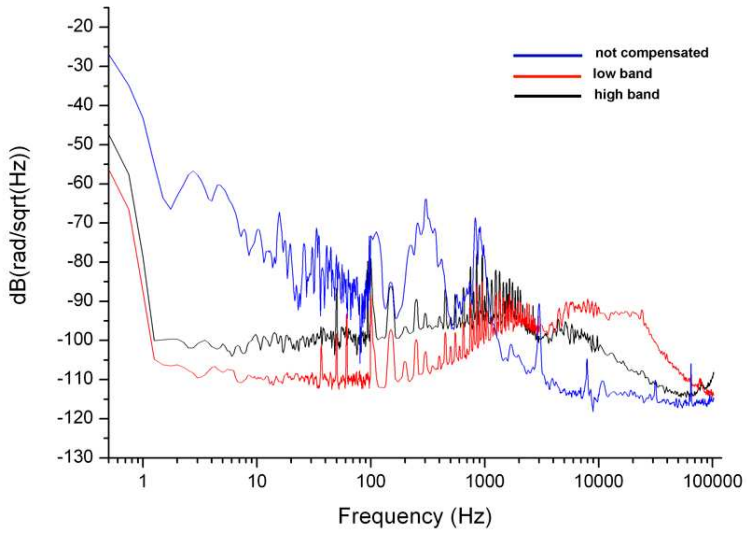

Figure 4.27: Residual phase noise for acoustic bandwidth compensated *PLL*, blue line not compensate, *black line* higher compensation bandwidth, *red line* lower compensation bandwidth.

in picture (4.28). The beat note is detected by a photodiode $G4176 - 03$ from HAMAMATSU connected to a *bias–tee*, two amplification stages lead to a signal output around $5 - 10$ dBm. The *PFD* integrated prescaler divide both input signals down to 1 MHz before generating the phase error signal. Such signal is driven to a Proportional–Integrator stage working as *loop-filter*, its output is divided into a slow control sent to the *ECL* piezo channel and a faster channel sent to the laser current driver, no direct modulation has been implemented for such loop. Unlike the *Raman master–slave* lock the proprieties of this *Phase Locked Loop* are non critical and higher residual phase noise, compared with the other implementation, will not affect the interferometer performances.

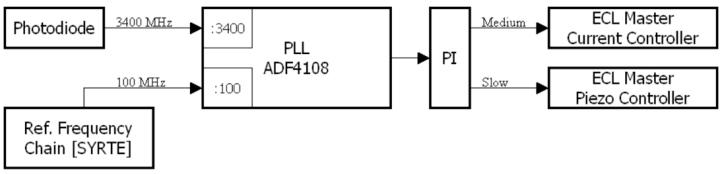

Figure 4.28: *Raman master* to *Reference Phase Lock* implementation [106].

Chapter 5

2D–MOT as cold atoms source

The *Two Dimensional Magneto Optical Trap 2D–MOT* can be considered as one of the simplest atom cooling and trapping system. It was introduced as an evolution of the first devices developed for neutral atoms velocity slowing down and then, as a new kind of collimated cold atoms source, have found an application in experiments operating into atom quantum–manipulation field. As we have already mentioned in the description of the interferometric sensor development, the production of a cold atomic beam as a source of cold atomic sample can represent for many experiments a solution to the problem of achieving a three dimensional atomic trapping and cooling preserving a low background pressure in the main physics chamber but also with a big loading rate enhancement. For the *Bose Einstein Condensate* experiments, working with a large number of atoms loaded, but also with a very low background pressure requirement, the employment of a source of this kind is fundamental. In our framework of the interferometers and of the atomic fountains, just like in the last case, these are also important conditions; it's very important shortening the experimental integration time but also ensuring at the same time an *Ultra High Vacuum* regime in order to minimize interaction of atomic sample and of the *Raman* beams with background gasses. Such further interactions can result in an additional output phase shift for the interferometer.
Considering for example the *gravimetric* application of the atom interferometer, the integration speed could be a very important parameter allowing the device to resolve possible temporal acceleration changes originated from local mass density changes; as it holds in presences of tides cycling or of volcanos steady condition variation or also of underground slides. A repetition rate of $\gtrsim$ 2 Hz with an initial number of atoms of 10^{10} atoms in the the sample can be considered perfect. This construction it's easily extended to the space inertial sensors development, this other sensors category must be able

to resolve accelerations changes due to spacecraft–satellite motion or space environment changes. The extension to microgravity tests with interferometers by means of dropping experiments, as for *Drop Tower*, or of parabolic flies, is consequent because of the short microgravity condition time. Specific issues concern differential accelerometers and *gradiometeric* sensors where a double acceleration measurement is performed at the same time between two falling atom clouds. Also in this experimental configuration an high sample loading rate is useful: in terrestrial conditions a time distance of the order of $\lesssim 100$ ms between the two sample launches can be considered as typical. The Space Atom Interferometer implementation illustrates in details how it's possible to develop a complex apparatus from the integration of an atomic source in a main apparatus for atomic manipulation. A differential vacuum condition between the two chambers is achievable connecting them by means of small diameters tubes and separating the two vacuum environments by means of specific diaphragm (section 2.5 and picture 2.8): a background gas pressure increase on the *2D–MOT* side will result in an atomic flux enhancement without any effect on the main chamber *Ultra High Vacuum* condition.

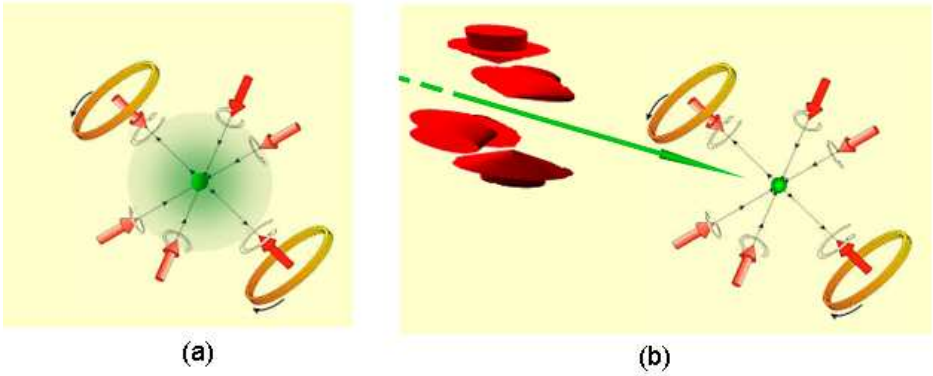

Figure 5.1: Atomic sample loading in a *3D–MOT*: (a) direct loading from background gas, (b) loading from a cold atom flux generated from a *2D–MOT* as a source.

In this chapter we report the experience with the *2D–MOT* device as an atomic cold atom source for the MAGIA[1] experiment. As illustrated in the introduction to this thesis such experiment operates as an atom interferometer in gradiometric regime. Before the integration of the *2D–MOT* in the

[1]MAGIA: **A**ccurate **M**easurement of **G**ravitational constant by means of **A**tom **I**nterferometry

main apparatus the atomic samples were loaded directly from the rubidium background gas and its pressure was controlled from an heated dispenser. In order to guarantee a short time distance between two launches and a reasonable repetition rate, an atomic sample *juggling* technics was implemented [67, 68, 69, 73].
In the following section we report some issues about the *2D–MOT* as a specific cooling and trapping setup and also some specific characterization measurements relative to the MAGIA *2D–MOT* performed before and after the integration on the main apparatus.

5.1 *2D–MOT* general features

The general *2D–MOT* setup features are illustrated in picture (5.2) where the basic elements and tasks are shown. The atomic gas (Rubidium in our case) is loaded into a vapor cell from a heated reservoir, lateral optical accesses allow the entrance of two cooling beam pairs, σ^+ and σ^- polarized, in counter-propagating configuration; an additional overlapped *repumping* beam is needed as already presented for the general magneto–optical trapping theory (see sec. (1.3.3)). Two sets of external coils generate a magnetic field gradient ranging around 10 G/cm $\div$ 20 G/cm (depending on the specific setup) with zero field on the symmetry axis. As we are going to see besides the cooling power and the magnetic field implementation, the geometric layout and the total length must be considered as strongly characterizing parameters for this specific apparatus. Unlike other atomic velocity slowing devices (such as the *Zeeman slower* [37, 38]) the cooling scheme works just on the radial direction and in principle no direct cooling action operates on the longitudinal direction; thus, at a first look, no effects on atomic longitudinal velocity distribution should be expected; at most we could suppose some heating due to statistical mechanical effects.
The indirect cooling effect on the longitudinal velocity distribution of the atomic beam can be explained starting form a simple geometric and kinematic reasoning. Considering a given atomic longitudinal velocity v_z, because the finite length of the cooling cell also identifies a finite longitudinal transit time, this means that we also dispose of a finite time to slow a given radial velocity v_r: thus, if the longitudinal velocity is too high, the transit time could be not enough to slow the radial velocity and to collimate the atom into the beam. This means that a lengthwise fast atom can not pass through the output diaphragm. From this point of view we can say that in the limit that $L_{cell} \to \infty$ then it holds $v_{z\ out} \to v_{thermal}$.

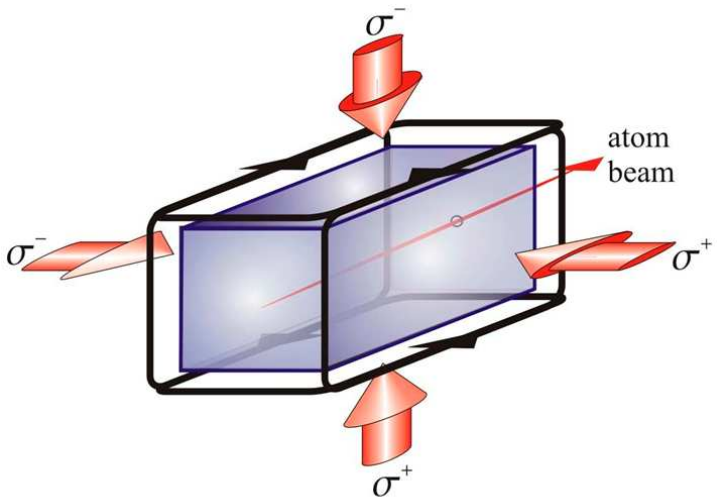

Figure 5.2: General scheme for a *2D–MOT*. Red arrows indicate the four cooling beams, the marked black path indicates the current directions into the four coils generating quadrupole magnetic field, the blue box is a sketch for the cooling cell.

A brief review of sources of slow neutral Atoms *2D–MOT*

We report here a very short description of the technics employed in various experiments to implement a source of cold atoms beams.

- *The Zeeman slower* was in term of time one of the first method applied for the production of slow atoms beam [37, 38], [44]. This method is based on the scattering cooling force generated by the electromagnetic radiation pressure. The atomic longitudinal velocity distribution is directly addressed by a cooling beam directed in the axial direction and opposite to the atomic propagation. The laser field works at a constant frequency and a *Doppler* compensation for the atomic speed reduction is realized by means of a non uniform axial magnetic field that shifts the atomic *Zeeman* hyperfine sublevels. A calibration of such magnetic field gradient and of the laser field frequency leads to a spatial matching between the atomic transition frequency and the laser detuning: once atoms travels into a tube and the velocity decrease the magnetic field intensity changes the in such a way to always get the laser beam in resonance with the laser field. A sketch of the experimental realization is illustrated in picture (5.3). Typical longitudinal velocities

are $\lesssim 15$ m/s with a big atomic flux $\approx 10^{11}$ atoms/s; a price in terms of large atom beam divergence is payed due to a transversal heating. Such effect is due to the configuration with the single cooling direction and it is strictly connected to the random nature of the spontaneous emission and to its isotropic behavior. For our purpose the *The Zeeman slower* is unsuitable also because of the typical long dimensions.

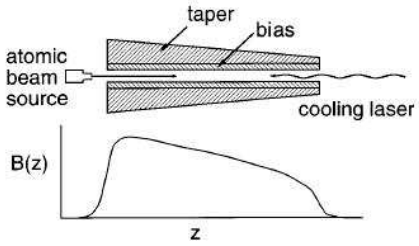

Figure 5.3: Scheme for a *Zeeman Slower*: a scaling coils winding results in a not uniform magnetic field with intensity variation along the z axial direction, the cooling beam is applied along the same direction.

- *3D–MOT as a source* and *Low Velocity Intense Source (LVIS)* [39, 40, 41, 45]. In this category we are grouping some devices directly derived from *3D–MOT* configuration with the introduction of some tricks breaking the geometrical symmetry in order to generate a cold atomic beam output. Starting from a *3D–MOT* with six counter–propagating beams the basic idea could be to make an hole into one of the reflection mirrors. This modification creates a retro–reflection shadowed cylinder in the central part of the cooling region that results in a power unbalance in the cooling force for the chosen direction (*extraction column*): the output beam rises thanks to this unbalance. The diverging atoms, whose radial velocity are large enough to be captured in the *extraction column*, move out the cylinder, but they can be recaptured and recycled into the cooling process inside the larger three–dimensional cooling region.
  In this framework, the fundamental characteristic that distinguishes the different solution stands into magnetic field configuration along the output axis. A very important device is the *LVIS* where a couple of coils in *anti-Helmholts* configuration are involved to generate a magnetic field gradient along the longitudinal axis (ranging around $5 \sim 20$ G/cm) (see picture 5.4). Typical results for this kind of devices are a very narrow longitudinal velocity distribution with $\langle v \rangle = 14$ m/s

and $FWHM = 2.7$ m/s and a total flux of 5×10^9 atoms/s. An intrinsic inconvenient is the big cooling power required $\gtrsim 500$ mW.

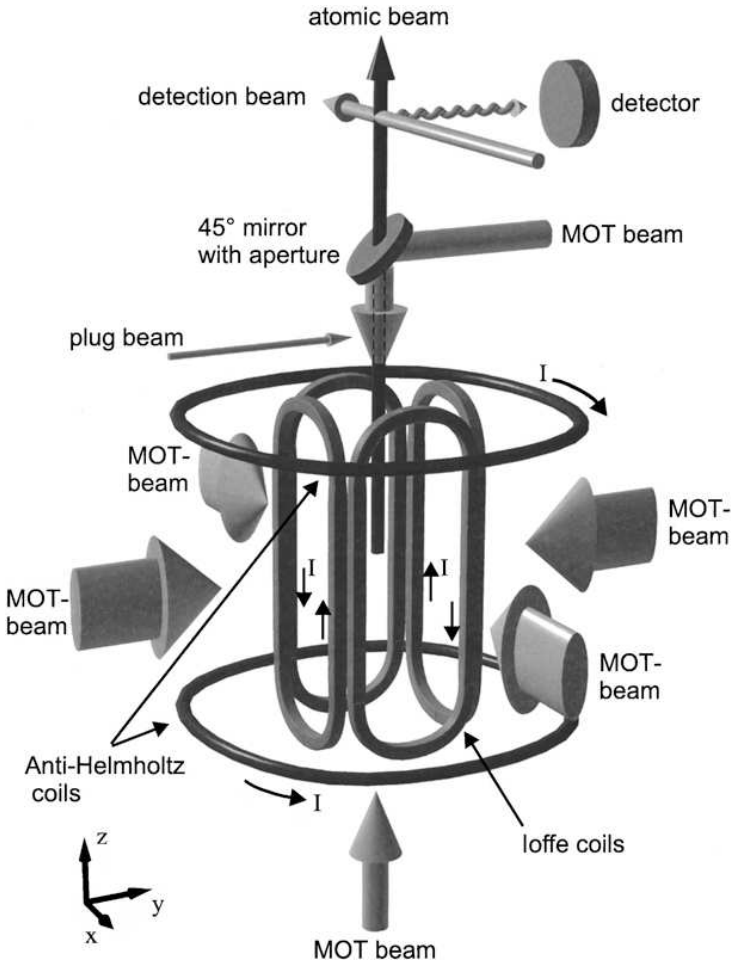

Figure 5.4: *LVIS* two dimensional trap, Experimental apparatus from Dieckmann et al. comparing performances of *LVIS*, *2D+ MOT*, and *2D–MOT*. In the last two configuration the *anti-Helmholts* coils are not working without additional field generation. For the bare *2D–MOT* configuration also the vertical beams are plugged off [41].

- *2D–MOT*, *2D+ MOT*, *2D–MOT with pusher* [41, 42, 43, 45, 46]
  The *2D–MOT* device basic features were already described in the previous section; we have seen that it consists in a simple transverse two dimensional optical cooling system with coils providing a quadrupole magnetic field with zero field along the whole zero axis. No direct cool-

ing operates in the longitudinal direction.
2D+ MOT is a typical improvement evolution of the basic device, here we consider a configuration with two independent laser beams in the longitudinal direction, with different intensities but without any additional magnetic field component contribution in such direction. The two laser beams realize a power unbalanced optical molasses in the axial direction that results in an unbalanced pressure radiation on the atoms with a consequent pushing–out effect (also shown in picture (5.4)). It yields a flux of slow atoms comparable with the one from the *LVIS*, but it can require an order of magnitude of less laser power than the latter.
2D–MOT with pusher is the typical configuration adopted for our specific experimental implementations. A simple fixed frequency *pushing beam* is added in axial direction from the rear side to the output side. This results in a very little effect in terms of total atom flux enhancement but gives rise to a narrower velocity distribution and to a slower *peak velocity*. The role played by the *pushing beam*, confirmed in our experience, is to address some atomic longitudinal negative velocity classes ($v_z < 0$). A class of atoms moving in opposite direction to the cell output is addressed from the radiation, the velocity is slowed down till to the motion inversion, such atoms are sent back into the right output direction.
A possible further improvement can be derived from *2D+ MOT* or from *2D–MOT + pusher* configuration by means of frequency control on the axial beams/ molasses. A frequency tuning on such beams could drive to a an enhancement on the axial capture velocity.

We suggest for a detailed approach to the comparison between the cold atomic sources configurations to consider as a starting point the paper from Dieckmann et al. [41].

5.1.1 A model for the cooling

Starting from the magneto optical trapping theory for neutral atoms (sec. 1.3.3) it's possible to draw a model for the *2D–MOT* as a specific setup, focusing on working principles and on characterizing parameters [42, 67]. In this framework it can be defined the capture radius r_c as the distance from the axis where the cooling laser detuning δ from resonance equals the atomic *Zeeman* shift due to magnetic field gradient: if g is the *Landè factor* and μ_B is the *Bohr Magneton*, under the cylindric symmetry hypothesis we can

express such definition as follows:

$$\delta = \frac{1}{\hbar}\mu_B g r_c \nabla_r \cdot B \tag{5.1}$$

Considering a cyclic process of absorbtion-emission with a timescale given from the transition linewidth, for the cooling process of rubidium atoms it follows a cyclic rate of $\Gamma = 2\pi \times 6\ MHz$ (see A.1). An atom with a radial velocity of v_r takes a time τ to be slowed to zero by $n_{ph} = \tau \times \Gamma/4\pi$ photons collision, thus from the momentum transfer budget it holds:

$$\hbar k \Gamma \tau = m v_r \tag{5.2}$$

We can suppose that the faster trappable atom (in the radial direction), is captured just after having traversed the whole capture cylinder o diameter $2r_c$. This means that if v_c is its radial velocity, the process will take a time $\tau_{max} = 2r_c/v_c$ and from the equation (5.2) we can define the maximum radial *capture velocity* in the cooling cell:

$$v_{r,ca} = \sqrt{2r_c \frac{\hbar k \Gamma}{m}} \equiv v_{c0} \tag{5.3}$$

For MAGIA *2D–MOT* device a typical value for the *capture velocity* is around 47 m/s (see sec. 5.2). From the other side it's possible to define a *longitudinal critical velocity* $v_{z,cr}$ as the velocity above that the longitudinal transit time $\tau_z = z/v_z$ is shorter than the radial transit time τ_{max}. In this picture $v_{z,cr}$ is position dependent and can be defined point by point on z axis from the condition $\tau_z = \tau_{max}$ and from (5.2), it follows:

$$v_{z,cr}(z) = \frac{\hbar k \Gamma}{m} \frac{z}{v_{c0}} \tag{5.4}$$

atoms with longitudinal velocity above the critical one $v_z > v_{z,cr}$ still have a chance to be captured if their radial velocity is below a certain *radial capture velocity*, thus inverting (5.4) and summarizing in a compact way the different situations for the *radial capture velocity*

$$v_{r,cap} = \begin{cases} \sqrt{2r_c \frac{\hbar k \Gamma}{m}} = v_{c0} & \text{if} \quad v_z < v_{z,cr} \\ \frac{\hbar k \Gamma}{m} \frac{z}{v_{c0}} = \frac{v_{z,cr} v_{c0}}{v_z} & \text{if} \quad v_z > v_{z,cr} \end{cases}$$

For a *2D–MOT* the *radial capture velocity* $v_{r,cap}$ is constant below a certain *longitudinal critical velocity* $v_{z,cr}$ and, below this value, it drops down as $1/v_z$; thus in a asymptotic picture the *capture velocity* becomes:

$$v_{r,ca}(v_z) = \frac{v_{c0}}{1 + v_z/v_{z,cr}} \tag{5.5}$$

The model for the atomic cloud is similar to other general atomic cooling and trapping systems, close to the center atoms experiment a friction plus a restoring harmonic force (see 1.3.3 at page 80) in the form

$$F = -m\beta v_r - m\omega_{trap}^2 r \tag{5.6}$$

where parameters depend on laser detuning from resonance δ, intensity (saturation parameter $s = I/I_{sat}$), magnetic field gradient, and recoil frequency $\omega_{rec} = \hbar k^2/2m$, as it follows:

$$\beta = 8\ s\ \omega_{rec}\frac{2|\delta|/\Gamma}{(1 + 4\delta^2/\Gamma^2)^2} \quad \text{and} \quad \omega_{trap}^2 = \beta\frac{\mu_B g\ gradB}{\hbar k} \tag{5.7}$$

the motion equation in radial direction for an atom in the trap is the equation of a dumped harmonic oscillator

$$\ddot{r} + \beta\dot{r} + \omega_{trap}^2 r = 0 \tag{5.8}$$

In a statistical framework, a diffusion coefficient must also be considered; a steady state for atom velocity and spatial distribution is well definite as solution of the *Fokker–Plank* equation [2] (for a detailed treatment see [36]):

$$w(v, z) = \frac{1}{\sqrt{2\pi}u}e^{-v_r^2/2u_r^2} \cdot \frac{1}{\sqrt{2\pi}s}e^{-r^2/2s^2} \tag{5.9}$$

A gaussian distribution is found, with the transversal velocity and position width given from:

$$u_r = \sqrt{\frac{k_B T_r}{m}} \quad \text{and} \quad s_r = \sqrt{\frac{k_B T_r}{m\omega_{trap}^2}} \tag{5.10}$$

From this treatment it is possible to define a *radial temperature* dependent on laser detuning from resonance

$$T_r = \frac{1 + \alpha}{8}\frac{\hbar\Gamma}{k_B}\Big(\frac{2|\delta|}{\Gamma} + \frac{\Gamma}{2|\delta|}\Big) \tag{5.11}$$

This equation represents the extension to the specific case of the generic equation (1.130) at page 75 defined for a three dimensional optical molasses.

[2] $\frac{\partial w}{\partial t} + v\frac{\partial w}{\partial r} = -\frac{\partial}{p}(F\ w) + \sum_{i=x,y,z}\frac{\partial^2}{\partial p^2}(D_{ii}w)$ where F is the force and D_{ii} the momentum diffusion tensor describing the broadening of the atomic momentum distribution, it accounts for the quantum fluctuations.

for the three dimensional setup Here the parameter α is a diffusion coefficient along $r - axis$ for circular polarized light, it takes the value 2/5. From this equation the minimum value for *2D–MOT radial temperature* is reached for $\delta = \Gamma/2$ and it is of the order of the *Doppler temperature* $T_{r,min} \approx T_D = \hbar\Gamma/2k_B$, about 140 μK for ^{87}Rb atoms.

5.1.2 The Rate Equations model for the *2D–MOT*

As in the paper from Shoster et al. [42] it's possible to give a theoretical description of the flux of a *2D–MOT* in terms of rate equation. The flux for atomic longitudinal velocities belonging to the interval $[v_z, v_z + dv_z]$ can be written as:

$$\hat{\Phi}(n, v_z) = \frac{\int_0^L R(n, v_z, z) exp(-\Gamma_{coll}(n_{tot})z/v_z)dz}{1 + \Gamma_{trap}(n_{tot})/\Gamma_{out}} \tag{5.12}$$

where Γ_{trap} identifies loss rate for collisions with the background gas, Γ_{coll} the output–coupling rate from the diaphragm and Γ_{coll} another loss term due to light assisted collisions (see also [67]). The total flux is given from the integral of (5.12) over all longitudinal velocity classes as follows: $\Phi = \int_0^\infty \hat{\Phi}(n, v_z)dv_z$.
The loading rate $R(n, v_z, z)$ can be derived as the flux of atoms through the cooling volume d considering only trappable radial velocities (see eq. 5.5) and weighting it with the radial part of *Boltzmann* distribution [3].

$$R(n, v_z, z) = nd\frac{16\sqrt{\pi}}{u^3}e^{\frac{v_z^2}{u^2}} \int_0^{v_c(v_z,z)} v_r^2 e^{\frac{v_r^2}{u^2}} dv_r \tag{5.13}$$

The velocity $u = \sqrt{2k_BT/m}$ is the most probable velocity for the *Maxwell–Boltzmann* distribution and T is the vapor temperature. Substituting expression (5.13) in (5.12) we find:

$$\begin{aligned}\hat{\Phi}(n, v_z) \;=\; & \underbrace{\frac{nd}{1 + \Gamma_{trap}(n_{tot})/\Gamma_{out}}}_{\text{A}} \frac{16\sqrt{\pi}}{u^3} \underbrace{\frac{v_z}{\Gamma_{coll}(n_{tot})}}_{\text{B}} \\ & \times e^{\frac{v_z^2}{u^2}} \underbrace{\Big[1 - exp\Big(-\Gamma_{coll}(n_{tot})\frac{L}{v_z}\Big)\Big]}_{\text{C}} \\ & \times \int_0^{v_c(v_z,z)} v_r^2 e^{\frac{v_r^2}{u^2}} dv_r \end{aligned} \tag{5.14}$$

[3] Maxwell–Boltzman distribution $f(v) = 4\pi\Big(\frac{m}{2\pi K_B T}\Big)^{3/2} v^2 e^{-\frac{mv^2}{2K_B T}}$

The collision rate for light assisted collision is given by $\Gamma_{coll} = n_{tot}\langle v\rangle\sigma$, where σ is the effective collision cross section ($\sigma_{eff} \approx 1.8 \times 10^{-12}$ cm^2 [4]). The terms A and B in equation (5.14) express the dependence from atom density, thus form vapor pressure, whereas term C contains also the dependence from the device length L. From the reached viewpoint some useful observation can be made to understand few topics about the *2D–MOT* behavior under parameters variation.

- Increasing the ***2D–MOT* length**
  - Higher longitudinal atomic flux: also faster atoms can be captured.
    For big increases of length $L > \langle v_z\rangle/\Gamma_{coll}(n_{tot})$ the flux exhibits saturation and becomes independent from the length (term C)
  - The mean longitudinal velocity $\langle v_z\rangle$ increases .
    Above the saturation length there are no total flux increments any more but only a mean velocity increase $\langle v_z\rangle \rightarrow \langle v_{thermal}\rangle$.
- **atomic density** changes (pressure)
  - *Low Pressure*: atomic flux linear increment, the $n/(1+\Gamma_{trap}(n_{tot})/\Gamma_{out})$ dominates in eq. (5.14)
  - *High Pressure*: collisional loss dominates with the term $1/\Gamma_{coll}(n_{tot}) \sim 1/n_{tot}$, atomic flux decrease. For a given value of the length L, of the magnetic field gradient, and of the cooling beam parameters, an optimal pressure value maximizing the atomic flux can be found.

5.2 *2D–MOT* Setup

The general opto–mechanical setup for the *MAGIA 2D–MOT* is shown in picture (5.5): it consists in a titanium made vapor cell of dimensions $25 \times 25 \times 90$ mm^3, the rubidium evaporates from an heated reservoir and accesses to the cell. The optical access for the cooling beams is guaranteed by four rectangular windows ($15\times80\times3$ mm^3) glued on each side. Two sets of coils of dimensions 15×5 mm^2 and 100 windings, in *anti-Helmholtz* configuration, attached to the cell, provide for a magnetic field gradient of 20 G/cm at 1.5 A. Cooling beams are split into three paths by a system of two 24.5 mm polarizing beam-splitter + $\lambda/2$ waveplate + mirror. On the other side three

[4] see [41] and [42]

mirrors provide for the counter–propagation, and six $\lambda/4$ waveplate provide for the circular polarization. The described setup configures three consecutive cooling cells delimitated form the couples mirror–polarizer (see picture). An additional beam is coupled on the axial direction for the pushing effect plugged from a 2 mm rear side hole.

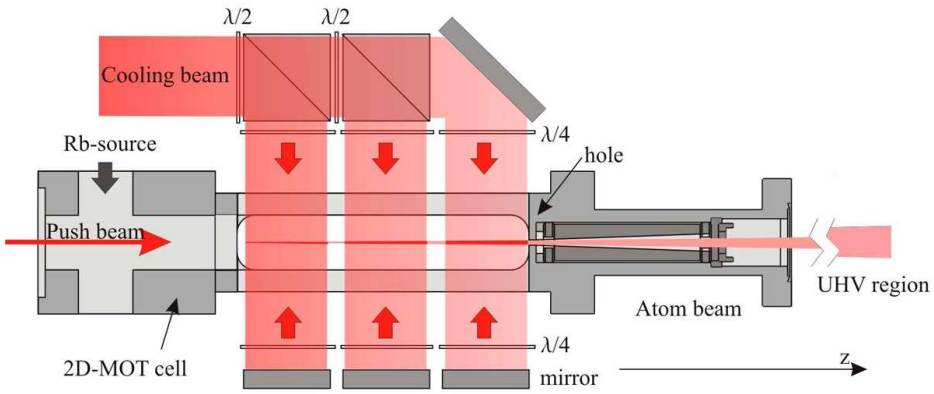

Figure 5.5: Technical Scheme for *MAGIA 2D–MOT*: a lengthwise cut

5.2.1 Laser system for the *2D–MOT*

The laser system configuration adopted for the *2D–MOT* is typical for a Rubidium cooling and trapping apparatus (see section 1.4). On the other side a frequency and cooling power optimization is furthermore needed in order to adopt to the specific geometric and magnetic configuration. Talking about tests and characterizations described in this chapter it's important to premise that two different lasers implementations were used before and after the integration on the main apparatus. In picture (5.6) the definitive setup is illustrated: the cooling laser was replaced by an *External Cavity Diode Laser* injecting a *Tapered Amplifier*, both devices are home made and of the same kind adopted for the transportable devices (see sections (3.1) and (3.3)). The amplifier utilized here is different from the ones for *Raman* board and for *SAI* because the lower output power (500 mW). In the first setup the *pusher* frequency was the same of the cooling beams whereas with the new implementation an independent frequency control has been realized for it by means of an *AOM* double pass. By means of *pusher* frequency fine tuning or by the application of a frequency sweep on it, it has been preserved the possibility to address largest atomic longitudinal velocity classes. A frequency sweep on the *pusher* could be useful to realize a complex detuning

	stand alone		*integrated*	
	freq.	pw.	freq	pw.
reference	$\nu_{2\to3} - 184.2$ MHz	$\sim$	$\nu_{2\to3} - 184.2$ MHz	$\sim$
cooling	-3Γ	110 mW	$\simeq -\Gamma$	≤ 140 mW
repumper	$\nu_{2\to3} + 5.6\ MHz$	6 mW	$\nu_{2\to1} + 5.6$ MHz	≤ 10 mW
pusher	$-3\ \Gamma$	1 mW	$-\Gamma \div -2\Gamma$	1 mW

Table 5.1: *2D MOT* Typical operative parameters, in blue optimized parameters, for post-integration operation parameters optimization details see text. $\Gamma = 2\pi 6.065(9)$ MHz, ^{87}Rb atomic natural linewidth (see app. A and [141])

changing axial optical molasses (see sections (5.1) and (1.3.1)).
Another significative improvement from the old to the new configuration concerns the *repumper* laser. In the first setup the light field was derived directly from *MAGIA repumper* thus it was limited to 6 mW of total power; in the new version the latter beam was utilized as injection of another laser without cavity to recover much power.
As we are going to see also different optimum operative parameters were found for *2D–MOT* before and after the integration due probably to the different operative conditions.
For both laser configurations cooling laser field is frequency locked to the *MAGIA* experiment *reference* laser that is locked to a rubidium saturation spectroscopy. The reference transition is $F = 1 \to F' = 3$ from $Rb\ D_2$ and the laser field is down shifted of 184.2 MHz from there by a double pass on an *AOM* (thus it has $\nu_{ref} = \nu_{2\to3} - 184.2$ MHz) (see [73]). The *repumping* beam is slight *blue–detuned* from the transition $F = 1 \to F' = 0$, $\nu_{rep} = \nu_{2\to1} + 5.6\ MHz$. Typical laser parameters are resumed into the table (5.1) parameters for the stand alone *2D–MOT* operative conditions must be considered as the optimized atomic flux values or hardware power–limited whereas details about optimized parameters for the integrated operative conditions are discussed into the incoming text.

5.3 *2D–MOT* characterization measurements before the integration

The most important parameters for a *2D–MOT* characterization are the atomic flux and the longitudinal velocity distribution. Of course the knowl-

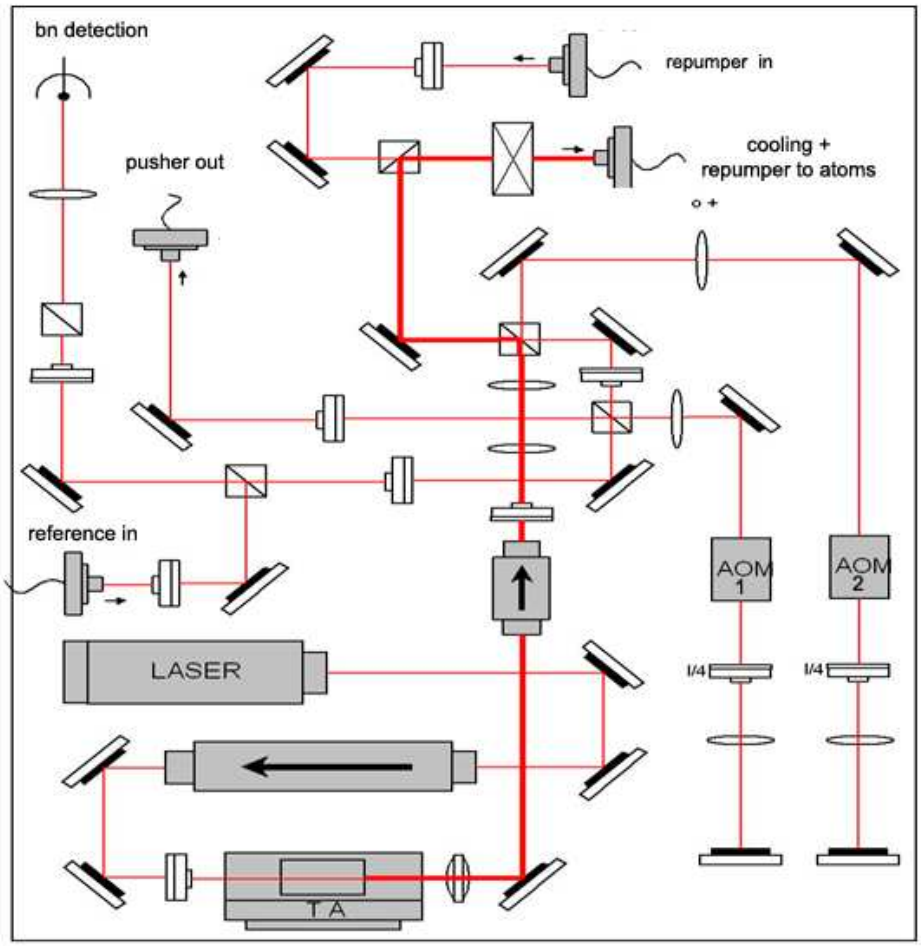

Figure 5.6: Cooling Laser Setup for *MAGIA 2D–MOT*. Double pass in *AOM1* shifts the cooling laser frequency of 146 MHz and *AOM2* allows a frequency control on the pushing beam.

edge of their dependence on lasers parameters and on vacuum parameters is fundamental for the optimization of the basic performances. Moreover we must recall that the atomic flux is strictly connected to the loading rate for a *3D–MOT* loading configuration. On the other side a good matching between a *2D–MOT* as a source and a *3D–MOT* also depends from the atomic beam divergence that is strictly connected with the radial temperature (see eq. (5.11) at page 179).
The longitudinal velocity distribution and the atomic flux measurement have been performed, before the integration in the main apparatus, by means of

two different methods, both based on atomic beam probing and on florescence detection[5]. The first method consists on a *Doppler Shift* measurement recorded from the fluorescence signal generated by crossing the cold atoms beam with a probe laser with a well known angle. The probe frequency beam has been spanned in order to to acquire the whole velocity distribution. The second one consists in a *Time–of–Flight* measurement method where the atom beam is crossed orthogonally to the propagation direction by a laser probe beam. In this case probe beam frequency is locked on the cooling transition, the velocity distribution results from the fluorescence signal by plugging on and off the atomic beam. In both cases we emphasize the differences between *2D–MOT* and *2D–MOT whit pusher beam.*

5.3.1 Velocity Distribution and Flux Measurement by *Doppler Shift* Method

This method is simply based on a *Doppler Shift* measurement recorded from a fluorescence signal generated crossing the cold atom beam with a well collimated laser beam with a well known relative angle. If $\vec{k}$ is the laser beam vector number, ν_0 the atomic resonance frequency and v the atomic atom velocity, the laser frequency seen from the atomic reference frame is given by:

$$\nu_{res} = \nu_0 - \vec{k} \cdot \vec{v} \tag{5.15}$$

In our setup the probe beam crosses the atomic beam with an angle of $\theta = 52°$, the choice of this value has been forced by the spatial *2D–MOT* configuration on our board respect to the experimental apparatus. Such parameter is the one affected by the biggest uncertainty for us. The experimental scheme is shown in picture (5.7), the probe laser beam is frequency spanned by a current modulation around the transition frequency ν_0. This spanning allows to achieve a complete addressing of longitudinal velocity classes the way to acquire the whole velocity distribution profile. By the other hand, part of the beam is sent to a doppler free saturation spectroscopy necessary for the signal timescale–to–frequency conversion, the well observable Rubidium transitions are involved as markers for such conversion. Working in the frequency domain, from the comparison between the absorbtion signal from the saturation spectroscopy spectroscopy and the fluorescence signal from cold atoms detection the doppler shift can be easily extrapolated (see picture 5.8).

[5]Also methods based on absorbtion are been performed by other groups but will be no discussed here

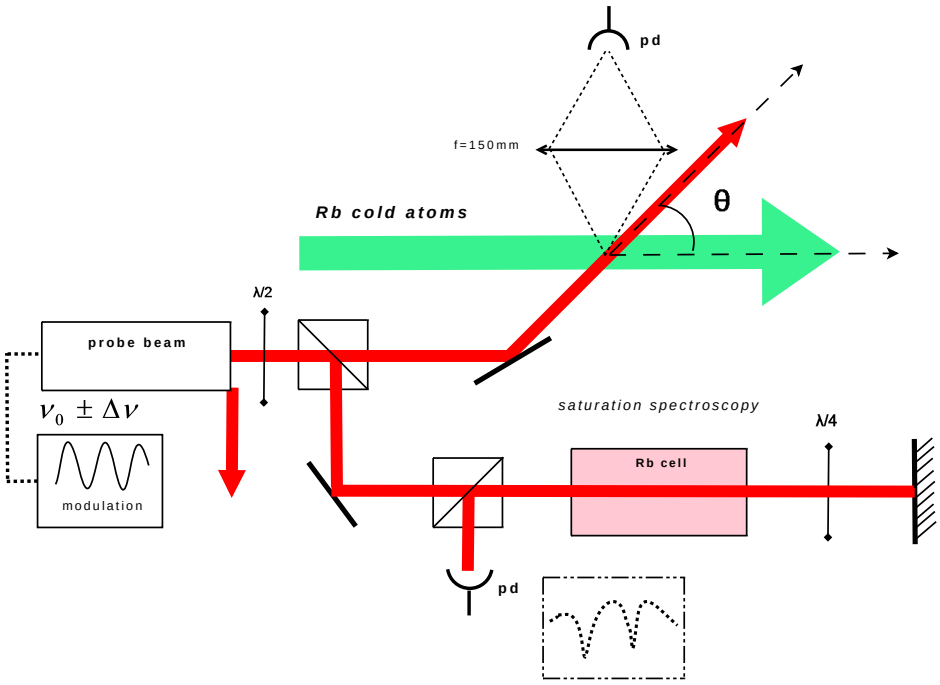

Figure 5.7: Atomic velocity distribution and flux measurement experimental scheme, *Doppler Shift* Method

The flux of a certain velocity class can be calculated from a light power diffusion measurement as a function of the detuning. If the total cold atoms flux is F and $f(v)$ is the velocity distribution function, it's possible to define the flux density at velocity v as $F\ f(v)$. The total power atomic absorbtion from the probe beam can be expressed as the convolution of the line broadening (see also eq.1.120 at page 72) waited with the velocity repartition function.

$$P_{abs}(\delta_L) = \int_0^\infty h\nu \frac{\Gamma}{2} \frac{s_0}{1 + s_0 + 4\frac{(\delta_L - \vec{k}\cdot\vec{v})^2}{\Gamma^2}} e\sqrt{2} F \frac{f(v)}{v} dv \tag{5.16}$$

Where Γ is the transition natural linewidth, e is the probe beam waist, $s_0 = I/I_s$ the saturation parameter with I the probe beam intensity and I_s the saturation intensity (see A and [141]). The fluorescence signal is related to the photons absorbtion by the relation:

$$S_{fluo}(\delta_L) = R\eta P_{abs}(\delta_L) \tag{5.17}$$

Where R is the conversion factor of the photodiode (V/W) and η the

light collection solid angle (in our case $\eta = 0.01$). From the equations (5.16) and (5.17) we find the expression for the fluorescence signal as[6]

$$S_{fluo}(\delta_L) = R\eta h\nu \frac{\Gamma}{2} s_0(\delta_L)\ e\sqrt{2}\ F \int_0^\infty \frac{s_0}{1 + s_0 + 4\frac{(\delta_L - \overrightarrow{k}\cdot\overrightarrow{v})^2}{\Gamma^2}} \frac{f(v)}{v} dv \qquad (5.18)$$

Performing the integral we can obtain a direct value for the total flux but loosing information about the velocity distribution. In order to obtain the velocity repartition function $f(v)$ in terms of fluorescence signal we perform the approximation to replace the Lorentian shape of the atomic resonance with a normalized Dirac's delta function:

$$\frac{s_0}{1 + s_0 + 4\frac{(\delta_L - \overrightarrow{k}\cdot\overrightarrow{v})^2}{\Gamma^2}} \simeq \frac{\Gamma\pi}{k\sqrt{2(1+s_0)}} \delta(\delta_L - k\cdot v) \qquad (5.19)$$

Now it's possible to express the flux density for velocity class $Ff(v)$ as a function of the fluorescence signal $S_{fluo}(\overrightarrow{k}\cdot\overrightarrow{v})$ thanks to the equality $\delta_L = k\cdot v$ that holds as a relation between the laser detuning and the doppler velocity shift.

$$Ff(v) = \left(\frac{2}{\Gamma}\right)^2 \frac{\sqrt{1+s_0}}{s_0} \frac{kv}{R\eta\nu he} S_{fluo}(\overrightarrow{k}\cdot\overrightarrow{v}) \qquad (5.20)$$

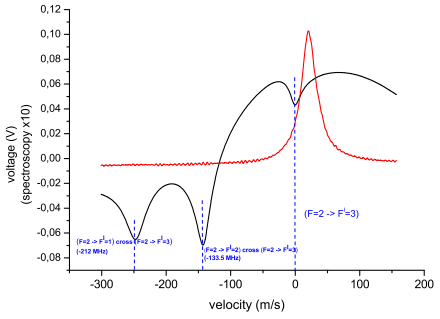

Figure 5.8: Comparison between saturation spectroscopy signal and doppler shifted signal from cold atoms.

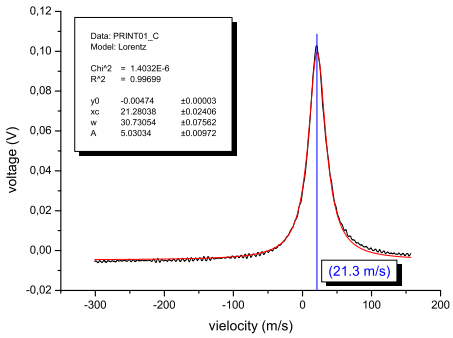

Figure 5.9: Cold Atoms velocity distribution, configuration *with pusher*.

[6] see also equation (1.120) at page 72

Optimal flux parameters for this *2D–MOT*, in stand alone operation, are: 130 mW of total cooling power, 3Γ frequency detuning from the cooling resonance, 1,3 mW for *repumping* beam power (hardware limited), *pusher* beam power 0,37 mW. From the velocity distribution acquisition (picture 5.9) we can extrapolate a *peak velocity* of 21.3 m/s, defined as the velocity for the most part of atoms. An estimation of the total flux can be obtained integrating the velocity distribution with the conversion provided from the equation (5.20), the value found is:

$$F \approx 3 \times 10^{10}\ atoms/sec$$

It's important to underline that measurement at this level are useful to have a reasonable idea of the order of magnitude for the *2D–MOT* operative performances. The flux ad velocity distribution measurement have been performed either with *2D–MOT* operating with *pusher* beam and without. No appreciable difference has been found for the the total flux whereas the configuration without pusher results in a higher mean velocity ($v_{peak} \simeq 26\ m/s$).

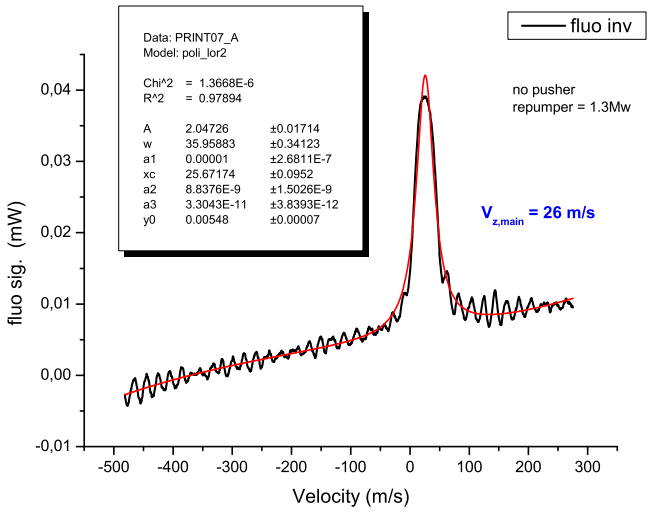

Figure 5.10: Cold Atoms velocity distribution, configuration *without pusher*.

For the estimation so far presented the natural atomic transition linewidth has been neglected; if we note that the conversion factor from frequency to velocity is $0,9$ MHz/(m $\cdot$ s^{-1}) this means that the transition width ($\Gamma \approx$ 6 MHz) corresponds to a velocity width of 7 m/s, so not far from the *FWHM*

of the velocity distribution. For this reason a new session of measurement with the *Time–Of–Flight* method is necessary.

5.3.2 Velocity Distribution and Flux Measurement by *Time–Of–Flight* Method

The basic principle of this method consists into a conversion of a time measurement into a velocity one once known the "*flying* distance". In our setup by switching on and off the atomic beam, we can measure how long the velocity classes take to travel from the cooling cell output to the probe position. The best way we have found to plug on and off the cold atoms beam has been to switch the *repumping* laser acting on an electronic controlled shutter and thus controlling the *MOT* process. As we are going to see the uncertainty coming from shutter time delay has been directly estimated.
The probe beam was crossing atoms beam in perpendicular way and fluorescence light coming from atoms has been collected by a lens on a *CCD* camera and acquired with the characteristic intensity shape (see picture (5.13)).
To obtain the complete velocity distribution directly in one shot from this method we have acquired the fluorescence signal as a function of time during the transient to cooling process stop (see picture 5.12). As we can see from the picture the fluorescence signal goes down once we plug off the *repumper* and the characteristic smooth profile following the plateaux constant signal already contains information about velocity distribution. The next step to obtain such distribution is to calculate the derivative of the curve outside the flat area and convert the time scale into a velocity scale ($atom\ path \times t^{-1}$). This way we obtain the picture for velocity distribution(5.12). With this method no approximation are made about the transition natural linewidth, the only systematic error sources that affect the measurement are the finite probe beam thickness that means a finite crossing time for the atoms and the finite shutting time to plug off the *repumper*. These effects drive velocity uncertainties of $0,2$ m/s and 2 m/s respectively. Now the value found for the *peak velocity* is $14,6$ m/s with an *HWHM* of 6.8 m/s, totally compatible with the values found with the *Doppler Shift* method.

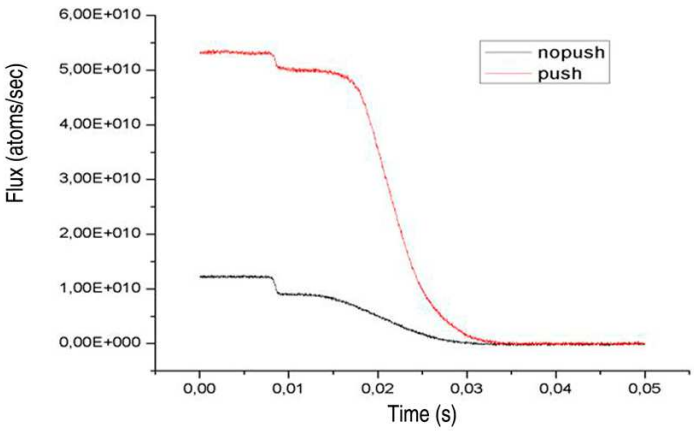

Figure 5.11: Total Atoms Flux decrease after switching off the *repumper* laser. Red curve for *pushing* laser on, black curve *pushing* laser off.

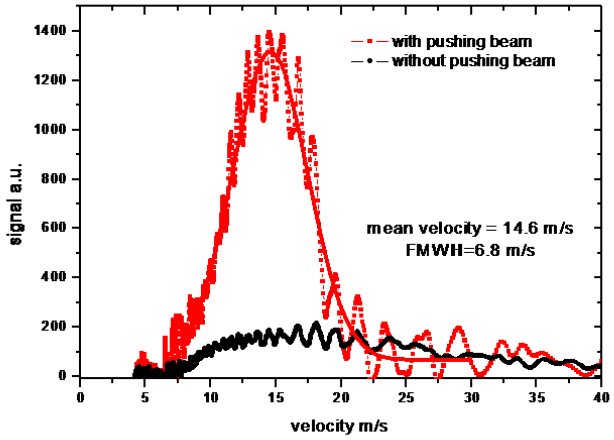

Figure 5.12: Atoms Velocity Distribution in *2D–MOT Time–Of–Flight* method. Red curve for *pushing* laser on, black curve *pushing* laser off.

In order to evaluate the atomic flux to calculate the conversion from the *Arbitrary Units* acquired from the *CCD* camera to the number of atoms passing through the probe beam in unit of time is needed.
We can start from considering a gaussian profile for the probe beam, thus it results that the acquired fluorescence shape can be fitted with a two dimen-

sional gaussian curve

$$s(x,y) = A\ exp\Big[-\frac{1}{2}\big(\frac{x-x_0}{\sigma_x}\big)^2 - \frac{1}{2}\big(\frac{y-y_0}{\sigma_y}\big)^2 \Big] + f \qquad (5.21)$$

Thus after the parameters evaluation from the integration it follows:

$$\int\int s(x,y)dxdy = A\ \sqrt{2\pi\sigma_x^2}\sqrt{2\pi\sigma_y^2} \quad = \quad 2.4\ \times\ 10^6 ADU \qquad (5.22)$$

If the camera's gain is 12.2 electrons/ADU, the efficiency is 0.4 (at 780 nm) and the solid angle through we collect the fluorescence is 7×10^{-4} the number of photons emitted is:

$$\begin{aligned} N_{photons} &= 2.4 \times 10^6 ADU \times \frac{12.2\ electrons/ADU}{7 \times 10^{-4}} \times \frac{1}{0.4}\frac{photons}{electrons} \\ &= 1\ \times 10^{11}\ photons \end{aligned}$$

If we also suppose that the transition is saturated by the probe beam we can say that each atom emits one photon every $\Gamma/2$ and if each atom spends $\approx 0.0025\ m/20$ m/s $= 1.24 \times 10^{-4}$ s into the laser beam each atom emits ≈ 42 photons as contribute to the camera picture. So the number of atoms detected is:

$$\begin{aligned} N_{atoms} &= \frac{1\ \times 10^{11}\ photons}{42 photons/atoms} \\ &= 25\ \times 10^8\ atoms \end{aligned}$$

the total flux can be evaluated dividing for the acquisition time (50 ms):

$$Flux\ =\ 5\ \times 10^{10}\ atoms/s \qquad (5.23)$$

In picture 5.14 a plot of the fluorescence signal from the cold atom flux versus the cooling power is shown (in A.U.), it's possible to see that for a power of 110 mW of cooling power the flux saturation is not achieved.

To have an estimation of the atomic beam divergence θ and of the radial temperature T_r the beam shape was acquired with the *CCD* camera in two consecutive points at a distance of $d = 1.7$ cm each other on the traveling path (pict.5.15). After a gaussian fit to estimate the transverse width the divergence found is $\theta \approx 23$ mrad (see picture (5.15)) and the radial temperature $T_r \approx 300\ \mu$K (values compatible with theoretical estimation (sec. 5.1)).

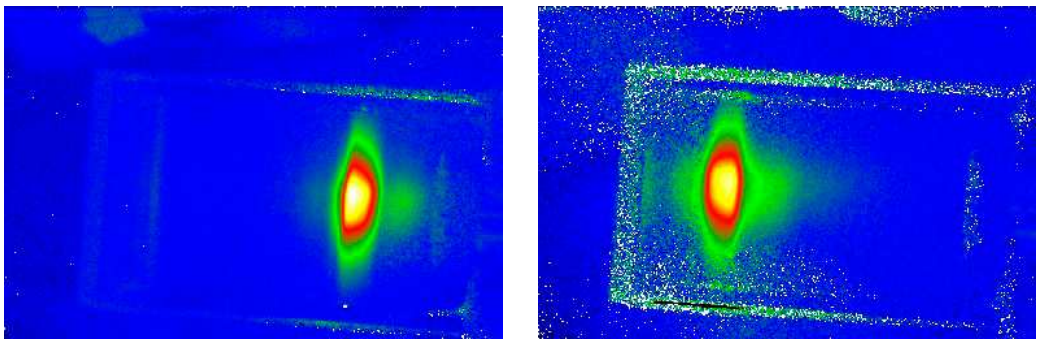

(a) position 1 (b) position 2

Figure 5.13: Fluorescence signal from CCD Camera: probe laser beam crossing *2D–MOT* atoms at 90 *degrees*, (position 1 and 2).

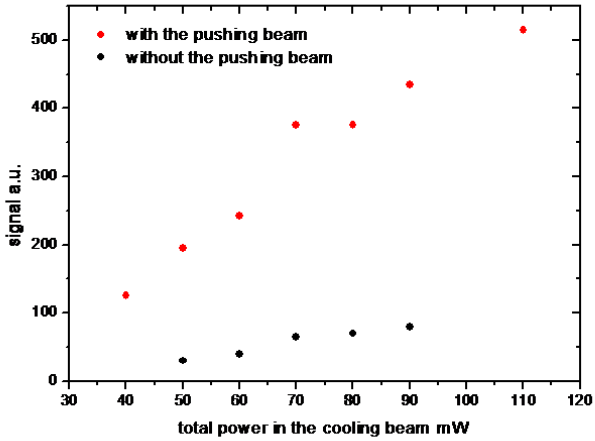

Figure 5.14: Fluorescence Signal from Atoms as a function of cooling beam power

5.4 Characterization measurement after the integration on the gradiometer

The measurement performed after the integration of the *2D–MOT* on the main apparatus have been finalized to confirm the advantages for the gradiometer in terms of the loading rate and background gasses pressure reduction. In this phase it has been not possible to perform a direct flux

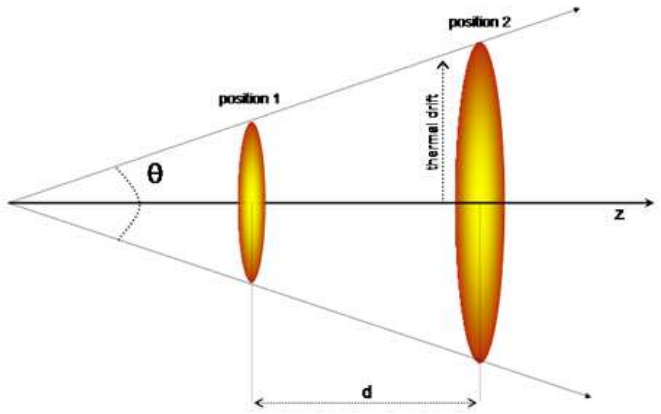

Figure 5.15: Sketch for cold atom radial thermal expansion and angular divergence in the *2D–MOT*

measurement by means of traditional methods as described so far; characterizing parameters have been determined from *3D–MOT* loading fluorescence signal acquisition. We did not implement an experimental setup for direct background gas pressure determination in the *2D–MOT*; thus we are going to refer to the rubidium dispenser temperature. A rough vapor pressure estimation can be derived as a superior limit from the *Antoine equation*[7]. The loading rate R has been evaluated by fitting the calibrated time varying fluorescence signal on *3D–MOT* loading law (see equation (1.147) with $N_0 = N(t = 0) = 0$):

$$N(t) = \frac{R}{\Gamma_c}(1 - e^{-t\Gamma_c}) \tag{5.24}$$

Fitting parameters are the stationary number of trapped atoms $N_{st} = R/\Gamma_c$ and Γ_c. Instead of trap lifetime τ it can be convenient to work with the collisional loss rate $\Gamma_c = 1/\tau$ that, as in equation (1.150), can be expressed in terms of collisional cross sections. It is also possible to account for different contributions from Rb background gas and from other gasses components as

[7] *Antoine equation* (derived from *Clausius-Clapeyron relation*) relates the vapor pressure P to the temperature T and to experimental parameters A,B,C:
$\log_{10} P = A + \frac{B}{C+T}$
and for rubidium
$P_{Rb}(T) = 10^{-4208/T+7.331}$

follows.

$$\Gamma_c = (\sigma_{Rb} n_{Rb} + \sigma_{bg} n_{bg}) \Big(\frac{3 k_B T}{m} \Big)^{1/2} \tag{5.25}$$

The atomic relative pressures can be simply evaluated from the *ideal gas law* $P_i = n_i k_B T$. With the actual setup there is no way to investigate the composition of background gas besides rubidium, but, at this level, we want just to address a comparison between background gas condition in the main chamber before and after the *2D–MOT* operative integration. We can thus assume the other background being composed from nitrogen ($\sigma_{bg} = \sigma_N = 3.5 \times 10^{-14}$ cm^2).
In order to estimate the differential pumping efficiency has been compared the background gas pressure in the main chamber generated from the traditional *3D–MOT* loading dispenser as single source, in typical and stationary condition, with the single contribution due to *2D–MOT* apparatus at full pressure regime but without atomic cooling operation.
As it was easy to expect the differential vacuum system drives a huge reduction in terms of rubidium background gas pressure, the result is shown as a comparison between the two configurations in picture (5.16); pressure is plotted as a function of *2D–MOT* rubidium dispenser temperature. The total rubidium reduction of background pressure in main chamber due to the *2D–MOT* effort is of two orders of magnitude: the total value can be now evaluated to 3×10^{-11} mbar. Of course the goal is realized if to such background reduction it corresponds at least a comparable *3D–MOT* loading rate.
A detail for the *Rb* background gas pressure in the *3D–MOT* chamber as a function of *2D–MOT* chamber background pressure is shown in picture (5.17a) whereas in (5.17b) there is a rough estimation for other components background gasses evaluated from equation (5.25). At this level we just find that the background gas component from other gasses contribution does not depend on the *2D–MOT* operative parameters.

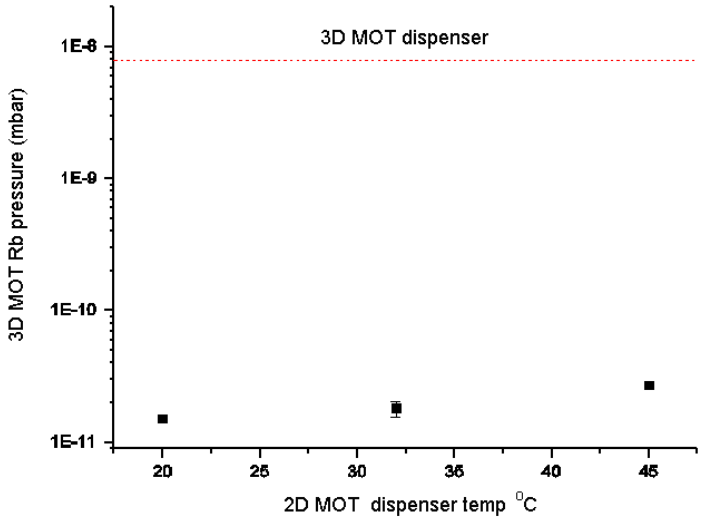

Figure 5.16: Rubidium background pressure in the main chamber of gradiometer apparatus as a function of *2D–MOT* rubidium background pressure, the latter can be evaluated from the dispenser temperature. As a comparison is plotted *Rb* pressure (mbar) generated from the *3D–MOT* dispenser measured at typical operative conditions (4 A) in the *MAGIA* experiment.

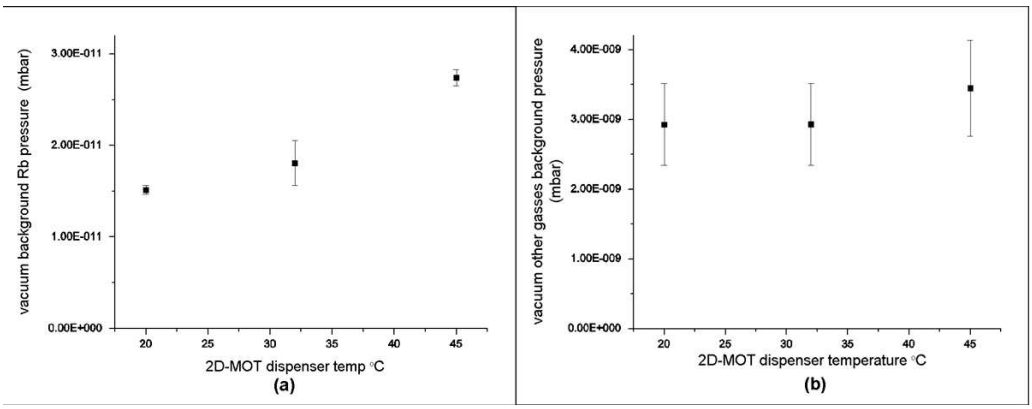

Figure 5.17: (a) Detailed trend for Rubidium background pressure in main chamber as a function of *2D–MOT* background pressure (dispenser temperature) (see 5.16), (b) estimation for the other gases contribution to the background pressure.

Once confirmed the big advantage due to the implementation of the cold atoms source for the background pressure we are going to find the best setup in terms of *3D–MOT* loading rate: typical operative parameters are changed optimizing the atomic sample loading for 300 ms. We start by the optimization of the *2D–MOT* flux as a function of the background gas in the device, the other initial parameters are shown in table (5.13). In picture (5.18) the resulting loading rate is shown in comparison with the loading rate resulting from the traditional method from the main chamber background gas. We can note that the cold atom source implementation results in a loading rate enhancement of a factor ≈ 6. On the other side is found a reduction of one order of magnitude from the atomic measured flux from *2D–MOT* (stand alone operation) to the *3D–MOT* loading rate (see results at page 188 and (5.23) at page 191), this discrepancy is not a surprising result: the two parameters must be considered as correlated but not the same size.
At this level we can not provide a complete explanation for the atomic loss. It is reasonable for now to consider that the our flux estimation for stand alone operation, provided in section 5.3, is characterized by a low accuracy, thus it can be affected by a large error and it must be considered just as a rough estimation for the order of magnitude. From another side it is also reasonable to consider that part of the atomic loss may be due to the cold atomic beam divergency. In fact, if the distance between the *2D–MOT* cell output and the center of the *3D–MOT* cell is $\lesssim 500$ mm, a divergency of 23 mrad leads to an atomic beam diameter at the center of the trap of ≈ 20 mm that is reasonably comparable or nearly larger than the *3D–MOT* capture radius (see [67, 73]).
As we have seen within the theoretical model framework for *2D–MOT* atomic flux we expect a linear enhancement at low pressure values and a decrement at high values due to collisions increase (equation 5.14 and text at page 181 for details). In the experimental plot it is possible to recognize a linear behavior of the flux from 25 °C ($\simeq 2.6 \times 10^{-7}$ mbar) up to 45 °C ($\simeq 1.5 \times 10^{-6}$ mbar), the upper is above rubidium melting temperature (38.89 °C) and corresponds to our hardware heating limit. Up to such limit no loading rate decrease have been recognized, at this level we can hold the *3D–MOT loading rate* from *2D–MOT* cold atoms source at:

$$R_{load} \approx 7 \times 10^9 \; atoms/s$$

From there a fine optimization of the flux as a function of the other parameters has been performed plotting the relative loading rate normalized to the peak value. We begin from a recognition of the dependence from the cooling beam power and from the frequency detuning (picture 5.19a-

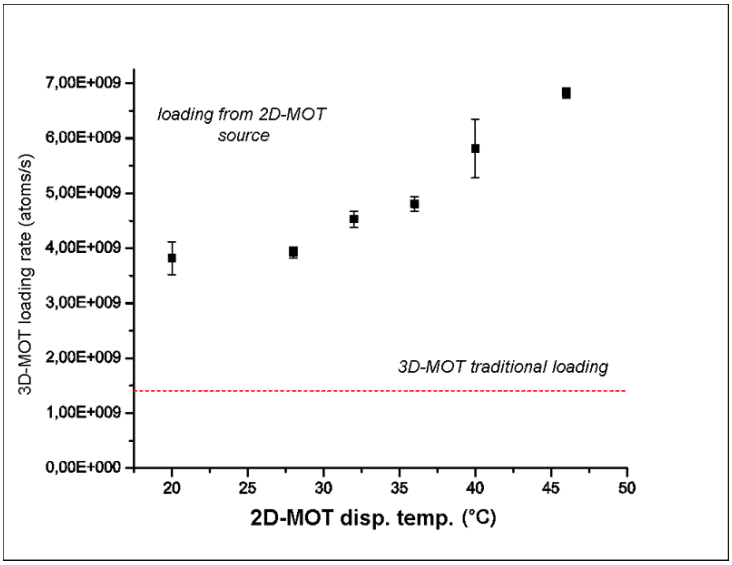

Figure 5.18: Loading rate for *3D–MOT* as a function of *2D–MOT* source background pressure (rubidium dispenser temperature), for comparison loading rate for traditional method with direct background gas loading (red line)

b). As it is shown, up to our maximum cooling beam power on the atoms (140 mW), no saturation effect is visible, the maximum atomic flux seems to be limited from hardware setup. In picture (5.19b) it is possible to note a drastic dependence of the loading rate from the frequency detuning from resonance; the flux is sharply maximized at $\delta = 7$ MHz $\simeq \Gamma$. This optimizing value is different from the value found for the stand alone working *2D–MOT* ($3\,\Gamma$). At the moment we don't have any specific investigation disposal about the reasons of such discrepancy, by other hand from the model we know that the cooling frequency detuning is strongly connected to the magnetic field gradient (eq. (5.1) at page 178), thus we can suppose an effective magnetic field condition change between the two configurations.

A similar optimization has regarded also the *pushing* beam power and its frequency detuning from the atomic resonance (picture (5.20)); as it was already found in the previous experience with the standing alone *2D–MOT*, an atomic flux reduction corresponds to high pushing beam power, the best value found for our device is 1 mW. The frequency dependence result is more interesting, a broaden peak is found ranging from 7 MHz up to 12 MHz, that means $\Gamma \div 2\Gamma$. From there it's possible to note a different optimizing frequency detuning for the *pushing* beam and for the cooling beams (plots 5.19b and 5.20b), this is due to the different tasks and implementation.

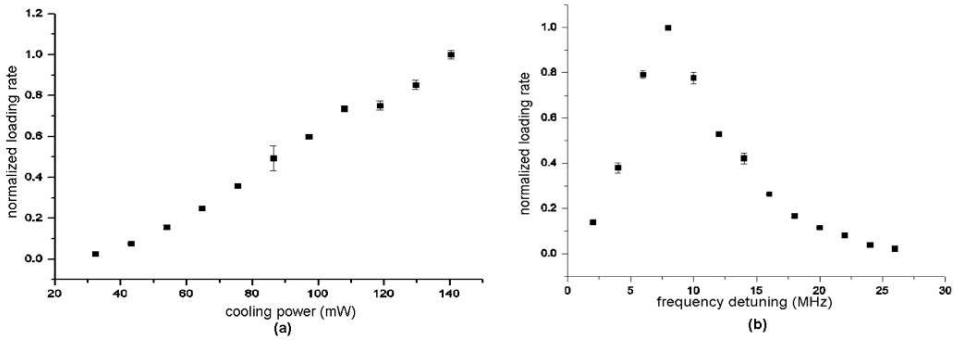

Figure 5.19: *3D–MOT* loading rate as a function of *2D–MOT* cooling total power (a) and as a function of cooling beam frequency detuning from resonance (b).

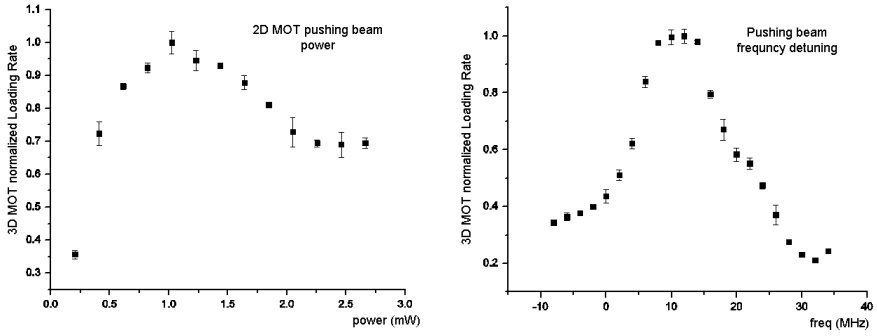

(a) (b)

Figure 5.20: *2D–MOT pushing* beam optimization,total loading rate dependence from the power (a) and from frequency detuning (b)

The *2D–MOT repumping* beam power efficiency has also been optimized in term of loading rate: the resulting trend points out a beginning of saturation effect around 8 mW (picture 5.21).

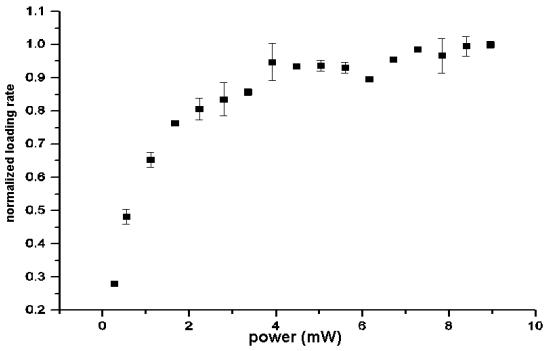

Figure 5.21: *3D–MOT* loading rate as a function of *repumper* total power.

Conclusions

In this Ph.D. thesis many steps relative to the study, the development and the realization of a transportable Atom Interferometer as an absolute acceleration sensor are illustrated.
Two items have been addressed, in the framework of international collaborations, during this experience: the realization of an absolute gravimeter for geophysical and metrological application and the realization of a Space Atom Interferometer for micro–gravity tests. My contribution for the absolute gravimeter has been concentrated on the laser system side and in particular on the realization of a compact subsystem for the interferometric atomic manipulation via two photons *Raman* transitions, in agreement with the system performance requirement. Laser sources specifically oriented to transportable devices have been introduced for the gravimeter laser system: very stable from the mechanical point of view, but also with a very narrow emission linewidth $\lesssim$ 200 kHz. Such innovation has represented a first enhancement for the apparatus performances. The atomic manipulation in our scheme is realized by means of two laser fields phase locked each other; the residual phase noise is not limiting the interferometer sensitivity as technical noise source any more. In our implementation a residual level of white phase noise of $-120\ dBrad^2/Hz$ has been achieved, full compatible with the requirements for the absolute gravimeter with a sensitivity $\Delta g/g = 10^{-10}/\sqrt{Hz}$.
The whole apparatus has been assembled in Berlin now and is going to be operative before a preliminary test and optimization stage.
The gravimeter realization has represented a fundamental progress in terms of know–how development also for the realization of the Space Atom Interferometer, even if the different task has leaded to deal with different specific issues. In this latest framework my contribution has been focused on the physics apparatus development, finding the best trade–off between interferometric performance enhancement and compatibility with micro–gravity test environment requirement. In particular the apparatus has been designed to be compatible with Bremen Drop Tower micro–gravity tests and thus to be

housed into the specific test capsule. The Space Atom Interferometer, with the efforts of groups involved into single subsystem realization, is being assembled in Firenze now, a terrestrial test stage will follow.
In this thesis a complete experience with a *Two Dimensional Magneto Optical Trap* has also been presented, integrated as cold atom source into the MAGIA experiment gradiometric apparatus. Such kind of implementation represents a fundamental issue in particular for the transportable gravimeter and for the Space Atom Interferometer. The realization of a differential vacuum pumping system, with the employment of a cold atom source for interferometer sample loading, guarantees a background gas pressure reduction in the physics chamber with also an enhancement of the loading rate that results into an experiment repetition rate improvement. In this specific case a background gas pressure reduction of two order of magnitude has been found respect to the traditional loading technique. A residual rubidium pressure of $\approx 10^{-11}$ mbar has been found. On the other side a loading rate enhancement of a factor ≈ 6 corresponds to this condition . The optimized loading rate value has been estimated in 7×10^9 atoms/s.

Prospectives

The target of this work is to demonstrate the technological readiness for the development of a new generation of quantum sensors. A new approach has been illustrated for atomic physics apparatuses realization at system and subsystem level. The realization of accurate transportable sensors based on Atom Interferometry, opens a new landscape either for applied physics and for the fundamental physics. Absolute gravity sensors, not affected from calibration drift, easily will find applications in geophysics and underground monitoring. On the other side such kind of devices represent a valid purpose for spaceborne accelerometric measurements.
The confirmed performances for an Atom Interferometry based sensor in micro–gravity conditions will lead to a wide range of fundamental physics applications. By the employment of two atomic different isotopes (^{85}Rb,^{87}Rb) high accuracy equivalence principle tests can be performed. On the other side, by the integration of gyroscope interferometric configurations, in the spaceborne experiments framework many gravitation and general relativity tests can be addressed (Lorentz invariance, Lense–Thirring effect, ...).
Nowadays Atom Interferometer based sensors are sensitivity limited from the quantum projection noise. From the recent studies on the number of atoms squeezing technics we can foresee that such a limit will be overcome. For this purpose the development of new interferometric setup will be furthermore needed.

Appendix A

Rubidium Data

Here are reported some typical quantities relative to ^{87}Rb that can be useful for the reading of this thesis. In table A.2 are reported specific data about D_2 transition. Data from [141].

Atomic Number	Z	36
Total Nucleons	$Z+N$	87
Nuclear Spin	I	3/2
Relative abundance	$\eta(^{87}Rb)$	27.83(2)%
Nuclear lifetime	τ_n	$4.88 \times 10^{10}\ yr$
Vapor Pressure ($25°C$)	P_v	$3.0 \times 10^{-7}\ torr$
Atomic mass	m	$1.44316060(11) \times 10^{-25}\ kg$
Ground State hyperf. splitting	ν_{ab}	6.834 682 610 90429(9) GHz
D_2 dipole matrix element	$\langle J=\frac{1}{2}\|er\|J'=\frac{3}{2}\rangle$	$3.584(4) \times 10^{-29}\ C\ m$
D_1 dipole matrix element	$\langle J=\frac{1}{2}\|er\|J'=\frac{1}{2}\rangle$	$2.537(3) \times 10^{-29}\ C\ m$

Table A.1: Rubidium Data Table (^{87}Rb)

Frequency	$\nu_{2\to3}$	384.2281152033(77) THz
Transition Energy	$h\nu_{2\to3}$	1.589049439(58) eV
		$2.5459376 \times 10^{-19}$ J
Wavelength (vacuum)	λ_{vac}	780.241209696(13) nm
Wavelength (air)	λ_{air}	780.03200 nm
Wavevector (vacuum)	k	80528.75481555 m^{-1}
Lifetime	τ	26.24(4) ns
Natural Linewidth	Γ	$2\pi \cdot 6.065(9)$ MHz
Saturation intensity	I_s	1.67 $mW\ cm^2$

Table A.2: Rubidium (^{87}Rb, D_2 transition data.)

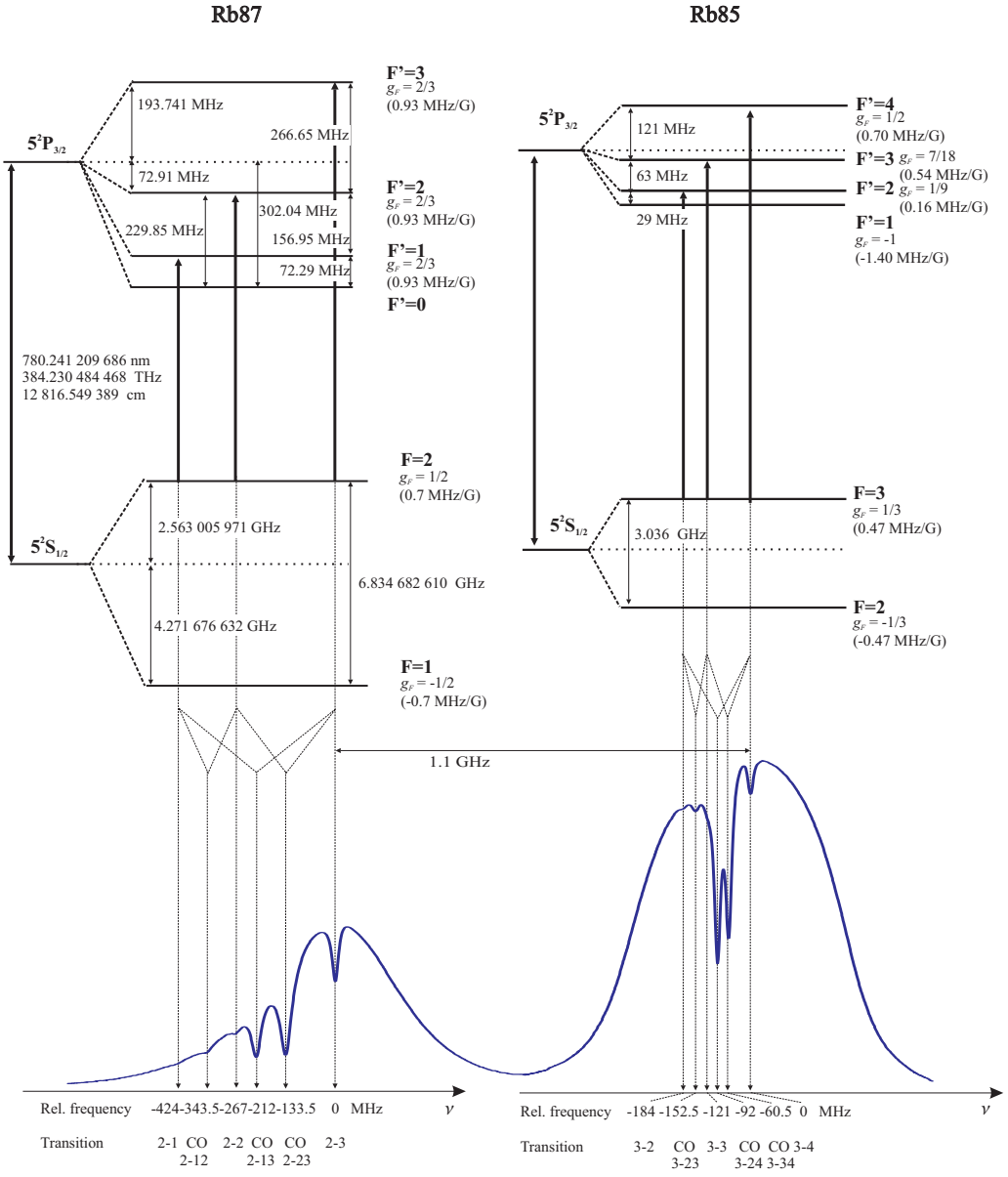

Figure A.1: Rubidium D_2 transitions from the upper hyperfine level $F = 2$ of the ground state, transitions frequencies are indicated. Below is reported the corresponding saturation spectroscopy signal with relative frequency distances. Indicated *Zeeman* shift must be multiplied by the m_F quantum number.

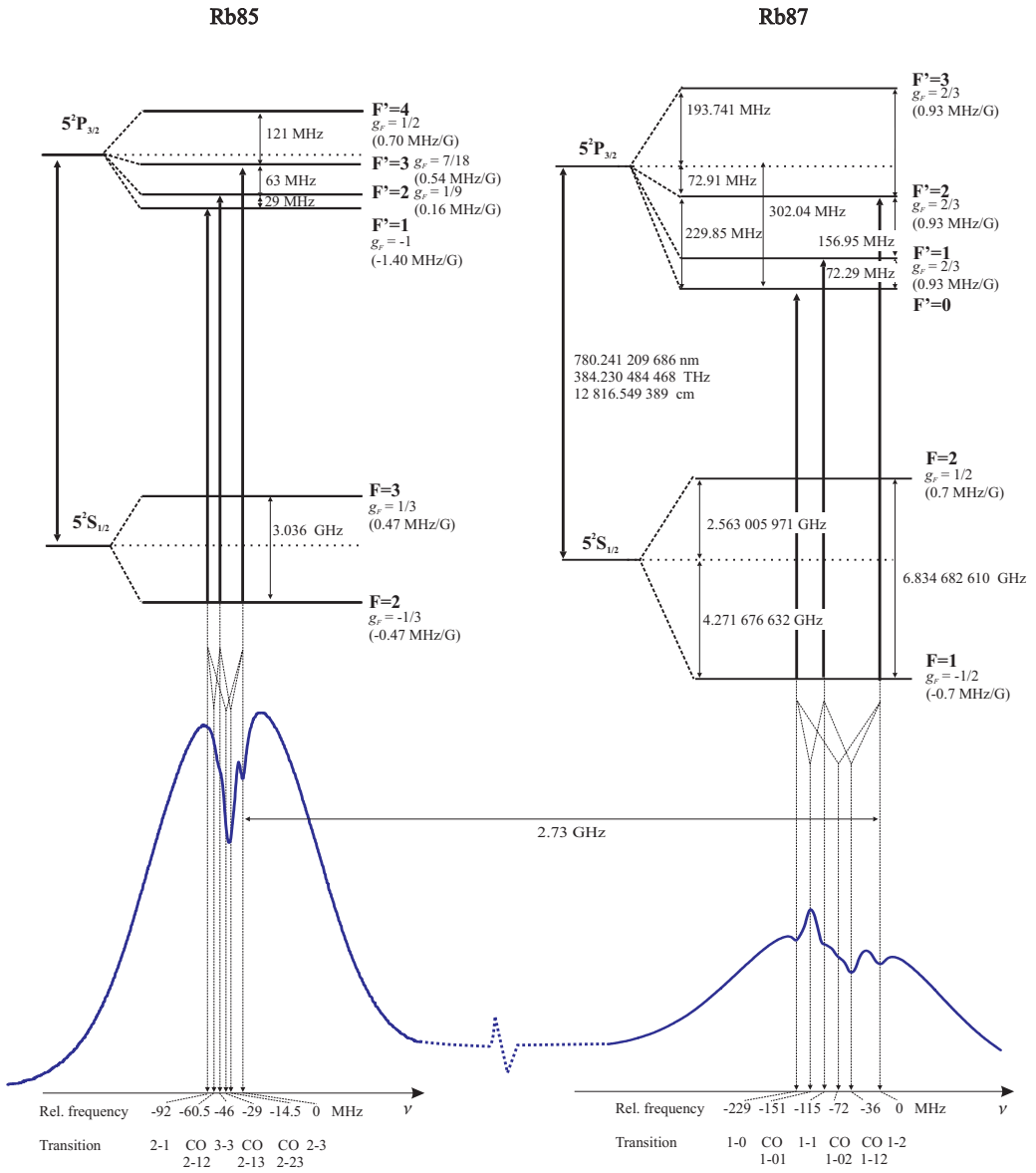

Figure A.2: Rubidium D_2 transitions from the upper hyperfine lower $F = 1$ of the ground state, transitions frequencies are indicated. Below is reported the corresponding saturation spectroscopy signal with relative frequency distances. Indicated *Zeeman* shift must be multiplied by the m_F quantum number

Appendix B

Space Atom Interferometer drawings and technical

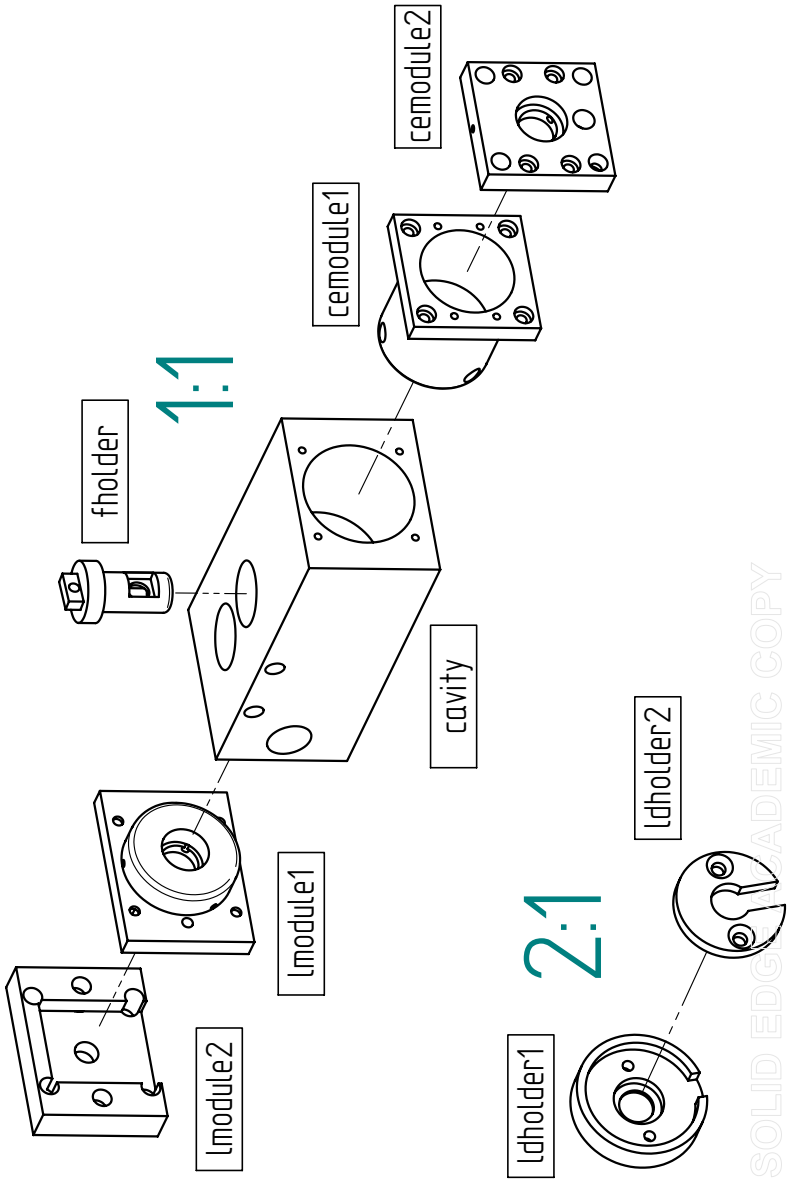

Figure B.1: *External Cavity Laser* Explosion draw [107].

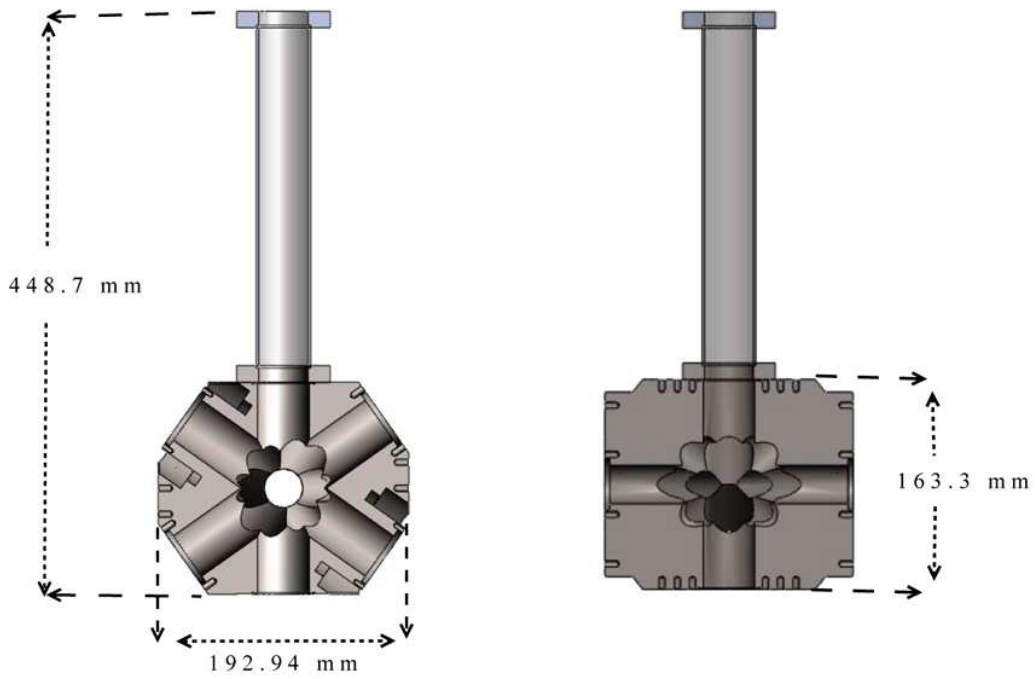

Figure B.2: *SAI* Physics Chamber Layout, cut view. On the left side optical access path for *3D-MOT* cooling beams is shown, on the right side optical accesses path for detection is visible. In both pictures *Raman* beams internal optical path along the vertical axis is visible.

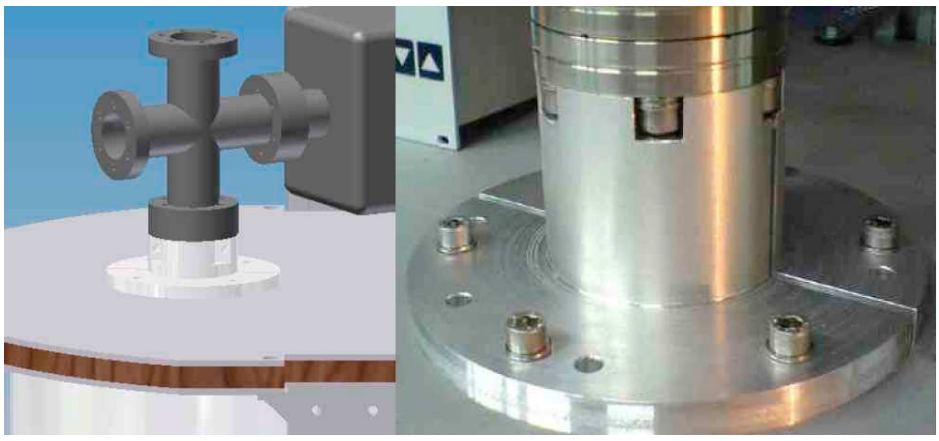

Figure B.3: Upper view of the clamp for *SAI* apparatus vacuum tube, on right side a picture from the realization for *AKTAT* apparatus [121, 138].

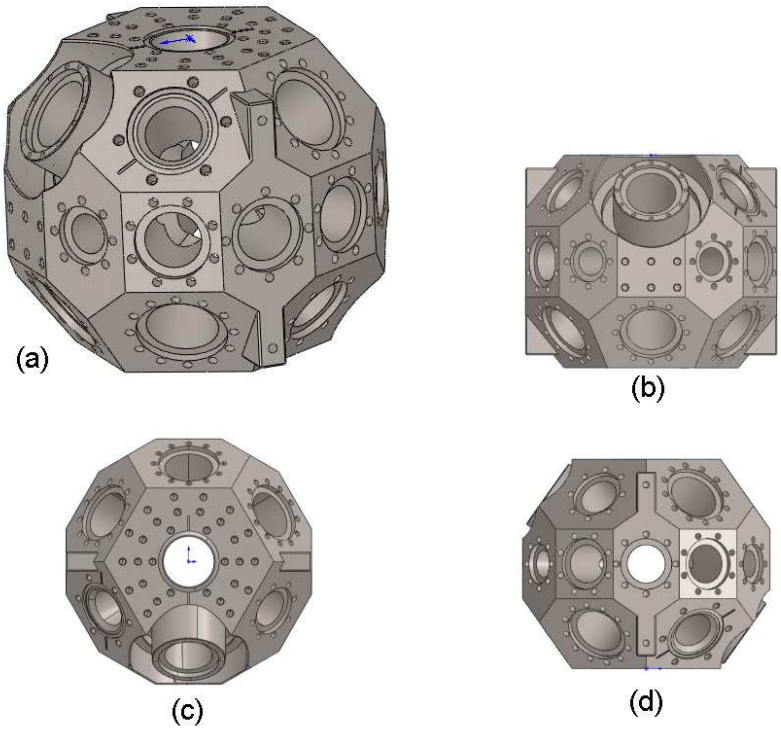

Figure B.4: *Space Atom Interferometer* main chamber four views [108, 135]. (a) 3D-view, (b) magnetic coils side, (c) top (bottom) view, (d) side machined for additional mechanical supports.

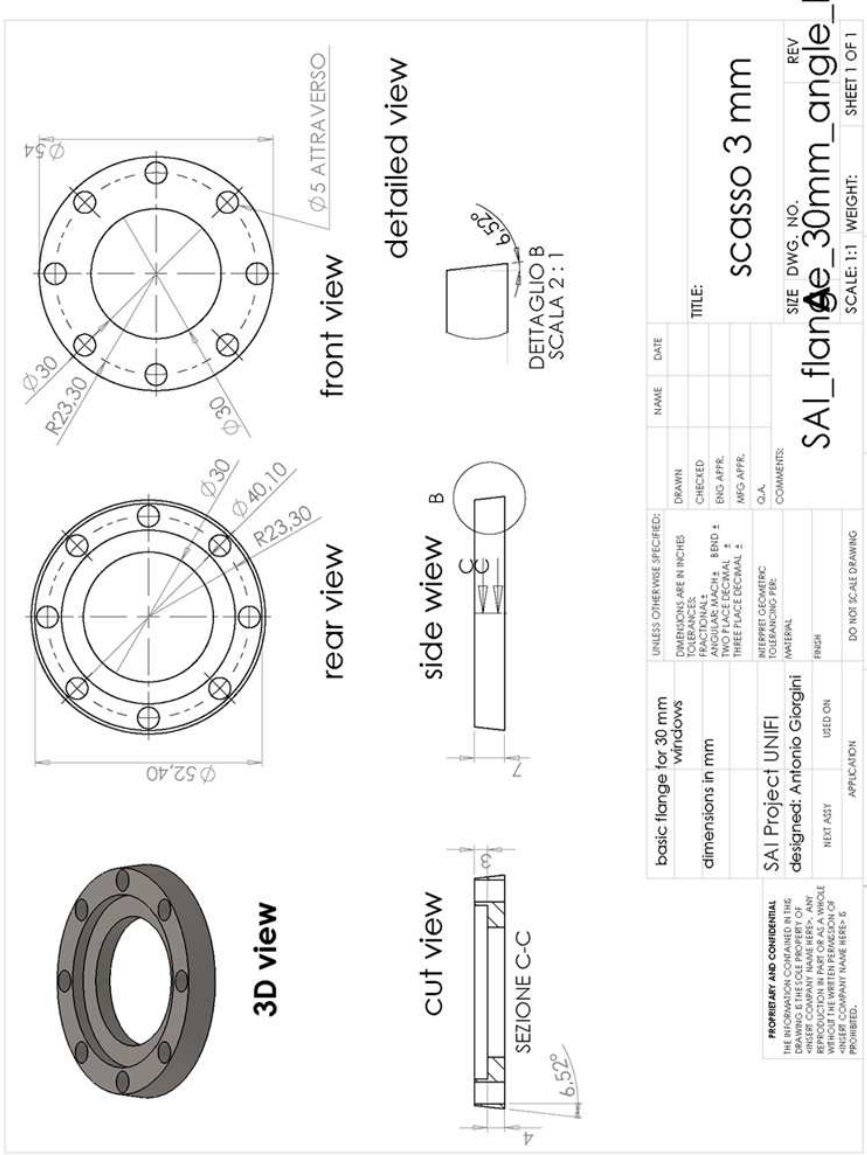

Figure B.5: *SAI* flange technical draw.

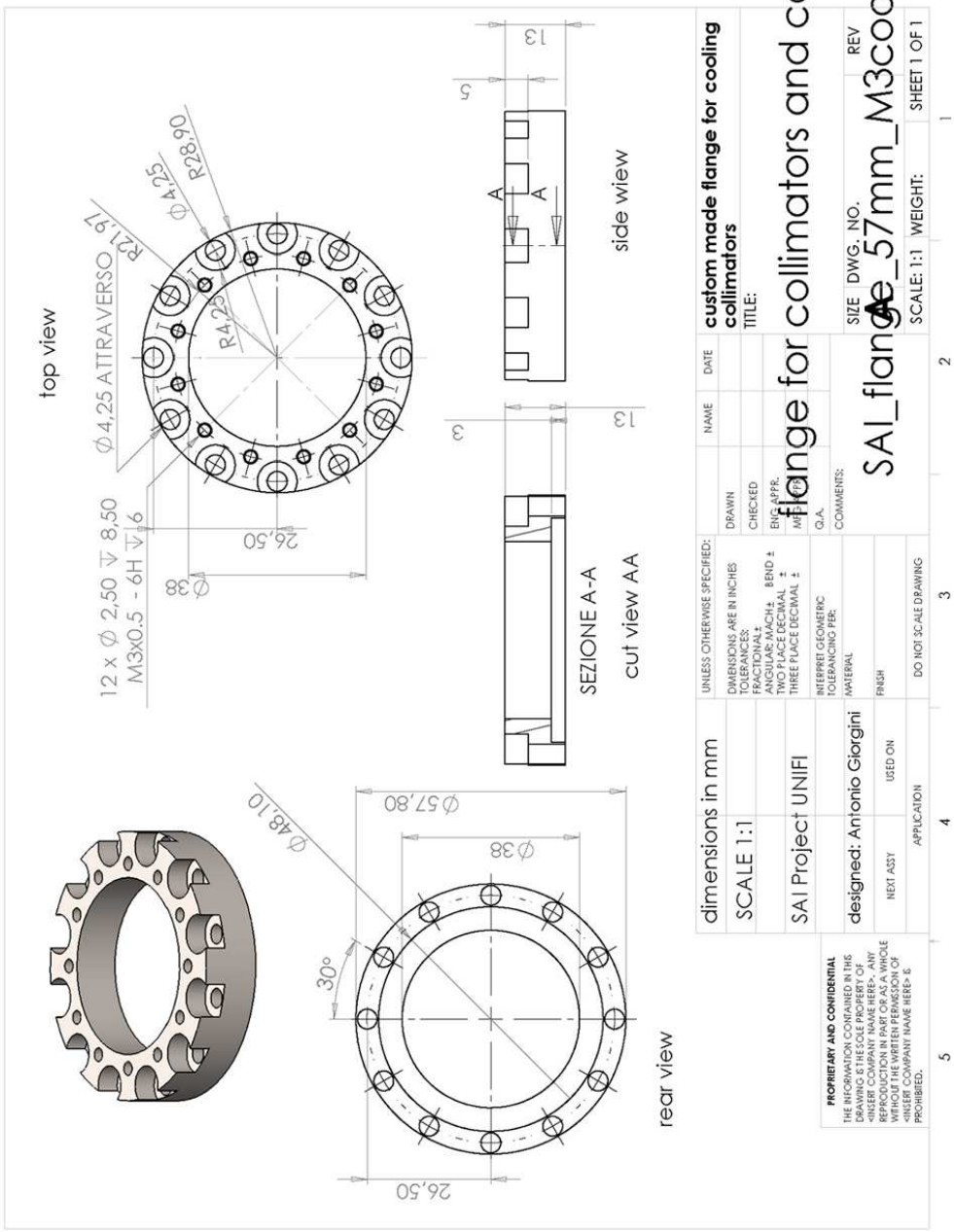

Figure B.6: *SAI* flange technical draw, *MOT* collimators special design.

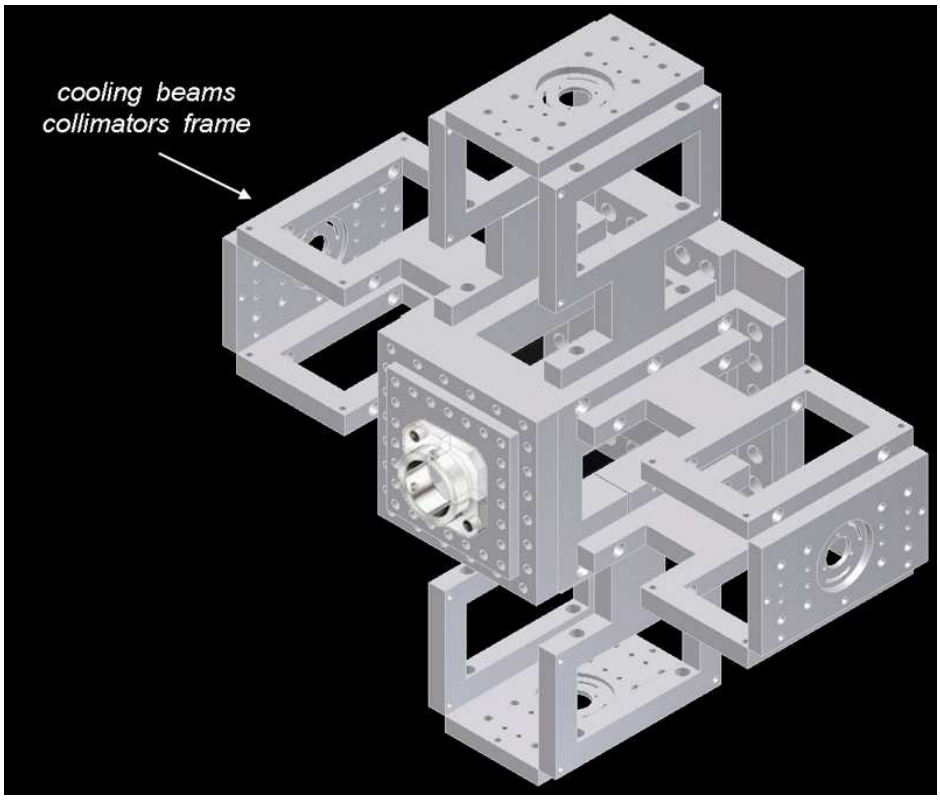

Figure B.7: 3D view of *Space Atom Interferometer 2D-MOT* mechanical frame, here seen from backside, the main body is at the center of the frame and four beam collimators are screwed on it in a crossing configuration. In back side an adaptor for pushing beam collimator [136].

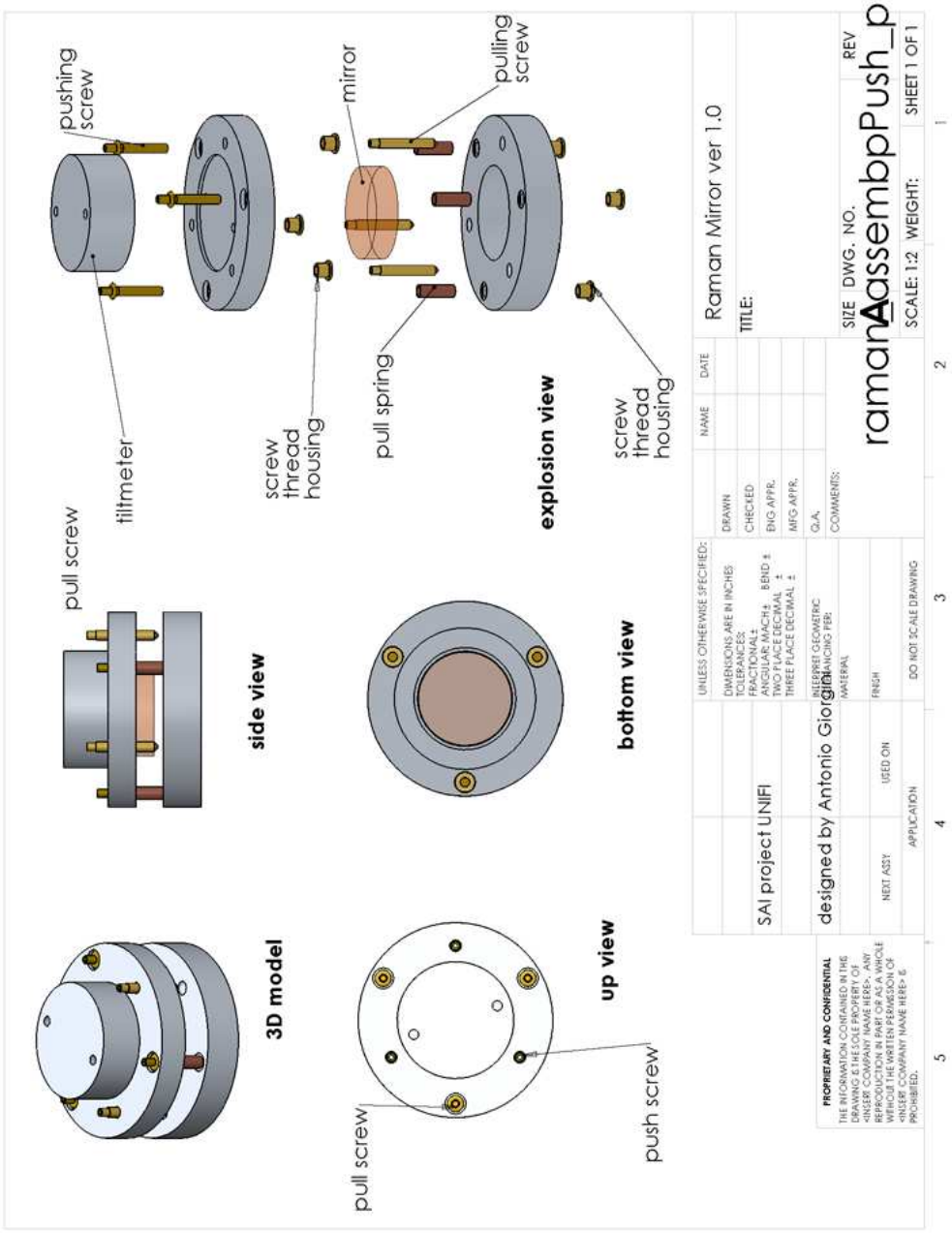

Figure B.8: Technical assembling draw for the *SAI Raman* retro–reflection mirror; basic concept and explosion view are shown.

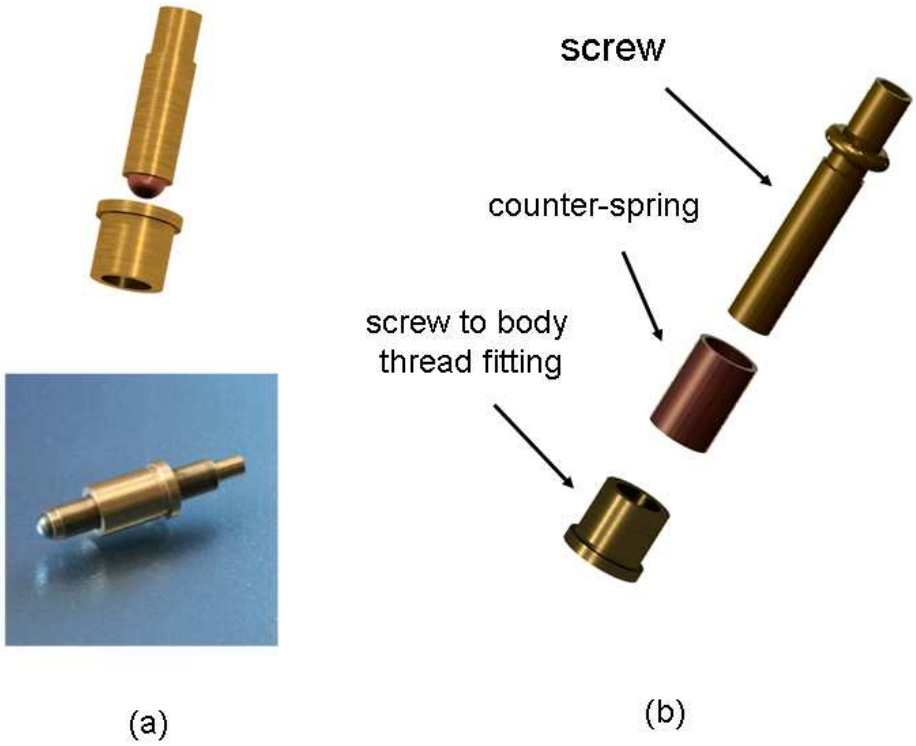

Figure B.9: Custom brass made non magnetic screws for *SAI* optomechanics apparatus, (a) pushing screw with ball, (b) pulling screw with counter-spring. (Typical $M4.15 \times 0.15$, $150\mu m/turn$ and hexagon socket) *MOT* collimators special design.

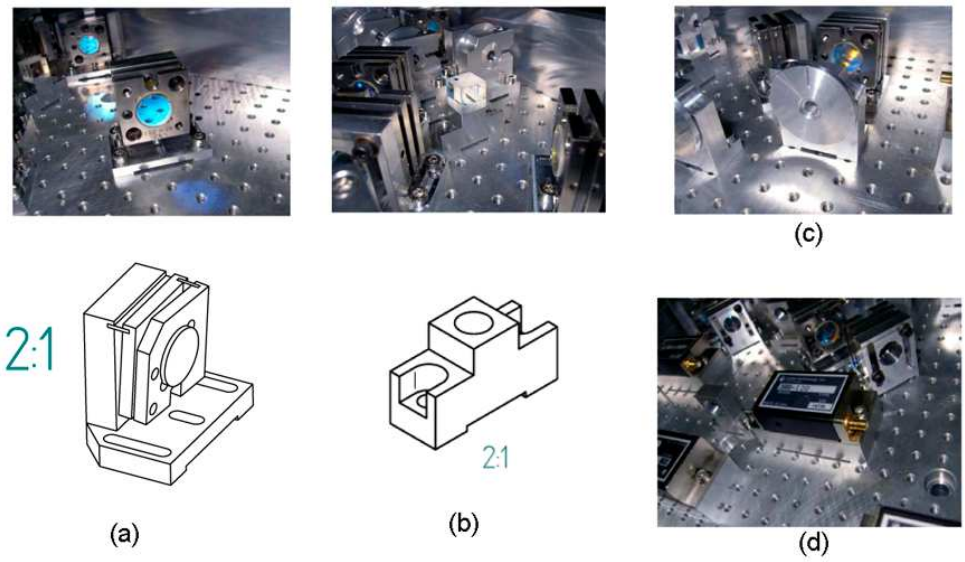

Figure B.10: Compact Opto-Mechanical components for *SAI* and *FINAQS* optical system. (a) tiltable mirror mount, (b) PBS mount, (c) waveplate mount, (d) *AOM* mount.

List of Figures

List of Tables

Bibliography

[1] Albert Camus, *Le Mythe de Sisyphe*, Gallimard, 1942 (ISBN 2070322882).

[2] Homer, *Iliad*, Book VI.

[3] Homer, *Odyssey*, Book XI.

[4] H. Kater, *An account of experiments for determining the length of the pendulum vibrating seconds in the latitude of London*, Philosophy. Trans. R. Soc. (London) 104 (33).

[5] E. Fermi and L. Marshall, *Interference Phenomena of slow neutrons*, Phys. Rev. 71, 666 (1947)

[6] L. Marton, *Electron interferometer*, Phys. Rev. 85, 1057 (1952)

[7] Y. Aharonov, D. Bohm, *Significance of Electromagnetic Potentials in the Quantum Theory*, Phys. Rev. 115, 485–491 (1959).

[8] Y. Aharonov, D. Bohm, *Further Considerations on Electromagnetic Potentials in the Quantum Theory*, Phys. Rev. 123, 1511–1524 (1961).

[9] Y. Aharonov, A. Casher, *Topological Quantum Effects for Neutral Particles*, Phys. Rev. Lett. 53, 319/321 (1984).

[10] A. Messiah, *Quantum Mechanics*, North–Holland Publishing Company, 1961.

[11] W.M. Itano, J.C. Bergquist, J.J. Bollinger, J.M. Gilligan, D.J. Heinzen, F.L. Moore, M.G. Raizen, D.J. Wineland, *Quantum Projection Noise: Population Fluctuation in two level system*, Phys. Rev. A, volume 47, nr.5 1993.

[12] D.J. Wineland, J.J. Bollinger, W.M. Itano, *Quantum Projection Noise: Population Fluctuation in two level system*, Phys. Rev. A, volume 50, nr.1 1994.

[13] L. D. Landau and L. M. Lifshitz, *Quantum Mechanics Non–Relativistic Theory*, Third Edition: Volume 3, ed. MIR, (1987).

[14] M. Battaglia, C. Roberts, P. Segall, *Magma Intrusion Beneath Long Valley Caldera Confirmed by Temporal Changes in Gravity*, 285 Science, 2119 (1999).

[15] A. Zollo, S. Judenherc, E. Auger, L. D'Auria, J. Virieux, P. Capuano, C. Chiarabba, R. de Franco, J. Makris, A. Michelini, G. Musacchio, *Evidence for the buried rim of Campi Flegrei caldera from 3d active seismic imaging*, Geophysical Research Letters, Vol. 30, NO. 19, 2002.

[16] S. Branca, D. Carbone, F. Greco, *Intrusive mechanism of the 2002 NE Rift eruption at Mt. Etna (Italy) inferred through continuous microgravity data and volcanological evidences*, Geophys. Res. Lett. 30(20), 2003.

[17] D. Carbone, L. Zuccarello, G. Saccorotti, F. Greco, *Analysis of simultaneous gravity and tremor anomalies observed during the 2002 / 2003 Etna eruption*, Earth and Planetary Science Letters 245 (2006).

[18] H. Rymer, *Microgravity change as a precursor to volcanic activity*, Journal of volcanology and geothermal research ISSN 0377–0273 CODEN JVGRDQ (1996).

[19] J. Dalibard Claude Cohen Tannoudji *Laser Cooling and Trapping of Neutral Atoms*

[20] P. Paul D. Lett, Richard N. Watts, Christoph I. Westbrook, William D. Phillips, Phillip L. Gould, Harold J. Metcalf, *Observation of Atoms Laser Cooled below the Doppler Limit*, Phys. Rev. Lett. 61, 169–172 (1988)

[21] A. Ashkin, J.P. Gordon, *Stability of Radiation Pressure Particle Traps: an Optical Earnshaw Theorem*, Opt. Lett. 8, 511 (1983).

[22] P. D. Lett, R. N. Watts, Ch. I. Westbrook, Ph. L. Gould, H. J. Metcalf and William D. Phillips *Observation of Atoms Laser Cooled below the Doppler Limit*, Phys. Rev. Lett. 61, 169–172 (1988).

[23] J. Dalibard and C. Cohen–Tannoudji *Laser cooling below the Doppler limit by polarization gradients: simple theoretical models*, J. Opt. Soc. Am. B 6, 2023–2045 (1989).

[24] S. Chu, D.S. Weiss, Y. Shevy, P.J. Ungar, in *Proceedings of the 11th Conference on Atomic Physics*, (Paris, July 1988). S Haroshe, J.C. Gray, and G. Grynberg editors, Word Scientific, Singapore, 1989.

[25] C. Monroe, W. Swann, H. Robinson, and C. Wieman, *Very cold trapped atoms in a vapor cell*, Phys. Rev. Lett. 65, 1571–1574 (1990).

[26] C. Salomon, J. Dalibard, W.D. Phillips, A. Clarion, S. Guellati, *Laser cooling of Cesium Atoms below* $3\mu k$, Europhys. Lett. 12 (8), pp 683–688 (1990).

[27] M. Kasevich and S. Chu, *Laser cooling below a photon recoil with three–level atoms*, Phys. Rev. Lett. 69, 1741–1744 (1992).

[28] L. Cacciapuoti, *Confinamento Magnetico ed Ottico di Atomi Raffreddati*, PhD Thesis, Università di Firenze (2000).

[29] W. Demtröder, *Laser Spectroscopy*, Springler–Verlag Berlin (1996).

[30] G. C. Bjorklund, M. D. Levenson, W. Lenth and C. Ortiz, *Frequency modulation (FM) spectroscopy*, Appl. Phys. B 32, 145–152 (1983).

[31] N.F. Ramsey *A Molecular Beam Resonance Method with Separated Oscillating Fields*, Phys. Rev. 78, 695–699 (1950).

[32] W. Demtröder, *Atom, Molecules and Photons*, Springler–Verlag, Berlin (2006).

[33] G.M. Tino, Lectures in Atomic Physics for Students, course at Università di Firenze, (feb. 2006).

[34] G.W.F. Drake (Ed.) AA.VV. , *Springer Handbook of Atomic, Molecular, and Optical Physics* Springler–Verlag, Berlin (2006).

[35] Claude Cohen Tannoudji, William Phillips Physics Today 43, No 10, 35 (1990).

[36] V.I. Balykin, V.G. Minogin, V.S. Letokhov, *Electromagnetic trapping of cold atoms*, Rep. Prog. Phys., 63, 1429 (2000).

[37] W.D. Phillips, H. Metcalf, *Laser Deceleration of an Atomic Beam*, Phys. Rev. Lett., 48, nr9 (1982).

[38] J.W. Prodan, W.D. Phillips, H. Metcalf, *Laser Production of a Very Slow Monoenergetic Atomic Beam*, Phys. Rev. Lett., 49, nr16 (1982).

[39] K. Lindquist, M. Stephens, C. Wieman, *Experimental and theoretical study of the vapor–cell Zeeman optical trap*, Physical Review A, volume 46, umber 7 (1992).

[40] Z. T. Lu, K. L. Corwin, M. J. Renn, M. H. Anderson, E. A. Cornell, and C. E. Wieman, *Low–Velocity Intense Source of Atoms from a Magneto–optical Trap*, Phys. Rev. Lett., volume 77, number 16 (1996).

[41] K. Dieckmann, R. J. C. Spreeuw, M. Weidemuller, J. T. M. Walraven, *Two–dimensional magneto–optical trap as a source of slow atoms*, Phys. Rev. A, volume 58, number 5, (1998).

[42] J. Schoser, A. Batär, R. Löw, V. Schweikhard, A. Grabowski, Yu. B. Ovchinnikov, and T. Pfau *Intense source of cold Rb atoms from a pure two–dimensional magneto–optical trap*, Physical Review A, 66, 023410, (2002).

[43] R.S. Conroy, Y. Xiao, M. Vengalattore, W. Rooijakkers, M. Prentiss, *Compact, robust source of cold atoms for efficient loading of a magnetic guide*, Optics Communications 226, 2003.

[44] K. J. Günter *Design and implementation of a Zeeman slower for 87Rb*, Groupe Atomes Froids, Laboratoire Kastler–Brossel Ecole Normale Superieure, Paris, March 2004

[45] J. Catani, P. Maioli, L. De Sarlo, F. Minardi, and M. Inguscio, *Intense slow beams of bosonic potassium isotopes*, Phys. Rev. A 73, 033415, 2006.

[46] S. Chaudhuri, S. Roy, C. S. Unnikrishnan, *Realization of an intense cold Rb atomic beam based on a two–dimensional magneto–optical trap: Experiments and comparison with simulations*, Phys. Rev. A 74, 023406 2006.

[47] T. Müller, T. Wendrich, M. Gilowski, C. Jentsch, E. M. Rasel, and W. Ertmer, *Versatile compact atomic source for high–resolution dual atom interferometry*, Phys. Rev. A 76, 063611 (2007).

[48] D. W. Allan, *Statistics of atomic frequency standards*, Proceedings IEEE, Volume 54 page 221, 1996.

[49] D.B. Sullivan, D. W. Allan, D. A. Howe, and F.L. Walls (authors–editors), *Characterization of Clocks and Oscillators*, NIST Technical note, NIST/TN–1337, March 1990.

[50] G.J. Dick *Local oscillator induced instabilities in trapped ion frequency standards*, Proc. of Precise Time and Time Interval, 133 147, Redendo Beach 1987.

[51] O. Carnal and J. Mlynek, *Youngs double–slit experiment with atoms: A simple atom interferometer*, Phys. Rev. Lett. 66, 2689–2692 (1991).

[52] D. W. Keith, Ch. R. Ekstrom, Q. A. Turchette, D. E. Pritchard, *An interferometer for atoms*, Phys. Rev. Lett. 66, 2693–2696 (1991).

[53] F. Riehle, Th. Kisters, A. Witte, J. Helmcke, Ch. J. Bordé, *Optical Ramsey spectroscopy in a rotating frame: Sagnac effect in a matter-wave interferometer*, Phys. Rev. Lett. 67, 177–180 (1991).

[54] M. Kasevich, S. Chu, *Atomic Interferometry Using Stimulated Raman Transitions*, Phys. Rev. Lett. Vol 67, Number 2 (1991).

[55] M. Kasevich, S. Chu, *Measurement of the Gravitational Acceleration of an Atom with a Light–Pulse Atom Interferometer*, Appl. Phys. B 54, 321 (1992).

[56] K. Moler, D. S. Weiss, M. Kasevich, S. Chu, *Theoretical analysis of velocity–selective Raman transitions*, Phys. Rev. A 45, 342 (1992).

[57] C. J. Bbordé, *Atomic Interferometry With Internal State Labelling*, Phys. Lett. A, Volume 140, number 1.2, 1989.

[58] C. J. Bbordé, *Theoretical tools for atom optics and interferometry*, C. R. Acad. Sci. Paris, t. 2, Série IV, p. 509/530, 2001.

[59] Pippa Storey, Claude Cohen–Tannoudji, *The Feynman path integral approach to atomic interferometry*, J. Phys. II France 4 (1994) 1999–2027.

[60] P. R. Berman, *Atom interferometry*, Academic press, 1997.

[61] A. Peters, *High Precision Gravity Measurement Using Atom Interferometry*, Ph.D. Thesis, Stanford University, (1998).

[62] A. Peters, C. K. Yeow, and S. Chu, *Measurement of gravitational acceleration by dropping atoms*, Nature 400, 849 (1999).

[63] A. Peters, K.Y. Chung, S. Chu, *High Precision Gravity Measurement Using Atom Interferometry*, Metrologia **38**, 25 (2001).

[64] Ch. J. Bordé, *Atomic clocks and inertial sensors*, Metrologia, 2002, 39, 435–463.

[65] M. J. Snadden, J. M. McGuirk, P. Bouyer, K. G. Haritos, and M. A. Kasevich, *Measurement of the Earths Gravity Gradient with an Atom Interferometer-Based Gravity Gradiometer*, Phys. Rev. Lett. 81, 971–974, (1998).

[66] J. M. McGuirk, G. T. Foster, J. B. Fixler, M. J. Snadden, M. A. Kasevich, *Sensitive absolute–gravity gradiometry using atom interferometry*, Phys. Rev. A 65, 033608 (2002).

[67] T. Petelski, *Atom Interferometers for Precision Gravity Measurements*, Ph.D. Thesis, European PhD School, Universitè Paris 6, Università degli Studi di Firenze, XVII Cycle, Submitted in February 2005.

[68] A. Bertoldi, G. Lamporesi, L. Cacciapuoti, M. de Angelis, M. Fattori, T. Petelski, A. Peters, M. Prevedelli, J. Stuhler and G. M. Tino, *Atom interferometry gravity–gradiometer for the determination of the Newtonian gravitational constant G*, Eur. Phys. Jour. D 40, 271, (2006).

[69] G. Lamporesi, A. Bertoldi, L. Cacciapuoti, M. Prevedelli and G. M. Tino, *Determination of the Newtonian gravitational constant using atom interferometry*, Phys. Rev. Lett. 100, 050801 (2008).

[70] P. Cheinet, B. Canuel, F.P.D. Santos, A. Gauguet, F. Leduc, A. Landragin, *Measurement of the sensitivity function in time–domain atomic interferometer*, submitted for publication to IEEE Trans. on Instrum. Meas. March 24 2005.

[71] P. Cheinet, *Conception et Réalisation dun Gravimètre à Atomes Froids*, Ph.D. Thesis, Universitè Pierre et Marie Curie, Laboratoire National de Metrologie et d'Essai Systemes de Reference Temps Espace, Paris, submitted in March 2006.

[72] J. Le Gouët, T. E. Mehlstäubler, J. Kim, S. Merlet, A. Clairon, A. Landragin, and F. Pereira Dos Santos, *Limits to the sensitivity of a low noise compact atomic gravimeter*, Appl. Phys. B 92, 133-144 (2008).

[73] G. Lamporesi, *Determination of the gravitational constant by atom interferometry*, Ph.D. Thesis, Università degli Studi di Firenze, XIX Cycle, Submitted in December 2006.

[74] F. Bongs, R. Launay, M. Kasevich, *High–order inertial phase shifts for time–domain atom interferometers*, Appl. Phys. B 84, (2006).

[75] R. P. Feynman and A. R. Hibbs, *Quantum Mechanics and Path Intagrals*, McGraw–Hill, New York, 1965.

[76] P. Meystre and M. Sargent, eds. III, *Elements of Quantum Optics*, Springer Verlag, Berlin, 1999.

[77] M. O. Scully, M. S. Zubairy *Quantum Optics*, Cambridge Univeristy Press, first ed. 1997, 2001.

[78] M. Born and E. Wolf, *Principles of Optics*, Pergamon Press, 1980.

[79] E. Hect, *Optics*, International Edition, ed. 4, Addison Wesley, 2002.

[80] O. Svelto *Principles of Lasers*, Plenum Press, New York 1998.

[81] A. Yariv *Optical Electronics*, Saunders College Publ., Fort Worth, TX, 1991, Sect. 10.7.

[82] A. L. Schawlow and C. H. Townes, *Infrared and Optical Masers*, Phys. Rev. 112, 1940 A958.

[83] C.H. Henry *Theory of the Linewidth of Semiconductor Lasers*, **IEEE** Journal of Quantum Electronics, VOL. $QE-18$, NO. 2, February 1982.

[84] G. Dick, *Local oscillator induced instabilities in trapped ion frequency standards. In Proc. of Precise Time and Time Interval*, Proc. of Precise Time and Time Interval, pages 133 147 , Redendo Beach, (1987).

[85] G. Santarelli, C. Audoin, A. Makdissi, P. Laurent, G.J. Dick, A. Clairon, *Frequency stability degradation of an oscillator slaved to aperiodically interrogated atomic resonator*, Ultrasonics, Ferroelectrics and Frequency Control, IEEE Transactions , Volume 45, Issue 4 (1998).

[86] S. S. Stein, *Frequency and Time, Their Measurement and Characterization*, from Precision Frequency Control, vol.2, (Academic Press, New York, 1985).

[87] A. Papoulis, *Probability, random variables and stochastic processes*, Third edition, chapter 10, Ed. Mcgraw Hill international (1991).

[88] K. Peterman, *Laser Diode Modulation and Noise*, Kluwer Academic Publishers, Tokyo (1991).

[89] M. Curtin, P. O'Brien *Phase–Locked Loops for High–Frequency Receivers and Transmitters*, Analog Dialogue 33–3, 33–5, 33–7, (1999 Analog Devices)

[90] M. Prevedelli, L. Cacciapuoti, M. de Angelis, M. Fattori, G. Lamporesi, T. Petelski, J. Stuhler, G. M. Tino*Analog+digital phase and frequency detector for phase locking of diode lasers*, Rev. Sci. Instrum. 76, 053111 (2005).

[91] M. Prevedelli, *Fast Phase–Frequency Detector*, *LENS* internal note, and private communication, April 28, (2006).

[92] G. Marro, *Controlli Automatici*, forth edition, ed. Zanichelli, Bologna, 1994.

[93] R. W. Fox, Chris W. Oates, L. W. Hollberg, *Stabilizing Diode Lasers to High–Finesse Cavities*, National Institute of Standards and Technology, Boulder, Colorado, USA, published in *Experimental Methods in the Physical Science*, Vol. 40, ISBN 0–12–475987–4.

[94] F.M. Gardner, *Phaselock Technique*, ed. Wiley Interscience, Wiley and Sons, Hoboken, New Jersey, 2005.

[95] P. Horowitz, W. Hill, *The Art of Electronics*, ed. Cambridge University Press, 1999.

[96] F. Sorrentino, *Laser frequency control for High resolution spectroscopy and metrological applications*, Ph.D. Thesis, Univ. Pisa.

[97] M. Tarallo, *Development of a Strontium optical lattice clock*, Ph.D. Thesis, Galileo Galilei School of Graduate Studies Course of Applied Physics, Univ. Pisa.

[98] P. Zorabedian, W.R. Trurna Jr. *Interference–filter–tuned, alignment–stabilized, semiconductor external–cavity laser* , Optics Letters, VOL. 13, NO. 10, October 1968. p 826–828.

[99] X. Balliard, A. Gauguet, S. Bize, P. Lemonde, Ph. Laurent, A. Clarion, P. Rosenbushc *Interference–filter–stabilized, external–cavity diode laser*, Optics Communications 266, p 609–613, (2006).

[100] C. Salomon et al., C.R. Acad. Sci. IV 2 (9) 2001, 1313

[101] M. de Angelis, A. Bertoldi, L. Cacciapuoti, A. Giorgini, G. Lamporesi, M. Prevedelli, G. Saccorotti, F. Sorrentino and G. M. Tino, *Precision gravimetry with atomic sensors* Meas. Sci. Technol. 20 (2009).

[102] G.Rosi, *Sviluppo di un gravimetro atomico trasportabile per applicazioni geofisiche*, Laurea thesis, Univ. Firenze, (2008).

[103] G.Campo, *Realizzazione di una trappola magneto–ottica in due dimensioni per atomi di rubidio*, Laurea thesis, Univ. Firenze, (2009).

[104] *Space Atom Interferometers* (***SAI***), ESA contract n.20578/07/NL/VJ AO–2004–064/082

[105] *Space Atom Interferometers* (***SAI***) *Technical Note TN3 - Laser System - Status*, ESA contract n.20578/07/NL/VJ AO–2004–064/082

[106] *Space Atom Interferometers* (***SAI***) *Technical Note TN5 - Raman Laser System for Wave–Packets Manipulation*, ESA contract n.20578/07/NL/VJ AO–2004–064/082

[107] M.Schmidt, AG Optical Metrology (Prof. A. Peters), Humboldt–Universität of Berlin, *FINAQS* and *SAI* collaborations, Private Communication. contact: `malte.schmidt@physik.hu-berlin.de`

[108] A.Senger, AG Optical Metrology (Prof. A. Peters), Humboldt–Universität of Berlin, *FINAQS* and *SAI* collaborations, Private Communications. contact: `senger@physik.hu-berlin.de`

[109] M. Schmidt, A. Senger, T. Gorkhover, S. Grede, E. Kovalchuk, A. Peters, *A Mobile Atom Interferometer for High Precision Measurements of Local Gravity* , In: Frequency Standards and Metrology - Proceedings of the 7th Symposium (2009), p. 511–516.

[110] M.Schmidt, M.Prevedelli, A.Giorgini, G.Tino, A.Peters, *A rack–mounted laser system for high precision atom interferometry*, in preparation.

[111] A. Vogel, M. Schmidt, K. Sengstock, K. Bongs, W. Lewoczko, T. Schuldt, A. Peters, T. Van Zoest, W. Ertmer, E. Rasel, T. Steinmetz, J. Reichel, T. Könemann, W. Brinkmann, E. Göklü, C. Lämmerzahl, H.J. Dittus, G. Nandi, W.P. Schleich, R. Walser, *Bose Einstein condensates in microgravity*, Appl. Phys. B84, (2006).

[112] N. Yu, J.M. Kohel, J.R. Kellogg, L. Maleki, *Development of an atom interferometer gravity gradiometer for gravity measurement from space*, Appl. Phys. B 84, (2006).

[113] T.L. Gustavson, A. Landragin, M.A, Kasevich, *Rotation sensing with a dual atom-interferometer Sagnac gyroscope*, Class. Quantum Grav. 17, 2385–2398 (2000).

[114] A. Gauguet, B. Canuel, T. Lévèque, W. Chaibi, A. Landragin, *Characterization and limits of a cold atom Sagnac interferometer*, arXiv:0907.2580v2 [physics.atom–ph] (2009).

[115] A. Landragin, P. Cheinet, F. Leduc, Ph. Bouyer, *Atom Interferometry*, NATO Science Series, Book, Springer Netherlands, ISSN: 1568–2609, (2006).

[116] P. Cheinet, F. Pereira dos Santos, T. Petelski, J. le Gouët, J. Kim, K.T. Therkildsen, A. Clairon, A. Landragin, *Compact laser system for atom interferometry*, Appl. Phys. B 84, 643–646, (2006).

[117] G. Stern, B. Battelier, R. Geiger, G. Varoquaux, A. Villing, F. Moron, O. Carraz, N. Zahzam, Y. Bidel, W. Chaibi, F. Pereira Dos Santos, A. Bresson, A. Landragin, and P. Bouyer, *Light pulse atom interferometry in microgravity*, Eur. Phys. J. D 53, (2009).

[118] J. H. Moore, Ch. C. Davis, M.A. Coplan, *Building Scientific Apparatus*, third ed., Advanced Books Program, Perseus Books, Cambridge, Massachusetts, (2003).

[119] W.Ertmer et al. *Matter wave explorer of gravity (MWXG)*, Exp Astron (2009).

[120] J. Appel, P. J. Windpassinger, D. Oblak, U. B. Hoff, N. Kjrgaard, E. S. Polzik, *Mesoscopic atomic entanglement for precision measurements beyond the standard quantum limit*, Submitted to Proceedings of the National Academy of Sciences of the United States of America arXiv:0810.3545v2 [quant-ph] 28 May 2009.

[121] T. Könemann, W. Brinkmann, E. Göklü, C. LämmerzahlH. Dittus, T. Van Zoest, E.M. Rasel, W. Ertmer, W. Lewoczko–AdamczykM. Schiemangk, A. Peters, A. Vogel, G. Johannsen, S.Wildfang, K. Bongs, K. Sengstock, E. Kajari, G. Nandi, R. Walser, W.P. Schleich, *A freely falling magneto–optical trap drop tower experiment*, Appl. Phys. B 89, 431–438 (2007).

[122] J. Kronjaeger, Cold Atoms Group (Prof. Kai Bongs), University of Birmingham, School of Physics and Astronomy, *SAI* collaboration, Private Communication. contact: `j.kronjaeger@bham.ac.uk`

[123] A. Rudge, Cold Atoms Group (Prof. Kai Bongs), University of Birmingham, School of Physics and Astronomy, *SAI* collaboration, Private Communication. contact: `ACR419@bham.ac.uk`

[124] M.Hauth, now at AG Optical Metrology, Humboldt–Universität of Berlin, *SAI* collaborations, Private Communications. contact: matthias.hauth@physik.hu-berlin.de

Web References

[125] Albert Camus, Nobel Prize in Literature 1957,

http://nobelprize.org
/nobel_prizes/literature/laureates/1957/camus-bio.html

[126] Steven Chu, The Nobel Prize in Physics 1997, *The Manipulation of Neutral Particles*, Nobel Lecture, December 8, 1997,

http://nobelprize.org/nobel_prizes/physics/
laureates/1997/chu-lecture.pdf

[127] Claude Cohen Tannoudji The Nobel Prize in Physics 1997, *Manipulating Atoms with Photons*, Nobel Lecture, December 8, 1997,

http://nobelprize.org/nobel_prizes/physics/
laureates/1997/cohen-tannoudji-lecture.pdf

[128] William D. Phillips The Nobel Prize in Physics 1997, *Laser Cooling and Trapping of Neutral Atoms*, Nobel Lecture, December 8, 1997,

http://nobelprize.org/nobel_prizes/physics/
laureates/1997/phillips-lecture.pdf

[129] NIST, *National Institute of Standards and Technology*,

http://www.nist.gov/

NIST, *Cesium Fountain Atomic Clock*,

http://tf.nist.gov/timefreq/cesium/fountain.htm

TUTORIALS, *Property of oscillators signal and measurement methods*,

http://tf.nist.gov/timefreq/phase/Properties/main.htm

[130] Micro–g LaCoste, A Division of LRS, gravimeter systems and gravity survey services,

http://www.microglacoste.com/

[131] GOCE, ESA's gravity mission,

http://www.esa.int/esaLP/LPgoce.html

[132] MatWeb material property data,

http://www.matweb.com

[133] Electronic Workshop, LENS *European Laboratory for Non–Linear Spectroscopy*, Università di Firenze

http://www.lens.unifi.it/ew/

[134] SYRTE department – Sytemes de Reference Temps Espace, belong to Paris Observatory, also associated with the CNRS – National Research Center and University Pierre and Marie Curie (Paris 6).

http://syrte.obspm.fr/

[135] AG Optische Metrologie (Prof. A. Peters), Humboldt–Universität zu Berlin Hausvogteiplatz 5–7, 10117 Berlin, Germany

http://www.physik.hu-berlin.de/qom

[136] Institut für Quantenoptik, Universität Hannover *Quantum Sensors Group* (Prof. E. Rasel), Welfengarten 1, 30167 Hannover, Germany

http://www.iqo.uni-hannover.de/

[137] Institut für Laser-Physik, Universität Hamburg, *Quantum Gases and Spectroscopy Group* (Prof. Kai Bongs), Luruper Chaussee 149, 22761 Hamburg, Germany

http://www.physnet.uni-hamburg.de/ilp/de/index.html

[138] ZARM, Center of Applied Space Technology and Microgravity, University of Bremen, Am Fallturm, 28359 Bremen, Germany

http://www.zarm.uni-bremen.de/

[139] Physics Department University of Firenze, Cold Atoms Group, Via Sansone 1, Sesto Fiorentino 50019, Firenze

http://coldatoms.lens.unifi.it/

[140] Future Inertial Atomic Quantum Sensors (FINAQS), A Specific Targeted Research Project (STREP) within NEST-2003-1, cooperation of the European Commission, Contr. No. 012986–2 NEST.

http://www.finaqs.uni-hannover.de/

[141] D. A. Steck, *Rubidium 87 D2 Line Data*, Alkali Data, http://steck.us/alkalidata